U.PORTO
FEUP FACULDADE DE ENGENHARIA
UNIVERSIDADE DO PORTO

High Purity H_2 Production in a Membrane Reactor Combined with CO_2 Sorption Through Glycerol Steam Reforming

Thesis presented to the

University of Porto

for the degree of

Doctor of Philosophy in Chemical and Biological Engineering

by

Joel Alexandre Moreira da Silva

Supervisor: Prof. Dr. Luís Miguel Palma Madeira

Co-Supervisor: Dr. Miguel Angel Soria

lepabe
Laboratory for Process Engineering, Environment, Biotechnology and Energy

Department of Chemical Engineering
Faculty of Engineering
University of Porto

November, 2018

Abstract

The main goal of this work was to combine the energetic valorization of glycerol, the main biodiesel by-product, by means of H_2 production through glycerol steam reforming (GSR) with the use of hybrid reactor concepts, such as sorption-enhanced reactor (SER), membrane reactor (MR) and sorption-enhanced membrane reactor (SEMR), whose performance should be compared with that of a traditional reactor (TR).

The thermodynamic analysis of GSR evidenced the presence of both CH_4 and coke as the main by-products, especially at lower temperatures and molar water/glycerol feed ratios (WGFR). The removal of CO_2 and H_2 from the reaction environment in the SEMR allowed the attainment of the maximum hydrogen yield of 7 $\mathrm{mol} \cdot \mathrm{mol}^{-1}_{\mathrm{converted\ glycerol}}$, at 700 K, WGFR of 9 and 1 atm. This corresponds to an enhancement of 217%, 47% and 22% comparatively to the TR, SER and MR, respectively.

In order to complement the GSR thermodynamic assessment, a phenomenological model, in a TR, capable of predicting both glycerol conversion and gas products generation (first time to the author's knowledge) under more realistic conditions was proposed. The model was validated against experimental data taken from the literature and a parametric analysis was carried out. While the conversion of glycerol was benefited at higher temperatures, WGFRs and pressures, both H_2 yield and selectivity were benefited at higher temperatures, but lower WGFRs and pressures.

The CO_2 sorption capacity of four prepared hydrotalcite-like materials was evaluated at 573 K. It was observed that the combination of partial substitution of aluminum with gallium, aging of the precipitated gel under microwave irradiation and impregnation with potassium (cK-HTCGa MW) significantly increased the sorption capacity. While the non-modified hydrotalcite (cHTC)

presented slightly faster CO_2 sorption, cK-HTCGa MW showed much higher sorption capacities.

For that reason, a deeper analysis of cK-HTCGa MW performance was carried out under conditions closer to those typically used in SERs. The material presented a CO_2 sorption working capacity of 0.7 $mol \cdot kg^{-1}$ at 6 bar, 673 K, 15 vol% CO_2 and under dry conditions. Moreover, in the presence of 10 vol% H_2O, an enhancement of 200% in sorption working capacity was observed, which could be partially associated to the observed mobilization of basic sites towards the surface of the hydrotalcite under wet conditions.

Catalytic GSR experiments were carried out over a Rh supported on alumina catalyst at 673 K, 4.5 bar and WGFR of 19, firstly in a TR. Even though high glycerol conversions into carbon-containing gaseous products were obtained during the first moments, rapid deactivation due to coke formation was observed. In order to maintain a superior catalytic performance over time, GSR was combined with periodic oxidative regeneration of the catalyst with air. This led to the attainment of total glycerol conversions above 99% for 16 h time-on-stream.

Finally, the GSR was performed in both SER and SEMR using a commercial hydrotalcite, K-MG30, and a Pd-Ag membrane, under the same conditions. The presence of the sorbent in the SER enhanced the production of H_2 not only in the CO_2 pre- and breakthrough regions, but also during the post-breakthrough. When the membrane was incorporated, the removal of both CO_2 and H_2 significantly increased the hydrogen yield from 1.6, in the SER, up to 3.6 $\mathrm{mol} \cdot \mathrm{mol}_{\mathrm{fed\ glycerol}}^{-1}$. Furthermore, besides the ultra-pure H_2 obtained in the permeate side, highly pure H_2 was obtained in the retentate side during the pre-breakthrough as no other gas products were produced.

Keywords: Glycerol; Steam Reforming; Hydrogen; Hydrotalcite; Sorption-Enhanced Membrane Reactor.

Resumo

O principal objetivo deste trabalho foi combinar a valorização energética do glicerol, principal subproduto do biodiesel, por meio da produção de H_2 através da reformação a vapor do glicerol (glycerol steam reforming, GSR) com a utilização de conceitos reacionais híbridos, tal como o reator de sorção (sorption-enhanced reactor, SER), reator de membrana (membrane reactor, MR) e o reator de sorção e membrana (sorption-enhanced membrane reactor, SEMR), cujo desempenho deve ser comparado com o de um reator convencional (traditional reactor, TR).

A análise termodinâmica de GSR demonstrou que os principais subprodutos do processo são o CH_4 e o coque, especialmente a temperaturas e razões molares água/glicerol na alimentação (molar water/glycerol feed ratios, WGFR) mais baixos. A remoção de CO_2 e H_2 do meio reacional no SEMR permitiu a obtenção do máximo rendimento de H_2 possível de 7 $\mathrm{mol} \cdot \mathrm{mol}^{-1}_{\text{glicerol convertido}}$, a 700 K, WGFR de 9 e 1 atm. Isto corresponde a um aumento de 217%, 47% e 22% comparativamente ao TR, SER e MR, respetivamente.

Com o objetivo de complementar a análise termodinâmica de GSR, foi proposto pela primeira vez um modelo fenomenológico, num TR, capaz de prever tanto a conversão de glicerol, como a formação de produtos gasosos em condições mais realistas. O modelo foi validado com resultados experimentais da literatura e foi realizada uma análise paramétrica. Enquanto a conversão de glicerol foi beneficiada a temperaturas, WGFRs e pressões mais altas, tanto o rendimento como a seletividade de H_2 foram beneficiados a temperaturas mais altas, mas a WGFRs e pressões inferiores.

A capacidade de sorção de CO_2 de quatro hidrotalcites preparadas foi avaliada a 573 K. Foi observado que a combinação da substituição parcial do alumínio por gálio, o envelhecimento do gel de precipitado sob radiação

microondas e a impregnação com potássio (cK-HTCGa MW) levou a um aumento significativo da capacidade de sorção. Enquanto a hidrotalcite não modificada (cHTC) apresentou captura de CO_2 ligeiramente mais rápida, cK-HTCGa MW apresentou capacidades de sorção muito mais elevadas.

Por essa razão, uma análise mais detalhada do desempenho da cK-HTCGA MW foi realizada sob condições mais próximas daquelas tipicamente usadas em SERs. O material apresentou uma capacidade de sorção de trabalho de 0.7 $mol \cdot kg^{-1}$ a 6 bar, 673 K, 15 vol% CO_2 e a seco. Para além disso, na presença de 10 vol% H_2O, um aumento de 200% na capacidade de sorção de trabalho foi observado, o que pode estar parcialmente associado à mobilização de centros alcalinos para a superfície, observada sob condições húmidas.

Testes catalíticos de GSR foram realizados utilizando um catalisador de Rh suportado em alumina a 673 K, 4.5 bar e WGFR de 19, em primeiro lugar num TR. Ainda que tenham sido obtidas inicialmente elevadas conversões de glicerol em produtos gasosos com carbono, foi observada desativação rápida devido à formação de coque. Com o objetivo de manter uma atividade catalítica superior ao longo de tempo, a GSR foi combinada com regeneração oxidativa periódica do catalisador com ar. Isto levou à obtenção de conversões totais de glicerol superiores a 99% durante 16 h de reação.

Finalmente, a GSR foi realizada no SER e no SEMR utilizando uma hidrotalcite comercial, K-MG30, e uma membrana de Pd-Ag, sob as mesmas condições. A presença do sorvente no SER aumentou a produção de H_2 não apenas durante o pre- e *breakthrough*, mas também durante o pós-*breakthrough*. Quando a membrana foi incorporada, a remoção de CO_2 e H_2 aumentou significativamente o rendimento de hidrogénio de 1.6, no SER, para 3.6 $\mathrm{mol} \cdot \mathrm{mol}^{-1}_{\mathrm{glicerol\ alimentado}}$. Além disso, para além do H_2 ultrapuro obtido no lado do permeado, H_2 altamente puro foi obtido no lado do retido durante o *pre-breakthrough* uma vez que mais nenhum produto gasoso foi produzido.

Palavras-chave: Glicerol; Reformação a Vapor; Hidrogénio; Hidrotalcite; Reator de Sorção e Membrana.

Agradecimentos

Ao Professor Miguel Madeira e ao Doutor Miguel Soria agradeço a disponibilidade para orientar este trabalho e toda a confiança que depositaram em mim ao longo destes 5 anos. Por todo o entusiasmo e dedicação, por todo o encorajamento que me foram transmitindo nos momentos mais difíceis e pela partilha festiva dos bons momentos, por toda a sabedoria que comigo foram partilhando e pela forma contínua como me foram desafiando, o meu mais sincero obrigado! Expresso também profunda gratidão por me terem visto crescer tão de perto ao longo dos últimos 5 anos como Engenheiro Químico, como investigador e acima de tudo, como ser humano!

Ao Professor Vicente Rives, à Professora Raquel Trujillano e ao Professor Miguel Vicente muito agradeço a hospitalidade com que me receberam durante a minha estadia no GIR-QUESCAT (Universidade de Salamanca, Salamanca, Espanha) e toda a sua colaboração na síntese e caracterização de hidrotalcites.

Ao Eng. Silvano Tosti agradeço pelo envio das membranas de Pd-Ag e pelo suporte que foi prontamente prestando.

Aos membros do grupo de investigação do Professor Madeira, a “Troop Madeira”, o meu muito obrigado pela vossa presença.

Ao Cláudio Rocha muito agradeço pelas discussões científicas diárias, pelos momentos descontraídos mais ou menos filosóficos, por todas as tainadas, por todas as partilhas musicais que tornaram o ambiente de trabalho mais leve, por toda a coragem que me foi transmitindo e pela forma como me vai inspirando. Acima de tudo agradeço-te pela tua profunda amizade!

À Catarina Faria e à Salomé Macedo, o meu muito obrigado por trazerem a vossa luz para o laboratório E-146. O meu muito obrigado por me terem permitido acompanhar parte da reta final do vosso percurso enquanto

estudantes do MIEQ e por me permitirem vislumbrar os vossos primeiros passos enquanto investigadoras.

Ao Carlos Miguel muito agradeço todas as sugestões e ideias que muito me foram ajudando durante o trabalho experimental que desenvolvi. Agradeço também pelos momentos de maior descontração que me foram permitindo ganhar algum fôlego para continuar.

À Carmen Rodrigues, ao Bruno Esteves, à Vanessa Lima, à Rose Duda e ao Samuel Queirós agradeço pela partilha do laboratório E203A durante os meus dias de bebé doutorando.

Ao Carlos Silva muito agradeço a forma como facilitou a minha chegada ao E-146 e a maneira descontraída e divertida com que tornou os meus dias de trabalho mais proveitosos. Pelos vários momentos partilhados, em ambiente académico ou boémio, e pela tua amizade, o meu muito obrigado.

À Natacha Rosa, pelas conversas profundas durante as pausas do trabalho que muito me vão inspirando para ser cada vez mais a pessoa que quero ser, e por todo o apoio dado na reta final deste percurso, o meu muito obrigado.

Ao Luís Carlos Matos muito agradeço por ter partilhado comigo parte da sua experiência profissional e por todo o apoio técnico que me foi dando ao longo deste percurso. Por todo o companheirismo e por toda a amizade, por ter acompanhado tão de perto o meu caminho profissional e pessoal e por ter contribuído tanto para a pessoa que sou hoje, o meu mais profundo obrigado!

Ao André Alves, à Joana Pereira e à Judith Pedroso muito agradeço pela vossa amizade de 10 anos que se iniciou no MIEQ e que segue caminho pela vida fora. Pela partilha do intenso percurso académico, pela oportunidade que me deram de vos conhecer melhor quando tudo indicava que os nossos caminhos iam divergir após finalizarmos o MIEQ, por todo o apoio que me têm dado e por todos os momentos mais ou menos boémios que temos partilhado, o meu mais profundo obrigado! Ao André Alves pela sua capacidade de catalisar a minha criatividade “javarda”; à Joana Pereira por me mostrar que o rumo das nossas vidas está nas nossas mãos e não em mãos alheias; à Judith pelos

pequenos-almoços animados e pela sua coragem e determinação inspiradoras; muito vos agradeço meus amigos! Um bem hajam!

Ao Danielson Pina muito agradeço pela sua amizade e companheirismo e pela sua capacidade de ir estando presente. Muito te agradeço também pelas longas horas que passamos em frente ao Aspen e por toda a sabedoria que me transmitiste.

À Alelí Rodríguez, muito obrigado por caminhares comigo nestes últimos anos e por todos os momentos de profunda inspiração danzantes. Tem sido um prazer partilhar este caminho contigo!

À Catarina Santos muito agradeço por todos os momentos de profunda partilha e inspiração danzantes. Por todas as experiências partilhadas e por todas as forcinhas que me tens transmitido ao longo deste percurso, o meu muito obrigado.

À Ana Cristina Azevedo, à Ana Cristina Sanches, ao Luís Marrafa e à Silvina Azevedo, a minha eterna profunda gratidão por me aceitarem plenamente em cada dança no meu valor único e absoluto e por me incentivarem a caminhar mais e mais em direção aos meus sonhos.

Ao José Oliveira e ao Tiago Azevedo (Sam), o meu muito obrigado por me acompanharem ao longo desta caminhada e por todo o ânimo que me têm transmitindo. Obrigado pelos momentos tão bem passados no “Tappas” que tanto me revitalizaram para continuar a caminhar.

Para com os meus amigos Junior, André Brandão, Diogo Leitão, Diogo Fula, Ana Pecegueiro e Ana Luísa Santos expresso a mais profunda das gratidões, sem motivos específicos, apenas pela vossa existência sagrada na minha vida! Sem vocês seria certamente muito menos do que o que sou... Ao Junior pela sua alegria de viver e coragem inabaláveis; ao André Brandão pela sua criatividade profundamente humana; ao Diogo Leitão pela sua coragem inspiradora de viver cada dia à sua maneira; ao Diogo Fula pelo seu companheirismo e carinho tão profundos; à Ana Pecegueiro pela sua espontaneidade e pureza tão intrínsecos; à Ana Luísa Santos pela sua doçura tão profunda; o meu mais sentido agradecimento meus amigos!

À Catarina, por estar sempre ao meu lado de uma forma tão profundamente presente; por me ter acompanhado de várias formas durante estes últimos anos; por sempre me ter apoiado incondicionalmente tanto nos momentos de grande realização como nos momentos de maior frustração; por aceitar e potencializar mais e mais a pessoa que sou; por todo o amor e carinho que me tem demonstrado; por trazer para a minha vida uma felicidade com todo um novo significado, que tanto tem contribuído para que esta tese seja um pouco mais a imagem da pessoa que sou; a ti Pi, o meu mais profundo e comovido obrigado!!!

Aos meus tios e primos agradeço as palavras de encorajamento que sempre me foram dando para que continuasse este caminho com coragem e alma.

Aos meus padrinhos, Vitor Moreira e Rosaria Sousa o meu muito obrigado por todo o apoio e força que sempre me deram e pelo profundo carinho com que sempre me presentearam.

Aos meus avós agradeço profundamente pela forma como foram estando presentes na minha vida e pelos seus exemplos de vida. Ao meu avô Almerindo Moreira e à minha avó Maria Alice Correia, os meus segundos pais, o meu eterno agradecimento pelo vosso amor e ternura que tanto me têm inspirado!

Ao meu irmão Gonçalo agradeço toda a leviandade e alegria com que me tem presenteado. Obrigado por me ires lembrando do que é ser criança e do quão importante é manter viva a criança que existe dentro de mim, pois como em tudo que faço na vida, nesta tese fica também uma grande marca dessa criança.

Aos meus pais, Joaquim e Marta, por sempre me terem apoiado incondicionalmente ao longo da minha vida, por sempre me motivarem para dar o melhor de mim em cada momento e por todo o amor que me têm transmitido, o meu muito obrigado! Ao meu pai muito agradeço por toda a força e capacidade de dedicação a aperfeiçoamento que me tem demonstrado e transmitido. À minha mãe agradeço profundamente a forma tão próxima, carinhosa e sensível

como tem acompanhado toda esta etapa da minha vida! Para com vocês os dois expresso a minha mais profunda e sentida gratidão!

Agradeço ao Laboratório para Engenharia do Processo, Ambiente, Biotecnologia e Energia (LEPABE), e ao projeto NORTE-01-0145-FEDER-000005 – LEPABE-2-ECO-INNOVATION, suportado pelo Programa Operacional Regional do Norte de Portugal, sob o acordo de parceria Portugal 2020, através do Fundo de Desenvolvimento Regional Europeu. Agradeço também ao Programa Doutoral em Engenharia Química e Biológica da Faculdade de Engenharia da Universidade do Porto e à Fundação para a Ciência e Tecnologia (FCT) pela bolsa de doutoramento com a referência (PD/BD/52625/2014), financiada pelo Fundo Social Europeu (ESF) e por fundos nacionais suportados pelo Ministério da Ciência, Tecnologia e Ensino Superior.

Contents

List of Figures

Chapter 2

Chapter 3

Subchapter 3.1

Subchapter 3.2

Chapter 4

Subchapter 4.1

Subchapter 4.2

Chapter 5

Subchapter 5.1

Subchapter 5.2

List of Tables

Chapter 2

Chapter 3

Subchapter 3.1

Subchapter 3.2

Chapter 4

Subchapter 4.1

Subchapter 4.2

Chapter 5

Subchapter 5.1

Subchapter 5.2

Chapter 1. General Introduction

This chapter presents the relevance and motivation behind this PhD thesis and provides a brief introduction to the study. At the end the objectives of this PhD work are established and the thesis outline is provided.

1.1 Relevance and Motivation

Resorting to fossil-based processes, such as steam reforming of methane, has been the solution that most industries have found economically more attractive for hydrogen production in the last century. However, an environmental caring mentality has been taking over. Replacing fossil fuels (natural gas, oil and coal) with cleaner fuels such as biodiesel-derived glycerol has been target of interest [1-3]. Such replacement would not only have a direct positive environmental impact, but would also promote both commercialization and further development of biodiesel production and industry [4].

On a different perspective and addressing the increasing need of ultra-pure hydrogen, pushed by the development of the fuel cell industry, two reaction-separation hybrid concepts have been proven to be highly beneficial when compared to the conventional process. The selective removal of hydrogen by means of a permselective membrane and carbon dioxide by means of a selective sorbent from the reaction medium can be achieved in membrane reactors (MRs) [5-7] and sorption-enhanced reactors (SERs) [7-9], respectively. The use of such concepts has been proven advantageous since they shift the equilibrium of thermodynamically-limited reactions towards higher reactants conversions and at the same time allow producing pure hydrogen streams, especially MRs where hydrogen is separated from all other gases. The SER with a CO_2 sorbent also allows reducing carbon dioxide emissions, being that if ways to valorize the captured CO_2 are found it would make the concept even more attractive. Moreover, since both these concepts combine reaction and separation in a single unit, the reduction of capital costs could be significant.

This thesis addresses, therefore, the production of H_2 through glycerol steam reforming (GSR), and to the proof-of-concept of the mentioned multifunctional reactor concepts (SER and MR) and of an even more intensified reaction-separation unit that combines both H_2 separation and CO_2

sequestration in the same device – the sorption-enhanced membrane reactor (SEMR).

1.2 Objective and Outline of the Thesis

The main objective of this PhD work was to better understand the GSR process and to enhance its operation by resorting to the application of SER and MR concepts (as compared to a traditional reactor –TR) and, ultimately, by carrying it in a SEMR, having in mind the maximization of the selective conversion of glycerol into H_2. In order to achieve this, several stages were required and are depicted in the following thesis outline.

Chapter 2 presents a comprehensive literature review on: GSR thermodynamics and the influence of removing H_2 or CO_2 from the reaction medium on the thermodynamic equilibrium of such process; an overview of the most relevant GSR catalysts reported in the literature and a summary of some of the proposed kinetics; a summary of experimental assessments of GSR on both SERs and MRs, focusing firstly on the most promising CO_2 sorbents and H_2-permselective membranes and later on the effects of the most relevant parameters affecting the GSR reaction in SERs and MRs.

Chapter 3 encompasses a predictive analysis of the GSR process towards H_2 production. The first subchapter presents a thermodynamic analysis, carried out in Aspen Plus software, to understand the thermodynamic limitations of the GSR process and how it is affected when H_2 and/or CO_2 are removed from the reaction medium. In the second subchapter a phenomenological model is proposed to describe the performance of a TR and, after validation of the model with data taken from the literature, a parametric analysis was carried out.

Chapter 4 addresses the synthesis, characterization and testing of hydrotalcite-based sorbents for high temperature CO_2 capture. In the first

subchapter several hydrotalcite-like materials were prepared at GIR-QUESCAT, at the University of Salamanca (Spain), characterized through several techniques, and the sorption equilibrium isotherms of all materials were determined through static CO_2 sorption tests at 573 K. Afterwards, the sorption kinetics during the CO_2 uptakes of the different materials was modeled. In the second subchapter, the sorbent considered as the most promising in the previous subchapter was submitted to a long term experimental campaign of CO_2 breakthrough experiments under different operating conditions, in order to evaluate its sorption capacity, stability and bed usage efficiency. The fresh, calcined and used sorbent samples were characterized through several techniques in order to assess how the 300 h long experimental campaign affected its structure and surface composition.

Chapter 5 deals with the experimental assessment of GSR towards H_2 production. In the first subchapter, a Rh-based catalyst supplied by Johnson Matthey was used during the catalytic tests in a TR. The formation of coke on the catalyst was assessed through several characterization techniques and a combination of the GSR process and oxidative regeneration of the used catalyst was tested. In the second subchapter, GSR experiments over the same catalyst and under the same operating conditions used in the TR were carried out firstly in a SER, where a commercial potassium-promoted hydrotalcite from Sasol was used as CO_2 sorbent. The SER tests were carried out combining or not both GSR and regenerative oxidation of both catalyst and sorbent. A Pd-Ag tubular membrane supplied by Eng. Silvano Tosti (ENEA, Frascati, Rome – Italy) was submitted to preliminary H_2 permeation tests at different pressures, being followed by the experimental assessment of GSR combined with oxidative regeneration in the SEMR. Ultimately, a comparison between the TR, SER and SEMR is presented in terms of total glycerol conversion and glycerol conversion into carbon-containing gaseous products, gas products yields and selectivities, coke formation and H_2 purity.

Chapter 6 presents the general conclusions of this work, some of its limitations and perspectives of future work.

1.3 References

[1] Avasthi, K.S., R.N. Reddy, and S. Patel, *Challenges in the production of hydrogen from glycerol – A biodiesel byproduct via steam reforming process.* Procedia Engineering, 2013, 51(0), 423-429.

[2] Dou, B., Y. Song, C. Wang, H. Chen, and Y. Xu, *Hydrogen production from catalytic steam reforming of biodiesel byproduct glycerol: Issues and challenges.* Renewable and Sustainable Energy Reviews, 2014, 30(0), 950-960.

[3] Lin, Y.-C., *Catalytic valorization of glycerol to hydrogen and syngas.* International Journal of Hydrogen Energy, 2013, 38(6), 2678-2700.

[4] Yang, F., M.A. Hanna, and R. Sun, *Value-added uses for crude glycerol--a byproduct of biodiesel production.* Biotechnology for Biofuels, 2012, 5(1), 13.

[5] Gallucci, F., E. Fernandez, P. Corengia, and M. van Sint Annaland, *Recent advances on membranes and membrane reactors for hydrogen production.* Chemical Engineering Science, 2013, 92, 40-66.

[6] Basile, A., J. Tong, and P. Millet, *2 - Inorganic membrane reactors for hydrogen production: an overview with particular emphasis on dense metallic membrane materials*, in *Handbook of Membrane Reactors*, A. Basile, Editor. 2013, Woodhead Publishing. p. 42-148.

[7] Rodrigues, A.E., L.M. Madeira, R. Faria, and Y.J. Wu, *Sorption Enhanced Reaction Processes*. 2017: World Scientific Publishing Company Pte Limited.

[8] Wu, Y.J., P. Li, J.G. Yu, A.F. Cunha, and A.E. Rodrigues, *Progress on sorption-enhanced reaction process for hydrogen production.* Reviews in Chemical Engineering, 2016, 32(3), 271-303.

[9] Shokrollahi Yancheshmeh, M., H.R. Radfarnia, and M.C. Iliuta, *High temperature CO2 sorbents and their application for hydrogen production by sorption enhanced steam reforming process.* Chemical Engineering Journal, 2016, 283, 420-444.

Chapter 2. Challenges and Strategies for Optimization of Glycerol Steam Reforming Process – State of the Art

The steam reforming of the main biodiesel by-product, glycerol, has been catching up the interest of the scientific community in the last years. The use of glycerol for hydrogen production is an advantageous option not only because glycerol is renewable but also because its use would lead to the decrease of the price of biodiesel, thus making it more competitive. Consequently, the use of biodiesel at large scale would significantly reduce CO_2 emissions comparatively to fossil fuels. Moreover, hydrogen itself is seen as a very attractive clean fuel for transportation purposes. Therefore, the industrialization of the glycerol steam reforming (GSR) process would have a tremendous global environmental impact. In the last years, intensive research regarding GSR thermodynamics, catalysts, reaction mechanisms and kinetics, and innovative reactor configurations (sorption-enhanced reactors (SERs) and membrane reactors (MRs)) has been done, aiming for improving the process effectiveness. In this review, the main challenges and strategies adopted for optimization of GSR process are addressed, namely the GSR thermodynamic aspects, the last developments on catalysis and kinetics, as well as the last advances on GSR performed in SERs and MRs.

The contents of this chapter were adapted from: Silva, J.M., M.A. Soria, and L.M. Madeira, *Challenges and strategies for optimization of glycerol steam reforming process.* Renewable and Sustainable Energy Reviews, 2015, 42, 1187-1213.

2.1 Introduction

Biodiesel is a promising alternative energy source because it is a renewable fuel and reduces greatly CO_2 emissions compared to fossil fuels (Fig. 2.1). The production of biodiesel is most commonly done through transesterification with methanol of triglycerides extracted from sunflower oils, soybean and rapeseed (Fig. 2.2). This process produces glycerol as the main by-product (100 kg of glycerol/ton of biodiesel) [1, 2]. Moreover, the annual worldwide production of biodiesel has been in an increasing trend lately, as can be seen in Fig. 2.3 [3]. However, biodiesel is not competitive in terms of price yet [4]. One way of lowering the production cost of biodiesel would be to use its main by-product, glycerol, to produce H_2 (or syngas) via steam reforming, for example, thus providing an extra value to such a waste.

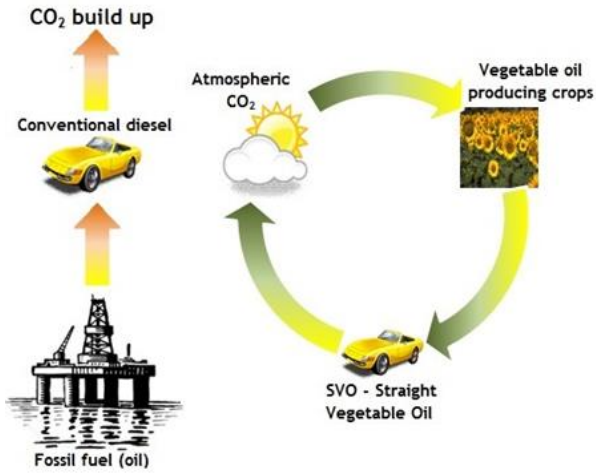

Fig. 2.1 - Comparison of CO_2 emission cycles between conventional diesel and biodiesel.

Hydrogen is a clean energy source with numerous uses and its demand is expected to greatly increase in the future, mainly due to the technological advancements in the fuel cell industry. Nowadays, nearly 48% of the worldwide produced hydrogen is generated through the steam reforming of methane

(SRM), while the reforming of naphtha/oil contributes with 30%, the coal gasification with 18% and electrolysis with only 3.9% [5]. The SRM, in particular, consists of CH_4 reacting with H_2O to yield syngas at high temperatures (700-1100 ºC) [4]. Stoichiometrically, 4 mol of H_2 can be obtained per mole of methane through SRM, while 7 mol of H_2 can be extracted from 1 mol of glycerol through glycerol steam reforming (GSR), as presented in Eq. (2.1).

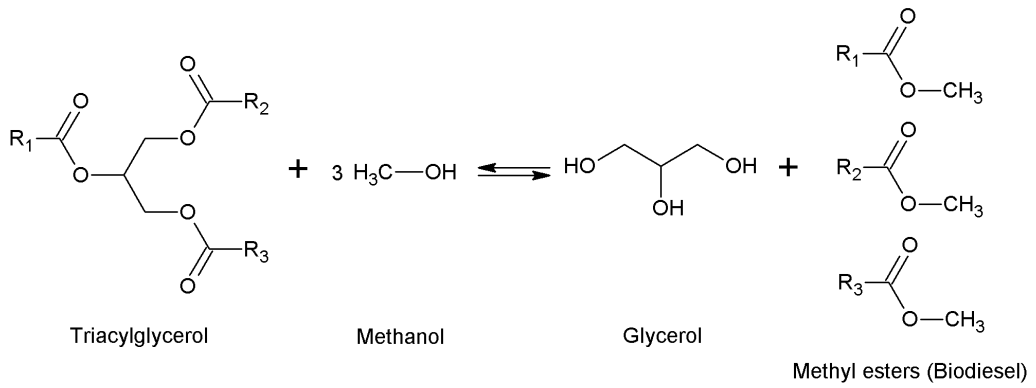

Fig. 2.2 - Overall reaction of triglycerides transesterification with methanol for biodiesel production yielding glycerol as by-product.

$$C_3H_8O_3 + 3H_2O \rightarrow 7H_2 + 3CO_2 \quad (\Delta H_r^{298\,K} = 128\,kJ \cdot mol^{-1}) \qquad \textbf{(2.1)}$$

Furthermore, while for SRM a fuel (CH_4) is consumed to produce another fuel, the same thing does not happen for GSR. Therefore, the use of glycerol instead of methane would be advantageous [4]. Even though steam reforming is the main target of focus in this review, there are other methods to convert glycerol into H_2:

- Auto-thermal reforming [6-8].
- Partial oxidation gasification [9-11].
- Aqueous-phase reforming [12-14].
- Supercritical water reforming [15-17].

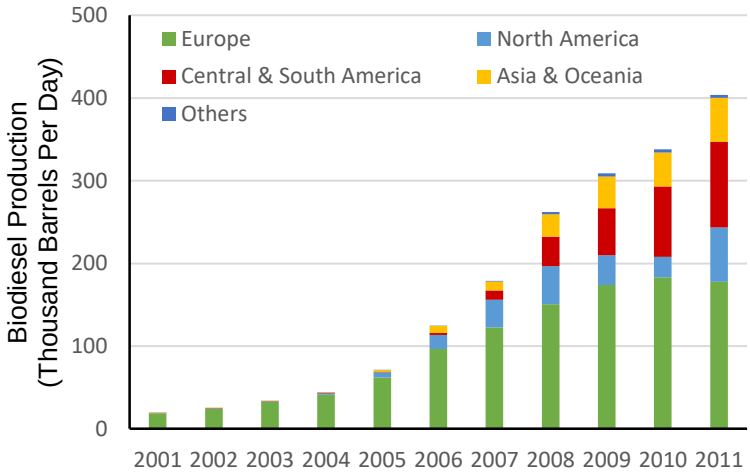

Fig. 2.3 - Evolution of worldwide biodiesel production between 2001 and 2011 [3].

The reason why GSR was chosen as focus of study instead of any of the other processes is mainly due to the fact that the steam reforming process is widely used in industry and it would not require many changes in the system if the feedstock was changed from natural gas or naphtha to glycerol [4].

The GSR process, like any other process, has some challenges that need to be overcome in order to accomplish its effective commercialization. Some of the main challenges are:

- The GSR is an endothermic reaction, thus requiring high temperatures and inherently high operating costs. Furthermore, more resistant reactors would be needed and so higher capital costs would be involved.
- The GSR process has side reactions, which affect both production and purity of H_2. The main side reactions represented by Eqs. (2.2-2.4) lead to methane formation either by reaction of carbon monoxide and hydrogen or reaction of carbon dioxide and hydrogen or through hydrogenolysis of glycerol, respectively.

$$CO + 3H_2 \rightleftharpoons CH_4 + H_2O \quad (\Delta H_r^{298\,K} = -206\ kJ \cdot mol^{-1}) \qquad \textbf{(2.2)}$$

$$CO_2 + 4H_2 \rightleftharpoons CH_4 + 2H_2O \quad (\Delta H_r^{298\,K} = -165\ kJ \cdot mol^{-1}) \qquad \textbf{(2.3)}$$

$$C_3H_8O_3 + 2H_2 \rightarrow 2CH_4 + CO + 2H_2O \quad (\Delta H_r^{298\,K} = -160\ kJ \cdot mol^{-1}) \qquad \textbf{(2.4)}$$

- Although 7 mol of hydrogen should theoretically be produced per each mole of glycerol that reacts, many authors have observed upper H_2 yield limits lower than 7 [18-23].
- The GSR is a thermodynamically-limited reaction (Eq. (2.1)), being inherently the conversion detrimentally affected in certain conditions, particularly at lower temperatures [24].
- The formation of coke is also an issue since it deactivates the catalyst, thus affecting H_2 yield and purity and long term operation.
- Besides producing hydrogen the GSR reaction also produces carbon dioxide, whose release is target of environmental concern and restricted by legislation.

With the aim of addressing these problems, new catalysts have been developed and different purification methods have been studied. Moreover, new reactor configurations combining the GSR reaction and hydrogen or carbon dioxide selective removal have also been target of intense research, due to their potential to solve some of the limitations previously mentioned. In this review some of the important developments regarding the GSR reaction (including thermodynamics, developed catalysts and reaction kinetics) and its combination with a hydrogen permselective membrane or a CO_2 sorbent, in the perspective of process intensification, are reviewed. Up to the author's knowledge, a review that conjugates a literature survey of all these subjects is still missing.

2.2 Thermodynamics of GSR – Influence of different parameters

2.2.1 Conventional GSR

The GSR is an equilibrium-limited process, as previously mentioned, that involves the decomposition of glycerol followed by the water-gas shift (WGS) reaction:

$$C_3H_8O_3 \rightarrow 3CO + 4H_2 \quad (\Delta H_r^{298\,K} = 251\ kJ \cdot mol^{-1}) \qquad \textbf{(2.5)}$$

$$CO + H_2O \rightleftharpoons H_2 + CO_2 \quad (\Delta H_r^{298\,K} = -41\ kJ \cdot mol^{-1}) \qquad \textbf{(2.6)}$$

In order to maximize the production of hydrogen, one must first fully understand how the thermodynamic boundaries are influenced by the different parameters.

There are several studies focused on the thermodynamics of the GSR [24-31]. One of the most important parameters affecting any reaction system is temperature. Once glycerol decomposition is highly endothermic and requires more heat than that produced in the WGS reaction, the overall GSR process is endothermic (Eq. (2.1)), thus meaning that higher temperatures benefit the H_2 production (glycerol conversion, H_2 yield and selectivity) (Fig. 2.4) [24]. Mathematically, the equilibrium of a system at constant pressure and temperature is given as follows:

$$dG = \sum_{i=1}^{K} \mu_i dn_i = 0 \qquad \textbf{(2.7)}$$

where G is the Gibbs free energy, μ_i is the chemical potential of component i and n_i is the number of moles of component i in the system. The goal is to determine the set of n_i values that minimize de value of G (thermodynamic equilibrium). There are two different thermodynamic approaches that can be

used to solve this: (i) stoichiometric [30, 32, 33] and (ii) nonstoichiometric [24-28, 31, 34-38]. By using the stoichiometric approach a set of stoichiometrically independent reactions, which are normally chosen arbitrarily from a set of possible reactions, is used to describe the system. Instead, if the nonstoichiometric method is used the equilibrium composition is calculated based on the direct minimization of the Gibbs free energy of a specific set of species [27]. Both methods have their own advantages, however there has been a significant tendency towards the nonstoichiometric one. In fact, the use of the latter does not require a selection of the possible set of reactions. Moreover, during computation there is no divergence and there is no need of an accurate initial estimation of the equilibrium composition [27].

Since the GSR is an endothermic process ($\Delta H^0 > 0$), if higher temperatures are used more hydrogen is produced, thus confirming the trend in Fig. 2.4. Furthermore, a variation of the number of moles of all products (H_2, CO, CO_2 and CH_4) with temperature is also observed in this figure. At lower temperatures, the formation of H_2, CO_2 and CH_4 as main products is seen. This might be due to the fact that the exothermic WGS and methane formation reactions are mainly favored at low temperatures. In contrast, endothermic reactions like GSR and reverse WGS are more favored at higher temperatures. This could explain the increase of both H_2 and CO contents and the small decrease of CO_2 observed at those temperatures. In any case, an optimum high temperature is normally determined. However, higher temperatures are not favorable from the economic point of view and so alternative ways to attain high H_2 production yields have to be considered.

The molar water/glycerol feed ratio (WGFR) has also been found to highly influence the production of H_2 (mainly the H_2 yield and selectivity) in the equilibrium. Considering the Le Chatelier's principle, it is expectable that for higher WGFRs the equilibrium shifts towards the consumption of the excess of water, thus producing more hydrogen. Such a behavior has been indeed verified

and, as can be seen in Fig. 2.5 [29], the H_2 yield increases as the WGFR increases from 4 to 15, whatever the temperature.

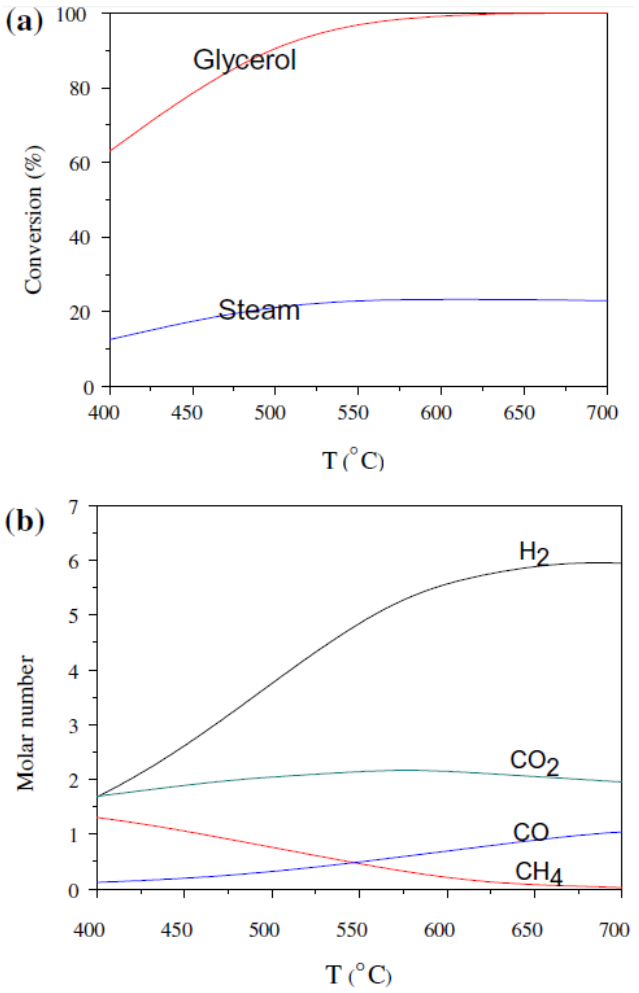

Fig. 2.4 - Thermodynamic equilibrium of GSR: (a) glycerol and steam conversions and (b) moles of gas products. Molar water/glycerol feed ratio (WGFR) = 9, atmospheric pressure and considering Eqs. (2.2), (2.5) and (2.6). Taken from [24].

For WGFRs above 9 the H_2 yield increases at a slower rate, especially at higher temperatures. However, the amount of water used should not be too high due to the excessive vaporization costs that it would bring at industrial scale. Moreover, it should be chosen taking into consideration the H_2O activation capacity of the catalyst used and the other operating conditions (temperature and pressure).

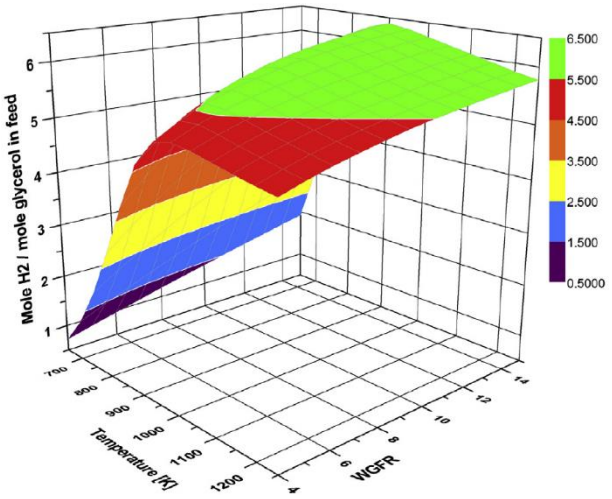

Fig. 2.5 - Moles of H_2 produced per mole of glycerol during GSR as function of WGFR and temperature at 1 atm and considering Eqs. (2.2), (2.3), (2.5) and (2.6). Taken from [29].

The influence of both operation temperature and WGFR on the formation of coke has been investigated as well [25, 28, 39]. Adhikari *et al.* [28] suggest that carbon formation may happen through the following reactions:

$$2CO \rightleftharpoons CO_2 + C \quad (\Delta H_r^{298\,K} = -172\ kJ \cdot mol^{-1}) \tag{2.8}$$

$$CH_4 \rightleftharpoons 2H_2 + C \quad (\Delta H_r^{298\,K} = 75\ kJ \cdot mol^{-1}) \tag{2.9}$$

$$CO + H_2 \rightleftharpoons H_2O + C \quad (\Delta H_r^{298\,K} = -131\ kJ \cdot mol^{-1}) \tag{2.10}$$

$$CO_2 + 2H_2 \rightleftharpoons 2H_2O + C \quad (\Delta H_r^{298\,K} = -90\ kJ \cdot mol^{-1}) \tag{2.11}$$

Fig. 2.6 [25] shows that, in order to avoid carbon formation, which poisons the catalysts, high WGFRs and temperatures should be used. In fact, for WGFRs higher than 5, carbon formation is completely inhibited for all the temperature range considered (550-1000 K). These results are in line with those obtained by Adhikhari *et al.* [28] and Authayanun *et al.* [39].

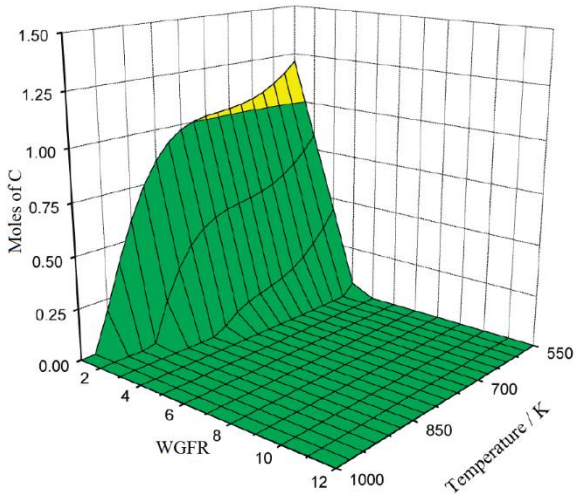

Fig. 2.6 - Moles of carbon formed as a function of WGFR and temperature at 50 atm. Adapted from [25].

Pressure is also an important parameter because it has a significant influence on the performance of reaction systems. That influence is even more noticeable for processes during which there is variation of the total number of moles, like the GSR, since it affects the thermodynamic equilibrium (Le Chatelier's principle). For the case of GSR, higher pressures lead to a lower hydrogen production in the equilibrium. Moreover, enhanced formation of methane has also been verified [25, 28-30]. Therefore, it results to be advantageous to use lower pressures not only because it is economically more attractive (as far as the pressure is not too low) but also because it leads, under equilibrium, to higher H_2 production (Fig. 2.7) [26]. Pressures lower than the atmospheric pressure would be desired, however, these pressures are more difficult to attain under economically attractive conditions in industrial practice. An alternative way to achieve this would be to use a carrier gas to dilute the reactants, thus decreasing their partial pressures. Chen *et al.* [26] came to the conclusion that by increasing the amount of carrier gas, not only the maximum H_2 production increased but also the optimum temperature dropped. Although it may seem a good solution, at industrial scale it is not so attractive since it would require complex separation processes after the reactor.

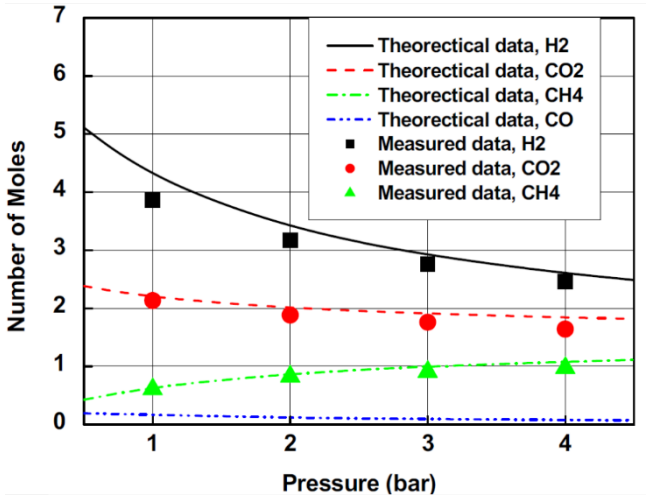

Fig. 2.7 - Effect of total pressure on the number of moles of different components in the equilibrium. T = 450 °C, WGFR = 9, feeding reactants to inert gas ratio = 1:4. Taken from [26].

In sum, it is clear that high temperatures, high WGFRs and low pressures favor hydrogen production in the equilibrium. Temperatures between 580-702 ºC, WGFRs between 9-12 and atmospheric pressure have been reported in the literature as optimum conditions [25-27, 29].

2.2.2 GSR with CO_2 sorption

It is clear that even at favorable conditions, the GSR equilibrium is still quite limiting in terms of H_2 yield, for example. For the cases analyzed in the previous section, the maximum H_2 yields observed were close to 6, due to the co-existence of several reaction apart GSR. However, according to the GSR reaction stoichiometry (Eq. (2.1)), a maximum H_2 yield close to 7 can be obtained. Such a yield could be reached by performing GSR simultaneously with CO_2 capture, since the selective removal of CO_2 shifts the thermodynamic equilibrium towards higher H_2 yields. The sorption-enhanced glycerol steam reforming (SEGSR) process also allows to work at milder operating conditions, thus leading to lower operation costs. Moreover, since the emissions of CO_2 are

diminished, the SEGSR can be considered as a good solution as long as there is a way to store/valorize captured CO_2 [40]. In this section a review of some thermodynamic studies on SEGSR is done.

Different approaches have been used to account for CO_2 sorption in thermodynamic simulations. Wang *et al.* [41] accounted for 17 species in SEGSR among which 13 were gases and 4 were solids. These solids include carbon, CaO, $CaCO_3$ and $Ca(OH)_2$. It is assumed that, in the presence of a CO_2 sorbent like CaO, the following reactions take place:

$$CaO(s) + CO_2(g) \rightleftharpoons CaCO_3(s) \quad \textbf{(2.12)}$$

$$CaO(s) + H_2O(g) \rightleftharpoons Ca(OH)_2(s) \quad \textbf{(2.13)}$$

$$Ca(OH)_2(s) + CO_2(g) \rightleftharpoons CaCO_3(s) + H_2O(g) \quad \textbf{(2.14)}$$

In Fig. 2.8 [41] the effect of temperature and WGFR on the equilibrium concentration of H_2 (dry basis) during (a) GSR and (b) SEGSR is presented. For the first case, the observed behavior is very similar to what has already been discussed in the previous section. Regarding the SEGSR, it can be observed that for increasing WGFR values, at constant temperature, the equilibrium hydrogen concentration also increases for the reason stated before. Therefore a balance should be sought, being that a value of 9 is proposed by Chen *et al.* [42] and Silva *et al.* [43] as the most favorable for hydrogen production. In terms of temperature, a more noticeable effect is observed. While for temperatures between 500-900 K and constant WGFR there is an increase of the equilibrium hydrogen concentration, for temperatures above 900 K this concentration decreases. The authors suggest that the increase of the H_2 concentration up to 900 K is associated to the compromise between Eqs. (2.2), (2.5), (2.6), (2.12) and (2.13). The decrease of the equilibrium hydrogen concentration observed thereafter is due to the fact that the CO_2 sorption described by Eq. (2.12) is inhibited due to its exothermic nature.

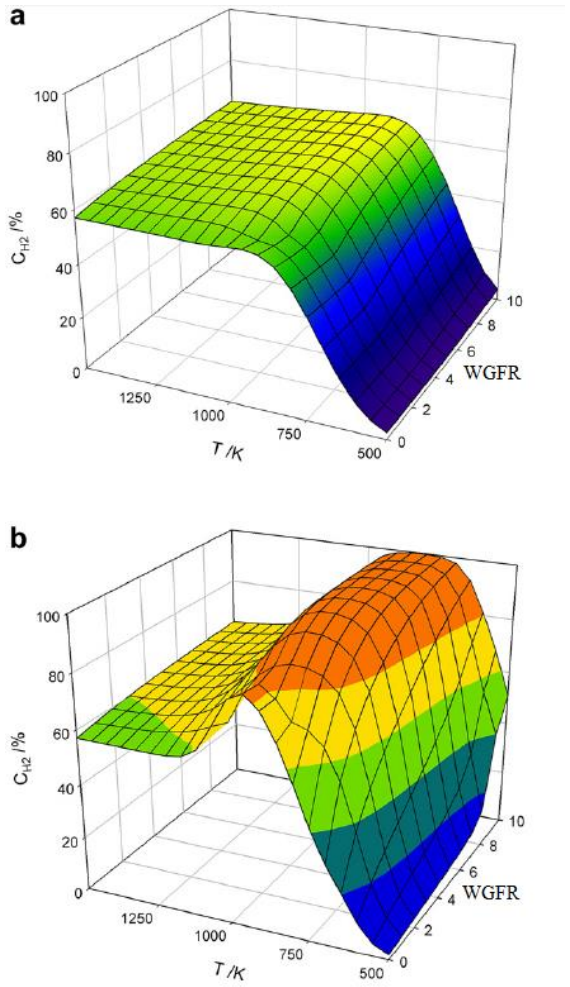

Fig. 2.8 - Hydrogen concentration (dry basis) in equilibrium as function of temperature and WGFR in (a) GSR and (b) SEGSR, at 1 atm. Adapted from [41].

By comparing Fig. 2.8 a) and b), it is clear that the removal of CO_2 during reaction enhances H_2 production (Le Chatelier's principle), especially at lower temperatures where CO_2 sorption is more intense. Chen *et al.* [42] observed that, while without CO_2 capture the maximum H_2 yield, at WGFR of 9 and 1 atm, was 6, H_2 yields of approximately 6.5 and 7 were obtained when 80% and 99% of the CO_2 was removed, respectively. Moreover, the increment of H_2 production due to CO_2 removal is higher for lower temperatures, which is related with the fact that lower temperatures favor CO_2 capture.

Regarding the variation of the concentration of CO_2, Wang *et al.* [41] observed very similar behavior between GSR and SEGSR at temperatures above 900 K. However, at temperatures below 900 K the CO_2 concentration was much lower in the SEGSR due to the already mentioned enhanced sorption, despite the higher CO_2 production (Le Chatelier's principle). On the other hand, the production of both methane and carbon monoxide is lower in the SEGSR.

Chen *et al*. [44] varied the operation pressure between 1-20 atm and analyzed its effect on both GSR and SEGSR in terms of hydrogen yield. The first thing that the authors noticed was that the H_2 yield decreased with increasing pressures for both processes. However, the SEGSR was less sensitive to pressure than GSR. This happens because, even though higher pressures do not favor SEGSR but methanation instead, higher pressures enhance CO_2 sorption. For this reason, the negative effects of pressure are diminished during SEGSR, being that the increment in the production of H_2 due to CO_2 removal is more noticeable at higher pressures.

The sorbent/glycerol ratio is also an important parameter to be taken into consideration. The concentration of H_2 increases for increasing CaO/glycerol ratios, while the concentrations of both CO and CO_2 highly decrease [41]. The concentration of methane presents a maximum. However, for increasing CaO/glycerol molar ratios above 10, there is almost no variation of H_2, CO, CO_2 and CH_4 concentrations. Therefore, 10 may be considered the optimum CaO/glycerol molar ratio.

Finally, the deposition of carbon has also been target of investigation. As already discussed for GSR, high temperatures and WGFRs inhibit coke formation. Wang and co-authors observed higher carbon deposition in GSR than in SEGSR. Therefore it can be concluded that the capture of CO_2 inhibits coke formation. This is supported by the lower concentrations of CO and CO_2, which origin coke formation, during SEGSR (Eqs. (2.8), (2.10) and (2.11)). On the other hand, by analyzing Fig. 2.9 [41] it can be observed, for SEGSR, that at 1 atm

coke is completely absent at temperatures above 500 K and WGFRs higher than 1.8.

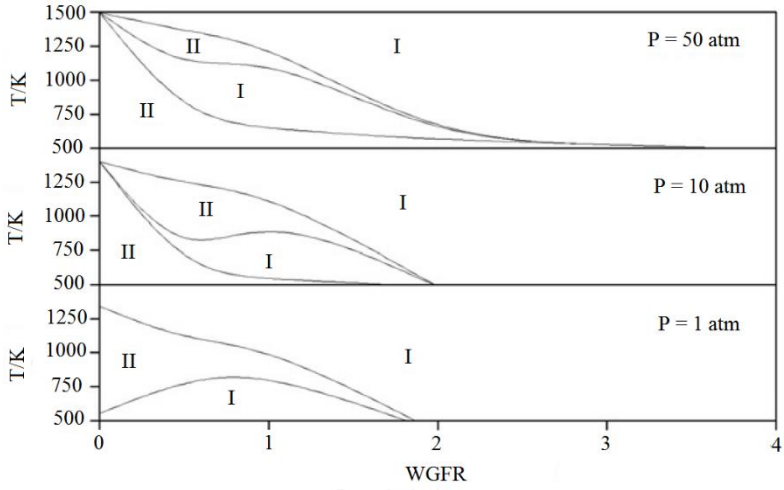

Fig. 2.9 - Coke free (I) and coke formed (II) regions in SEGSR as a function of temperature and WGFR, at 1 atm, 10 atm and 50 atm. Taken from [41].

By increasing the pressure from 1 to 50 bar, the formation of a second carbon formed region occurs. This might be because of the enhancement of the reactions in Eqs. (2.8), (2.10) and (2.11). In this case coke formation is only completely avoided at WGFRs above 3 (again for temperatures above 500 K). In another work, Silva *et al*. [43] concluded that even using a WGFR as low as 1.5, it would be possible to work at temperatures below 885 K (1 atm) without any carbon formation. Furthermore, in order to eliminate the possibility of carbon formation in all the temperature range (500-1400 K) under atmospheric pressure, WGFRs higher than 2 would have to be used. This value is very similar to the one reported by Wang *et al*. [41] – Fig. 2.9.

2.2.3 GSR with H_2 removal

The removal of hydrogen from the reaction medium instead of CO_2 is another possibility that has been target of some interest. Analogously to the

SEGSR, the selective removal of H_2 during GSR by means of a membrane reactor (MR) also shifts the thermodynamic equilibrium towards higher H_2 yields. Moreover a highly pure H_2 stream, which is suitable to be used in polymer electrolyte membrane fuel cells (PEMFCs), is generated. There have been several studies that have focused on the experimental assessment of GSR in MRs, however the study of the thermodynamic behavior of the process has seldom been done. A revision of such work is briefly reported in this section.

Wang *et al*. [45] investigated the effect of temperature, WGFR, pressure and fraction of hydrogen removal on a MR. Regarding the operation pressure, it was found that higher pressures benefit the permeation of hydrogen through the membrane due to the increase of the driving force. However, the thermodynamics of GSR is not favored by high pressures as already discussed. The authors observed that superior hydrogen production occurs at 1 atm and, for that reason, all the analysis was performed at this pressure. Fig. 2.10 [45] depicts the influence of both temperature and WGFR on the production of H_2 through GSR in a MR. It is observable that, as expected, the increase of both temperature and WGFR provoke an enhancement in the production of hydrogen. However, H_2 production reaches a maximum at a certain temperature and then starts decreasing for higher temperatures (such effect is not verified for H_2 removals of 99% and 100%). Regarding the fraction of H_2 removal, removing more hydrogen shifts the thermodynamic equilibrium towards higher hydrogen production according to the Le Chatelier's principle. Moreover, higher H_2 removal dislocates the maximum hydrogen production to lower temperatures (Fig. 2.10 a)). While with no H_2 removal the maximum H_2 yield is approximately 6 at 925 K, the maximum yield becomes close to 7 at 825 K for 80% of H_2 removal, and with fractional hydrogen removal of 0.99 and 1, the H_2 yield is close to 7 for all range of temperatures considered. The same is verified for all range of WGFRs considered (Fig. 2.10 b)). Furthermore, the increase in H_2 production when the WGFR increases from 9 to 12 is very small. Consequently, the

optimum conditions for GSR in the MR were found to be 825-875 K, WGFR of 9 and 1 atm. The formation of both CO and CH_4 is decreased by selectively removing H_2.

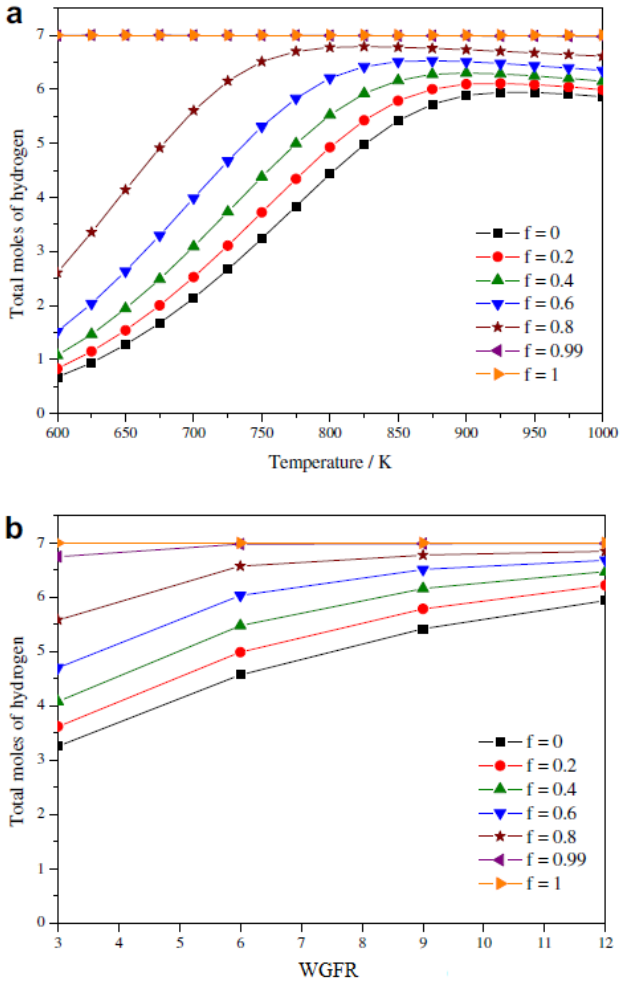

Fig. 2.10 - Effect of (a) temperature (WGFR = 9) and (b) WGFR (T = 850 K) at 1 atm and fraction of hydrogen removal (f) on the production of H_2. Adapted from [45].

The formation of carbon was also analyzed by Wang *et al.* [45]. As can be seen in Fig. 2.11 [45], a WGFR value of 4.5 is enough to completely inhibit carbon formation for all range of temperatures and fractions of hydrogen removal tested. With exception to the case of fractional H_2 removal of 0.99, the minimum

WGFR required to avoid carbon formation decreases slightly with the increase of temperature up to 800 K. From that point on, the decrease with temperature is much faster and from approximately 873 K on, the influence of the H_2 removal fraction on the minimum WGFR is practically negligible. For a fraction of hydrogen removal of 0.99 the minimum WGFR required to inhibit carbon formation decreases very rapidly. By comparing the different levels of hydrogen removal, it can be observed that higher hydrogen removal leads to higher minimum WGFRs necessary to inhibit carbon formation, except for 99% hydrogen removal (where the minimum WGFR necessary to avoid carbon formation becomes lower than that for lower hydrogen removal fractions at temperatures lower than 923 K). In any case, if the optimum WGFR of 9 is used, no problems with carbon formation will exist.

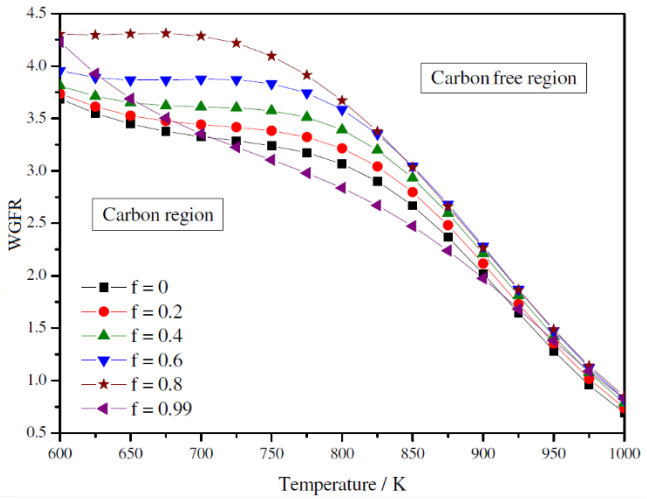

Fig. 2.11 - Carbon formation as function of WGFR and temperature at 1 atm, for different values of f. Adapted from [45].

2.3 GSR catalysts developments

In the last decade extensive research has been done regarding the heterogeneous catalysis of the GSR reaction for either synthesis gas or H_2

production. The most investigated materials until now have been Ni, Pt, Co and Ru-based catalysts. Other less researched materials like Rh, Ir and Pd have also shown interesting attributes. Among the above mentioned catalysts, Ni-based catalysts, as non-noble metal-based catalysts, have been extensively studied. At the moment, the main goal is to design highly reducible and with high oxygen mobility redox catalysts for low-temperature GSR [46].

2.3.1 Ni-based catalysts

Nickel catalysts for the GSR have been extensively studied over the last years. A big advantage that Ni catalysts present when compared to the noble metal-based ones is their lower price.

2.3.1.1 Effect of the support on the catalytic performance

It has been found that the use of different supports in Ni-based catalysts results in much different catalytic performances [47-51]. Table 2.1 summarizes the catalytic performance and operating conditions of different Ni-based catalysts on GSR. Adhikari *et al*. [48] compared the performance of Ni catalysts on different supports: MgO, CeO_2 and TiO_2. At 600 ºC and WGFR of 9, it was observed the following order of H_2 selectivity: CeO_2 (70%) > MgO (40%) > TiO_2 (15%). Moreover, the ceria supported catalyst was found to present the lowest carbon deposition. It was suggested that ceria establishes a better interaction with the nickel active phase, which leads to a higher metal dispersion and inherently available surface area. Pant *et al.* [50] observed that the presence of ceria affects the reduction of Ni^{2+} species, thus enhancing the catalyst activity.

It has also been suggested that the dual oxidation state (+4/+3) that ceria presents leads to oxygen release which reacts with the carbon that is deposited, thus reducing coke formation [15, 52-55].

Table 2.1 - Summary of the catalytic performance and operating conditions of different Ni-based catalysts on GSR.

Catalyst	Operating Conditions	Conversion / %	Type of Conversion	H_2 Yield / %[a]/ Selectivity / %	Reference
11.6 wt% Ni/CeO_2	600 ºC, 1 atm, feed flow rate = 0.5 $mL \cdot min^{-1}$ and WGFR = 9	100	Glycerol conversion[b]	n.d.[c]/70	[48]
9.62 wt% Ni/MgO	600 ºC, 1 atm, feed flow rate = 0.5 $mL \cdot min^{-1}$ and WGFR = 9	100	Glycerol conversion[b]	n.d.[c]/40	[48]
12.7 wt% Ni/TiO_2	600 ºC, 1 atm, feed flow rate = 0.5 $mL \cdot min^{-1}$ and WGFR = 9	60	Glycerol conversion[b]	n.d.[c]/15	[48]
10 wt% Ni/ZrO_2	650 ºC, 1 atm, feed flow rate = 0.06 $mL \cdot min^{-1}$ and 10 wt% glycerol	72 (20 h)[d]	Glycerol conversion to gaseous products[e]	65/n.d.[c]	[51]
12.6 wt% Ni/γ-Al_2O_3	500 ºC, 4 atm, WHSV[f] = 7.7 h^{-1} and 10 wt% glycerol	100 (8 h)[d]	Glycerol conversion[b]	50/n.d.[c]	[53]
10 wt% Ni/SiC	400 ºC, 1 atm, WHSV[f] = 33.3 h^{-1} and WGFR = 9	95.2 (60 h)[d]	Glycerol conversion to gaseous products[e]	n.d.[c]/n.d.[c]	[60]

[a] Based on the thermodynamic limit established in each work.
[b] Calculation based on the total amount of glycerol converted.
[c] n.d.: not determined.
[d] Time of operation after which the data was collected.
[e] Calculation based on the amount of carbon (in glycerol) converted into gaseous products (CO_2, CO and CH_4).
[f] WHSV: weight hourly space velocity.

Moreover, Ni/CeO_2 catalyst is able to enhance both methane reforming and WGS reaction and presents high hydrogen selectivity through GSR [28, 56-58]. Also, it has been reported that the H_2 yield is highly dependent on the nature of the active phase as well as its interaction with ceria [28, 56, 57, 59].

The acidic character of TiO_2 is responsible for the higher coke formation on Ni/TiO_2, which leads to a worse GSR performance [48]. Nichele *et al.* [51] showed that Ni/TiO_2 has very low activity in C-C bond rupture, even at high temperatures, and that the contribution of the WGS reaction is even smaller. This is due to the fact that anatase, where nickel ions are incorporated after being oxidized and then reduced under H_2 flow, is stable only at relatively low temperatures and its weak interaction with Ni is not able to avoid re-oxidation of the metallic active phase in the steam reforming conditions [51].

Sánchez *et al.* [49], Pant *et al.* [50] and Adhikari *et al.* [56] analyzed the performance of Ni/Al_2O_3 catalysts for the GSR. The first group observed catalyst deactivation after 8h time on stream (at 600 and 650 ºC). Wen *et al.* [61] verified that $Ni\text{-}Al_2O_3$ supported catalysts undergo quick deactivation. However, as already stated, deactivation is highly dependent on, among another things, the support nature. Many authors have verified the formation of carbonaceous deposits over Ni/Al_2O_3, which led to relatively fast catalyst deactivation [49, 50, 61, 62]. Normally, the formation of coke deposits is associated to dehydration, cracking and polymerization reactions which take place on the acid sites of alumina [63]. Besides presenting higher carbon deposition, Pant *et al.* [50] also concluded that the prepared Ni/Al_2O_3 catalyst presented higher catalyst sintering than the Ni-ceria supported one. It has been suggested that the sintering of the Ni active phase is associated to a transition of alumina to crystalline phase during reaction [64].

Nichele *et al.* [51] also tested a Ni/ZrO_2 catalyst, having concluded that it presented high surface area, high stability at 650 ºC and strong interaction of the support with the metal phase. Also, it was found that for lower temperatures (500

ºC) the zirconia supported catalyst was even more active. However, there was a lower stability. In the same work a Ni/SBA-15 was also used, having presented insufficient hydrothermal resistance, which led to catalyst deactivation. However, sintering was avoided since it provided a good stabilization of the Ni active phase.

Nickel supported on neutral SiC has been reported to present outstanding stability and high yield of syngas [60]. The neutral nature of this material promotes an intrinsic nickel contribution to GSR, especially in terms of dehydrogenation and decarbonylation. Simultaneously, SiC leads to minimal side reactions from the condensation and the dehydration induced by the basic and acid properties, respectively. Because of this, the Ni/SiC catalyst is able to present high stability for GSR and low carbon deposition.

It is, therefore, evident that the nature of the support affects mainly the stability of the active phase. In order to reach a highly stable active phase, strong interactions between the metal phase and the support are required. These strong interactions also lead to higher activity and selectivity.

2.3.1.2 Effect of the addition of a promoter on the catalytic performance

In many studies reported in the literature, promoters have been used in Ni-supported catalysts in order to improve their performance towards the GSR reaction. Table 2.2 presents, in summary, the effect of the promoter on the catalytic activity.

As previously mentioned, ceria presents good characteristics for GSR, having for that reason been used by many authors as a promoter [53, 67-69]. In general the addition of CeO_2 promoter enhances the activity of the non-promoted catalyst. This is mainly related to the capacity of ceria to stabilize the nickel active phase and to promote the steam reforming of the oxygenated hydrocarbons intermediates, thus leading to a reduction of coke deposition.

Table 2.2 - Summary of the catalytic performance and operating conditions of different promoted Ni-based catalysts on GSR.

Catalyst	Operating Conditions	Conversion / %	Type of Conversion	H_2 Yield / %[a]/ Selectivity / %	Reference
8.4% Ni/γ-Al_2O_3/6 wt% La_2O_3	500 ºC, 4 atm, WHSV[b] = 7.7 h^{-1} and 10 wt% glycerol	100 (8 h)[c]	Glycerol conversion[d]	99.7/n.d.[e]	[22]
11.9 wt% Ni/γ-Al_2O_3/4.3 wt% CeO_2	500 ºC, 4 atm, WHSV[b] = 7.7 h^{-1} and 10 wt% glycerol	100 (8 h)[c]	Glycerol conversion[d]	80.3/n.d.[e]	[53]
13.4 wt% Ni/γ-Al_2O_3 – 7 wt% ZrO_2	500 ºC, 4 atm, WHSV[b] = 7.7 h^{-1} and 10 wt% glycerol	100 (7-8 h)[c]	Glycerol conversion[d]	62/n.d.[e]	[65]
10 wt% Ni/MoLaCa-LTA	600 ºC, feed flow rate = 0.63 $mL \cdot min^{-1}$ and 35 wt% glycerol	82.03 (100 h)[c]	Glycerol conversion to gaseous products[f]	n.d.[e]/n.d.[e]	[66]

[a] Based on the thermodynamic limit established in each work.
[b] WHSV: weight hourly space velocity.
[c] Time of operation after which the data was collected.
[d] Calculation based on the total amount of glycerol converted.
[e] n.d.: not determined.
[f] Calculation based on the amount of carbon (in glycerol) converted into gaseous products (CO_2, CO and CH_4).

It has also been suggested that Ce inhibits secondary dehydration reactions, which are normally favored by the presence of support acid sites, which lead to the formation of hydrocarbons that are coke precursors and generate fast catalyst deactivation [68]. It is, nonetheless, important to notice that the ceria loading must not be too high. Iriondo *et al*. [53] suggest that for a 20 wt% ceria promoter content on alumina, ceria tends to interact with alumina instead of Ni, thus decreasing the stabilization of the nickel active phase and lowering the available surface for Ni dispersion. In the same way, it is also possible that the bigger size of ceria crystallites could also diminish the interaction between ceria and nickel active phase [70]. On the other hand, Cui *et al*. [54] showed that the activity of the $La_{0.3}Ce_{0.7}NiO_3$ mixed oxide catalyst for GSR is enhanced compared to $LaNiO_3$ catalysts and that its performance is comparable to that of a noble metal like Pt [54].

The use of ZrO_2 as a catalyst modifier has also been reported as an alternative promoter [18, 65, 67, 68], despite the fact that ZrO_2 alone is not very active for steam reforming [71]. Iriondo *et al.*[67] observed that the addition of zirconia promoter to alumina not only enhanced the performance of the non-promoted catalyst but also presented better GSR performance than the ceria-promoted catalyst. The addition of an intermediate ZrO_2 content [65, 72, 73] enhanced the H_2 yield and the capacity of the catalyst to reform intermediate products (thus suppressing secondary reactions), even at 500 ºC, due to the enhancement of H_2O activation by ZrO_2. It is suggested that this improvement is associated to the formation of ZrO_2-Al_2O_3 species, which facilitates the reduction of Ni^{2+} [65]. Pant and co-workers [18] came to similar conclusions after performing GSR over a ZrO_2-promoted Ni/CeO_2 catalyst. Zirconia is able to make the ceria support more crystalline, consequently improving the metal dispersion. It is also known that, in general, ZrO_2 inhibits sintering of metallic active sites in the presence of water at high temperatures [64].

With the aim of reducing the acidity of alumina supports, thus preventing metal sintering and catalyst deactivation, alumina supports have been modified with basic La_2O_3 [22, 66, 67, 74, 75]. It has also been reported the performance of a Ni/SiO_2 modified with La_2O_3 for the GSR [76]. The combination of SiO_2, which is known to present large surface area and weak acidity, and La_2O_3, favored the formation of H_2 and CO_2 and reduced carbon formation. This decrease in the carbon formation with increasing La_2O_3 content was due to the formation of a La carbonate that removes C species deposited on the nickel sites. Therefore, the 30 wt% (highest La_2O_3 content used) La_2O_3 catalyst presented itself as promising system for GSR, since it was stable (Fig. 2.12) [76], while presenting good glycerol conversion, good H_2 yield and low carbon formation.

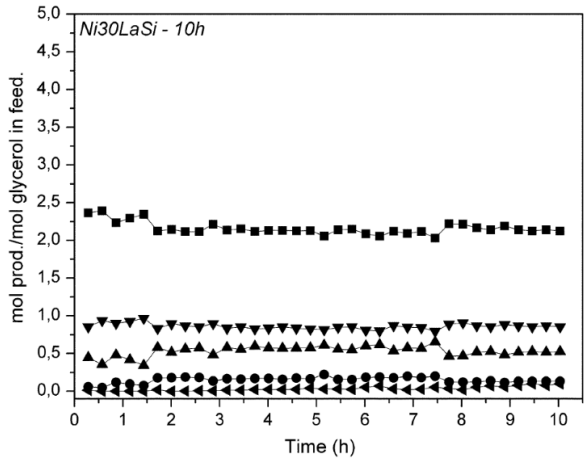

Fig. 2.12 - Yield of gaseous products formed during the stability reaction of GSR with the 30 wt% La_2O_3 content catalyst (■H_2 ● CH_4 ▲ CO ▼ CO_2 ◀ C_2H_4). Taken from [76].

The addition of basic Mg(II) to Ni/Al_2O_3 catalysts has been reported to prevent carbon formation by favoring both the adsorption of H_2O, O_2, CO_2 or –OH fragments and the spillover of such fragments from the support to the metal particles [20, 77, 78], thus facilitating carbon gasification. Moreover, the use Mg(II) promoter in Ni/Al_2O_3 materials enhances the stability of Ni against sintering, since it decreases the degree of interaction of Ni with alumina through

intercalation between the nickel active phase and alumina. Consequently, the incorporation of nickel in the alumina phase is inhibited [67]. It has been found that the use of low amounts of Mg(II) promoter leads to higher metal dispersion, thus favoring glycerol conversion into gaseous products, while higher loadings result in lower coke deposition [20]. Other basic promoters such as Mo [66, 79-83] and Ca [66, 69, 79] have also been reported to enhance the GSR performance of non-promoted catalyst, for the same reasons previously mentioned for basic modifiers. Huang *et al*. [66] observed that the simultaneous presence of Mo-La-Ca inhibits the interaction between nickel and the commercial Ca-containing Linde-type 5A zeolite support, thus resulting in a remarkable stability during GSR (no deactivation during 100 h time-on-stream). Gong and co-workers [84] verified that the synergetic effect caused by the partial substitution of La by Ca in the perovskite structure leads to enhanced metal dispersion and stronger metal-support interaction.

Hakim *et al*. [85] studied the GSR reaction over hydroxyapatite-supported Ni-Ce-Cu catalysts. It was found that doping with Cu influenced the catalytic performance of the catalyst. Also, higher Cu contents led to higher glycerol conversions and hydrogen production. Hakim's group came to the conclusion that the interaction between CuO and CeO_2 on the hydroxyapatite support in the GSR reaction enhanced the active sites (more active sites) of the catalysts. Moreover, the presence of ceria facilitated the reduction and increased the dispersion of the copper species on the surface of the catalysts. In terms of Ni content, it was found that it does not enhance significantly the production of H_2. As a matter of fact, it is suggested that since for the catalysts with higher Ni loading there is a greater presence of NiO phase on the surface of the catalysts during preparation and calcination, not all the nickel ions substituted the position of Ca^{2+} in the hydroxyapatite support and some metallic nickel became agglomerated.

Profeti *et al*. [86] studied the catalytic activity of Ni/CeO_2-Al_2O_3 catalysts modified with noble metals (Pt, Ir, Pd and Ru) for the GSR reaction. The addition of noble metals stabilizes the Ni sites in the reduced state, increasing the glycerol conversion and decreasing the coke formation. Moreover, this stabilization of the nickel surface species interacting with the support occurs at lower temperatures in the presence of small amounts of noble metals due to hydrogen spillover effect. A more detailed review on noble metal-based catalysts for GSR is done in further sections.

2.3.2 Pt-based catalysts

Noble metal catalysts normally are more active and stable towards the GSR reaction that Ni-based materials [87]. Pt-based catalysts are no exception and because of that, many authors have studied the potential of these catalysts for H_2 production through this process.

2.3.2.1 Effect of the support on the catalytic performance

Platinum catalysts supported on carbon have been investigated for the GSR either for syngas or hydrogen production [88-90]. A summary of the catalytic performance and operating conditions of some Pt-based catalysts is presented in Table 2.3. It has been found that Pt/C supported catalysts present higher stability during GSR than other Pt-based materials making use of different supports (Al_2O_3, ZrO_2, MgO/ZrO_2, and CeO_2/ZrO_2); this is due to the very low formation of C_2-hydrocarbons, which is symptomatic of lower carbon formation on the Pt/C catalyst [88]. Sutar *et al.* [89] attained catalytic results for GSR over a Pt/C sample that are in general comparable to the ones presented in the previous section for some Ni-based catalysts. However, for nickel catalysts those results were obtained at temperatures around 600-700 ºC, while in this case the temperature used was 400 ºC – Table 2.3.

Table 2.3 - Summary of the catalytic performance and operating conditions of different Pt-based catalysts on GSR.

Catalyst	Operating Conditions	Conversion / %	Type of Conversion	H_2 Yield / %[a]/ Selectivity / %	Reference
3 wt% Pt/Y_2O_3	600 ºC, 1atm, feed flow rate = 0.06 $mL \cdot min^{-1}$, carrier gas flow rate = 33 $mL \cdot min^{-1}$ and WGFR = 24	100 (2.5-3 h)[b]	Glycerol conversion to gaseous products[c]	90.0/n.d.[d]	[54]
5 % Pt/C	400 ºC, 5 atm, volumetric flow rate at reactor inlet = 210 $mL \cdot min^{-1}$ and WGFR = 9	60 (3 h)[b]	Glycerol conversion[e]	37.0/n.d.[d]	[89]
1 wt% Pt/SiO_2	350 ºC, 1 atm, Space time = 0.88 min, feed flow rate = 0.5 $mL \cdot min^{-1}$ and 10 wt% glycerol	85 (2 h)[b]	Glycerol conversion to gaseous products[c]	n.d.[c]/n.d.[d]	[91]
2 wt% Pt/SiO_2	350 ºC, 1 atm, Space time = 0.88 min, feed flow rate = 0.5 $mL \cdot min^{-1}$ and 10 wt% glycerol	100 (2 h)[b]	Glycerol conversion to gaseous products[c]	n.d.[d]/n.d.[d]	[91]
3 wt% Pt/Al_2O_3	350 ºC, 1 atm, feed flow rate = 0.32 $mL \cdot min^{-1}$ and 30 wt% glycerol	≈ 21.0	Glycerol conversion to gaseous products[c]	n.d.[d]/n.d.[d]	[92]

[a] Based on the thermodynamic limit established in each work.
[b] Time of operation after which the data was collected.
[c] Calculation based on the amount of carbon (in glycerol) converted into gaseous products (CO_2, CO and CH_4).
[d] n.d.: not determined.
[e] Calculation based on the total amount of glycerol converted.

Simonetti *et al.* [88] reported an even more noticeable superior activity of Pt-based catalysts for the GSR compared to nickel ones.

Although Pt/C supported catalysts present very interesting results at relatively low temperatures, they are more suitable for syngas production.
Oxide supports, on the other hand, promote the WGS reaction, thus being more appropriated for hydrogen production with lower CO content [88, 93-96]. Despite this, acid ZrO_2 and Al_2O_3 supports lead to fast deactivation of platinum catalysts mainly due to coke deposition, which results from the promotion of lateral reactions of dehydration, hydrogenolysis, dehydrogenation and condensation [88, 97], as seen for Ni-based catalysts. It has been reported that the acidity of supports decreases in the order Al_2O_3 > ZrO_2 > SiO_2 [97, 98]. Therefore, a solution for this deactivation problem includes the use of a support with lower acidity, like SiO_2 [91, 97, 99]. According to Pompeo *et al.* [91, 97], the silica support allows the Pt catalysts to promote mainly dehydrogenation reactions and subsequent cleavage of C-C bonds, thus presenting excellent activity to gaseous products, high H_2 selectivity and remarkable stability over time. It was also observed for Pt/SiO_2 supported catalyst that increasing the Pt content maintains the same active phase (same metal dispersion and average particle size). Therefore, the 2 wt% Pt catalyst shown in Table 2.3 presented better performance than the 1 wt% Pt one. Moreover, a comparison between Pt and Ni catalysts supported on SiO_2 was done at 350 and 450 ºC.

At these temperatures the Ni-based catalysts ended up deactivating after a couple of hours, while the Pt-based catalysts presented higher stability; moreover, at 350 ºC the 2 wt% Pt catalyst was considerably more stable than the 1 wt% Pt catalyst (Fig. 2.13) [91].

A Pt/Y_2O_3 catalyst was tested for GSR by Cui *et al.* [54], having presented high glycerol conversion into gaseous products as well as high hydrogen yield.

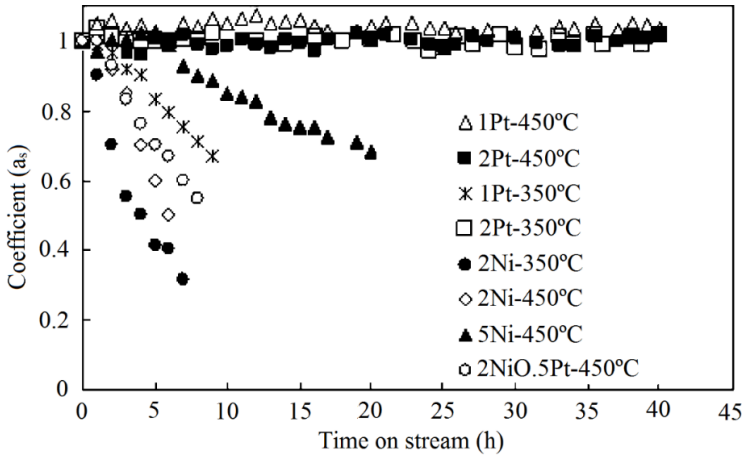

Fig. 2.13 - Activity over time-on-stream at 350 ºC and 450 ºC with different catalysts supported on SiO_2 (feed flow rate of 0.5 mL·min^{-1}, 10 wt% aqueous solution of glycerol and for a residence time of 0.88 min). Taken from [91].

2.3.2.2 Effect of the addition of a promoter on the catalytic performance

Similarly to Ni-based catalysts, the performance of Pt-based catalysts can be enhanced by adding promoters. Table 2.4 summarizes the effect of different promoters on the GSR catalytic activity of Pt-based catalysts. It has been demonstrated that the heat of CO adsorption on Pt-based catalysts can be decreased by the formation of metal alloys [100, 101]. Simonetti *et al*. [90] came to the conclusion that bimetallic Pt-Re/C catalysts with atomic Pt/Re ratios ≤ 1 are 5 times more active to syngas production through GSR than monometallic Pt/C and Pt-Re with a higher Pt/Re ratio (10). The authors suggest that the primary promotional effect of Re is to weaken the interaction between CO and the surface, thus leading to faster turnover of catalytic sites. Kunkes *et al.* [93] added Fe; Cu; Sn; Ir; Co; Ni; Rh; Os; Ru; or Re to Pt supported on C. The addition of Fe; Cu; Sn; Ir; Co; Ni; or Rh had a detrimental or neutral effect on the catalytic activity for all reaction temperatures (275-350 ºC).

Table 2.4 - Summary of the catalytic performance and operating conditions of different promoted Pt-based catalysts on GSR.

Catalyst	Operating Conditions	Conversion / %	Type of Conversion	H_2 Yield / %[a]/ Selectivity / %	Reference
Pt/4 wt% CeO_2-1 wt% ZrO_2-α-Al_2O_3	350 ºC, space time = 6 min, feed flow rate = 0.1 mL·min^{-1} and 10 wt% glycerol	78.0 (1 h)[b]	Glycerol conversion to gaseous products [c]	n.d.[d]/72.5	[97]
3 wt% Pt/20 wt% CeO_2/Al_2O_3	350 ºC, 1 atm, feed flow rate = 0.32 mL·min^{-1} and 30 wt% glycerol	88.0	Glycerol conversion to gaseous products [c]	n.d.[d]/n.d.[d]	[92]
3 wt% Pt/5 wt% La_2O_3/Al_2O_3	350 ºC, 1 atm, feed flow rate = 0.32 mL·min^{-1} and 30 wt% glycerol	91.0	Glycerol conversion to gaseous products [c]	n.d.[d]/n.d.[d]	[92]

[a] Based on the thermodynamic limit established in each work.
[b] Time of operation after which the data was collected.
[c] Calculation based on the amount of carbon (in glycerol) converted into gaseous products (CO_2, CO and CH_4).
[d] n.d.: not determined.

According to Pompeo *et al*. [91], the fact that the coexistence of Pt and Ni did not improve the catalytic performance suggests that the formation of a bimetallic Pt-Ni phase affects the platinum electronic properties. On the other hand, the addition of Os; Ru; or Re to Pt enhanced the syngas production comparatively to Pt/C, being that Re was the promoter that allowed the best syngas production improvement.The addition of ceria promoter has been verified as advantageous, but in this case for platinum-based catalysts [88, 92, 97]. As already mentioned, the addition of ceria to a support like alumina reduces its acidity, thereby improving the catalyst stability and H_2 selectivity and reducing the formation of undesirable products and coke deposition. Montini *et al*. [92] verified that the $Pt/CeO_2/Al_2O_3$ catalyst, despite presenting improved performance, still deactivated after 20 h time-on stream (Fig. 2.14) [92]. This deactivation could be due to coke deposition on the active sites and only marginally due to Pt sintering. Similar behavior, in terms of performance enhancement, has been observed for Pt-based catalysts promoted with basic oxides like La_2O_3 [92] and MgO [88]. However, the La_2O_3 promoted catalyst only deactivated after 50 h time-on-stream, as can be seen in Fig. 2.14.

On the other hand, Pompeo *et al.* [97] reported the attainment, for a $Pt/Ce_4Zr_1\alpha$ catalyst, of higher H_2 selectivity and glycerol conversion to gaseous products than both $Pt/\gamma\text{-}Al_2O_3$ and Pt/ZrO_2 catalyst. The promoted catalyst presented higher average platinum particle size than the other two catalysts. Claus and co-authors [102] suggested that larger particles present a higher number of face atoms of the metal crystallite. Moreover, the adsorption of oxygenated hydrocarbons for posterior C-C cleavage can be preferably performed at face positions, thus leading to higher hydrogen selectivity. Furthermore, the simultaneous presence of Ce and Zr promotes the WGS reaction, thus enhancing the H_2 selectivity [93].

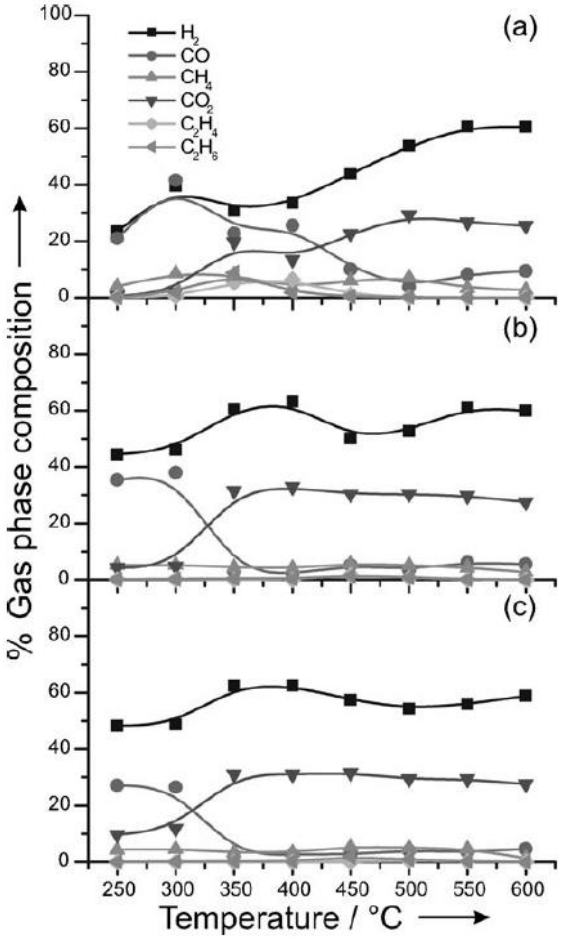

Fig. 2.14 - Stability tests over doped Pt/Al_2O_3 catalysts. Top: glycerol conversion to gas-phase products. Bottom: gas-phase composition using (a) $Pt/La_2O_3/Al_2O_3$ and (b) $Pt/CeO_2/Al_2O_3$ catalyst. Conditions: 1.00 g catalyst, 0.32 $mL \cdot min^{-1}$ of $C_3H_8O_3$ (30 wt%; aqueous solution), $T = 350$ ºC. Taken from [92].

2.3.3 Co-based catalysts

Cobalt catalysts have shown good performance in ethanol reforming for hydrogen production and are proposed as appropriate catalytic systems [103-105]. However they have shown significant deactivation through sintering and surface cobalt deactivation. Even so, many authors have investigated in the last years the catalytic behavior of Co-based materials for GSR [23, 106-109].

2.3.3.1 Effect of the support on the catalytic performance

The use of alumina as support for Co active phase has been reported [107], having been observed the existence of both strong and weak acid sites on the catalyst surface with an acidic/basic ratio of approximately 5.5. Therefore, expected carbon deposition was verified. Moreover, TPO-TPR and TPR-TPO cycles showed different reactivity of the carbon deposited on the surface of the coked catalyst, meaning that there were at least two types of carbon pools on the surface. One of the pools was reactive in the presence of H_2 while the other was inert to H_2, reacting only in the presence of O_2.

Zhang *et al.* [106] verified that Co/CeO_2 catalyst for GSR originated small concentrations of CH_4 and CO at the reactor outlet stream. Furthermore, only slight changes on their concentrations were observed while increasing the reaction temperature, meaning that the Co/CeO_2 catalyst did not catalyze effectively both WGS and steam reforming of methane. Dehydration of glycerol was not observed over the ceria-supported catalyst, and so no significant deactivation occurred.

A comparison of the catalytic performance of both types of catalysts described along this section for GSR is presented in Table 2.5.

2.3.3.2 Effect of the addition of a promoter on the catalytic performance

It has been found that bimetallic $Co\text{-}Ni/Al_2O_3$ catalyst, used by Adesina *et al.* [108], presents an enhanced activity for steam reforming of methane and propane due to the synergism between the Ni and Co metals [110]. The reasons of such synergism are not, however, disclosed. The coexistence of both Lewis and Bronsted acid sites was discovered through physicochemical characterization. However, the bimetallic catalyst presents a net surface acidity (acidic/basic ratio of 9). Analogously to what was reported elsewhere [107], it was verified the occurrence of carbon deposition during reaction, which led to a

reduction of the surface area and pore volume of the catalyst. Furthermore two types of carbon deposits were observed once again, being that one of them is inert to H_2 as well. The GSR catalytic activity of this promoted catalyst is compared in Table 2.5 with that for the non-promoted catalysts presented in the previous section.

CeZr mixed oxides have also been target of attention since they allow the insertion of transition metals, like Co and Ni, and/or noble metals, like Ru and Rh, into the oxide structure, thus increasing the active phase-support interaction [111-113]. Araque *et al.* [23] evaluated the effect of the active phase by using two mixed oxide catalysts: $Ce_2Zr_{1.5}Co_{0.5}O_{8-\delta}$ and $Ce_2Zr_{1.5}Co_{0.47}Rh_{0.07}O_{8-\delta}$. Rhodium did not significantly affect the glycerol total conversion. However, it highly affected the conversion of glycerol into gaseous products at the expense of liquid ones. It was also observed an enhancement of the 24 h average H_2 production from 1.6 $\mathrm{mol} \cdot \mathrm{mol}_{\mathrm{fed\ glycerol}}^{-1}$ up to 5.8 $\mathrm{mol} \cdot \mathrm{mol}_{\mathrm{fed\ glycerol}}^{-1}$ when Rh was added to the mixed oxide catalyst. Also, for the Rh-containing catalyst, an average production of H_2 of 6.7 $\mathrm{mol} \cdot \mathrm{mol}_{\mathrm{fed\ glycerol}}^{-1}$ was obtained for over 16 h, while the other catalyst kept stable only for 1 h. The enhanced behavior of the Rh containing catalyst is related to the capacity of Rh to break the C-C bonds. The loss of activity verified is due to the loss of the C-C bond breaking capacity, since C_2H_4 formation was observed when deactivation occurred. In another work, Roger and co-authors [109] studied the effect of the Ce/Zr ratio in fluorite-type mixed oxides of CeZr-CoRh catalysts on the H_2 production by GSR. Catalysts with three different Ce/Zr ratios were prepared: $Ce_{0.53}Zr_{2.97}Co_{0.47}Rh_{0.03}O_{8-\delta}$ with poor ceria content ($CZ^{P}CoRh$), $Ce_2Zr_{1.5}Co_{0.47}Rh_{0.03}O_{8-\delta}$ with intermediate ceria content ($CZ^{I}CoRh$), and $Ce_{2.59}Zr_{0.91}Co_{0.47}Rh_{0.03}O_{8-\delta}$ rich in ceria ($CZ^{R}CoRh$). It was observed that the increase of the Ce content enhances both the stability (Fig. 2.15) [109] and selectivity towards H_2 and CO_2.

Table 2.5 - Summary of the catalytic performance and operating conditions of different non-promoted and promoted Co-based catalysts on GSR.

Catalyst	Operating Conditions	Conversion / %	Type of Conversion	H_2 Yield / %[a]/ Selectivity / %	Reference
15 % Co/CeO_2	425 ºC, 1 atm, GHSV[b] = 11 000 $mL \cdot g_{cat.}^{-1} \cdot h^{-1}$ and G/W/He[c] = 2/18/80 vol%	100	Not specified	n.d.[d]/88.0	[106]
15 wt% Co/Al_2O_3	500 ºC, 1 atm, GHSV[b] = 50 000 $mL \cdot g_{cat.}^{-1} \cdot h^{-1}$ and $p_{glycerol}$ = 7.40 kPa and p_{steam} = 57.02 kPa	≈ 13.0	Glycerol conversion to gaseous products[e]	77.0[f]/63.0	[107]
5 wt% Co-10 wt% Ni/Al_2O_3	525 ºC, 1 atm, GHSV[b] = 50 000 $mL \cdot g_{cat.}^{-1} \cdot h^{-1}$ and 30 wt%	-	-	79.1/65.3	[108]

[a] Based on the thermodynamic limit established in each work.
[b] GHSV: gas hourly space velocity.
[c] G/W/He: glycerol/water/helium volumetric composition.
[d] n.d.: not determined.
[e] Calculation based on the amount of carbon (in glycerol) converted into gaseous products (CO_2, CO and CH_4).
[f] Assuming a thermodynamic limit of 7.

This happens because of the improved cobalt reducibility and re-oxidation properties, oxygen storage capacity and metal support interaction. Also, the catalytic stability and activity of the catalysts is related to their capacity to activate H_2O under reaction conditions, thus favoring the steam reforming reaction over the decomposition reaction. By increasing the Ce content, the H_2O activation is favored for a longer period of time, thus allowing carbon gasification and delaying the catalyst deactivation; even so this effect is not very pronounced (Fig. 2.15).

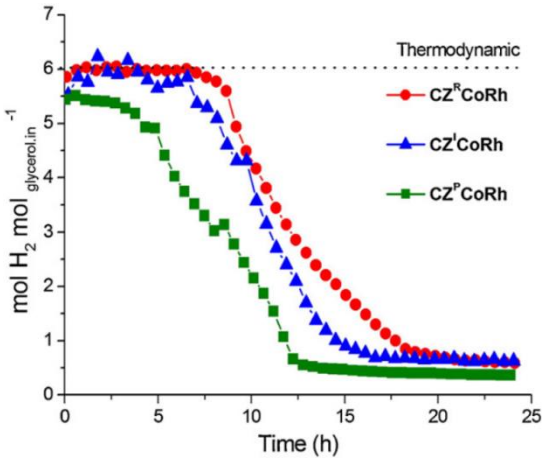

Fig. 2.15 - Evolution of the H_2 production in GSR over $Ce_{0.53}Zr_{2.97}Co_{0.47}Rh_{0.03}O_{8-\delta}$ with poor ceria content (CZ^PCoRh), $Ce_2Zr_{1.5}Co_{0.47}Rh_{0.03}O_{8-\delta}$ with intermediate ceria content (CZ^ICoRh), and $Ce_{2.59}Zr_{0.91}Co_{0.47}Rh_{0.03}O_{8-\delta}$ with rich ceria content (CZ^RCoRh). Conditions: temperature 650 ºC, WGFR of 9 and atmospheric pressure. Thermodynamic value expected using the UNIQUAC model: 6.06 $\mathrm{mol} \cdot \mathrm{mol}_{\mathrm{fed\ glycerol}}^{-1}$. Taken from [109].

2.3.4 Ru-based catalysts

Ruthenium is currently, along with nickel and platinum, one of the most promising materials to catalyze hydrogen production through GSR. Moreover, Ru is the least expensive among all noble metals [114]. Ru-based catalysts have been reported has having superior catalytic activity for H_2 production, not only through GSR but also through methane steam reforming, for example [1, 115,

116]. By comparing the GSR activity of catalysts loaded with Group 8-10 metals supported on oxides (Y_2O_3, ZrO_2, CeO_2, La_2O_3, SiO_2, MgO, Al_2O_3), the order Ru ≈ Rh > Ni > Ir > Co > Pt > Pd > Fe was found in La_2O_3-supported materials [117]. It has also been reported that the order of the catalytic activity of Group 8-10 metal catalysts over SiO_2 is as follows: Ru ≈ Rh > Ni > Ir > Pt ≈ Pd ≫ Co ≈ Fe [117].

2.3.4.1 Effect of the support on the catalytic performance

Hirai *et al.* [117] prepared several catalysts loaded with Group 8-10 metals supported on Y_2O_3, ZrO_2, CeO_2, La_2O_3, SiO_2, MgO, and Al_2O_3 via a conventional impregnation method. Among all the metals used, Ru was the one that showed the best catalytic activity. Therefore, since ruthenium allowed the attainment of the highest H_2 yield, the effects of the previously mentioned supports for ruthenium on GSR were evaluated at 600 ºC. The Ru/MgO supported catalyst showed very low glycerol conversion to gaseous products compared to the other samples. This low activity is due to the fact that ruthenium on MgO is hard to be reduced to metallic ruthenium and so the number of active sites would decrease [118]. The Ru/Al_2O_3 supported catalyst presented the lowest glycerol conversion into gaseous products. It also showed low H_2 yield because of the higher selectivity towards methane production and lower selectivity to CO_2. On the other hand, both Ru/Y_2O_3 and Ru/ZrO_2 supported catalysts presented high glycerol conversion into gaseous products and H_2 yield. In fact, the Ru/Y_2O_3 sample was the one that presented the best results. This has been attributed to the ability of yttria to promote de WGS reaction [119]. Considering this, an optimization of the loading level of ruthenium was performed at 500 ºC, to compare the catalytic activity at lower conversions [117]. The H_2 yield kept increasing as the ruthenium loading increased up to 3 wt%. A further increase in the ruthenium loading to 5 wt% did not affect the H_2 yield and so, the optimal loading was found to be 3 wt%. Finally, it was observed that both glycerol conversion into gaseous products and H_2 yield did not decrease during a 24 h

time-on-stream test, as shown in Fig. 2.16 [117]. Very small carbon deposition was verified after 24 h reaction, thus meaning that the 3 wt% Ru/Y_2O_3 material is apparently resistant for the deactivation caused by carbon deposition. However, some deactivation caused by sintering of the dispersed catalytic metal clusters was observed. Ultimately the authors concluded that the Ru/Y_2O_3 catalyst presents very high performance in GSR. The catalytic performance of some of these Ru-based catalysts for GSR is presented in Table 2.6.

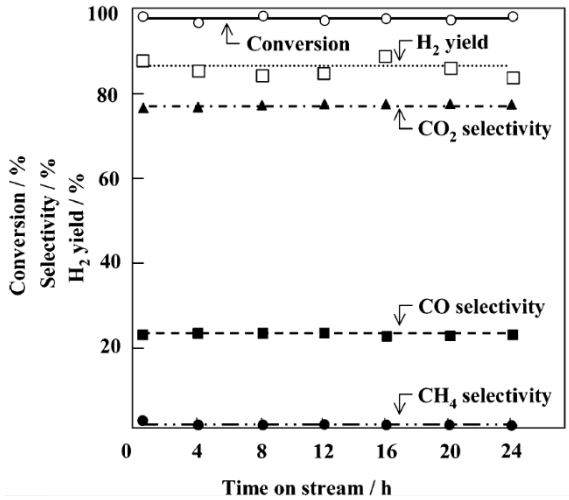

Fig. 2.16 - Stability tests over 3 wt% Ru/Y_2O_3 catalyst for 24 h in the GSR, at 600 ºC and sweep gas space velocity of 80 000 $mL \cdot g_{cat}^{-1} \cdot h^{-1}$. Taken from [117].

2.3.4.2 Effect of the addition of a promoter on the catalytic performance

Kim and Lee [119] studied the GSR on Ru and Ru-Me (Me = Fe, Co, Ni, and Mo) catalysts supported on Y_2O_3, $Ce_{0.5}Zr_{0.5}O_2$, and commercial γ-Al_2O_3. It was verified that the use of different supports affects the performance of the catalysts, being that for the Ru-based catalysts supported on reducible yttria and ceria-zirconia there was a significant enhancement of the H_2 production turnover rate and selectivity.

Table 2.6 - Summary of the catalytic performance and operating conditions of different non-promoted and promoted Ru-based catalysts on GSR.

Catalyst	Operating Conditions	Conversion / %	Type of Conversion	H_2 Yield / %[a]/ Selectivity / %	Reference
5 % Ru/Al_2O_3	400 ºC, 1 atm, feed flow rate = 0.20 $mL \cdot min^{-1}$ and WGFR = 9	68.1 (2 h)[b]	Glycerol conversion[c]	37.0/n.d.[d]	[114]
3 wt% Ru/Y_2O_3	600 ºC, 1 atm, GHSV[e] = 80 000 $mL \cdot g_{cat.}^{-1} \cdot h^{-1}$ and WGFR = 9	≈ 100 (24 h)[b]	Glycerol conversion to gaseous products[f]	85/90.0[g]	[117]
0.59 wt% Ru- 0.23 wt% Sn/Mg(Al)O	650 ºC, 1 atm, feed flow rate = 0.06 $mL \cdot min^{-1}$ and 10 wt% glycerol	87.5 (20 h)[b]	Glycerol conversion to gaseous products[f]	60/n.d.[d]	[120]
0.06 wt% Ru/Mg(Al)O	550 ºC, 1 atm, WHSV[h] = 327.3 h^{-1}[i] and 10 wt% glycerol	97 (20 h)[b]	Glycerol conversion to gaseous products[f]	91.0/97.0[j]	[121]

[a] Based on the thermodynamic limit established in each work.
[b] Time of operation after which the data was collected.
[c] Calculation based on the total amount of glycerol converted.
[d] n.d.: not determined.
[e] GHSV: gas hourly space velocity.
[f] Calculation based on the amount of carbon (in glycerol) converted into gaseous products (CO_2, CO and CH_4).
[g] Taken from [122].
[h] WHSV: weight hourly space velocity.
[i] Calculated value.
[j] CO_2 selectivity.

This happens because these supports tend to facilitate the WGS reaction. On the other hand, the acidic γ-alumina supported Ru-based catalysts showed low H_2 production turnover rate, high CO selectivity and formation of C_1-C_2 hydrocarbons for the reasons already stated.

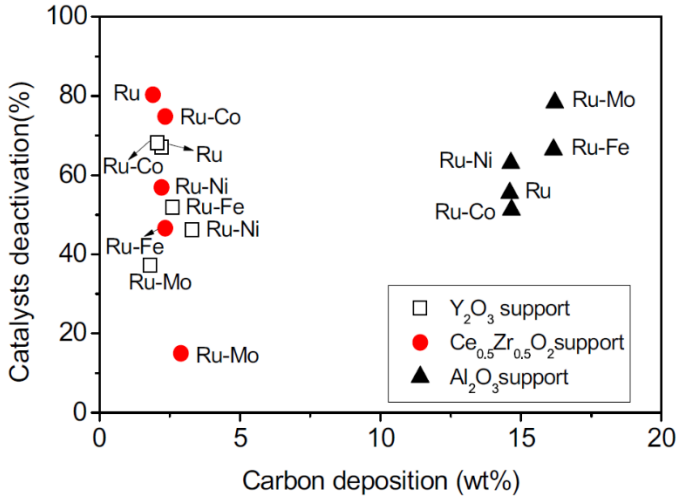

Fig. 2.17 - Deactivation of catalysts (%) with respect to the amount of solid carbonaceous species deposited (wt%) on the catalysts after 10 h of reaction at 600 ºC (feed conditions: WGFR of 12, spatial velocity of 876-2340 $\mu mol \cdot g_{cat.}^{-1} \cdot min^{-1}$). Taken from [119].

In opposition to what was verified for the different supports, the metallic promoters did not influence much neither H_2 production rate nor selectivity. On the other hand, the addition of metallic promoters led to lower catalysts deactivation. In terms of coke deposition, both yttria and ceria-zirconia supports showed superior resistance against coke formation on the catalysts. In fact, very small deposited amounts of carbonaceous species were verified for these supports (< 3 wt%). However, deactivation of the catalysts at levels between 15% and 80% was observed. Since the low amounts of deposited coke could never lead to such deactivation levels, the authors suggest that sintering of the dispersed catalytic metal clusters was the cause of the verified activity drop. As can be seen in Fig. 2.17 [119], the Ru-Mo/$Ce_{0.5}Zr_{0.5}O_2$ and Ru-Mo/Y_2O_3 catalysts exhibited superior stability against deactivation by sintering and lower carbon

deposition. The results suggest that the MoO_x species effectively diminished sintering of the surface metal clusters.

Ru-based catalysts supported on Mg(Al)O mixed oxide were reported by Gallo *et al.* [120, 121]. The Mg(Al)O mixed oxide support plays an important role in enhancing the performance of the catalyst. Ru based catalysts supported on Mg(Al)O mixed oxides have been reported in the literature to present good performance in steam reforming of ethanol [123], acetic acid [124] and hydrocarbons [125-127]. It is known that Mg(Al)O oxides are able to stabilize supported metal nanoparticles, even at high operating temperatures and/or glycerol concentrations, thus avoiding metal nanoparticles sintering [120]. The presence of Mg in the support is, in part, responsible for this good behavior. The effect of Sn doping on the bimetallic Ru-Sn/Mg(Al)O supported catalysts was assessed as well by using catalysts with different Sn loadings [120]. The Ru-based catalyst without tin showed very high glycerol conversion with high selectivity towards H_2 and CO_2, and CO selectivity lower than 10% during the entire catalytic run. By increasing the tin loading, a progressive increase in both CO and CH_4 selectivity was verified. On the other hand, the CO_2 selectivity decreased gradually. Therefore, the catalysts that showed the most attractive results in terms of specific H_2 productivity (mmol H_2·mmol Ru_{exp}^{-1}·min^{-1}) and specific activity (mmol glycerol·mmol Ru_{exp}^{-1}·min^{-1}) was the catalyst with the lowest tin content (Sn/Ru molar ratio of 0.33). It was concluded that the addition of tin has different effects depending on the Sn/Ru molar ratios. For low Sn/Ru molar ratios it was verified that both activity and H_2 productivity per exposed Ru sites are significantly enhanced, since tin selectively coated Ru faces, and only co-ordinatively unsaturated Ru sites, which are the most active ones, are exposed. However, by increasing the ratio a large amount of acidic tin oxides is unselectively deposited onto support materials. Therefore, glycerol decomposition is promoted rather than GSR, thus leading to high amounts of CO and finally to coke deposition responsible for the catalyst deactivation [120].

A comparison between the GSR performance of some of the promoted ruthenium catalysts here discussed and the non-promoted catalysts discussed in the previous section is presented in Table 2.6.

2.3.5 Other noble metal-based catalysts

In addition to the materials analyzed in the previous sections, there are others that have not been so frequently reported in the literature for H_2 production through GSR, but still present some interesting results. In this section some of those materials are reviewed.

Zhang *et al.* [106] studied, has already mentioned, the performance of ceria-supported Ir, Co and Ni catalysts for GSR in the temperature range between 250-600 ºC. Among all the catalysts tested, the Ir/CeO_2 sample was the one that presented the best performance. It was verified that the methane concentration greatly decreased with increasing temperature, thus meaning that the steam reforming of methane has occurred in a significant extent. Consequently, most of the produced methane was converted into H_2. Also, the increasing concentrations of CO_2 in the outlet gas stream and progressively lower CO content for increasing temperatures, indicates that the Ir/CeO_2 catalyst successfully catalyzes the WGS reaction. Therefore, Ir/CeO_2 seems to be a very promising catalyst for GSR.

Chiodo *et al.* [128] reported the comparison between a Rh/Al_2O_3 catalyst and several Ni supported materials for the GSR. The group came to the conclusion that the rhodium catalyst is more active and stable than the nickel-based ones. However, after approximately 8 h fast deactivation of the catalyst was verified. Rodhium catalysts are more resistant to coke formation than Ni-based due their high activity in hydrogenation reactions which, in case of removal of unsaturated compounds from the catalyst surface, is fundamental to avoid coke formation. Furthermore, Rh materials are active in C=C bond activation. Considering that the main species that reach the catalyst surface are

CO and olefins (C_2H_4, C_3H_6), it is therefore deducible that the catalytic performance depends on the tendency towards C=C cleavage and coke formation inhibition through polymerization of CH_x species and/or CO dissociation (Boudouard reaction) [129-132]. Despite this, there are still some improvements that need to be done regarding the relatively fast deactivation of Rh-based catalysts.

Ebshish *et al.* [133] compared the catalytic performance of 1 wt% Ce/Al_2O_3 and 1 wt% Pd/Al_2O_3 catalysts, as well as the performance of 1 wt% Ce/Al_2O_3 and 10 wt% Ce/Al_2O_3. The authors observed that the 1 wt% palladium catalyst supported on alumina presented better glycerol conversion to gaseous products as well as better H_2 yield than both 1 wt% Ce/Al_2O_3 and 10 wt% Ce/Al_2O_3 catalysts. In terms of H_2 selectivity, the 10 wt% Ce/Al_2O_3 sample was superior to the other two catalysts, having low amounts of carbon oxides been formed. This enhancement was suggested to be due to the higher metal loading. However, it also presented higher carbon formation than the other Ce-based catalyst. It has been concluded that in general Pd is more active and more stable than Ce because of its favorable lattice parameters. It is also important to remark the fact that this was the first time that Ce was reported as having been used as a catalyst for GSR. In all the previous works, only its oxide had been used as catalyst support.

A summary of some of the catalysts reviewed in this section and their catalytic performances in GSR is presented in Table 2.7.

Table 2.7 - Summary of the catalytic performance and operating conditions of different noble metal-based catalysts on GSR.

Catalyst	Operating Conditions	Conversion / %	Type of Conversion	H_2 Yield / %[a]/ Selectivity / %	Reference
Ir/CeO_2	400 ºC, 1 atm, GHSV[b] = 11 000 $mL \cdot g_{cat.}^{-1} \cdot h^{-1}$ and G/W/He[c] = 2/18/80 vol%	100	Not specified	n.d.[d]/85.6	[106]
5 wt% Rh/Al_2O_3	650 ºC, 1 atm, GHSV[b] = 5000 h^{-1} and WGFR = 9	50.0 (100 h)[e]	Glycerol conversion to gaseous products[f]	35.7[g]/n.d.[d]	[128]
1 wt% Pd/Al_2O_3	600 ºC, 1 atm, feed flow rate = 0.05 $mL \cdot min^{-1}$ and WGFR = 6	80.0 (2 h)[e]	Glycerol conversion to gaseous products[f]	55.0/70.0	[133]
10 wt% Ce/Al_2O_3	600 ºC, 1 atm, feed flow rate = 0.05 $mL \cdot min^{-1}$ and WGFR = 6	55.0 (2 h)[e]	Glycerol conversion to gaseous products[f]	42.0/80.0	[133]

[a] Based on the thermodynamic limit established in each work.
[b] GHSV: gas hourly space velocity.
[c] G/W/He: glycerol/water/helium volumetric composition.
[d] n.d.: not determined.
[e] Time of operation after which the data was collected.
[f] Calculation based on the amount of carbon (in glycerol) converted into gaseous products (CO_2, CO and CH_4).
[g] Assuming a thermodynamic limit of 7.

2.4 Mechanisms and kinetics

Establishment of reaction rate equations for any process, and for GSR in particular, is crucial for reactor design, while the comprehension of the associated mechanism may lead to improvements in catalyst design with the inherent implications at industrial scale. In the last years many authors have studied the kinetics of the GSR over different catalysts and have proposed different reaction mechanisms, being that there has not been full agreement on this matter. In this section a review of the proposed reaction kinetics, as well as the most accepted reaction mechanisms is done. This is, as mentioned above, fundamental for reactor modeling, design, optimization and operation.

Normally the reaction rate data for the GSR have been fitted to a general power-law type equation with the following form:

$$-r_{GSR} = k p_G^a p_W^b \quad \textbf{(2.15)}$$

where k is the reaction rate constant (defined by the Arrhenius equation), p_G and p_W and a and b are the partial pressures and the reaction orders of glycerol and steam, respectively.

Normally it is difficult to compare activation energies reported in the literature since the conditions used differ from study to study. Moreover, special attention should be put on whether or not mass (and even heat) transfer resistances are absent, so that cases of kinetics falsification can be identified. In Table 2.8 are presented some literature values of kinetic parameters obtained for some of the most relevant GSR catalysts in the absence of any resistances. In terms of activation energy, a comparison between all the Ni-based and Co-based catalysts presented in Table 2.8, which were tested at higher temperatures, can however be done.

Table 2.8 - Activation energies and reaction orders for the GSR reaction over different catalyst.

Catalyst	Operating conditions[a]	Preparation method	E_a / kJ·mol^{-1}	Reaction order for glycerol[b]	Reaction order for steam[b]	Reference
15 wt% Ni- 10 wt% ZrO_2/CeO_2	1 atm, 600 – 700 ºC	Wet impregnation of CeO_2 with $Ni(NO_3)_2{\cdot}6H_2O$ and $ZrO(NO_3)_2{\cdot}xH_2O$ aqueous solutions	43.4	0.3	0	[18]
24.1 wt% Ni- 26.1 wt% Mg- 49.8 wt% Al	1 atm, 400 - 600 ºC	Co-precipitation method with rising pH technique using $Ni(NO_3)_2{\cdot}6H_2O$, $Al(NO_3)_3{\cdot}9H_2O$ and $Mg(NO_3)_2{\cdot}6H_2O$ aqueous solutions	37.8	1.0 (WGFR = 9)	0	[24]
15 wt% Ni/CeO_2	1 atm, 400-700 ºC[c]	Deposition-precipitation using $Ni(NO_3)_2{\cdot}6H_2O$ aqueous solution	36.5	n.d.[d]	n.d.[d]	[50]
15 wt% Ni/Al_2O_3	1 atm, 450–550 ºC	Wet impregnation of γ-Al_2O_3 with $Ni(NO_3)_2{\cdot}6H_2O$ aqueous solution	59.8	0.48 (30 – 60 wt%)	0.34 (40 – 70 wt%)	[134]
Ni/CeO_2[c]	1 atm, 600 – 650 ºC	Wet impregnation of CeO_2 with $Ni(NO_3)_2{\cdot}6H_2O$ aqueous solution	103.4	0.23	0	[135]
15 wt% Co/Al_2O_3	1 atm, 450 – 550 ºC	Wet impregnation of Al_2O_3 with $Co(NO_3)_2{\cdot}6H_2O$ aqueous solution	67.2	0.08 (30 – 60 wt%)	0.39 (40 – 70 wt%)	[107]

Table 2.8 - Activation energies and reaction orders for the GSR reaction over different catalyst (cont.).

Catalyst	Operating conditions[a]	Preparation method	E_a / kJ·mol^{-1}	Reaction order for glycerol[b]	Reaction order for steam[b]	Reference
5 wt% Co-10 wt% Ni/Al_2O_3	1atm, 500 – 550 ºC	Co-impregnation of Al_2O_3 with $Co(NO_3)_2{\cdot}6H_2O$ and $Ni(NO_3)_2{\cdot}6H_2O$ aqueous solutions	63.3	0.25 (4.5-16.5 kPa)	0.36 (25-88 kPa)	[108]
Pt/C	5 atm , 350 – 400 ºC	Supplied by Arora-Matthey Ltd., Kolkata	n.d.[d]	1.0 (10-34 kPa)	0	[89]
5% Ru/Al_2O_3	1 atm, 350 – 500 ºC	Supplied by Johnson-Matthey Ltd., Delhi.	21.2	1.0 (x_G = 0.068-0.091)	0	[114]

[a] Temperature and total pressure at which the experiments were carried out.
[b] The values between brackets are the ranges of each species in the feed or their partial pressure.
[c] Metal loading not specified.
[d] n.d.: not determined.

Among these catalysts, it is possible to notice that while the Ni or Co/Al_2O_3 supported catalysts present activation energies around 60-70 $kJ \cdot mol^{-1}$, both the 24.1 wt% Ni- 26.1 wt% Mg- 49.8 wt% Al sample and the 15 wt% Ni- 10 wt% ZrO_2/CeO_2 material present activation energies of 38 $kJ \cdot mol^{-1}$ and 43 $kJ \cdot mol^{-1}$, respectively. This suggests that the reaction mechanism or the rate-determining step for the last two samples may be different from that over the other catalysts. On the other hand, both Ru-based and Pt-based catalysts were tested at lower temperatures, being that the 5% Ru/Al_2O_3 sample, among all catalysts in Table 2.8, is the one that presents the lowest activation energy. Vaidya and co-authors [114] suggest that this might occur due to the enhanced catalyst activity even at low reaction temperatures, which is associated to the high loading level of Ru. It should also be noticed the substantial difference between the activation energies of both Ni/CeO_2 catalysts (36.5 vs. 103.4 $kJ \cdot mol^{-1}$). Since for both cases, external and internal mass transfer limitations were minimized by selecting suitable flow rates and an appropriate particle size range, respectively, this peculiar difference may be associated to the different temperature ranges used, possibly different metal loadings, and different preparation methods. The last factor is probably the one that contributes the most to the verified significant difference. In comparison to the wet impregnation technique, the deposition-precipitation method improves, among other things, the metallic dispersion and decreases catalyst sintering.

In terms of glycerol partial reaction order, all Ni-based catalysts presented similar values (0.2-0.5) except for the Ni-Mg-Al sample, which presents a value of 1.0. This difference suggests that different reaction mechanisms or different rate-determining steps may exist for these catalysts. Regarding the Co-based materials, both present low values of glycerol partial reaction order, especially the Co/Al_2O_3 catalyst. As a matter of fact, this catalyst also presents small values of glycerol partial reaction order for the production of C_1 products (CO_2, CO and CH_4). This might indicate the existence of a cancellation effect of the molecularly

adsorbed glycerol in the rate-controlling step and the presence of a glycerol adsorption term in the denominator of the Langmuir-Hinshelwood rate expression (see Eq. (2.30)) [107]. Therefore, an apparent reduced order for glycerol in the overall reaction rate is obtained. For the Pt- and the Ru-based catalysts, glycerol partial reaction orders of 1 were considered as a valid approach for the low glycerol concentrations used. However, this assumption may not be valid for more concentrated solutions, which can be used during real operation in reformers. In terms of H_2O reaction order, for most of the catalysts in Table 2.8 it is considered to be zero due to the use of excess of water. For the others, however, values between 0.3 and 0.4 were obtained despite the excess steam used.

The formation rates of H_2, CO_2, CO and CH_4 have been often fitted to a power-law expression (Eq. (2.15)) as well [107, 108, 134]. For all cases, the formation rate of CO was inhibited by steam (negative value of b). This can either be because of the competitive adsorption of steam on the same active sites as the surface precursor for CO production (especially at high steam partial pressures), or because of CO consumption via WGS reaction [134]. For the other gases, positive values of a and b were obtained, meaning that both glycerol and steam positively contribute to H_2, CO_2 and CH_4 formation. In terms of activation energy, H_2, CO_2 and CO formation present similar values (in the range 60-75 kJ·mol^{-1}) [108, 134] while the formation of methane presents a much higher activation energy (100-120 kJ·mol^{-1}) [107, 108, 134].

In what concerns the reaction mechanism, Adesina and co-workers [108] came to the conclusion that the most adequate one for the GSR reaction over the 5 wt% Co-10 wt% Ni/Al_2O_3 catalyst is the Langmuir-Hinshelwood dual site mechanism with molecular adsorption of both glycerol and steam. This mechanism involves the following steps:

$$C_3H_8O_3 + X_1 \rightleftharpoons C_3H_8O_3 - X_1 \qquad \textbf{(2.16)}$$

$$H_2O + X_2 \rightleftharpoons H_2O - X_2 \quad \textbf{(2.17)}$$

$$C_3H_8O_3 - X_1 + H_2O - X_2 \rightarrow HCOO - X_2 + CH_2OHCHOH - X_1 + 2H_2 \quad \textbf{(2.18)}$$

$$HCOO - X_2 \rightarrow CO_2 + H - X_2 \quad \textbf{(2.19)}$$

$$CH_2OHCHOH - X_1 + H - X_2 \rightarrow CH_2OH - X_1 + CH_3O - X_2 \quad \textbf{(2.20)}$$

$$CH_2OH - X_1 + X_2 \rightarrow CH_2 - X_1 + OH - X_2 \quad \textbf{(2.21)}$$

$$CH_2 - X_1 + H - X_2 \rightarrow CH_3 - X_1 + X_2 \quad \textbf{(2.22)}$$

$$CH_3 - X_1 + H - X_2 \rightarrow CH_4 + X_1 + X_2 \quad \textbf{(2.23)}$$

$$CH_3O - X_1 + X_2 \rightarrow CH_2O - X_1 + H - X_2 \quad \textbf{(2.24)}$$

$$CH_2O - X_1 + X_2 \rightarrow HCO - X_1 + H - X_2 \quad \textbf{(2.25)}$$

$$HCO - X_1 + X_2 \rightarrow CO - X_1 + H - X_2 \quad \textbf{(2.26)}$$

$$CO - X_1 \rightleftharpoons CO + X_1 \quad \textbf{(2.27)}$$

$$CO - X_1 + OH - X_2 \rightleftharpoons CO_2 + H - X_2 + X_1 \quad \textbf{(2.28)}$$

$$2H - X_2 \rightleftharpoons H_2 + 2X_2 \quad \textbf{(2.29)}$$

where X_1 and X_2 represent the basic and the acid active sites, respectively. The authors suggested that surface reaction was rate-controlling, and so the following kinetic expression was proposed [108]:

$$r = \frac{k p_G p_W}{(1 + K_G p_G)(1 + K_W p_W)} \quad \textbf{(2.30)}$$

where K_G and K_W are the adsorption constants of glycerol and steam, respectively. In another work, Cheng *et al*. [134] concluded that the GSR reaction rate over a Ni/Al_2O_3 supported catalyst is better described by a Langmuir-Hinshelwood model considering molecular adsorption of glycerol and dissociative chemisorption of steam, on two different sites, with the surface reaction as rate-determining step. The authors proposed the following mechanism represented by Eqs. (2.31-2.44).

$$C_3H_8O_3 + X_1 \rightleftharpoons C_3H_8O_3 - X_1 \quad \textbf{(2.31)}$$

$$H_2O + 2X_2 \rightleftharpoons OH - X_2 + H - X_2 \quad \textbf{(2.32)}$$

$$C_3H_8O_3 - X_1 + H - X_2 \rightarrow CH_2OHCHOH - X_1 + CHOH - X_2 + 2H_2 \quad \textbf{(2.33)}$$

$$CHOH - X_2 \rightarrow CO - X_2 + H_2 \quad \textbf{(2.34)}$$

$$CH_2OHCHOH - X_1 + H - X_2 \rightarrow CH_2OH - X_1 + CH_3O - X_2 \quad \textbf{(2.35)}$$

$$CH_2OH - X_1 + X_2 \rightarrow CH_2 - X_1 + OH - X_2 \quad \textbf{(2.36)}$$

$$CH_2 - X_1 + H - X_2 \rightarrow CH_3 - X_1 + X_2 \quad \textbf{(2.37)}$$

$$CH_3 - X_1 + H - X_2 \rightarrow CH_4 - X_1 + X_2 \quad \textbf{(2.38)}$$

$$CH_3O - X_1 + X_2 \rightarrow CH_2O - X_1 + H - X_2 \quad \textbf{(2.39)}$$

$$CH_2O - X_1 + X_2 \rightarrow HCO - X_1 + H - X_2 \quad \textbf{(2.40)}$$

$$HCO - X_1 + X_2 \rightarrow CO - X_1 + H - X_2 \quad \textbf{(2.41)}$$

$$CO - X_1 \rightleftharpoons CO + X_1 \quad \textbf{(2.42)}$$

$$CO - X_1 + OH - X_2 \rightleftharpoons CO_2 + H - X_2 + X_1 \quad \textbf{(2.43)}$$

$$\mathrm{H} - X_2 + \mathrm{H} - X_2 \rightleftharpoons \mathrm{H}_2 + 2X_2 \quad \textbf{(2.44)}$$

This mechanism yielded the following rate equation [134]:

$$r = \frac{kP_G\sqrt{P_W}}{(1 + K_G P_G)\left(1 + \sqrt{K_W P_W}\right)} \quad \textbf{(2.45)}$$

In another mechanistic study, Byrd *et al*. [15] observed the presence of very low concentrations of organic carbon in the product stream, which suggests that intermediates like alcohols or organic acids, formed from C-O cleavage, were further transformed into gaseous products. For this reason, a different mechanism was proposed to describe the GSR over the 5% Ru/Al_2O_3 catalyst [114] and was also admitted to be valid for the 15 wt% Ni/CeO_2 one [50]. This mechanism involves the reversible adsorption of glycerol on the catalyst active sites followed by its reaction with water, thus forming an adsorbed complex molecule. This complex on its hand decomposes into intermediate products, which irreversibly yield H_2 and CO_2. These steps are described by the following equations:

$$\mathrm{C_3H_8O_3} + X \overset{k_1,k_{-1}}{\longleftrightarrow} \mathrm{C_3H_8O_3} - X \quad \textbf{(2.46)}$$

$$\mathrm{C_3H_8O_3} - X + \mathrm{H_2O} \overset{k_2}{\rightarrow} \text{Complex}-X \quad \textbf{(2.47)}$$

$$\text{Complex}-X \overset{k_3}{\rightarrow} \text{Intermediates} \overset{k_4}{\rightarrow} \mathrm{CO_2} + \mathrm{H_2} \quad \textbf{(2.48)}$$

By applying steady state hypothesis to $C_3H_8O_3 - X$ and Complex$-X$ and assuming that the decomposition of Complex$-X$ into intermediate products is the rate-determining step, the reaction rate was expressed as [50, 114]:

$$r = \frac{k_1 k_2 p_G p_W}{[k_{-1} + k_1 p_G + k_2 p_W + (k_1 k_2 p_G p_W / k_3)]} \quad \textbf{(2.49)}$$

Considering that water is in excess and that the operation pressure is constant, p_W can be assumed to be almost equal to p_{W0}. Therefore, Eq. (2.49) is simplified to:

$$r = \frac{kp_G}{1 + bp_G} \quad \textbf{(2.50)}$$

where k and b are defined as:

$$k = \frac{k_1 k_2 p_{W0}}{k_{-1} + k_2 p_{W0}} \quad \textbf{(2.51)}$$

$$b = \frac{k_1 + (k_1 k_2 p_{W0}/k_3)}{k_{-1} + k_2 p_{W0}} \quad \textbf{(2.52)}$$

Carbon deposition, as already discussed, is one of the most common causes of catalyst deactivation in GSR reaction. The influence of carbon deposition on the physical properties of the catalyst has already been discussed, as well as the nature of these deposits. On the other hand, the determination of carbon deposition kinetics is very helpful in terms of creation of more realistic reactor models, and better reactor design and operation. Cheng et al. [136] observed that the coke deposition rate on a 5 wt% Co-10 wt% Ni/Al2O3 catalyst during GSR can be relatively well described by a power-law model as follows:

$$r_{coke\ deposition} = k_C p_G^a p_W^b \quad \textbf{(2.53)}$$

where k_C is the coke deposition reaction rate constant. At temperatures between 500-550 ºC and glycerol partial pressures between 4.5-16.5 kPa, the parameters a and b were determined to be 0.55 and -0.22, respectively, being the activation energy 40.9 kJ·mol^{-1}. These values were found to be lower than those obtained for carbon deposition caused by C_3H_8 [137, 138], which is structurally very similar to glycerol. Regarding the lower activation energy, it may be explained by the

presence of the functional OH group on each of the carbon atoms in the parent chain of glycerol, which makes it more reactive than propane (less electron-withdrawing H on each C atom). Moreover, the equilibrium constant of propane dehydrogenation into hydrogen and carbon is lower than that of glycerol decomposition into carbon. Therefore, the authors concluded that the adsorption of glycerol is stronger than for propane, in other words, it leads to easier carbon deposition [136]. Keeping this in mind and considering the empirical rate law, it was suggested that glycerol adsorbs dissociatively while steam is molecularly chemisorbed. Therefore, a Langmuir-Hinshelwood rate model considering a bimolecular rate-controlling step was proposed [136], yielding the following rate equation for coke deposition.

$$r_{coke\ deposition} = \frac{k_C p_W \sqrt{p_G}}{\left(1 + K_W P_W + \sqrt{K_G p_G}\right)^2} \quad \textbf{(2.54)}$$

2.5 Sorption-enhanced reactors

In the last years, alternatives for improving the catalytic GSR process have been investigated. The main common reason that motivates this search is the necessity of overcoming equilibrium limitations, and also producing highly pure hydrogen that is suitable to be used in PEMFCs, for example. One of those alternatives is the SEGSR process, which consists on combining the catalytic GSR and CO_2 capture in the same physical device. This innovative configuration allows “affecting” the thermodynamic equilibrium of the GSR reaction by removing one of the reaction products from the reaction medium. Some of the more important advantages of sorption-enhanced reactors (SER) comparatively to tradition reactors (TR) are:

- Shift the equilibrium of reversible reactions towards higher conversions.
- Enhancement of both hydrogen yield and selectivity.

- Attainment of better performance than in a TR at the same (or even less drastic) operating conditions.

However, the main disadvantage of this system is that the CO_2 sorbent gets saturated at some point and then regeneration is necessary. In order to be possible to run continuously, the system must encompass, for example, two reactors, being that while one of them is used as SER the other is used as regenerator; the approach is the same as used in other cyclic processes like PSA (Pressure Swing Adsorption), etc. Another example of such a continuous SEGSR system is presented in Fig. 2.18 [139].

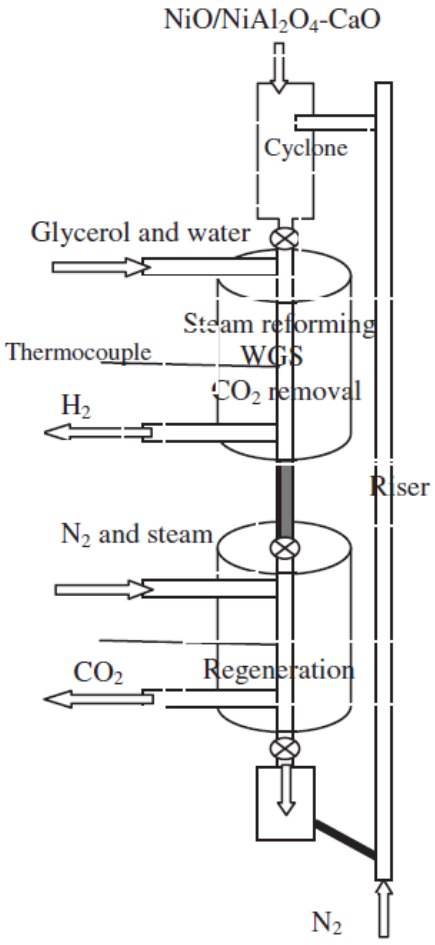

Fig. 2.18 - Scheme of the continuous SEGSR system. Taken from [139].

Besides the two moving-bed reactors in which both catalyst and sorbent are moved at a velocity of 9-11 cm·min^{-1}, a riser is used for transporting the particles with N_2. There is also a system for injecting the particles of catalyst and sorbent at the top of the reactor (cyclone section) in order to compensate for the losses during the runs, which amount is close to 5% every 5 min [139].

The successful use of SERs for GSR depends, above all, on choosing an sorbent with suitable characteristics and selecting appropriate operating conditions. Such matters are target of focus in the following section.

2.5.1 CO_2 sorbents

Different materials like hydrotalcites [140-144], CaO-based materials [145-149], lithium zirconates [150-154] and lithium silicates [155-159], among others, have been reported in the literature as CO_2 sorbents for SERs applications. It is expected from a good CO_2 sorbent to couple in a GSR process to present high CO_2 capture capacity and selectivity at moderated temperatures (300-500 ºC), good regenerability (adequate sorption-desorption kinetics), good hydrothermal and mechanical stability and low-cost [160-163]. The sorption capacities and sorption/regeneration temperatures of several sorbents are summarized is Table 2.9.

Hydrotalcites are a family of clay minerals that consist of a double-layered hydroxide structure with the general formula $\left[\mathrm{M}_x^{\mathrm{II}}\mathrm{M}_{(1-x)}^{\mathrm{III}}(\mathrm{OH})_2\right][\mathrm{A}^{n-}]_{x/n} \cdot m\mathrm{H_2O}$, where M^{II} and $\mathrm{M}^{\mathrm{III}}$ represent di- and trivalent metal ions inside the brucite-like layers and A^{n-} is a charge compensating anion [143, 167]. Aschenbrenner *et al.* [143] observed that NiMgAl hydrotalcite presented 53% more sorption capacity than NiMgAlFe hydrotalcite and high stability. A comparison between a commercial hydrotalcite and two potassium and potassium-sodium containing hydrotalcites allowed to conclude that the last one presented the highest sorption capacity while the potassium containing hydrotalcite presented no significative

deactivation after more than 50 cycles of operation [142]. K-doped hydrotalcite-based sorbents have been reported elsewhere to present a CO_2 capture capacity as high as 9 mol·kg^{-1} at 300 ºC but under wet conditions (Table 2.9) [141]. Under dry conditions, the maximum value reported was around 1.8 mol·kg^{-1} (Table 2.9), which is an outstanding value taken into account the temperature (300 ºC) and that it was not tested under the presence of steam. It has also been found that the physical and chemical properties of hydrotalcites are highly influenced by the charge compensating anion used. Wang *et al*. [168] analyzed several charge compensating anions (CO_3^{2-};HCO_3^-; NO^{3-}; SO_4^{2-}; and Cl^-) having observed that when using CO_3^{2-}, a spheroidal "sand rose" type of hydrotalcite with very high BET surface area (114.3 m^2·g^{-1}) was produced. On the other hand, the other anions led to the formation of "stone" type hydrotalcites with very low surface areas (< 9 m^2·g^{-1}). For this reason, the Mg_3Al_1-CO_3 hydrotalcite presented the highest CO_2 capture capacity. The thermal stability was also found to depend on the anion used, being that the Mg_3Al_1-SO_4 was the one that presented the highest thermal stability.

Other sorbents like CaO-based materials, and lithium zirconates and silicates present in general a lower CO_2 capacity and slower sorption kinetics at 300-400 ºC, higher regeneration temperature (> 650 ºC) and gradual deactivation due to sintering of the active surface [140]. They have however significant sorption capacities, but at much higher temperatures (Table 9). Wang *et al*. [145] avoided sintering of nano $CaCO_3$ during multiple carbonation/calcination cycles by applying a TiO_2 coating. Akgsornpeak *et al*. [149] avoided the same problem by preparing CaO sorbents through sol-gel synthesis in the presence of cetyltrimethyl ammonium bromide (CTAB). Besides that, the CaO sorbents prepared with CTAB also exhibited high carbonation reaction rates, and the best CaO sorbent presented carbonation conversion 154% more effective than the CaO prepared in the absence of CTAB.

Table 2.9 - Sorption capacities and sorption/regeneration temperatures of several CO_2 sorbents reported in the literature for SERs applications.

Sorbent	Sorption capacity / mol·kg^{-1}	Sorption temperature / ºC	Regeneration temperature / ºC	p_{CO_2} / bar	p_{H_2O} / bar	Reference
K-doped hydrotalcite (20 wt% K_2CO_3 and Mg/Al ratio = 2)	9.40[a]	300	600	0.34	4.5	[141]
K-Na-doped hydrotalcite	1.11[a]	300	300	0.40	0.42	[142]
Hydrotalcite	1.18	400	n.s.	0.15	0	[164]
Ga-K-doped hydrotalcite (10 wt% Ga and 20 wt% K)	1.82	300	300	1.08	0	[165]
CaO-Y_2O_3 (20 wt% Y_2O_3)	12.95	850	850	n.s.[b]	0	[147]
CaO from calcium acetate	17.30	600	700	0.30	0	[164, 166]
Dolomite	8.40	750	n.s.	0.15	n.s.[b]	[164]
Li_2ZrO_3	5.00[a]	500	n.s.	n.s.[bc]	n.s.[bc]	[153]
K-doped Li_4SiO_4 (30 wt% K_2CO_3)	5.23	580	700	0.04	0	[156]
Li_4SiO_4 (treated with glacial acetic acid)	0.77	550	625	0.1	0	[157]

[a] Wet conditions.
[b] n.s.: not specified.
[c] Total pressure = 4.47 bar.

The incorporation of Y_2O_3 has been recently reported to significantly enhance the carbonation rate and sorption capacity of CaO-based CO_2 sorbents [147]. Similarly to hydrotalcites, the addition of optimized amounts of K to Li_2ZrO_3 sorbents was reported to enhance its CO_2 sorption rate and capacity. Moreover, they showed good stability [152]. However, Lapkin and co-workers [154] came to the conclusion that a traditional route to K-doped materials result in slow regeneration. On the other hand, a new soft chemistry route that produces high surface area undoped materials led to much higher rates of reaction/regeneration. Seggiani *et al*. [156] analyzed the performance of different doped-Li_4SO_4 CO_2 sorbents, having observed that the K-doped and Na-doped presented the highest CO_2 sorption capacities and sorption rates. In terms of stability, only the potassium-doped sorbent was able to keep its properties after 25 sorption/desorption cycles. In another work, it was shown that Li_4SiO_4 treated with glacial acetic acid presented stable CO_2 sorption capacity, higher specific surface area and higher porosity than limestone and Li_4SiO_4 without acid treatment [157].

The decision on which kind of CO_2 sorbent is more adequate to be used in SEGSR strongly depends on the operating temperature at which it will be employed. Since one of the main goals at the moment is to reduce the GSR temperature in order to reduce operation costs, it is desirable to work at relatively low temperatures (300-500 ºC). For such temperatures hydrotalcites have been reported to present higher CO_2 capacities and faster sorption kinetics, as well as easier regeneration, and lower loss of sorption capacity [140, 141]. Moreover, the fact that the CO_2 capacity of hydrotalcites is strongly enhanced under wet conditions (steam reforming conditions) makes them an even better candidate for use in SEGSR.

2.5.2 Sorption-enhanced glycerol steam reforming

The catalytic GSR performed in TRs presents some limitations as already mentioned, including the thermodynamic constrains. On the other hand, when CO_2 capture is performed simultaneously with the GSR reaction in a SER, the thermodynamic equilibrium is shifted towards higher glycerol conversions and hydrogen yields. A typical evolution profile of the product gas composition (N_2 free and dry basis) in a SEGSR over a mixture of Ni-Co/hydrotalcite-like catalyst and calcined dolomite as CO_2 sorbent is illustrated in Fig. 2.19 [169]. The performance of the SEGSR is highly dependent on the CO_2 capture. It can be seen in Fig. 2.19 that there are 3 distinct regimes along time: pre-breakthrough, breakthrough and post-breakthrough. In the pre-breakthrough regime (up to 140 min), most of the CO_2 was removed by fast carbonation reaction with CaO, thus enhancing hydrogen production. In the breakthrough regime the H_2 concentration starts decreasing.

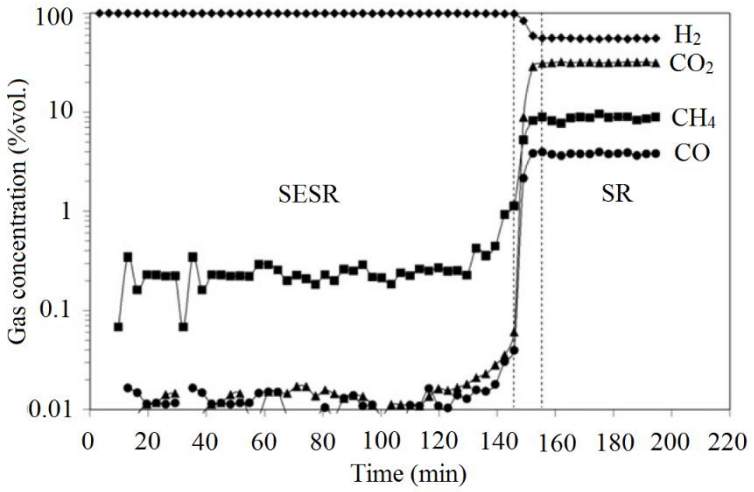

Fig. 2.19 - Evolution with time of the gas product composition (N_2 free and dry basis) during SEGSR at 550 ºC, WGFR of 9, 1 atm, contact time of 1.09 h and sorbent/catalyst = 5).

In the post-breakthrough regime the CaO sorbent is already saturated and so the enhancement of hydrogen production due to CO_2 removal disappears; at this stage the SEGSR becomes GSR (conventional fixed-bed reactor).

In the following sections are shown the effects of the main operating conditions in the SEGSR, comparing, whenever possible, with the thermodynamic equilibrium.

2.5.2.1 Effect of temperature

The influence of temperature on the performance of a SEGSR reactor has been analyzed by several authors, due to the crucial importance of choosing an appropriate temperature range in order to fully benefit of the advantages of this innovative reaction-separation system.

Chen *et al*. [44] compared the product gas composition of a GSR reactor obtained with and without in situ CO_2 removal, and each of them with the respective thermodynamic equilibrium limits. Such comparison is depicted in Fig. 2.20 [44]. The SEGSR tests were performed until the calcined dolomite was saturated, being that from that point on the GSR took place. A Co-Ni/hydrotalcite-like catalyst and ARCTIC dolomite (98.5% $CaMg(CO_3)_2$) CO_2 sorbent were used. Regarding the GSR product gas composition, the thermodynamic equilibrium trends are in general followed by CO and CH_4. However, the H_2 content is slightly higher and the CO_2 content is slightly lower than the equilibrium values for GSR. The authors suggested that this happened because of the very slow CO_2 removal by the dolomite sample in the second carbonation regime (i.e. the reactor was not yet operating as a conventional GSR one, because some carbon dioxide sorption was still occurring). By comparing both SEGSR and GSR it is observed, as expected, that the in situ selective removal of CO_2 enhanced the hydrogen production and originated a lower CO content due to the promotion/shift of the WGS reaction equilibrium, which consequently promoted SRM.

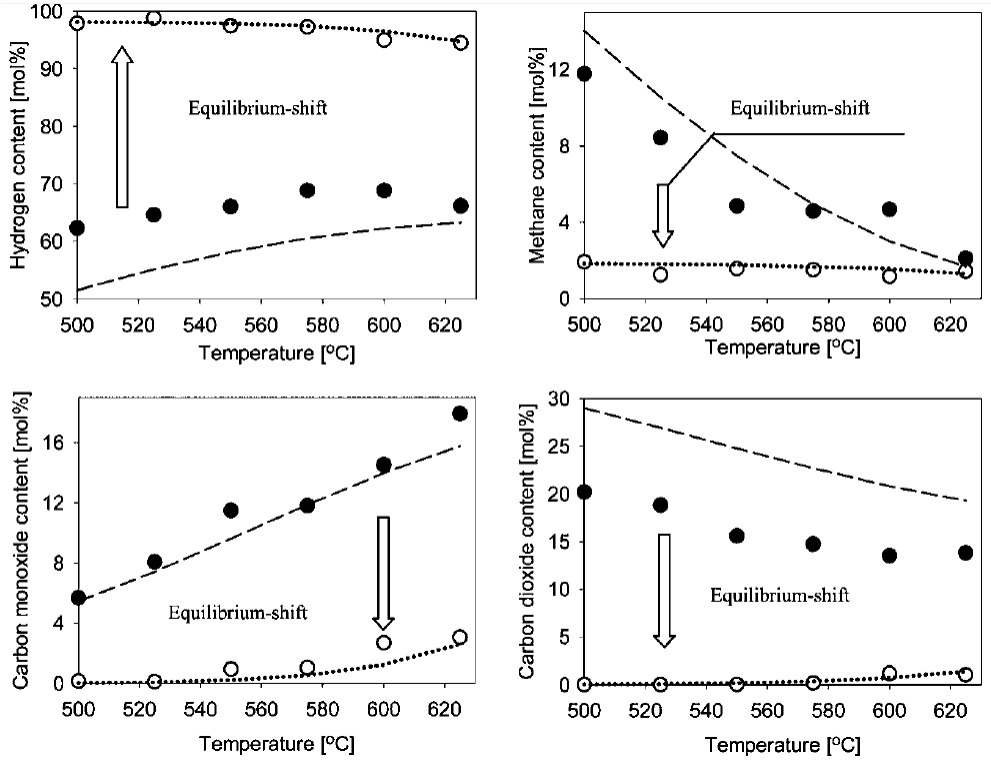

Fig. 2.20 - Product gas composition (dry basis) of GSR with and without in situ CO_2 removal at WGFR of 4, 1 atm, catalyst/sorbent ratio of 5/2.5 and contact time of 1 h (··· thermodynamic equilibrium of SEGSR, --- thermodynamic equilibrium of GSR, ○ experimental results for SEGSR, ● experimental results for GSR). Taken from [44].

Both experimental and thermodynamic equilibrium gas composition values are in agreement for SEGSR. In terms of the effect of temperature, a compromise between the WGS reaction, SRM and CO_2 sorption has to be considered. At higher temperatures, both exothermic WGS reaction and CO_2 sorption are less favored while the endothermic SRM is benefited. As can be seen for SEGSR, both CO and CO_2 contents increase with temperature, being that CO is more influenced because of both the increase of CO_2 concentration in the sorption equilibrium and decrease of the WGS reaction equilibrium constant. The methane content, on the other hand, decreased since high temperatures favor SRM. Finally, the hydrogen purity decreased as well due to the presence of higher amounts of CO and CO_2.

Dou *et al*. [122, 170] analyzed the purity of hydrogen as a function of time at distinct temperatures (400-700 ºC [122] and 500-700ºC [170]) while using dolomite as CO_2 sorbent. As expected, the highest hydrogen purity was obtained in the pre-CO_2 breakthrough period. The periods of production of hydrogen with purity higher than 90% were 3.6, 6.8 and 5 min at 400, 500 and 600 ºC, respectively. At 700 ºC, the maximum H_2 purity was 77% with a CO_2 breakthrough time of 0.7 min [122]. A similar behavior was observed in [170]. The authors suggest that the effect of SEGSR was particularly low at 700 ºC because the carbonate decomposition (calcination) in the presence of steam is significantly active at that temperature for dolomite. Moreover, the calcined dolomite presents some affinity towards steam in order to form $Ca(OH)_2$ (Eq. (2.13)). In another work, Dou and co-workers [139] observed that the high-purity hydrogen production period did not vary much when the operation temperature was increased from 500 ºC to 600 ºC, while using CaO as CO_2 sorbent. Chen *et al*. [171] observed, while using an hydrotalcite CO_2 sorbent, a decrease of the GSR enhancement when the temperature was increased from 400 to 500 ºC. Thus, the operating temperature should be chosen so that the GSR enhancement caused by in situ CO_2 capture is maximized.

2.5.2.2 Effect of the molar water/glycerol feed ratio

It is well known that the WGFR has an important influence on the GSR reaction. It was verified in section 2.2.2 that increasing the WGFR affects the thermodynamic equilibrium of the SEGSR process. However, in actual operation additional effects may occur. Such effects are target of discussion here.

Chen and co-workers [44] analyzed the performance of the SEGSR for different values of WGFR in the range of 3-9. A comparison between the evolution of product composition with time on stream at WGFRs of 3, 4 and 9 was done. During the pre-CO_2 breakthrough period, in particular, the authors observed that for a WGFR of 9 the maximum H_2 purity is higher than that for a

WGFR of 3. Moreover, at the lower WGFR the H_2 purity decreased with time on stream. This decay was caused exclusively by the gradual increase of the methane content, since both CO_2 and CO content remained almost constant and low. The authors suggested that the relatively high methane content was not exclusively due to methanation reaction, since only low amounts of CO_2 and CO were present in the gas phase and in the catalyst surface. Thus, considering that SEGSR was performed at high temperatures and glycerol is thermally unstable, the pyrolysis of glycerol to yield CH_4, CO_2, H_2O, coke and volatiles may have happened even before glycerol reached or passed through the catalyst bed. Therefore, pyrolysis of glycerol may have occurred and caused the carbonaceous deposits that were found on the front of the reactor bed and that led to catalyst deactivation. At a WGFR of 4 the purity of H_2 was lower than that for a WGFR of 9, however gradual decrease of the H_2 content due to methane formation through glycerol pyrolysis was not observed at such water content as compared to WGFR of 3.

A comparison between the H_2 yields obtained experimentally and in the thermodynamic equilibrium at different WGFRs was also done by Chen *et al.* [44]. The biggest difference was obtained for a WGFR of 3. This happened because of the pyrolysis of glycerol that hindered hydrogen production by favoring the formation of CH_4, CO_2 and carbon deposits. As the WGFR increased, the experimental H_2 yield went close to the thermodynamic boundaries, being that at a WGFR of 9 the experimental H_2 yield achieved the theoretical maximum value. In another work, Chen *et al*. [169] obtained lower H_2 yields than in [44] using the same WGFR of 9 but at 550 ºC. They suggested that this lower performance was associated to the formation of carbonaceous deposits through glycerol pyrolysis. The reason for such difference is that while in [44] pure glycerol was used, in [169] Chen's group used crude glycerol, whose impurities lead to pyrolysis, thus enhancing coke formation.

Wang *et al*. [172] analyzed the impact of changing the WGFR from 6 to 9 on the product composition (dry basis) of SEGSR. While for a WGFR of 6 a dry product composition of 87% H_2, 9% CH_4, 3% CO and 1% CO_2 was attained, for a WGFR of 9 a dry product composition of 95% H_2 and 5% of CH_4 was reached. This is due to the enhancement of GSR performance at higher WGFRs. Even though the H_2 concentrations obtained for both cases were high, they were still below the thermodynamic values. Methane concentrations, on the other hand, were higher than the thermodynamic values, which the authors suggested to be due to lack of activity to convert excess methane into hydrogen with the Ni/ZrO_2 catalyst used.

On the other hand, the steam content has been reported to influence the capacity of CO_2 sorbents [141, 142]. By comparing the sorption capacity of hydrotalcite-based sorbents under dry and wet conditions, Martunus *et al*. [142] and Maroño *et al*. [141] concluded that under wet conditions the CO_2 capture capacities of the sorbents were higher. Dou *et al.* [170] compared the performance of SEGSR using crude glycerol and pure glycerol in the same conditions, having come to the conclusion that when crude glycerol was used longer breakthrough times were observed. This might be explained by the fact that steam conversions obtained while using crude glycerol were approximately half of those obtained for pure glycerol, thus resulting in higher steam partial pressures in the reactor when crude glycerol was used. However, excessive amounts of steam may lead to reduction of CO_2 capture capacity of sorbents, since it causes shrinkage of pore mouths due to sorption of both steam and CO_2 on the active sorbent surfaces, especially near the pore mouth. Consequently, the pores may be closed, thus increasing the diffusional resistance [142].

2.5.2.3 Effect of pressure

It was discussed in section 2 that, in equilibrium, lower pressures favor the production of hydrogen through both GSR and SEGSR and lead to low carbon

formation, especially for SEGSR. Chen and co-workers [171] observed that by increasing the operation pressure, the hydrogen yield decreased for both GSR and SEGSR (Fig. 2.21 [171]). However, as expected, higher values of hydrogen yield were obtained in SEGSR for all pressure range. Moreover, it was observed that the difference between the values of H_2 yield in GSR and SEGSR increased with pressure, as can be seen in Fig. 2.21. This happens because higher pressures favor CO_2 sorption. Therefore higher pressures allow taking more advantage of the benefits of the SEGSR process.

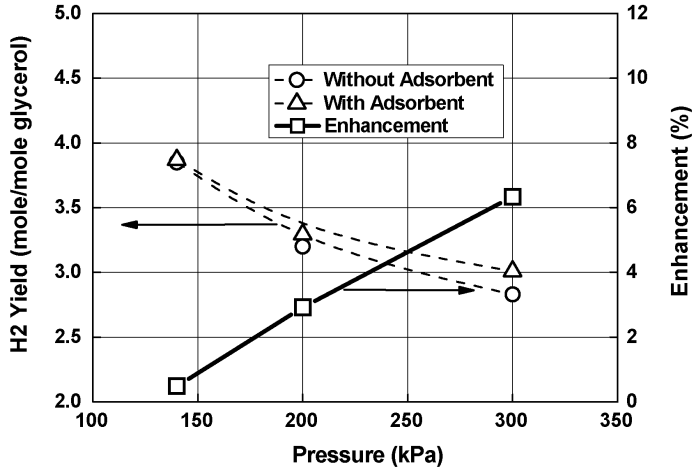

Fig. 2.21 - Effect of pressure on the hydrogen yield during SEGSR at 450 ºC, WGFR of 9, glycerol/N_2 volume ratio of 0.025, using a Ni-based catalyst and microsized hydrotalcite as CO_2 sorbent. Taken from [171].

2.6 Membrane reactors

The international union of pure and applied chemistry (IUPAC) defined MR as a device for simultaneously carrying out a reaction and a membrane-based separation in the same physical enclosure [173]. In a MR the membrane not only selectively separates one or more components but also plays a crucial role, e.g. in overcoming the thermodynamic boundaries of equilibrium-limited reactions like the GSR. Regarding its advantages compared to TRs, they are basically the

same as SERs, with exception to the reduction of CO_2 emissions, being that the capital costs reduction is even higher in the case of MRs since only one reactor is needed instead of two reactors. In fact, this cost reduction is feasible as long as cheap and long-lasting membranes can be produced. Moreover, in MRs it is possible to produce ultra-pure hydrogen streams. The scheme of a MR for GSR is presented in Fig. 2.22 [174]. In this particular case, a hydrogen permselective membrane is used to selectively separate hydrogen from the other components; however, a CO_2 permselective membrane could be used instead. Still, since one of the main goals of using MRs for GSR reaction is to produce ultra-pure hydrogen that can later be used in PEMFCs, it is preferable to use a H_2 permselective membrane in order to isolate H_2 instead of using CO_2 permselective membranes and having H_2 mixed with steam, some unreacted CO and glycerol.

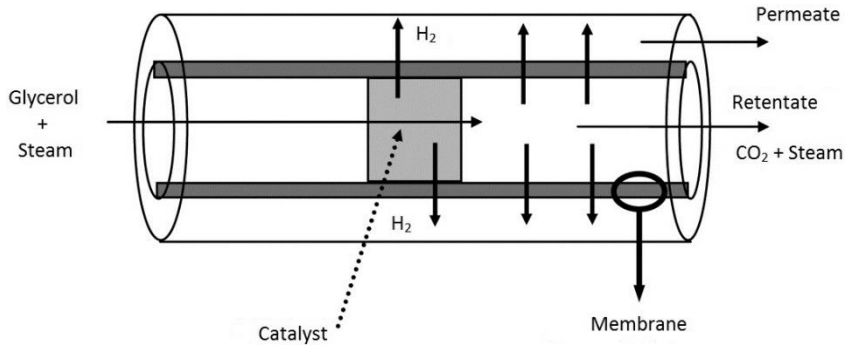

Fig. 2.22 - Scheme of a MR for the GSR reaction. Adapted from [174].

2.6.1 Hydrogen permselective membranes for membrane reactors

Hydrogen permselective membranes may be classified as dense metallic membranes (palladium and palladium alloys), proton conducting dense ceramic membranes (perovskites like $SrCeO_{3-\delta}$ and $BaCeO_{3-\delta}$), dense polymeric membranes (polyimide, cellulose acetate, polysulfone, etc.), microporous ceramic membranes (silica, alumina, zirconia, titania, zeolites, metal-organic

frameworks (MOF)) and porous carbon membranes (carbon) [175, 176]. The main advantage of dense metallic membranes is that usually they withstand high temperatures (e.g. as compared to polymeric ones) and present higher selectivity towards H_2, thus being possible to obtain high purity hydrogen-permeate streams [175]. Therefore, dense metallic membranes are preferable for ultra-pure hydrogen production and will be the main target of focus.

When choosing a membrane to be used in a MR, one has to consider the operating conditions under which the membrane will be used. In the last years there has been a tremendous effort in order to find suitable membranes for MR applications. Palladium-based membranes are currently the most promising for high purity hydrogen production in MRs, especially palladium alloys (e.g. Pd-Ag and Pd-Cu) which are less sensitive than pure Pd to embrittlement (caused by the presence of H_2 at temperatures below 300 ºC and pressures below 2 MPa) and poisoning (caused by contact with CO or H_2S - present in crude glycerol) [175, 177]. Tosti *et al*. [178] verified that self-supported dense Pd-Ag 23 wt% tubular membranes with finger-type configuration are highly durable and reliable since they allowed to attain complete hydrogen selectivity and no failures were observed after at least one year of thermal and hydrogenation cycles. These characteristics, together with high permeability, make such materials very promising for ultra-pure hydrogen production in industrial and energetic applications (chemical industry, PEMFCs, etc.) [178]. However, the cost of these dense membranes is still a limiting factor, reason why a strong effort has been put in the preparation of thinner Pd films over different supports, by several techniques.

In terms of preparation methods, electroless plating (EP) and chemical vapor deposition (CVD) are the most used ones. The EP method normally consists on producing Pd particles through reduction of a plating solution containing Pd-amine complexes. This technique allows to attain high coating adhesion, involves low operation costs and allows simple operation. However,

the impurities present in the plating solution may lead to the presence of defects on the palladium layer deposited on the support. The CVD technique allows to very easily deposit a metal film on a support. On the other hand, using both of these techniques it may be difficult to control the metal alloy composition [179].

Usually the permeation of hydrogen through a palladium-based membrane is described by a solution-diffusion mechanism, being that the flux of hydrogen that permeates through the membrane (J_{H_2}) can be illustrated by the following equation:

$$J_{H_2} = {}^{P_{Pd,H_2}}/_{\delta} \left(p^x_{H_2,retentate} - p^x_{H_2,permeate}\right) \quad \textbf{(2.55)}$$

where P_{Pd,H_2} is the permeability of the membrane, δ is the membrane thickness, $p_{H_2,retentate}$ and $p_{H_2,permeate}$ are the partial pressures of hydrogen in the retentate and in the permeate side, respectively, and x is the pressure exponent. The ratio $\frac{P_{Pd,H_2}}{\delta}$ is normally called permeance or pressure normalized flux. The pressure exponent takes values between 0.5 and 1, being 0.5 (Sievert's law) when the diffusion of atomic hydrogen through the metal lattice of the membrane is the limiting step. On the other hand, the pressure exponent becomes close to 1 if the surface adsorption is rate limiting. The permeability is typically described by an Arrhenius-type dependency on the temperature:

$$P_{Pd,H_2} = P^0_{Pd,H_2} exp\left(-{}^{E_{a,Pd}}/_{RT}\right) \quad \textbf{(2.56)}$$

where P^0_{Pd,H_2} is the pre-exponential factor and $E_{a,Pd}$ is the activation energy of the membrane.

Table 2.10 encompasses a summary of different Pd-based membranes that have been reported in the last years. Some parameters such as membrane thickness, hydrogen permeance, ideal H_2/N_2 selectivity and activation energy are reported.

Table 2.10 - Characteristics of different Pd-based membranes reported in the literature.

Membrane	T / ºC[a]	ΔP / kPa[b]	δ / μm	Permeance to H_2 / mol·m^{-2}·s^{-1}·Pa$^{-0.5}$	Ideal selectivity H_2/N_2	$E_{a,Pd}$ / kJ·mol^{-1}	Reference
Pd-25 wt% Ag	300	10-150	50	1.15×10^{-4}[c]	∞	10.72	[180]
Pd-23-25 wt% Ag	350	700	84	2.26×10^{-4}[c]	∞	2.92	[181]
$Pd_{46.6}$-$Cu_{53.4}$	400	345	40	4.50×10^{-4}[c]	-	5.80	[182]
$Pd_{45.8}$-$Cu_{51.9}$-$Ag_{2.3}$	400	345	40	$3.50 \times 10 - 4$[c]	-	10.20	[182]
Pd-5 wt% Pt/YSZ	400	57.9-609.5	6.6	1.18×10^{-3}[c]	994	-	[183]
Pd/Ag/PSS	400	100	4.0	1.71×10^{-3}[c]	1000	11.90	[184]
Pd/Pencil/PSS	450	100	7.0	1.40×10^{-3}[c]	120	13.80	[185]
Pd/TiO_2/Ti-Al	500	588-704[c]	14.0	1.07×10^{-3}	∞	13.65	[186]
$Pd_{78}Ag_9Au_{13}$	450	-	14.0	1.16×10^{-3}[c]	-	-	[187]
$Ti_{50.864}Ni_{46.961}Pd_{4.175}$	450	100	45.0	3.84×10^{-6}[c]	-	42.23	[188]
$Pd_{95}Au_5$	400	-	2.5	4.40×10^{-3}[c]	≥ 10 000	-	[189]
$Pd_{95}Y_5$	400	-	2.0	5.50×10^{-3}[c]	≥ 10 000	-	[189]
$Pd_{73}Cu_{26}Y_1$	400	-	2.0	2.50×10^{-3}[c]	≥ 10 000	-	[189]

YSZ: Yttria-stabilized zirconia.
PSS: Porous stainless steel.
[a] Temperature at which the permeance was obtained.
[b] Trans-membrane pressure difference at which the permeance was obtained.
[c] Calculated values.

2.6.2 Glycerol steam reforming in membrane reactors

Experimental studies featuring the use of MRs for hydrogen production through several reactions (GSR, SRM, WGS, steam reforming of ethanol, etc.) have been extensively reported in the last decade. This growing interest in such technology is explained by the fact that, among other things, MRs allow to overcome the thermodynamic boundaries of equilibrium-limited reactions, thus allowing to reach high purity hydrogen streams that are suitable for use in PEMFCs. The experimental studies on GSR in MRs reported in the literature [190-193] assessed the effects of temperature, pressure and weight hourly space velocity (WHSV) and will be summarized in the next section.

2.6.2.1 Effects of temperature, pressure and weight hourly space velocity

In a MR, it was observed that, by increasing the operating temperature from 400 ºC to 450 ºC, both glycerol conversion and hydrogen yield increased [190, 192]. This happens not only because of the endothermic nature of the GSR reaction, but also because at higher temperatures the Pd-Ag/PSS membrane becomes more permeable towards hydrogen (Eq. (2.56)). Such enhancement in the performance was also proved by the observed increase in the hydrogen recovery (ratio between the amount of hydrogen collected in the permeate side and the total amount of hydrogen produced in the GSR reaction) when temperature was increased from 400 ºC to 450 ºC [190]. This way, a higher shift of the thermodynamic equilibrium at higher temperatures is observed.

When it comes to the successful operation of a MR, pressure is a fundamental parameter to be taken into consideration. As can be seen by analyzing Eq. (2.55), higher differences between the retentate and permeate pressures (driving force) lead to higher permeating hydrogen fluxes. Therefore, higher driving forces favor the dislocation of the thermodynamic constraints (Fig. 2.23 [193]). On the other hand, the production of hydrogen through GSR reaction

is not favored at higher pressures, as already discussed in previous sections and illustrated in the same figure. Thus, a compromise between these two factors must be taken into consideration, being, for the conditions employed in Fig. 2.23, the hydrogen permeation through the membrane the dominant one.

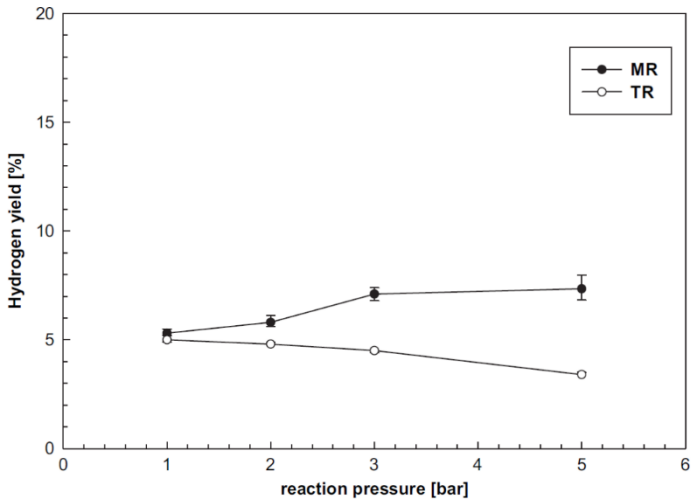

Fig. 2.23 - Effect of reaction pressure on the hydrogen yield for the traditional reactor (TR) and membrane reactor (MR) at 400 ºC, WGFR of 6, WHSV of 1.0 h^{-1}, counter-current configuration of sweep-gas, atmospheric pressure in the permeate side and $Q_{sweep\text{-}gas}/Q_{glycerol\text{-}in}$=11.9. Taken from [193].

In terms of glycerol conversion, a clear increase was verified with the increase of pressure in several works with MRs [190, 192, 193]. However, Iulianelli *et al*. [191] observed a high increase of glycerol conversion from 1.0 to 4.0 bar and a small decrease from 1.0 to 1.5 bar (Fig. 2.24 [191]). The authors suggested that this happens because while for the first case the enhancement of the hydrogen permeation prevails over the thermodynamic restrictions, for the second case the opposite occurs. Regarding the hydrogen yield, it increased less and, at higher pressures, it was observed that it stabilized or even decreased. This happens due to the occurrence of methanation reactions which consume hydrogen. Basile and co-workers [191] observed an increase of the methane selectivity as well as a decrease of hydrogen selectivity for increasing pressures. Such behavior is also due to the low capacity of the used Co-based

catalyst to promote SRM [191]. Contrarily, the recovery of hydrogen increased even more rapidly at higher reaction pressures.

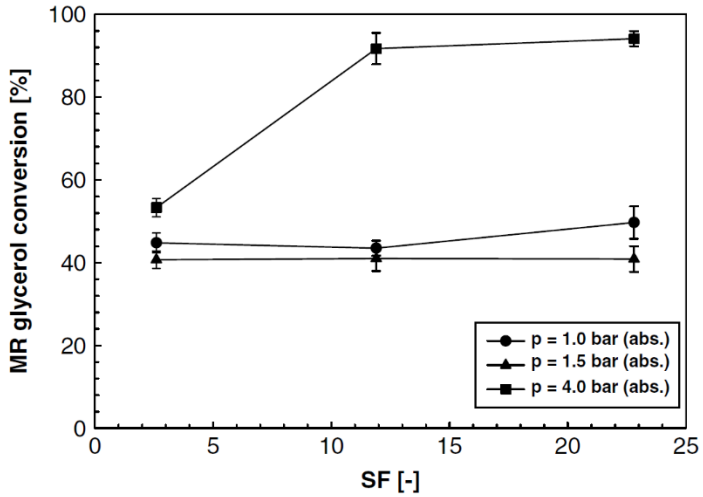

Fig. 2.24 - Dependency of glycerol conversion the sweep factor (SF) in the Pd-Ag MR at different reaction pressures, 400 ºC, WGFR of 6 and WHSV of 1.01 h^{-1}.

The use of an inert sweep gas to dilute the hydrogen in the permeate side and decrease its partial pressure has been one of the best ways of increasing the driving force for hydrogen permeation in MRs. Iulianelli *et al*. [191] analyzed the effect of the sweep factor (SF) (molar ratio between the sweep gas and the feed glycerol flow rates) on glycerol conversion and hydrogen recovery at different reaction pressures. By increasing the SF from 2.6 to 11.9 at 4.0 bar, the glycerol conversion increased from 55.0 to 92.0% (Fig. 2.24). However, for increasing SFs beyond 11.9 the enhancement of the glycerol conversion is very low. This happens because from a SF of 11.9 on, the increase in the dilution of the hydrogen in the permeate side is almost null and so the driving force almost does not increase. In terms of hydrogen recovery, the best result was around 63.0% and was obtained at 4.0 bar and SF of 22.8.

The effect of the WHSV has also been analyzed by Iulianelli *et al*. [193]. The authors observed that increasing WHSV have a negative impact on the glycerol conversion and on both hydrogen yield and recovery. The lower the

WHSV, the higher is the residence time of gases inside the reactor bed and so higher glycerol conversions and hydrogen yields are obtained. Higher residence times also allow hydrogen to permeate more easily, not only because of the higher amounts of hydrogen produced and thus higher driving force, but also because hydrogen has more time to reach the membrane surface and permeate.

Besides affecting the performance of the GSR catalyst, the deposition of carbonaceous deposits was also found to negatively affect the performance of the membrane in terms of hydrogen permeating flux [191]. Moreover, the presence of CO during GSR reaction is often responsible for the loss of membranes permeability, being far more important than CO_2 [177]. One way of reducing this effect is to use higher WGFRs (e.g. 9).

2.7 Conclusions

In the last decades hydrogen has been seen as a promising energy carrier to be used in energy systems. For this reason, different ways of producing hydrogen have been target of interest. However, most of these processes are based on the use of fossil origin raw materials (natural gas, naphtha, coal, etc.) whose environmental sustainability is highly questionable.

Glycerol produced as by-product in the biodiesel manufacturing process has been found to be a very attractive non-fossil alternative for hydrogen production. The GSR process is seen as one of the most promising ways of converting glycerol into hydrogen, mainly because its scale-up would not require many changes in the current industrial processes for hydrogen production from fossil fuels, which are mostly based on steam reforming. In order to enhance the GSR process performance for improved hydrogen production the choice of an appropriate catalyst is fundamental. Nickel and noble metals like platinum and ruthenium have been widely studied. While nickel catalysts are cheaper, noble

metals are more active and stable, thus allowing to work at lower temperatures. Nonetheless, in the last years a huge effort has been put on the search for nickel-based catalysts whose performance is comparable to that of noble metal materials. The influence of catalyst supports must also be taken into consideration, being that neutral supports (e.g. SiO_2) present higher stability and lower carbon deposition. The use of promoters may also be necessary in order to further improve the catalyst stability, a key issue in this field. Consequently, further research has to be done on this area, especially the search for low-temperature active and stable Ni-based catalysts.

Different mechanisms have been proposed for the GSR reaction (e.g. Langmuir-Hinshelwood dual site mechanism with molecular adsorption of glycerol and molecular or dissociative adsorption of water). However, a consensus on this matter hasn't been reached yet and so further studies are required. Moreover, since the GSR reaction highly promotes the formation of carbonaceous deposits, the study of the coke deposition kinetics has also been done, being that a Langmuir-Hinshelwood single site mechanism with dissociative adsorption of glycerol and molecular adsorption of water was proposed to describe the deposition of coke over a Co-Ni/Al_2O_3 catalyst. Despite this, more focus on this subject is required as well, so that the possible existence of different mechanisms of coke deposition on other types of catalysts may be disclosed.

Even if a good catalyst together with favoring operating conditions are used in catalytic GSR in a TR (e.g. fixed bed reactor), thermodynamic limitations in terms of glycerol conversion and hydrogen yield are still present. In order to avoid such constraints, intensified processes combining GSR reaction and CO_2 or H_2 selective removal in the same physical device have been found as an excellent alternative. It has been observed that removing CO_2 or H_2 from the reaction medium shifts the thermodynamic equilibrium towards higher glycerol conversions and higher hydrogen yields. Moreover, such processes allow to

work at lower temperatures and attain similar or even better performances than TRs at higher temperatures. However, in order for the implementation of these processes be successful, CO_2 sorbents with high sorption capacity, stability and low sorption and regeneration temperatures (e.g. 300-500 ºC), as well as hydrogen permselective membranes with high hydrogen selectivity and permeability and high resistance to embrittlement and poisoning have to be used. At the moment, hydrotalcite-based CO_2 sorbents (that require lower sorption and regeneration temperatures) and Pd-based membranes are seen as promising systems for use in SEGSR and GSR in MRs, respectively, at lower temperatures (300-400 ºC). Moreover, appropriate operating conditions (temperature, WGFR, pressure and WHVS) have to be carefully chosen.

Regarding CO_2 emissions, these can be easily avoided through SEGSR, however MRs with H_2 permselective membranes are not efficient on this. On the other hand, highly pure H_2 streams suitable for use in PEMFCs can only be produced in MRs. Therefore, new solutions combining catalytic GSR with in situ CO_2 and H_2 removal would be interesting to explore.

Notation and Glossary

E_a	Activation energy
$E_{a,Pd}$	Activation energy of a Pd-based membrane
f	Fraction of H_2 removal
G	Gibbs free energy
J_{H_2}	Flux of H_2 through the membrane
K	Equilibrium constant
k	Reaction rate constant
K_i	Adsorption constant of component i

k_0	Pre-exponential factor
k_C	Coke deposition reaction rate constant
n_i	Molar number of component i
$p_{H_2,permeate}$	Partial pressure of H_2 in the permeate side
$p_{H_2,retentate}$	Partial pressure of H_2 in the retentate side
p_i	Partial pressure of component i
P_{Pd,H_2}	Permeability of a Pd-based membrane to H_2
P^0_{Pd,H_2}	Pre-exponential factor
R	Ideal gas constant
$r_{coke\ deposition}$	Reaction rate of coke deposition
r_{GSR}	Reaction rate of glycerol steam reforming
T	Absolute temperature
X_1, X_2	Basic and acid active sites, respectively

Greek letters

δ	Membrane thickness
ΔH^0	Standard enthalpy
$\Delta H_r^{298\ K}$	Reaction enthalpy at 298 K
μ_i	Chemical potential of component i

Superscripts

a, b	Partial reaction orders for glycerol and steam, respectively
x	Pressure exponent

List of acronyms

CTAB	Cetyltrimethyl Ammonium Bromide
CVD	Chemical Vapor Deposition
EP	Electroless Plating
GHSV	Gas Hourly Space Velocity
GSR	Glycerol Steam Reforming
IUPAC	International Union of Pure and Applied Chemistry
MR	Membrane Reactor
PEMFC	Polymer Electrolyte Membrane Fuel Cell
PSA	Pressure Swing Adsorption
PSS	Porous Stainless Steel
SEGSR	Sorption-Enhanced Glycerol Steam Reforming
SER	Sorption-Enhanced Reactor
SRM	Steam Reforming of Methane
TR	Traditional Reactor
WGFR	Molar Water/Glycerol Feed Ratio
WGS	Water-Gas Shift
WHSV	Weight Hourly Space Velocity
YSZ	Yttria-Stabilized Zirconia

2.8 References

[1] Zhou, C.-H., J.N. Beltramini, Y.-X. Fan, and G.Q. Lu, *Chemoselective catalytic conversion of glycerol as a biorenewable source to valuable commodity chemicals.* Chemical Society Reviews, 2008, 37(3), 527-549.

[2] Dou, B., Y. Song, C. Wang, H. Chen, and Y. Xu, *Hydrogen production from catalytic steam reforming of biodiesel byproduct glycerol: Issues and challenges.* Renewable and Sustainable Energy Reviews, 2014, 30(0), 950-960.

[3] *U.S. Energy Information Administration*. [cited 2013 06-12]; Available from: http://www.eia.gov/cfapps/ipdbproject/iedindex3.cfm?tid=79&pid=81&aid=1&cid=ww,r1,r2,r3,r4,r5,r6,r7,&syid=2001&eyid=2011&unit=TBPD.

[4] Avasthi, K.S., R.N. Reddy, and S. Patel, *Challenges in the Production of Hydrogen from Glycerol – A Biodiesel Byproduct Via Steam Reforming Process.* Procedia Engineering, 2013, 51(0), 423-429.

[5] Ewan, B.C.R. and R.W.K. Allen, *A figure of merit assessment of the routes to hydrogen.* International Journal of Hydrogen Energy, 2005, 30(8), 809-819.

[6] Liu, Y., R. Farrauto, and A. Lawal, *Autothermal reforming of glycerol in a dual layer monolith catalyst.* Chemical Engineering Science, 2013, 89(0), 31-39.

[7] Liu, Y. and A. Lawal. *Synthesis gas production by autothermal reforming of crude glycerol using a dual layer monolith catalyst*. in *AIChE 2013 - 2013 AIChE Spring Meeting and 9th Global Congress on Process Safety, Conference Proceedings*. 2013.

[8] Nahar, G. and V. Dupont, *Recent advances in hydrogen production via autothermal reforming process (ATR): A review of patents and research articles.* Recent Patents on Chemical Engineering, 2013, 6(1), 8-42.

[9] Wang, W., *Thermodynamic analysis of glycerol partial oxidation for hydrogen production.* Fuel Processing Technology, 2010, 91(11), 1401-1408.

[10] Camargo, G., S. Cardozo, and M.V. Pena. *Thermodynamical analysis of glycerol partial oxidation reaction using zeolites catalyst*. in *2012 AIChE Annual Meeting, AIChE 2012, October 28, 2012 - November 2, 2012*. 2012. Pittsburgh, PA, United states: American Institute of Chemical Engineers.

[11] Liu, S.-K. and Y.-C. Lin, *Autothermal partial oxidation of glycerol to syngas over Pt-, LaMnO 3-, and Pt/LaMnO3-coated monoliths.* Industrial and Engineering Chemistry Research, 2012, 51(50), 16278-16287.

[12] Tuza, P.V., R.L. Manfro, N.F.P. Ribeiro, and M.M.V.M. Souza, *Production of renewable hydrogen by aqueous-phase reforming of glycerol over Ni–Cu catalysts derived from hydrotalcite precursors.* Renewable Energy, 2013, 50(0), 408-414.

[13] Ciftci, A., B. Peng, A. Jentys, J.A. Lercher, and E.J.M. Hensen, *Support effects in the aqueous phase reforming of glycerol over supported platinum catalysts.* Applied Catalysis A: General, 2012, 431–432(0), 113-119.

[14] Manfro, R.L., A.F. da Costa, N.F.P. Ribeiro, and M.M.V.M. Souza, *Hydrogen production by aqueous-phase reforming of glycerol over nickel catalysts supported on CeO2.* Fuel Processing Technology, 2011, 92(3), 330-335.

[15] Byrd, A.J., K.K. Pant, and R.B. Gupta, *Hydrogen production from glycerol by reforming in supercritical water over Ru/Al2O3 catalyst.* Fuel, 2008, 87(13–14), 2956-2960.

[16] Pairojpiriyakul, T., E. Croiset, W. Kiatkittipong, K. Kiatkittipong, A. Arpornwichanop, and S. Assabumrungrat, *Hydrogen production from catalytic supercritical water reforming of glycerol with cobalt-based catalysts.* International Journal of Hydrogen Energy, 2013, 38(11), 4368-4379.

[17] Gutiérrez Ortiz, F.J., A. Serrera, S. Galera, and P. Ollero, *Experimental study of the supercritical water reforming of glycerol without the addition of a catalyst.* Energy, 2013, 56(0), 193-206.

[18] Dave, C.D. and K.K. Pant, *Renewable hydrogen generation by steam reforming of glycerol over zirconia promoted ceria supported catalyst.* Renewable Energy, 2011, 36(11), 3195-3202.

[19] Dieuzeide, M.L., V. Iannibelli, M. Jobbagy, and N. Amadeo, *Steam reforming of glycerol over Ni/Mg/γ-Al2O3 catalysts. Effect of calcination temperatures.* International Journal of Hydrogen Energy, 2012, 37(19), 14926-14930.

[20] Dieuzeide, M.L., M. Jobbagy, and N. Amadeo, *Glycerol steam reforming over Ni/γ-Al2O3 catalysts, modified with Mg(II). Effect of Mg (II) content.* Catalysis Today, 2013, 213(0), 50-57.

[21] Araque, M., L.M. Martínez T, J.C. Vargas, M.A. Centeno, and A.C. Roger, *Effect of the active metals on the selective H2 production in glycerol steam reforming.* Applied Catalysis B: Environmental, 2012, 125(0), 556-566.

[22] Iriondo, A., V.L. Barrio, J.F. Cambra, P.L. Arias, M.B. Güemez, R.M. Navarro, M.C. Sanchez-Sanchez, and J.L.G. Fierro, *Influence of La2O3 modified support and Ni and Pt active phases on glycerol steam reforming to produce hydrogen.* Catalysis Communications, 2009, 10(8), 1275-1278.

[23] Araque, M., L.M. Martínez T, J.C. Vargas, and A.C. Roger, *Hydrogen production by glycerol steam reforming over CeZrCo fluorite type oxides.* Catalysis Today, 2011, 176(1), 352-356.

[24] Wang, C., B. Dou, H. Chen, Y. Song, Y. Xu, X. Du, T. Luo, and C. Tan, *Hydrogen production from steam reforming of glycerol by Ni–Mg–Al based catalysts in a fixed-bed reactor.* Chemical Engineering Journal, 2013, 220(0), 133-142.

[25] Wang, X., S. Li, H. Wang, B. Liu, and X. Ma, *Thermodynamic analysis of glycerin steam reforming.* Energy and Fuels, 2008, 22(6), 4285-4291.

[26] Chen, H., Y. Ding, N.T. Cong, B. Dou, V. Dupont, M. Ghadiri, and P.T. Williams, *A comparative study on hydrogen production from steam-glycerol reforming: thermodynamics and experimental.* Renewable Energy, 2011, 36(2), 779-788.

[27] Adhikari, S., S. Fernando, and A. Haryanto, *A comparative thermodynamic and experimental analysis on hydrogen production by steam reforming of glycerin.* Energy and Fuels, 2007, 21(4), 2306-2310.

[28] Adhikari, S., S. Fernando, S.R. Gwaltney, S.D. Filip To, R. Mark Bricka, P.H. Steele, and A. Haryanto, *A thermodynamic analysis of hydrogen production by steam reforming of glycerol.* International Journal of Hydrogen Energy, 2007, 32(14), 2875-2880.

[29] Hajjaji, N., A. Chahbani, Z. Khila, and M.-N. Pons, *A comprehensive energy–exergy-based assessment and parametric study of a hydrogen production process using steam glycerol reforming.* Energy, 2014, 64(0), 473-483.

[30] Dieuzeide, M.L. and N. Amadeo, *Thermodynamic analysis of Glycerol steam reforming.* Chemical Engineering and Technology, 2010, 33(1), 89-96.

[31] Rossi, C.C.R.S., C.G. Alonso, O.A.C. Antunes, R. Guirardello, and L. Cardozo-Filho, *Thermodynamic analysis of steam reforming of ethanol and glycerine for hydrogen production.* International Journal of Hydrogen Energy, 2009, 34(1), 323-332.

[32] Fishtik, I., A. Alexander, R. Datta, and D. Geana, *Thermodynamic analysis of hydrogen production by steam reforming of ethanol via response reactions.* International Journal of Hydrogen Energy, 2000, 25(1), 31-45.

[33] Mas, V., R. Kipreos, N. Amadeo, and M. Laborde, *Thermodynamic analysis of ethanol/water system with the stoichiometric method.* International Journal of Hydrogen Energy, 2006, 31(1), 21-28.

[34] Authayanun, S., A. Arpornwichanop, W. Paengjuntuek, and S. Assabumrungrat, *Thermodynamic study of hydrogen production from crude glycerol autothermal reforming for fuel cell applications.* International Journal of Hydrogen Energy, 2010, 35(13), 6617-6623.

[35] Gutiérrez Ortiz, F.J., P. Ollero, and A. Serrera, *Thermodynamic analysis of the autothermal reforming of glycerol using supercritical water.* International Journal of Hydrogen Energy, 2011, 36(19), 12186-12199.

[36] Gutiérrez Ortiz, F.J., P. Ollero, A. Serrera, and A. Sanz, *Thermodynamic study of the supercritical water reforming of glycerol.* International Journal of Hydrogen Energy, 2011, 36(15), 8994-9013.

[37] Wang, H., X. Wang, M. Li, S. Li, S. Wang, and X. Ma, *Thermodynamic analysis of hydrogen production from glycerol autothermal reforming.* International Journal of Hydrogen Energy, 2009, 34(14), 5683-5690.

[38] Cheng, C.K., S.Y. Foo, and A.A. Adesina, *Thermodynamic analysis of glycerol-steam reforming in the presence of CO 2 or H 2 as carbon gasifying agent.* International Journal of Hydrogen Energy, 2012, 37(13), 10101-10110.

[39] Authayanun, S., A. Arpornwichanop, Y. Patcharavorachot, W. Wiyaratn, and S. Assabumrungrat, *Hydrogen production from glycerol steam reforming for low- and high-temperature PEMFCs.* International Journal of Hydrogen Energy, 2011, 36(1), 267-275.

[40] Olajire, A.A., *Valorization of greenhouse carbon dioxide emissions into value-added products by catalytic processes.* Journal of CO2 Utilization, 2013, 3–4(0), 74-92.

[41] Li, Y., W. Wang, B. Chen, and Y. Cao, *Thermodynamic analysis of hydrogen production via glycerol steam reforming with CO2 adsorption.* International Journal of Hydrogen Energy, 2010, 35(15), 7768-7777.

[42] Chen, H., T. Zhang, B. Dou, V. Dupont, P. Williams, M. Ghadiri, and Y. Ding, *Thermodynamic analyses of adsorption-enhanced steam reforming of glycerol for*

hydrogen production. International Journal of Hydrogen Energy, 2009, 34(17), 7208-7222.

[43] Lima da Silva, A. and I.L. Müller, *Hydrogen production by sorption enhanced steam reforming of oxygenated hydrocarbons (ethanol, glycerol, n-butanol and methanol): Thermodynamic modelling.* International Journal of Hydrogen Energy, 2011, 36(3), 2057-2075.

[44] He, L., J.M.S. Parra, E.A. Blekkan, and D. Chen, *Towards efficient hydrogen production from glycerol by sorption enhanced steam reforming.* Energy and Environmental Science, 2010, 3(8), 1046-1056.

[45] Wang, X., N. Wang, M. Li, S. Li, S. Wang, and X. Ma, *Hydrogen production by glycerol steam reforming with in situ hydrogen separation: A thermodynamic investigation.* International Journal of Hydrogen Energy, 2010, 35(19), 10252-10256.

[46] Lin, Y.-C., *Catalytic valorization of glycerol to hydrogen and syngas.* International Journal of Hydrogen Energy, 2013, 38(6), 2678-2700.

[47] Adhikari, S., S.D. Fernando, and A. Haryanto, *Hydrogen production from glycerin by steam reforming over nickel catalysts.* Renewable Energy, 2008, 33(5), 1097-1100.

[48] Adhikari, S., S.D. Fernando, S.D.F. To, R.M. Bricka, P.H. Steele, and A. Haryanto, *Conversion of glycerol to hydrogen via a steam reforming process over nickel catalysts.* Energy and Fuels, 2008, 22(2), 1220-1226.

[49] Sánchez, E.A., M.A. D'Angelo, and R.A. Comelli, *Hydrogen production from glycerol on Ni/Al2O3 catalyst.* International Journal of Hydrogen Energy, 2010, 35(11), 5902-5907.

[50] Pant, K.K., R. Jain, and S. Jain, *Renewable hydrogen production by steam reforming of glycerol over Ni/CeO 2 catalyst prepared by precipitation deposition method.* Korean Journal of Chemical Engineering, 2011, 28(9), 1859-1866.

[51] Nichele, V., M. Signoretto, F. Menegazzo, A. Gallo, V. Dal Santo, G. Cruciani, and G. Cerrato, *Glycerol steam reforming for hydrogen production: Design of Ni supported catalysts.* Applied Catalysis B: Environmental, 2012, 111–112(0), 225-232.

[52] Patel, S. and K.K. Pant, *Production of hydrogen with low carbon monoxide formation via catalytic steam reforming of methanol.* Journal of Fuel Cell Science and Technology, 2006, 3(4), 369-374.

[53] Iriondo, A., V.L. Barrio, J.F. Cambra, P.L. Arias, M.B. Guemez, M.C. Sanchez-Sanchez, R.M. Navarro, and J.L.G. Fierro, *Glycerol steam reforming over Ni catalysts supported on ceria and ceria-promoted alumina.* International Journal of Hydrogen Energy, 2010, 35(20), 11622-11633.

[54] Cui, Y., V. Galvita, L. Rihko-Struckmann, H. Lorenz, and K. Sundmacher, *Steam reforming of glycerol: The experimental activity of La1−xCexNiO3 catalyst in comparison to the thermodynamic reaction equilibrium.* Applied Catalysis B: Environmental, 2009, 90(1–2), 29-37.

[55] Franchini, C.A., W. Aranzaez, A.M. Duarte de Farias, G. Pecchi, and M.A. Fraga, *Ce-substituted LaNiO3 mixed oxides as catalyst precursors for glycerol steam reforming.* Applied Catalysis B: Environmental, 2014, 147(0), 193-202.

[56] Adhikari, S., S. Fernando, and A. Haryanto, *Production of hydrogen by steam reforming of glycerin over alumina-supported metal catalysts.* Catalysis Today, 2007, 129(3–4), 355-364.

[57] Matas Güell, B., I. Babich, K.P. Nichols, J.G.E. Gardeniers, L. Lefferts, and K. Seshan, *Design of a stable steam reforming catalyst—A promising route to sustainable hydrogen from biomass oxygenates.* Applied Catalysis B: Environmental, 2009, 90(1–2), 38-44.

[58] Hagh, B.F., *Optimization of autothermal reactor for maximum hydrogen production.* International Journal of Hydrogen Energy, 2003, 28(12), 1369-1377.

[59] Slinn, M., K. Kendall, C. Mallon, and J. Andrews, *Steam reforming of biodiesel by-product to make renewable hydrogen.* Bioresource Technology, 2008, 99(13), 5851-5858.

[60] Kim, S.M. and S.I. Woo, *Sustainable production of syngas from biomass-derived glycerol by steam reforming over highly stable Ni/SiC.* ChemSusChem, 2012, 5(8), 1513-1522.

[61] Wen, G., Y. Xu, H. Ma, Z. Xu, and Z. Tian, *Production of hydrogen by aqueous-phase reforming of glycerol.* International Journal of Hydrogen Energy, 2008, 33(22), 6657-6666.

[62] Sanchez, E.A. and R.A. Comelli, *Hydrogen by glycerol steam reforming on a nickel–alumina catalyst: Deactivation processes and regeneration.* International Journal of Hydrogen Energy, 2012, 37(19), 14740-14746.

[63] Ni, M., D.Y.C. Leung, and M.K.H. Leung, *A review on reforming bio-ethanol for hydrogen production.* International Journal of Hydrogen Energy, 2007, 32(15), 3238-3247.

[64] Seo, J.G., M.H. Youn, S. Park, J.S. Chung, and I.K. Song, *Hydrogen production by steam reforming of liquefied natural gas (LNG) over Ni/Al2O3-ZrO2 xerogel catalysts: Effect of calcination temperature of Al2O3-ZrO2 xerogel supports.* International Journal of Hydrogen Energy, 2009, 34(9), 3755-3763.

[65] Iriondo, A., J.F. Cambra, M.B. Güemez, V.L. Barrio, J. Requies, M.C. Sánchez-Sánchez, and R.M. Navarro, *Effect of ZrO2 addition on Ni/Al2O3 catalyst to produce H2 from glycerol.* International Journal of Hydrogen Energy, 2012, 37(8), 7084-7093.

[66] Huang, Z.-Y., C.-H. Xu, J. Meng, C.-F. Zheng, H.-W. Xiao, J. Chen, and Y.-X. Zhang, *Glycerol steam reforming to syngas over Ni-based catalysts on commercial Linde-type 5A zeolite modified by metal oxides.* Journal of Environmental Chemical Engineering, 2014, 2(1), 598-604.

[67] Iriondo, A., V.L. Barrio, J.F. Cambra, P.L. Arias, M.B. Güemez, R.M. Navarro, M.C. Sánchez-Sánchez, and J.L.G. Fierro, *Hydrogen production from glycerol over nickel catalysts supported on Al2O3 modified by Mg, Zr, Ce or La.* Topics in Catalysis, 2008, 49(1-2), 46-58.

[68] Buffoni, I.N., F. Pompeo, G.F. Santori, and N.N. Nichio, *Nickel catalysts applied in steam reforming of glycerol for hydrogen production.* Catalysis Communications, 2009, 10(13), 1656-1660.

[69] Kitamura, S., T. Su-Enaga, N.O. Ikenaga, T. Miyake, and T. Suzuki, *Steam reforming of glycerin using Ni-based catalysts loaded on CaO-ZrO 2 solid solution.* Catalysis Letters, 2011, 141(6), 895-905.

[70] Damyanova, S. and J.M.C. Bueno, *Effect of CeO2 loading on the surface and catalytic behaviors of CeO2-Al2O3-supported Pt catalysts.* Applied Catalysis A: General, 2003, 253(1), 135-150.

[71] Takanabe, K., K.-i. Aika, K. Seshan, and L. Lefferts, *Sustainable hydrogen from bio-oil—Steam reforming of acetic acid as a model oxygenate.* Journal of Catalysis, 2004, 227(1), 101-108.

[72] Seo, J.G., M.H. Youn, and I.K. Song, *Hydrogen production by steam reforming of LNG over Ni/Al2O3–ZrO2 catalysts: Effect of Al2O3–ZrO2 supports prepared by a grafting method.* Journal of Molecular Catalysis A: Chemical, 2007, 268(1–2), 9-14.

[73] Seo, J.G., M.H. Youn, J.C. Jung, K.M. Cho, S. Park, and I.K. Song, *Preparation of Ni/Al2O3–ZrO2 catalysts and their application to hydrogen production by steam reforming of LNG: Effect of ZrO2 content grafted on Al2O3.* Catalysis Today, 2008, 138(3–4), 130-134.

[74] Mawdsley, J.R. and T.R. Krause, *Rare earth-first-row transition metal perovskites as catalysts for the autothermal reforming of hydrocarbon fuels to generate hydrogen.* Applied Catalysis A: General, 2008, 334(1–2), 311-320.

[75] Liguras, D.K., D.I. Kondarides, and X.E. Verykios, *Production of hydrogen for fuel cells by steam reforming of ethanol over supported noble metal catalysts.* Applied Catalysis B: Environmental, 2003, 43(4), 345-354.

[76] Thyssen, V.V., T.A. Maia, and E.M. Assaf, *Ni supported on La2O3–SiO2 used to catalyze glycerol steam reforming.* Fuel, 2013, 105(0), 358-363.

[77] Rostrup-Nielsen, J.R., J. Sehested, and J.K. Nørskov, *Hydrogen and synthesis gas by steam- and C02 reforming*. 2002. p. 65-139.

[78] Basagiannis, A.C. and X.E. Verykios, *Steam reforming of the aqueous fraction of bio-oil over structured Ru/MgO/Al2O3 catalysts.* Catalysis Today, 2007, 127(1-4), 256-264.

[79] Huang, Z.Y., C.H. Xu, C.Q. Liu, H.W. Xiao, J. Chen, Y.X. Zhang, and Y.C. Lei, *Glycerol steam reforming over Ni/γ-Al2O3 catalysts modified by metal oxides.* Korean Journal of Chemical Engineering, 2013, 30(3), 587-592.

[80] Suelves, I., M.J. Lázaro, R. Moliner, Y. Echegoyen, and J.M. Palacios, *Characterization of NiAl and NiCuAl catalysts prepared by different methods for hydrogen production by thermo catalytic decomposition of methane.* Catalysis Today, 2006, 116(3), 271-280.

[81] Maluf, S.S. and E.M. Assaf, *Ni catalysts with Mo promoter for methane steam reforming.* Fuel, 2009, 88(9), 1547-1553.

[82] Youn, M.H., J.G. Seo, P. Kim, and I.K. Song, *Role and effect of molybdenum on the performance of Ni-Mo/γ-Al2O3 catalysts in the hydrogen production by auto-thermal reforming of ethanol.* Journal of Molecular Catalysis A: Chemical, 2007, 261(2), 276-281.

[83] Huang, T., W. Huang, J. Huang, and P. Ji, *Methane reforming reaction with carbon dioxide over SBA-15 supported Ni-Mo bimetallic catalysts.* Fuel Processing Technology, 2011, 92(10), 1868-1875.

[84] Wu, G., S. Li, C. Zhang, T. Wang, and J. Gong, *Glycerol steam reforming over perovskite-derived nickel-based catalysts.* Applied Catalysis B: Environmental, 2014, 144(0), 277-285.

[85] Hakim, L., Z. Yaakob, M. Ismail, W.R.W. Daud, and R. Sari, *Hydrogen production by steam reforming of glycerol over Ni/Ce/Cu hydroxyapatite-supported catalysts.* Chemical Papers, 2013, 67(7), 703-712.

[86] Profeti, L.P.R., E.A. Ticianelli, and E.M. Assaf, *Production of hydrogen via steam reforming of biofuels on Ni/CeO2–Al2O3 catalysts promoted by noble metals.* International Journal of Hydrogen Energy, 2009, 34(12), 5049-5060.

[87] Zhou, C.H., H. Zhao, D.S. Tong, L.M. Wu, and W.H. Yu, *Recent advances in catalytic conversion of glycerol.* Catalysis Reviews - Science and Engineering, 2013, 55(4), 369-453.

[88] Soares, R.R., D.A. Simonetti, and J.A. Dumesic, *Glycerol as a Source for Fuels and Chemicals by Low-Temperature Catalytic Processing.* Angewandte Chemie International Edition, 2006, 45(24), 3982-3985.

[89] Sutar, P.N., P.D. Vaidya, and A.E. Rodrigues, *Glycerol-reforming kinetics using a Pt/C catalyst.* Chemical Engineering and Technology, 2010, 33(10), 1645-1649.

[90] Simonetti, D.A., E.L. Kunkes, and J.A. Dumesic, *Gas-phase conversion of glycerol to synthesis gas over carbon-supported platinum and platinum-rhenium catalysts.* Journal of Catalysis, 2007, 247(2), 298-306.

[91] Pompeo, F., G.F. Santori, and N.N. Nichio, *Hydrogen production by glycerol steam reforming with Pt/SiO2 and Ni/SiO2 catalysts.* Catalysis Today, 2011, 172(1), 183-188.

[92] Montini, T., R. Singh, P. Das, B. Lorenzut, N. Bertero, P. Riello, A. Benedetti, G. Giambastiani, C. Bianchini, S. Zinoviev, S. Miertus, and P. Fornasiero, *Renewable H2 from glycerol steam reforming: Effect of La2O3 and CeO2 addition to Pt/Al2O3 catalysts.* ChemSusChem, 2010, 3(5), 619-628.

[93] Kunkes, E.L., R.R. Soares, D.A. Simonetti, and J.A. Dumesic, *An integrated catalytic approach for the production of hydrogen by glycerol reforming coupled with water-gas shift.* Applied Catalysis B: Environmental, 2009, 90(3–4), 693-698.

[94] Roh, H.-S., H.S. Potdar, D.-W. Jeong, K.-S. Kim, J.-O. Shim, W.-J. Jang, K.Y. Koo, and W.L. Yoon, *Synthesis of highly active nano-sized (1 wt.% Pt/CeO2) catalyst for water gas shift reaction in medium temperature application.* Catalysis Today, 2012, 185(1), 113-118.

[95] González, I.D., R.M. Navarro, W. Wen, N. Marinkovic, J.A. Rodriguéz, F. Rosa, and J.L.G. Fierro, *A comparative study of the water gas shift reaction over platinum catalysts supported on CeO2, TiO2 and Ce-modified TiO2.* Catalysis Today, 2010, 149(3–4), 372-379.

[96] Jeong, D.-W., H.S. Potdar, J.-O. Shim, W.-J. Jang, and H.-S. Roh, *H2 production from a single stage water–gas shift reaction over Pt/CeO2, Pt/ZrO2, and Pt/Ce(1−x)Zr(x)O2 catalysts.* International Journal of Hydrogen Energy, 2013, 38(11), 4502-4507.

[97] Pompeo, F., G. Santori, and N.N. Nichio, *Hydrogen and/or syngas from steam reforming of glycerol. Study of platinum catalysts.* International Journal of Hydrogen Energy, 2010, 35(17), 8912-8920.

[98] Gervasini, A., J. Fenyvesi, and A. Auroux, *Study of the acidic character of modified metal oxide surfaces using the test of isopropanol decomposition.* Catalysis Letters, 1997, 43(1-2), 219-228.

[99] Zhang, X.H., F.W. Yan, C.Y. Guo, and G.Q. Yuan, *Steam reforming of glycerol over Pt-MCM-41 synthesized in a one-step process.* Russian Journal of Physical Chemistry A, 2012, 86(13), 1957-1961.

[100] Greeley, J. and M. Mavrikakis, *Alloy catalysts designed from first principles.* Nature Materials, 2004, 3(11), 810-815.

[101] Ishikawa, Y., M.-S. Liao, and C.R. Cabrera, *Energetics of H2O dissociation and COads+OHads reaction on a series of Pt–M mixed metal clusters: a relativistic density-functional study.* Surface Science, 2002, 513(1), 98-110.

[102] Lehnert, K. and P. Claus, *Influence of Pt particle size and support type on the aqueous-phase reforming of glycerol.* Catalysis Communications, 2008, 9(15), 2543-2546.

[103] Frusteri, F., S. Freni, L. Spadaro, V. Chiodo, G. Bonura, S. Donato, and S. Cavallaro, *H2 production for MC fuel cell by steam reforming of ethanol over MgO*

supported Pd, Rh, Ni and Co catalysts. Catalysis Communications, 2004, 5(10), 611-615.

[104] Llorca, J., N.s. Homs, J. Sales, J.-L.G. Fierro, and P. Ramírez de la Piscina, *Effect of sodium addition on the performance of Co–ZnO-based catalysts for hydrogen production from bioethanol.* Journal of Catalysis, 2004, 222(2), 470-480.

[105] Batista, M.S., R.K.S. Santos, E.M. Assaf, J.M. Assaf, and E.A. Ticianelli, *High efficiency steam reforming of ethanol by cobalt-based catalysts.* Journal of Power Sources, 2004, 134(1), 27-32.

[106] Zhang, B., X. Tang, Y. Li, Y. Xu, and W. Shen, *Hydrogen production from steam reforming of ethanol and glycerol over ceria-supported metal catalysts.* International Journal of Hydrogen Energy, 2007, 32(13), 2367-2373.

[107] Cheng, C.K., S.Y. Foo, and A.A. Adesina, *H2-rich synthesis gas production over Co/Al2O3 catalyst via glycerol steam reforming.* Catalysis Communications, 2010, 12(4), 292-298.

[108] Cheng, C.K., S.Y. Foo, and A.A. Adesina, *Glycerol Steam Reforming over Bimetallic Co−Ni/Al2O3.* Industrial & Engineering Chemistry Research, 2010, 49(21), 10804-10817.

[109] Martínez T, L.M., M. Araque, J.C. Vargas, and A.C. Roger, *Effect of Ce/Zr ratio in CeZr-CoRh catalysts on the hydrogen production by glycerol steam reforming.* Applied Catalysis B: Environmental, 2013, 132–133(0), 499-510.

[110] Opoku-Gyamfi, K. and A.A. Adesina, *Forced composition cycling of a novel thermally self-sustaining fluidised-bed reactor for methane reforming.* Chemical Engineering Science, 1999, 54(13–14), 2575-2583.

[111] Ambroise, E., C. Courson, A.C. Roger, A. Kiennemann, G. Blanchard, S. Rousseau, X. Carrier, E. Marceau, C. La Fontaine, and F. Villain, *Exhaust gas recirculation for on-board hydrogen production by isooctane reforming: Comparison of performances of metal/ceria-zirconia based catalysts prepared through pseudo sol-gel or impregnation methods.* Catalysis Today, 2010, 154(1-2), 133-141.

[112] Vargas, J.C., S. Libs, A.C. Roger, and A. Kiennemann, *Study of Ce-Zr-Co fluorite-type oxide as catalysts for hydrogen production by steam reforming of bioethanol.* Catalysis Today, 2005, 107-108, 417-425.

[113] Romero-Sarria, F., J.C. Vargas, A.C. Roger, and A. Kiennemann, *Hydrogen production by steam reforming of ethanol. Study of mixed oxide catalysts Ce2Zr1.5Me0.5O8: Comparison of Ni/Co and effect of Rh.* Catalysis Today, 2008, 133-135(1-4), 149-153.

[114] Sundari, R. and P.D. Vaidya, *Reaction Kinetics of Glycerol Steam Reforming Using a Ru/Al2O3 Catalyst.* Energy & Fuels, 2012, 26(7), 4195-4204.

[115] Piscina, P.R.D.L. and N. Homs, *Use of biofuels to produce hydrogen (reformation processes).* Chemical Society Reviews, 2008, 37(11), 2459-2467.

[116] Soria, M.A., C. Mateos-Pedrero, I. Rodríguez-Ramos, and A. Guerrero-Ruiz, *Catalytic steam reforming of methane under conditions of applicability with Pd membranes over supported Ru catalysts.* Catalysis Today, 2011, 171(1), 126-131.

[117] Hirai, T., N.O. Ikenaga, T. Miyake, and T. Suzuki, *Production of hydrogen by steam reforming of glycerin on ruthenium catalyst.* Energy and Fuels, 2005, 19(4), 1761-1762.

[118] Nakagawa, K., S. Hideshima, N. Akamatsu, N.O. Matsui, N.O. Ikenaga, and T. Suzuki, *CO2 Reforming of Methane over Ru-Loaded Lanthanoid Oxide Catalysts*. 2002. p. 205-223.

[119] Kim, J. and D. Lee, *Glycerol steam reforming on supported Ru-based catalysts for hydrogen production for fuel cells.* International Journal of Hydrogen Energy, 2013, 38(27), 11853-11862.

[120] Gallo, A., C. Pirovano, M. Marelli, R. Psaro, and V. Dal Santo, *Hydrogen Production by Glycerol Steam Reforming with Ru-based Catalysts: A Study on Sn Doping.* Chemical Vapor Deposition, 2010, 16(10-12), 305-310.

[121] Gallo, A., C. Pirovano, P. Ferrini, M. Marelli, R. Psaro, S. Santangelo, G. Faggio, and V. Dal Santo, *Influence of reaction parameters on the activity of ruthenium based catalysts for glycerol steam reforming.* Applied Catalysis B: Environmental, 2012, 121–122(0), 40-49.

[122] Dou, B., V. Dupont, G. Rickett, N. Blakeman, P.T. Williams, H. Chen, Y. Ding, and M. Ghadiri, *Hydrogen production by sorption-enhanced steam reforming of glycerol.* Bioresource Technology, 2009, 100(14), 3540-3547.

[123] Rass-Hansen, J., C.H. Christensen, J. Sehested, S. Helveg, J.R. Rostrup-Nielsen, and S. Dahl, *Renewable hydrogen: Carbon formation on Ni and Ru catalysts during ethanol steam-reforming.* Green Chemistry, 2007, 9(9), 1016-1021.

[124] Basagiannis, A.C. and X.E. Verykios, *Influence of the carrier on steam reforming of acetic acid over Ru-based catalysts.* Applied Catalysis B: Environmental, 2008, 82(1-2), 77-88.

[125] Basile, F., G. Fornasari, V. Rosetti, F. Trifirò, and A. Vaccari, *Effect of the Mg/Al ratio of the hydrotalcite-type precursor on the dispersion and activity of Rh and Ru catalysts for the partial oxidation of methane.* Catalysis Today, 2004, 91-92, 293-297.

[126] Park, S.Y., J.H. Kim, D.J. Moon, N.C. Park, and Y.C. Kim, *Autothermal reforming of propane over Ni-based hydrotalcite catalysts.* Journal of Nanoscience and Nanotechnology, 2010, 10(5), 3175-3179.

[127] Lee, H.J., Y.S. Lim, N.C. Park, and Y.C. Kim, *Catalytic autothermal reforming of propane over the noble metal-doped hydrotalcite-type catalysts.* Chemical Engineering Journal, 2009, 146(2), 295-301.

[128] Chiodo, V., S. Freni, A. Galvagno, N. Mondello, and F. Frusteri, *Catalytic features of Rh and Ni supported catalysts in the steam reforming of glycerol to produce hydrogen.* Applied Catalysis A: General, 2010, 381(1–2), 1-7.

[129] Palmeri, N., V. Chiodo, S. Freni, F. Frusteri, J.C.J. Bart, and S. Cavallaro, *Hydrogen from oxygenated solvents by steam reforming on Ni/Al2O3 catalyst.* International Journal of Hydrogen Energy, 2008, 33(22), 6627-6634.

[130] Cavallaro, S., V. Chiodo, S. Freni, N. Mondello, and F. Frusteri, *Performance of Rh/Al2O3 catalyst in the steam reforming of ethanol: H2 production for MCFC.* Applied Catalysis A: General, 2003, 249(1), 119-128.

[131] Frusteri, F., L. Spadaro, F. Arena, and A. Chuvilin, *TEM evidence for factors affecting the genesis of carbon species on bare and K-promoted Ni/MgO catalysts during the dry reforming of methane.* Carbon, 2002, 40(7), 1063-1070.

[132] Bartholomew, C.H., *CARBON DEPOSITION IN STEAM REFORMING AND METHANATION.* Catalysis reviews, 1982, 24(1), 67-112.

[133] Ebshish, A., Z. Yaakob, Y.H. Taufiq-Yap, A. Bshish, and A. Shaibani, *Catalytic Steam Reforming of Glycerol Over Cerium and Palladium-Based Catalysts for Hydrogen Production.* Journal of Fuel Cell Science and Technology, 2013, 10(2), 021003-021003.

[134] Cheng, C.K., S.Y. Foo, and A.A. Adesina, *Steam reforming of glycerol over Ni/Al2O3 catalyst.* Catalysis Today, 2011, 178(1), 25-33.

[135] Adhikari, S., S.D. Fernando, and A. Haryanto, *Kinetics and Reactor Modeling of Hydrogen Production from Glycerol via Steam Reforming Process over Ni/CeO2 Catalysts.* Chemical Engineering & Technology, 2009, 32(4), 541-547.

[136] Cheng, C.K., S.Y. Foo, and A.A. Adesina, *Carbon deposition on bimetallic Co–Ni/Al2O3 catalyst during steam reforming of glycerol.* Catalysis Today, 2011, 164(1), 268-274.

[137] Sundaram, K.M. and G.F. Froment, *Kinetics of coke deposition in the thermal cracking of propane.* Chemical Engineering Science, 1979, 34(5), 635-644.

[138] Van Damme, P.S., S. Narayanan, and G.F. Froment, *THERMAL CRACKING OF PROPANE AND PROPANE-PROPYLENE MIXTURES: PILOT PLANT VERSUS INDUSTRIAL DATA.* AIChE Journal, 1975, 21(6), 1065-1073.

[139] Dou, B., C. Wang, H. Chen, Y. Song, and B. Xie, *Continuous sorption-enhanced steam reforming of glycerol to high-purity hydrogen production.* International Journal of Hydrogen Energy, 2013, 38(27), 11902-11909.

[140] Hanif, A., S. Dasgupta, S. Divekar, A. Arya, M.O. Garg, and A. Nanoti, *A study on high temperature CO2 capture by improved hydrotalcite sorbents.* Chemical Engineering Journal, 2014, 236(0), 91-99.

[141] Maroño, M., Y. Torreiro, and L. Gutierrez, *Influence of steam partial pressures in the CO2 capture capacity of K-doped hydrotalcite-based sorbents for their application to SEWGS processes.* International Journal of Greenhouse Gas Control, 2013, 14(0), 183-192.

[142] Martunus, Z. Helwani, A.D. Wiheeb, J. Kim, and M.R. Othman, *Improved carbon dioxide capture using metal reinforced hydrotalcite under wet conditions.* International Journal of Greenhouse Gas Control, 2012, 7(0), 127-136.

[143] Aschenbrenner, O., P. McGuire, S. Alsamaq, J. Wang, S. Supasitmongkol, B. Al-Duri, P. Styring, and J. Wood, *Adsorption of carbon dioxide on hydrotalcite-like compounds of different compositions.* Chemical Engineering Research and Design, 2011, 89(9), 1711-1721.

[144] Wang, Q., H.H. Tay, Z. Guo, L. Chen, Y. Liu, J. Chang, Z. Zhong, J. Luo, and A. Borgna, *Morphology and composition controllable synthesis of Mg–Al–CO3 hydrotalcites by tuning the synthesis pH and the CO2 capture capacity.* Applied Clay Science, 2012, 55(0), 18-26.

[145] Wang, Y., Y. Zhu, and S. Wu, *A new nano CaO-based CO2 adsorbent prepared using an adsorption phase technique.* Chemical Engineering Journal, 2013, 218(0), 39-45.

[146] Sanchez-Jimenez, P.E., L.A. Perez-Maqueda, and J.M. Valverde, *Nanosilica supported CaO: A regenerable and mechanically hard CO2 sorbent at Ca-looping conditions.* Applied Energy, 2014, 118(0), 92-99.

[147] Zhang, X., Z. Li, Y. Peng, W. Su, X. Sun, and J. Li, *Investigation on a novel CaO-Y2O3 sorbent for efficient CO2 mitigation.* Chemical Engineering Journal, 2014, 243(0), 297-304.

[148] Nieto-Sanchez, A.J., M. Olivares-Marin, S. Garcia, C. Pevida, and E.M. Cuerda-Correa, *Influence of the operation conditions on CO2 capture by CaO-derived sorbents prepared from synthetic CaCO3.* Chemosphere, 2013, 93(9), 2148-2158.

[149] Akgsornpeak, A., T. Witoon, T. Mungcharoen, and J. Limtrakul, *Development of synthetic CaO sorbents via CTAB-assisted sol–gel method for CO2 capture at high temperature.* Chemical Engineering Journal, 2014, 237(0), 189-198.

[150] Wang, S., C. An, and Q.-H. Zhang, *Syntheses and structures of lithium zirconates for high-temperature CO2 absorption.* Journal of Materials Chemistry A, 2013, 1(11), 3540-3550.

[151] Duan, Y., *Structural and electronic properties of Li8ZrO6 and its CO2 capture capabilities: an ab initio thermodynamic approach.* Physical Chemistry Chemical Physics, 2013, 15(24), 9752-9760.

[152] Xiao, Q., X. Tang, Y. Liu, Y. Zhong, and W. Zhu, *Citrate route to prepare K-doped Li2ZrO3 sorbents with excellent CO2 capture properties.* Chemical Engineering Journal, 2011, 174(1), 231-235.

[153] Halabi, M.H., M.H.J.M. de Croon, J. van der Schaaf, P.D. Cobden, and J.C. Schouten, *Reactor modeling of sorption-enhanced autothermal reforming of methane. Part I: Performance study of hydrotalcite and lithium zirconate-based processes.* Chemical Engineering Journal, 2011, 168(2), 872-882.

[154] Iwan, A., H. Stephenson, W.C. Ketchie, and A.A. Lapkin, *High temperature sequestration of CO2 using lithium zirconates.* Chemical Engineering Journal, 2009, 146(2), 249-258.

[155] Mizunuma, M., M. Tsuda, Y. Maruo, and T. Nakagaki, *CO2 Capture System Using Lithium Silicate for Distributed Power Supply.* Energy Procedia, 2013, 37(0), 1194-1201.

[156] Seggiani, M., M. Puccini, and S. Vitolo, *Alkali promoted lithium orthosilicate for CO2 capture at high temperature and low concentration.* International Journal of Greenhouse Gas Control, 2013, 17(0), 25-31.

[157] Chowdhury, M.B.I., M.R. Quddus, and H.I. deLasa, *CO2 capture with a novel solid fluidizable sorbent: Thermodynamics and Temperature Programmed Carbonation–Decarbonation.* Chemical Engineering Journal, 2013, 232(0), 139-148.

[158] Shan, S., Q. Jia, L. Jiang, Q. Li, Y. Wang, and J. Peng, *Novel Li4SiO4-based sorbents from diatomite for high temperature CO2 capture.* Ceramics International, 2013, 39(5), 5437-5441.

[159] Duan, Y., H. Pfeiffer, B. Li, I.C. Romero-Ibarra, D.C. Sorescu, D.R. Luebke, and J.W. Halley, *CO2 capture properties of lithium silicates with different ratios of Li2O/SiO2: an ab initio thermodynamic and experimental approach.* Physical Chemistry Chemical Physics, 2013, 15(32), 13538-13558.

[160] Yong, Z. and A.E. Rodrigues, *Hydrotalcite-like compounds as adsorbents for carbon dioxide.* Energy Conversion and Management, 2002, 43(14), 1865-1876.

[161] Yong, Z., V. Mata, and A.E. Rodrigues, *Adsorption of carbon dioxide at high temperature - a review.* Separation and Purification Technology, 2002, 26(2–3), 195-205.

[162] Yong, Z., V.G. Mata, and A.E. Rodrigues, *Adsorption of Carbon Dioxide on Chemically Modified High Surface Area Carbon-Based Adsorbents at High Temperature.* Adsorption, 2001, 7(1), 41-50.

[163] Gupta, H. and L.-S. Fan, *Carbonation−Calcination Cycle Using High Reactivity Calcium Oxide for Carbon Dioxide Separation from Flue Gas.* Industrial & Engineering Chemistry Research, 2002, 41(16), 4035-4042.

[164] Oliveira, E.L.G., *Sorption enhanced steam methane reforming process for continuous production of hydrogen in pressure swing adsorptive reactors*. PhD Thesis, 2009, University of Porto.

[165] Miguel, C.V., R. Trujillano, V. Rives, M.A. Vicente, A.F.P. Ferreira, A.E. Rodrigues, A. Mendes, and L.M. Madeira, *High temperature CO2 sorption with gallium-substituted*

and promoted hydrotalcites. Separation and Purification Technology, 2014, 127, 202-211.

[166] Lu, H., E.P. Reddy, and P.G. Smirniotis, *Calcium oxide based sorbents for capture of carbon dioxide at high temperatures.* Industrial and Engineering Chemistry Research, 2006, 45(11), 3944-3949.

[167] Wang, L., D. Li, H. Watanabe, M. Tamura, Y. Nakagawa, and K. Tomishige, *Catalytic performance and characterization of Co/Mg/Al catalysts prepared from hydrotalcite-like precursors for the steam gasification of biomass.* Applied Catalysis B: Environmental, 2014, 150–151(0), 82-92.

[168] Wang, Q., Z. Wu, H.H. Tay, L. Chen, Y. Liu, J. Chang, Z. Zhong, J. Luo, and A. Borgna, *High temperature adsorption of CO2 on Mg–Al hydrotalcite: Effect of the charge compensating anions and the synthesis pH.* Catalysis Today, 2011, 164(1), 198-203.

[169] Fermoso, J., L. He, and D. Chen, *Production of high purity hydrogen by sorption enhanced steam reforming of crude glycerol.* International Journal of Hydrogen Energy, 2012, 37(19), 14047-14054.

[170] Dou, B., G.L. Rickett, V. Dupont, P.T. Williams, H. Chen, Y. Ding, and M. Ghadiri, *Steam reforming of crude glycerol with in situ CO2 sorption.* Bioresource Technology, 2010, 101(7), 2436-2442.

[171] Chen, H., Y. Ding, N.T. Cong, B. Dou, V. Dupont, M. Ghadiri, and P.T. Williams, *Progress in low temperature hydrogen production with simultaneous CO2 abatement.* Chemical Engineering Research and Design, 2011, 89(9), 1774-1782.

[172] Wang, X., M. Li, S. Li, H. Wang, S. Wang, and X. Ma, *Hydrogen production by glycerol steam reforming with/without calcium oxide sorbent: A comparative study of thermodynamic and experimental work.* Fuel Processing Technology, 2010, 91(12), 1812-1818.

[173] *Terminology for membranes and membrane processes (IUPAC Recommendation 1996).* Journal of Membrane Science, 1996, 120(2), 149-159.

[174] Haag, S., M. Burgard, and B. Ernst, *Beneficial effects of the use of a nickel membrane reactor for the dry reforming of methane: Comparison with thermodynamic predictions.* Journal of Catalysis, 2007, 252(2), 190-204.

[175] Gallucci, F., E. Fernandez, P. Corengia, and M. van Sint Annaland, *Recent advances on membranes and membrane reactors for hydrogen production.* Chemical Engineering Science, 2013, 92(0), 40-66.

[176] Adhikari, S. and S. Fernando, *Hydrogen membrane separation techniques.* Industrial and Engineering Chemistry Research, 2006, 45(3), 875-881.

[177] Miguel, C.V., A. Mendes, S. Tosti, and L.M. Madeira, *Effect of CO and CO2 on H2 permeation through finger-like Pd–Ag membranes.* International Journal of Hydrogen Energy, 2012, 37(17), 12680-12687.

[178] Tosti, S., A. Basile, L. Bettinali, F. Borgognoni, F. Chiaravalloti, and F. Gallucci, *Long-term tests of Pd–Ag thin wall permeator tube.* Journal of Membrane Science, 2006, 284(1–2), 393-397.

[179] Mendes, D., A. Mendes, L.M. Madeira, A. Iulianelli, J.M. Sousa, and A. Basile, *The water-gas shift reaction: From conventional catalytic systems to Pd-based membrane reactors- A review.* Asia-Pacific Journal of Chemical Engineering, 2010, 5(1), 111-137.

[180] Mendes, D., V. Chibante, J.M. Zheng, S. Tosti, F. Borgognoni, A. Mendes, and L.M. Madeira, *Enhancing the production of hydrogen via water-gas shift reaction using Pd-based membrane reactors.* International Journal of Hydrogen Energy, 2010, 35(22), 12596-12608.

[181] Santucci, A., F. Borgognoni, M. Vadrucci, and S. Tosti, *Testing of dense Pd–Ag tubes: Effect of pressure and membrane thickness on the hydrogen permeability.* Journal of Membrane Science, 2013, 444(0), 378-383.

[182] Nayebossadri, S., J. Speight, and D. Book, *Effects of low Ag additions on the hydrogen permeability of Pd–Cu–Ag hydrogen separation membranes.* Journal of Membrane Science, 2014, 451(0), 216-225.

[183] Lewis, A.E., D.C. Kershner, S.N. Paglieri, M.J. Slepicka, and J.D. Way, *Pd–Pt/YSZ composite membranes for hydrogen separation from synthetic water–gas shift streams.* Journal of Membrane Science, 2013, 437(0), 257-264.

[184] Wei, L., J. Yu, and Y. Huang, *Silver coating on porous stainless steel substrate and preparation of H2-permeable palladium membranes.* International Journal of Hydrogen Energy, 2013, 38(25), 10833-10838.

[185] Wei, L., J. Yu, X. Hu, and Y. Huang, *Fabrication of H2-permeable palladium membranes based on pencil-coated porous stainless steel substrate.* International Journal of Hydrogen Energy, 2012, 37(17), 13007-13012.

[186] Zhang, D., S. Zhou, Y. Fan, N. Xu, and Y. He, *Preparation of dense Pd composite membranes on porous Ti–Al alloy supports by electroless plating.* Journal of Membrane Science, 2012, 387–388(0), 24-29.

[187] Braun, F., A.M. Tarditi, J.B. Miller, and L.M. Cornaglia, *Pd-based binary and ternary alloy membranes: Morphological and perm-selective characterization in the presence of H2S.* Journal of Membrane Science, 2014, 450(0), 299-307.

[188] Basile, A., F. Gallucci, A. Iulianelli, G.F. Tereschenko, M.M. Ermilova, and N.V. Orekhova, *Ti–Ni–Pd dense membranes—The effect of the gas mixtures on the hydrogen permeation.* Journal of Membrane Science, 2008, 310(1–2), 44-50.

[189] Peters, T.A., T. Kaleta, M. Stange, and R. Bredesen, *Development of thin binary and ternary Pd-based alloy membranes for use in hydrogen production.* Journal of Membrane Science, 2011, 383(1–2), 124-134.

[190] Chang, A.C.C., W.-H. Lin, K.-H. Lin, C.-H. Hsiao, H.-H. Chen, and H.-F. Chang, *Reforming of glycerol for producing hydrogen in a Pd/Ag membrane reactor.* International Journal of Hydrogen Energy, 2012, 37(17), 13110-13117.

[191] Iulianelli, A., T. Longo, S. Liguori, and A. Basile, *Production of hydrogen via glycerol steam reforming in a Pd-Ag membrane reactor over Co-Al2O3 catalyst.* Asia-Pacific Journal of Chemical Engineering, 2010, 5(1), 138-145.

[192] Lin, K.-H., W.-H. Lin, C.-H. Hsiao, H.-F. Chang, and A.C.C. Chang, *Hydrogen production in steam reforming of glycerol by conventional and membrane reactors.* International Journal of Hydrogen Energy, 2012, 37(18), 13770-13776.

[193] Iulianelli, A., P.K. Seelam, S. Liguori, T. Longo, R. Keiski, V. Calabrò, and A. Basile, *Hydrogen production for PEM fuel cell by gas phase reforming of glycerol as byproduct of bio-diesel. The use of a Pd–Ag membrane reactor at middle reaction temperature.* International Journal of Hydrogen Energy, 2011, 36(6), 3827-3834.

Chapter 3. Predictive Analysis of Glycerol Steam Reforming Process for H_2 Production

This chapter encompasses two theoretical assessments of glycerol steam reforming (GSR). In subchapter 3.1 a thermodynamic analysis is discussed and in subchapter 3.2 a modeling study is carried out.

3.1 Thermodynamic Analysis of Glycerol Steam Reforming for Hydrogen Production with in situ Hydrogen and Carbon Dioxide Separation

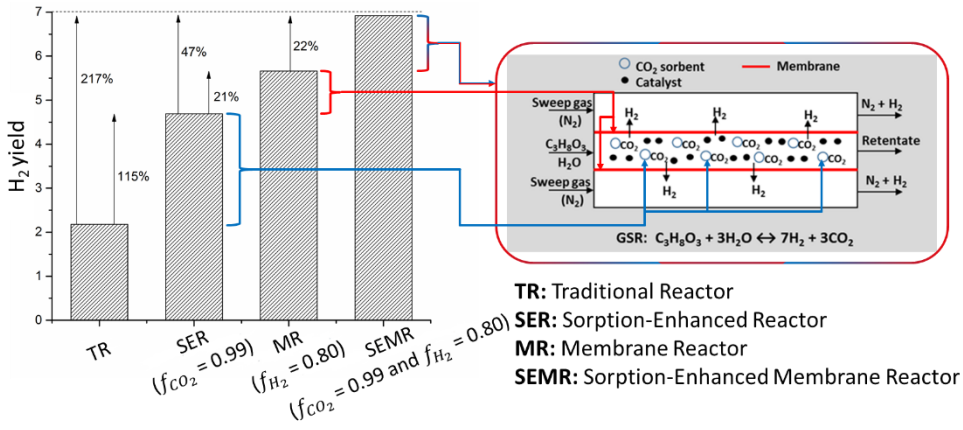

- *A thermodynamic analysis of a SEMR for glycerol steam reforming was performed.*
- *Thermodynamically, higher temperatures, WGFRs and lower pressures are better.*
- *The SEMR produces 217% more hydrogen than a traditional reactor.*

A thermodynamic study of Glycerol Steam Reforming (GSR) for hydrogen production with in situ carbon dioxide and hydrogen (reaction products) simultaneous removal was performed. The sorption-enhanced membrane reactor (SEMR) was divided into multiple sub-Gibbs reactors and the Gibbs free energy minimization method was employed. The effects of temperature (600-800 K), molar water/glycerol feed ratio (WGFR) (3-9), pressure (1-5 atm) and fraction of hydrogen and carbon dioxide removal (f, 0-0.99) on the GSR process were target of investigation. A hydrogen yield ($mol \cdot mol^{-1}_{converted\ glycerol}$) very close to the stoichiometric value of 7 was obtained at 700 K, WGFR of 9, 1 atm and for $f_{CO_2} = 0.99$ and $f_{H_2} = 0.80$. This corresponds to an enhancement of 217%, 47% and 22% in terms of hydrogen yield comparatively to the traditional reactor (TR), sorption-enhanced reactor (SER) with carbon dioxide capture ($f_{CO_2} = 0.99$) and membrane reactor (MR) with hydrogen separation ($f_{H_2} = 0.80$), respectively. In terms of coke, its formation was only observed under WGFRs below the stoichiometric value of 3.

The contents of this chapter were adapted from: Silva, J.M., M.A. Soria, and L.M. Madeira, *Thermodynamic analysis of glycerol steam reforming for hydrogen production with in situ hydrogen and carbon dioxide separation.* Journal of Power Sources, 2015, 273, 423-430.

3.1.1 Introduction

The use of glycerol, the main by-product of the biodiesel manufacture process, for hydrogen production is not only environmentally more attractive than fossil-based routes, but also valorizes glycerol itself thus making biodiesel more competitive. The Glycerol Steam Reforming (GSR) is an endothermic and equilibrium-limited process that requires high operating temperatures (Eq. (3.1.1) – cf. Table 3.1.1). The GSR process involves the decomposition of glycerol (Eq. (3.1.2) – cf. Table 3.1.1) followed by the water-gas shift (WGS, Eq. (3.1.3) – cf. Table 3.1.1) reaction (multiplied by a factor of 3).

Table 3.1.1 - Reactions in equilibrium considered during the GSR thermodynamic simulations.

Reaction	$\Delta H_r^{298\,K}$ / kJ·mol^{-1}	Reaction number
$C_3H_8O_3 + 3H_2O \rightarrow 7H_2 + 3CO_2$ (GSR – glycerol steam reforming)	128	(3.1.1)
$C_3H_8O_3 \rightarrow 3CO + 4H_2$ (decomposition of glycerol)	251	(3.1.2)
$CO + H_2O \rightleftharpoons H_2 + CO_2$ (WGS – water-gas shift)	-41	(3.1.3)
$CO + 3H_2 \rightleftharpoons CH_4 + H_2O$ (methanation)	-206	(3.1.4)
$CO_2 + 4H_2 \rightleftharpoons CH_4 + 2H_2O$[a]	-165	(3.1.5)

Table 3.1.1 - Reactions in equilibrium considered during the GSR thermodynamic simulations (cont.).

Reaction	$\Delta H_r^{298\,K}$ / kJ·mol^{-1}	Reaction number
$2CO + 2H_2 \rightleftharpoons CH_4 + CO_2$[b] (dry reforming of methane)	-247	(3.1.6)
$2CO \rightleftharpoons CO_2 + C$ (Boudouard reaction)	-172	(3.1.7)
$CH_4 \rightleftharpoons 2H_2 + C$ (methane cracking)	75	(3.1.8)
$CO + H_2 \rightleftharpoons H_2O + C$ (carbon monoxide reduction)	-131	(3.1.9)
$CO_2 + 2H_2 \rightleftharpoons 2H_2O + C$ (carbon dioxide reduction)	-90	(3.1.10)

[a] Sum of both reverse of Eq. (3.1.3) and Eq. (3.1.4).
[b] Sum of Eqs. (3.1.3 and 3.1.4).

Even though a theoretical H_2 production of 7 mol· $\mathrm{mol}^{-1}_{\mathrm{converted\ glycerol}}$ should be observed, the existence of side reactions (e.g. methanation) leads to a decrease in hydrogen production. Theoretical studies on new reactor configurations that combine GSR and carbon dioxide [1, 2] or hydrogen [3] selective removal (reaction products in Eq. (3.1.1)) have allowed to conclude that such intensified processes permit to enhance the hydrogen production and decrease the production of both methane and carbon monoxide by-products by shifting the thermodynamic equilibrium. Moreover, such processes allow the attainment of similar or even better performance than in a traditional reactor (TR) while operating at milder operating conditions. However, the effect of the selective removal of both products simultaneously during GSR has never been

studied. Such a process could be achieved with a multifunctional Sorption Enhanced Membrane Reactor (SEMR), which would simultaneously carry out the GSR reaction and remove pure hydrogen and carbon dioxide from the reaction zone by means of a hydrogen selective membrane and a carbon dioxide selective sorbent, respectively (Fig. 3.1.1). The continuous use of such reactor configuration would require two parallel reactors, being that while one of them is producing pure H_2 through GSR (which exits in the permeate stream and is not mixed with any other species, apart from the inert carrier gas, due to membrane selective permeation - left side of Fig. 3.1.1), the other is being regenerated, i.e., carbon dioxide is being removed and exits in the retentate stream (again N_2 can be used as purge gas - right side of Fig. 3.1.1). In other words, each reactor has two operation modes being that along time each of them goes through the reaction-regeneration cycle repeatedly. Since the goal is to shift the thermodynamic equilibrium of GSR during reaction mode by retaining CO_2 in the sorbent, once the sorbent gets saturated and CO_2 starts breaking through the column the reaction is ended (Fig. 3.1.1 (a)). At this point, the set of valves moves this reactor feed (glycerol and steam) to e.g. N_2 so that the sorbent bed can be regenerated (Fig. 3.1.1 (b)). During this last step no H_2 is produced in this reactor, being produced in the other reactor that is now in the reaction stage. Moreover, although CO_2 might affect membrane permeability towards H_2, this is not very pronounced as, for instance, it occurs with CO, and such effect is reversible (thus, as long as CO_2 is removed, high permeability towards H_2 is restored) [4]. The main requirement is that operating conditions, namely in terms of temperature, are compatible for the GSR catalyst, CO_2 sorbent and H_2-selective membrane, which is the case [5].

In this work an equilibrium thermodynamic analysis of GSR in a SEMR was done, for the first time, with ASPEN PLUS software and the effect of the operating temperature, pressure, molar water/glycerol feed ratio (WGFR) and H_2 removal fraction (for constant CO_2 removal) on hydrogen production was

assessed. Moreover, a comparison between the results obtained under equilibrium conditions for the SEMR and for the other types of reactors (TR, membrane reactor (MR) and sorption enhanced reactor (SER)) was done as well. Finally, the limits in terms of WGFR for avoiding coke formation at different temperatures was discussed. This thermodynamic analysis is crucial as it may indicate the suitability of applying such intensified reaction-separation process for hydrogen production from glycerol. Moreover, and although thermodynamic considerations alone do not provide evidence for the practicability of the design, it provides valuable information about the limits that can be attained in actual operation, and gives indication on how to proceed and which conditions have to be applied in order to achieve maximum performance.

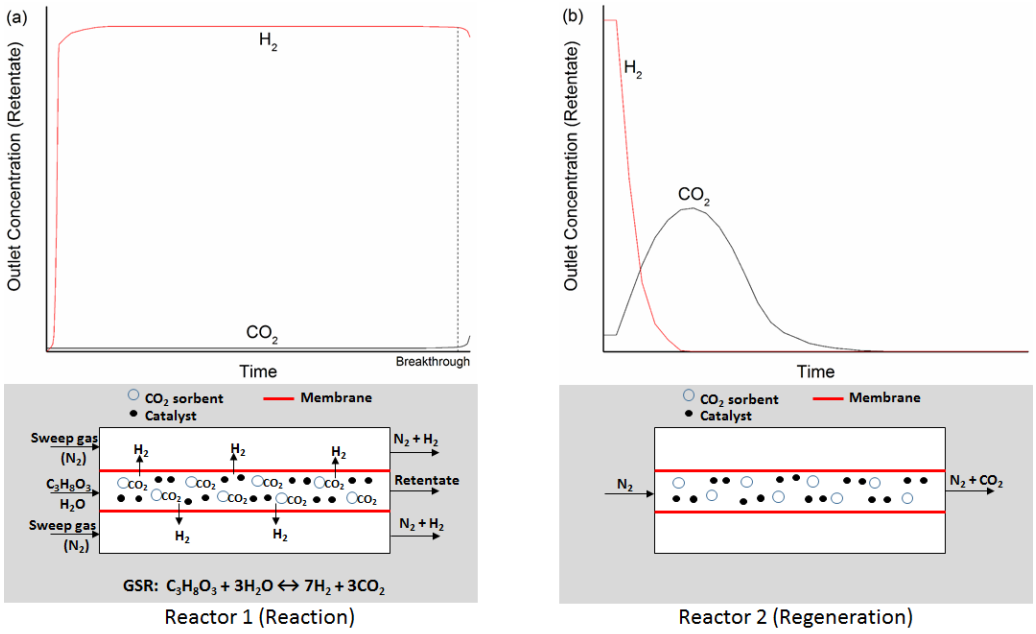

Fig. 3.1.1 - Schematic view of the conceived SEMR based on 2 parallel reactors configuration for continuous operation and corresponding outlet concentrations histories in the retentate stream during (a) reaction and (b) regeneration stages.

3.1.2 Methodology

ASPEN PLUS V7.3 was used to perform all the simulations. The Gibbs free energy minimization methodology (nonstoichiometric method), which calculates the equilibrium composition through the minimization of the Gibbs free energy of a specific set of species was applied (a more detailed description of the methodology is available in the Supplementary data).

For such simulations, the species included were hydrogen, carbon dioxide, carbon monoxide, methane, glycerol, water and solid carbon. By considering these species, some of the possible reactions that might be in equilibrium together with GSR (Eqs. (3.1.2) and (3.1.3)), are the ones shown in Table 3.1.1. The reaction in Eq. (3.1.5), which is the sum of both reverse of Eq. (3.1.3) and Eq. (3.1.4), is included in Table 3.1.1 with the single purpose of facilitating the analysis of the stoichiometric relations in the SEMR.

The modular approach used to simulate the SEMR (Appendix A, Fig. A.1) is represented by $(n+1)$ sub-reformers and n sub-separators. Each sub-reformer consists on a Gibbs reactor which performs the thermodynamic equilibrium calculations through the method previously explained. The sub-separators consist on component separators that separate chemical species based on specified flows or split fractions, which in practice is related with factors like membrane and sorbent selectivities, membrane area and sorbent quantity, etc. For $n = 0$ a simple Gibbs reactor is simulated; for $n = 1$ a single separator and two sub-reformers are used; and so on. The value of n depends on the values of the global removal fractions of CO_2 (f_{CO_2}) and H_2 (f_{H_2}) specified (higher values of f imply higher values of n). It is worth mentioning that a similar methodology has been used in previous works [1, 3].

The thermodynamic analysis was performed for temperatures in the range of 600-800 K, pressures between 1 and 5 atm, WGFRs between 3 and 9 (realistic operation conditions for hydrogen selective membranes [6, 7] and carbon dioxide sorbents [5, 8, 9], which are close to those typically employed in

the GSR [10, 11]); the study considered also hydrogen removal fractions in the range of 0-0.99 and a carbon dioxide removal fraction of 0.99 (for the reasons explained in a posterior section). For all the cases, the yields of hydrogen, methane, carbon dioxide and carbon monoxide were analyzed. These were defined as follows:

$$Y_i = \left(n_{i,separated} + n_{i,unseparated}\right) / n_{converted\ glycerol} \quad \textbf{(3.1.1)}$$

where Y_i is the yield of species i and $n_{converted\ glycerol}$ is the molar flow rate of glycerol that is converted into all reaction products.

3.1.3 Results and discussion

3.1.3.1 GSR with in situ hydrogen or carbon dioxide removal – comparison

Before performing the thermodynamic equilibrium calculations for the SEMR, the thermodynamics of GSR performed in a TR, SER or MR was analyzed. In order to fully understand the effect of the simultaneous removal of both hydrogen and carbon dioxide during GSR on the thermodynamic equilibrium, it is essential to analyze first the effect of the individual removal of either hydrogen or carbon dioxide on the GSR thermodynamics. A comparison between both individual effects (hydrogen and carbon dioxide removal), which to the best of our knowledge has never been done before, is included as well.

Complete conversion of glycerol was observed for all the range of temperatures analyzed (data not shown), in agreement to what was observed by other authors [1-3, 12, 13]. This means that in the subsequent analysis Eq. (3.1.2) is almost not taken into account as it is completely shifted towards

reaction products. Coke formation was not observed for all the conditions used in this section, so Eqs. (3.1.7-10) will now be discarded.

3.1.3.1.1 Traditional reactor ($f_i = 0$)

The variation with temperature of the dimensionless (normalized with the molar flow rate of glycerol fed to the reactor) molar flow rate of glycerol, water, hydrogen, carbon dioxide, carbon monoxide and methane in the thermodynamic equilibrium of a TR is presented in Fig. 3.1.2.

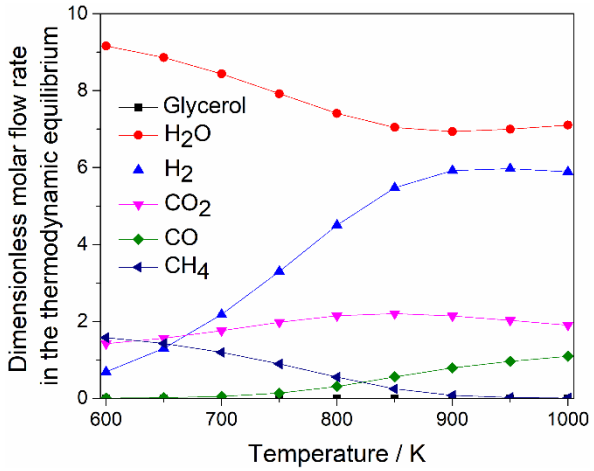

Fig. 3.1.2 - Effect of temperature on the thermodynamic equilibrium composition of a traditional reactor at WGFR of 9 and 1 atm.

In terms of hydrogen and carbon dioxide dimensionless molar flow rates, it can be seen that they increase with temperature up to a certain point, stabilize and then suffer a slight decrease (Fig. 3.1.2). In order to understand this behavior, the reactions in Eqs. (3.1.3) and (3.1.4) should be considered. At lower temperatures (~600 K), the strongly exothermic methanation reaction (Eq. (3.1.4)) is favored, in agreement with the maximum methane and water and minimum carbon monoxide dimensionless molar flow rates observed. Particularly, the dimensionless molar flow rate of water for such temperature is slightly higher than the value of 9 in the feed, thus indicating water formation. When temperature increases the methanation reaction is more disfavored

(progressive inhibition of methane production as compared to WGS reaction (less exothermic – Eq. (3.1.3)), which progressively becomes dominant (CO_2 and H_2 production and H_2O consumption). The stabilization of the hydrogen and carbon dioxide production at higher temperatures is related to the highly enhanced reverse WGS (RWGS), which leads to an increase in the water production. The faster stabilization of the carbon dioxide production observed (maximum at lower temperature than hydrogen) is due to the fact that while hydrogen is being consumed through RWGS and saved through the inhibition of methanation (3 mol of H_2 per mole of CH_4 unproduced), carbon dioxide is only being consumed through RWGS. When the temperature is high enough so that there is no methane formation, the yield of hydrogen starts decreasing and the RWGS becomes the only dominant reaction (hydrogen and carbon dioxide decrease at a similar rate). Since carbon monoxide is consumed through WGS and methanation, which are both exothermic reactions, higher temperatures lead to higher carbon monoxide production. For the conditions here analyzed the material balances performed for each species considering only stoichiometry of reactions 2, 3 and 4 were all consistent with the simulations results, thus indicating that there are no other reactions occurring besides the ones previously indicated.

Regarding the dry reforming of methane (Eq. (3.1.6)), suggested by Adhikari *et al.* [12] to be responsible for the behavior of carbon dioxide production, once it depends on both WGS and methanation (Eqs. (3.1.3) and (3.1.4)), which have been target of discussion already, it is implicitly already analyzed here.

3.1.3.1.2 Sorption-enhanced reactor versus membrane reactor

The variation of the yield of hydrogen, methane, carbon monoxide and carbon dioxide with temperature and carbon dioxide removal fraction (in the SER) and hydrogen removal fraction (in the MR) is presented in Fig. 3.1.3 and Fig. 3.1.4, respectively.

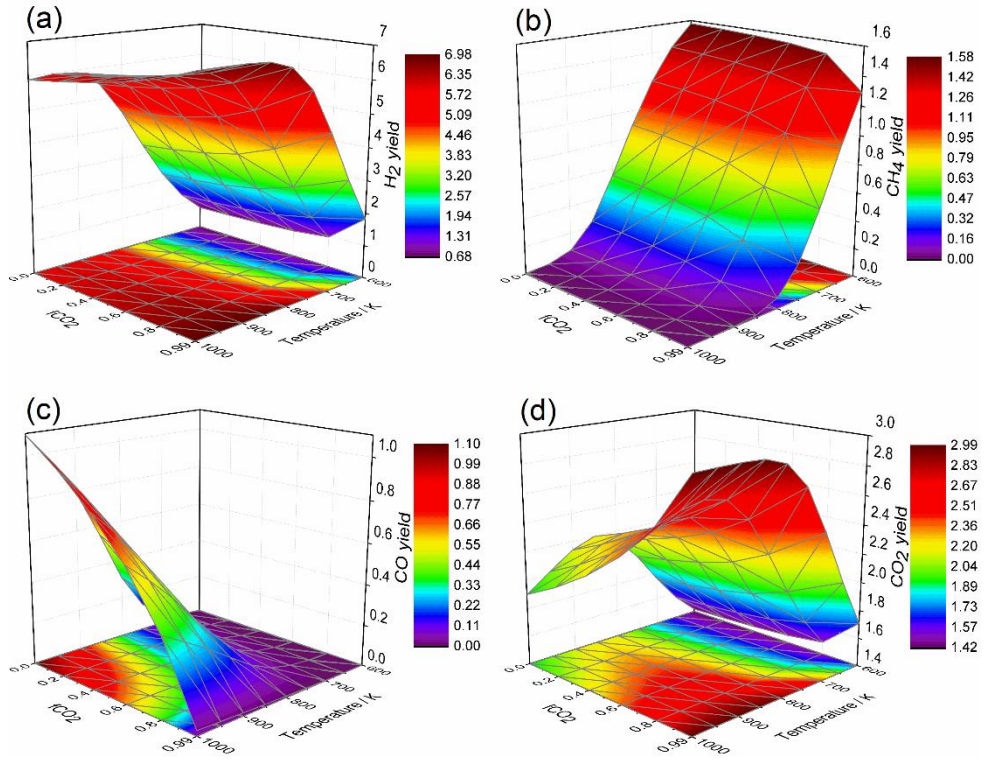

Fig. 3.1.3 - Effect of temperature and carbon dioxide removal fraction of the SER on the yield of (a) hydrogen, (b) methane, (c) carbon monoxide and (d) carbon dioxide, at WGFR of 9 and 1 atm.

Besides increasing with temperature, the yield of hydrogen increases with the fraction of carbon dioxide or hydrogen removal as well. It can be observed by comparing Fig. 3.1.3 (a) and Fig. 3.1.4 (a) that higher hydrogen production can be attained by selectively removing hydrogen from the reaction medium instead of carbon dioxide, especially at lower temperatures. This difference is associated to the inhibition of the formation of the main GSR by-product, methane. When carbon dioxide is removed from the reactor, the equilibrium of the WGS reaction (Eq. (3.1.3)) is shifted towards the production of more carbon dioxide, and inherently hydrogen, and carbon monoxide consumption. Since carbon dioxide does not participate in the reversible methanation reaction (Eq. (3.1.4)), its removal does not directly affect this reaction. Instead, it is only

affected by the enhanced production of hydrogen and carbon monoxide consumption (opposite effects).

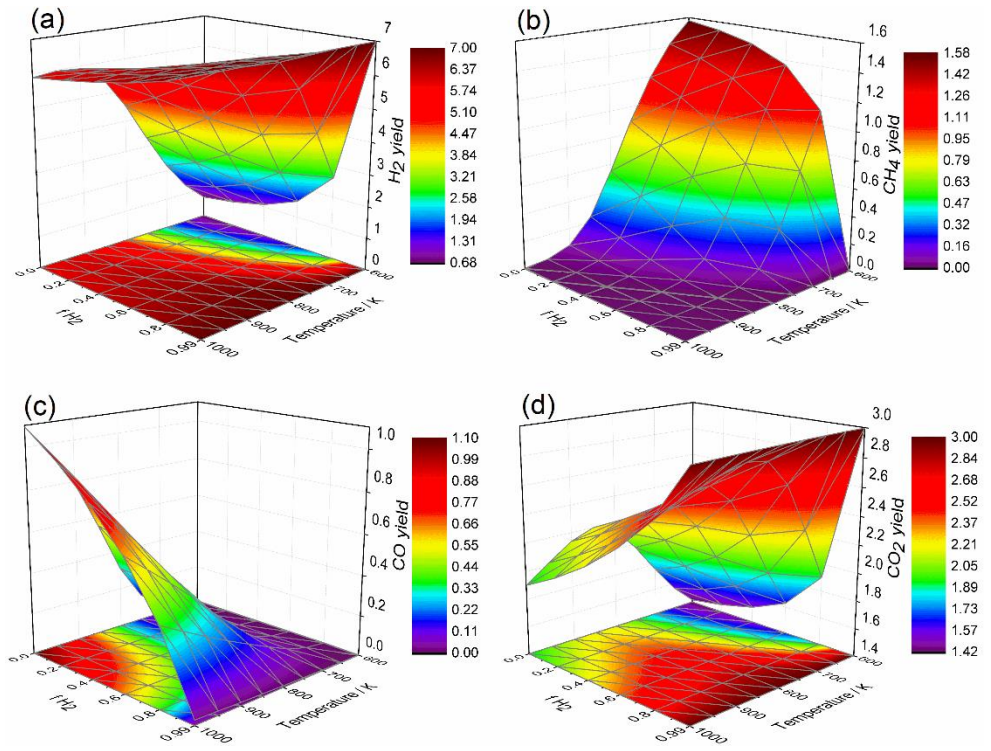

Fig. 3.1.4 - Effect of temperature and hydrogen removal fraction of the MR on the yield of (a) hydrogen, (b) methane, (c) carbon monoxide and (d) carbon dioxide, at WGFR of 9 and 1 atm.

On the other hand, when hydrogen is removed from the reactor, it does not only directly affect the WGS reaction but also the methanation reaction, thus inhibiting the last reaction to a higher extent, which converts hydrogen into methane. Therefore, higher hydrogen yields are obtained in the MR than in the SER at the expense of higher methane production inhibition (Fig. 3.1.3 (b) and Fig. 3.1.4 (b)).

As already stated, when there is no methane generation, higher hydrogen yields are reached, being that the temperature of maximum hydrogen yield depends on how fast methane production is completely inhibited. In the SER,

this maximum occurs at approximately 950 K for all carbon dioxide removal fractions since carbon dioxide does not directly interfere in the methanation reaction. On the other hand, in the MR the temperature at which the maximum hydrogen yield is obtained decreases for increasing hydrogen removal fractions (e.g. 900 K for 40% hydrogen removal vs. 850 K for 80% hydrogen removal). This emphasizes once again the effect that hydrogen removal has on avoiding more intensively methane formation and thus, hydrogen consumption.

A similar behavior as recorded for hydrogen is observed for the carbon dioxide yield in both reactors (Figs. 3.1.3 (d) and 3.1.4 (d)). However, on the contrary to hydrogen, the yield of carbon dioxide starts declining at a temperature bellow the one that completely inhibits methane production, for the reason already mentioned in the previous section. When methane production is completely inhibited, carbon dioxide, in the same way as hydrogen, is consumed through RWGS. Once again, in a SER this maximum happens approximately at the same temperature for all carbon dioxide removal fractions while in the MR the maximum's temperature decreases with increasing hydrogen removal fractions, for the same reasons presented for hydrogen. Regarding carbon monoxide, a similar behavior is observed in both SER and MR (Figs. 3.1.3 (c) and 3.1.4 (c)). Since carbon monoxide is consumed through WGS and methanation, which are both exothermic reactions, higher temperatures shift the opposite reactions, leading to higher carbon monoxide yields. Finally, when higher carbon dioxide or hydrogen removals are applied, more carbon monoxide is consumed through WGS and so lower carbon monoxide yields are obtained, as intended.

3.1.3.2 GSR with in situ hydrogen and carbon dioxide simultaneous removal

In this section the effect of the simultaneous removal of hydrogen and carbon dioxide during GSR, as well as the influence of temperature, WGFR and pressure on the yield of hydrogen, methane, carbon monoxide and carbon

dioxide is assessed. Moreover, an analysis of the boundaries of operating conditions for solid carbon formation is included as well. During the simulations for the SEMR, the carbon dioxide removal fraction was kept at 0.99 (approximate removal normally obtained before the breakthrough in a packed bed) while the hydrogen removal was varied between 0 (SER only) and 0.99. Once again, complete glycerol conversion and no coke formation were observed for all the range of conditions analyzed.

3.1.3.2.1 Effect of temperature

The variation of the yield of hydrogen and methane with temperature and hydrogen removal fraction is presented in Fig. 3.1.5. Since the variation of the carbon dioxide yield with temperature follows a trend very similar to that of hydrogen, its graphic is not presented here for brevity reasons.

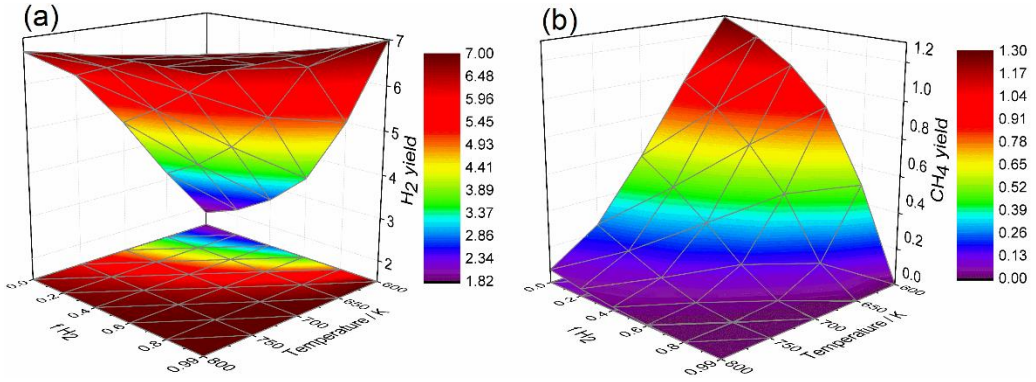

Fig. 3.1.5 - Effect of temperature and hydrogen removal fraction on the yield of (a) hydrogen and (b) methane at WGFR of 9, 1 atm and carbon dioxide removal fraction of 0.99 in a SEMR.

The carbon monoxide yield is not included here as well since only residual amounts were observed. Constant WGFR and pressure of 9 and 1 atm, respectively, were used since such conditions have been reported in many works [13-16] as the most favourable conditions for GSR. However, their effects will be analyzed separately in a later section.

As can be seen in Fig. 3.1.5, higher temperatures highly enhance the hydrogen yield and decrease the methane formation because of the exothermic nature of the main secondary reaction, methanation (Eq. (3.1.4)), which takes place mainly at lower temperatures. Regarding the hydrogen removal fraction, it clearly enhances hydrogen production, especially at lower temperatures. For hydrogen and carbon dioxide removals of 99%, the theoretical hydrogen yield of 7 is obtained for all the range of temperatures tested. However, such hydrogen removal in a membrane reactor operating at 1 atm is pratically impossible. Therefore, a hydrogen removal of 80% [17] is considered to be much more realistic while operating at 1 atm. Under such conditions a hydrogen production of 5 and 7 $\mathrm{mol} \cdot \mathrm{mol}^{-1}_{\mathrm{converted\ glycerol}}$ at 600 K and 800 K, respectively, was obtained. Compared to the other reactor configurations (SER and MR), the SEMR allows higher hydrogen generation, especially at lower temperatures. Therefore, from the thermodynamic point of view, the use of such reactor configuration would be much more beneficial if temperatures around 600 K are used. However, this decreases reaction kinetics and hydrogen permeation, so that longer reactors and thus, longer and/or more permeable membranes, would be required.

In terms of methane formation, the maximum methane production of 0.5 $\mathrm{mol} \cdot \mathrm{mol}^{-1}_{\mathrm{converted\ glycerol}}$ for $f_{CO_2} = 0.99$ and $f_{H_2} = 0.80$ was observed at 600 K (no considerable methane at 750 K) – Fig. 3.1.5, while for the SER with $f_{CO_2} = 0.99$ and for the MR with $f_{H_2} = 0.80$, maximum methane productions of 1.29 (Fig. 3.1.3 (b)) and 1.09 (Fig. 3.1.4 (b)) $\mathrm{mol} \cdot \mathrm{mol}^{-1}_{\mathrm{converted\ glycerol}}$ were obtained, respectively, for the same temperature. Regarding carbon dioxide, its yield varies with temperature and hydrogen removal fraction in a similar way as hydrogen (data not shown) since it is a product of the same reaction that origins hydrogen (WGS (Eq. (3.1.3)). Moreover, since the base case here already considers a carbon dioxide removal fraction as high as 0.99, which already leads to a very similar behavior between hydrogen and carbon dioxide yields in the

SER (the effect of carbon dioxide removal outweighs the effect of temperature – Fig. 3.1.3), then it is expected that by adding hydrogen removal, the similarities between the behavior of both species yields increase. Finally, it is again worth stressing that only residual amounts of carbon monoxide (< 0.01 $\mathrm{mol} \cdot \mathrm{mol}^{-1}_{\mathrm{converted\ glycerol}}$) were observed during the simulations for all the range of temperatures and hydrogen removal fractions.

It was observed, for all the range of temperatures and hydrogen removal fractions under which methane formation occurs that the variation of temperature or hydrogen removal fraction resulted in variations of the moles of hydrogen 4 times higher than the variations of the moles of methane and carbon dioxide (absolute value). This clearly indicates that both WGS (Eq. (3.1.3)) and SRM (reverse of Eq. (3.1.4)) control the GSR process in the SEMR. On the other hand, under conditions that do not allow methane formation (high hydrogen removal fractions and high temperatures), the process is solely controlled by the WGS reaction.

By comparing the SEMR with the other three reactor configurations in terms of hydrogen yield, it is clear that the SEMR presents better performance than both the SER and MR and much better performance than the TR. In fact, while in the TR, at 700 K, 1 atm and WGFR of 9, a hydrogen yield of 2.18 was attained, in the SER with $f_{CO_2} = 0.99$, MR with $f_{H_2} = 0.80$ and SEMR with $f_{CO_2} = 0.99$ and $f_{H_2} = 0.80$, hydrogen yields of 4.69, 5.66 and 6.92 were observed, respectively, under the same conditions. This corresponds to an enhancement of the hydrogen yield of aproximately 115% when the SER with $f_{CO_2} = 0.99$ is used instead of the TR, an enhancement of approximately 21% when the MR with $f_{H_2} = 0.80$ is used instead of the SER with $f_{CO_2} = 0.99$ (enhancement of approximately 160% comparatively to the TR) and an increase of around 22% when the SEMR with $f_{CO_2} = 0.99$ and $f_{H_2} = 0.80$ is used instead of the MR with $f_{H_2} = 0.80$ (enhancement of 217% and 47% comparatively to the TR and the SER with $f_{CO_2} = 0.99$, respectively).

3.1.3.2.2 Effect of molar water/glycerol feed ratio

The effect of both hydrogen removal fraction and WGFR on the yield of hydrogen and methane was target of investigation as well. Such study is depicted in Fig. 3.1.6. The WGFR was varied between 3 (stoichiometric value) and 9, which has been considered by many authors as the most favorable value, as already mentioned. Higher values were not considered because this would imply, in practice, excessive costs for water vaporization.

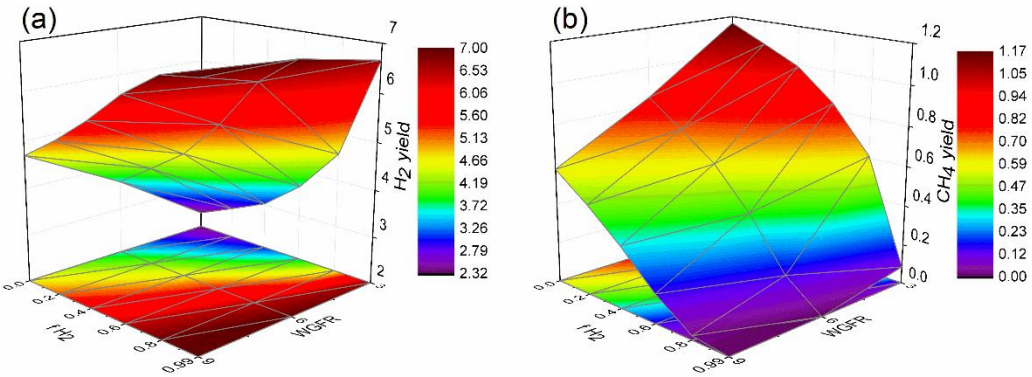

Fig. 3.1.6 - Effect of WGFR and hydrogen removal fraction on the yield of (a) hydrogen and (b) methane at 700 K, 1 atm and carbon dioxide removal fraction of 0.99 in a SEMR.

In terms of hydrogen production, the increase of the WGFR enhances the production of hydrogen, especially at lower hydrogen removal fractions. By increasing the water content in the reaction environment, the thermodynamic equilibrium of both GSR and SRM (reverse of Eq. (3.1.4)) is dislocated, according to the Le Chatelier's principle, towards the conversion of the excess of water into hydrogen. Thus, the methane yield decreases, as can be seen in Fig. 3.1.6 (b). Regarding the carbon dioxide yield, its behavior is very similar to hydrogen (data not shown) because of the reasons already stated in the previous section. Once again, only residual amounts of carbon monoxide were observed. The process is controlled by the reactions in Eqs. (3.1.2-4) for all the WGFRs involved. When there is no methane, only Eqs. (3.1.2) and (3.1.3) are relevant.

Concerning the effect of increasing hydrogen removal fractions, it is clear that higher removal fractions of hydrogen lead to higher hydrogen production and methane production inhibition. Moreover, this enhancement is more pronounced for less favorable conditions (WGFR = 3).

In sum, considering again the case in which $f_{CO_2} = 0.99$ and $f_{H_2} = 0.80$, when the WGFR increased from 3 to 9, the hydrogen yield increased from 4.57 to 6.92 $\mathrm{mol} \cdot \mathrm{mol}^{-1}_{\text{converted glycerol}}$, while the yield of methane decreased from 0.61 to 0.02.

If higher WGFRs had been tested, higher hydrogen yields would have been obtained, especially at lower hydrogen removal fractions. However, such water contents are considered to be disadvantageous due to the high vaporization costs involved at industrial scale. Moreover, even if they allow avoiding coke formation, high water contents may lead to catalyst and sorbent deactivation due to pore blocking [18]. On the contrary, lower WGFRs are not so problematic from the economic point of view since the glycerol produced through the biodiesel production process is composed by low amounts of water (3.2% water, 40% fatty matter, 33% glycerol, 23% methanol and 3.8% ash) [19]. Therefore, if lower WGFRs are employed, less water has to be added. Even if low WGFRs are not so advantageous in terms of hydrogen production, the use of a hybrid reaction-separation process like the one here described allows reducing the constraints imposed by such low water contents.

3.1.3.2.3 Effect of pressure

Finally, the effect of pressure and hydrogen removal fraction on the yield of hydrogen and methane was analyzed, as can be seen in Fig. 3.1.7. It can be observed that when higher pressures are used, the yield of hydrogen suffers a negative effect, except for very high hydrogen removal fractions where constant hydrogen yields are observed. Such effect is once again related to the Le Chatelier's principle, because during GSR the total number of moles varies (Eq.

(3.1.1)). Therefore, when higher pressures are applied, the thermodynamic equilibrium will be shifted towards the production of a lower total number of moles. However, once the glycerol conversion was complete for all the range of pressures used, the decrease of the hydrogen yield cannot be associated to GSR. Instead, it is associated to the enhancement of the methanation reaction (Eq. (3.1.4)), which consumes hydrogen and yields methane. As already stated, this is not valid for very high hydrogen removal fractions, where there is no methane. While at 1 atm, and considering $f_{CO_2} = 0.99$ and $f_{H_2} = 0.80$, the hydrogen and methane yields were 6.92 and 0.02, respectively, at 5 atm the hydrogen yield decreased to 6.06 and the methane one increased to 0.23.

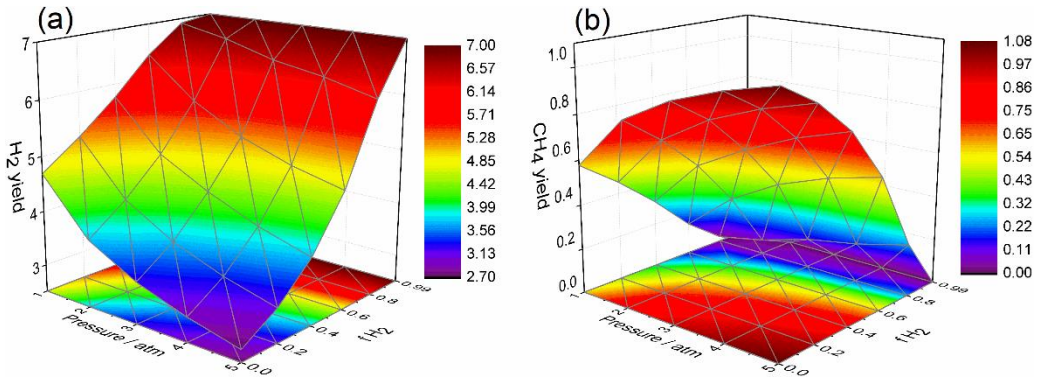

Fig. 3.1.7 - Effect of pressure and hydrogen removal fraction on the yield of (a) hydrogen and (b) methane at 700 K, WGFR of 9 and carbon dioxide removal fraction of 0.99 in a SEMR.

In terms of carbon dioxide, its yield varies with pressure in a very similar way as hydrogen does (data not shown), for the reasons already mentioned. The production of carbon monoxide was once again negligible. Also, both RWGS (reverse of Eq. (3.1.3)) and methanation (Eq. (3.1.4)) control the process for all the range of pressures analyzed, except when the formation of methane is completely inhibited. In this last case, WGS is the only relevant reaction.

Regarding the effect of the hydrogen removal fraction, analogously to the previous cases, the hydrogen yield is favoured by increasing hydrogen removals, while methane suffers an opposite effect. The higher enhancement of

the hydrogen yield is observed at the less thermodynamically favorable pressure (5 atm). It is, nonetheless, important to mention that the approach used here ignores the effect of pressure on the removal of both carbon dioxide and hydrogen, as well as in the reaction kinetics. It is known that pressure influences the driving force for carbon dioxide sorption and for hydrogen permeation through a hydrogen permselective membrane. Thus, higher pressures lead to higher carbon dioxide and hydrogen removal fractions, meaning that if high pressures are used in the SEMR, high hydrogen removals are attained and inherently higher hydrogen yields. Moreover, in the case of $f_{CO_2} = 0.99$ and $f_{H_2} = 0.80$, when the pressure increases from 1 to 5 atm, the hydrogen yield at equilibrium decreases much less than for lower hydrogen removals, namely for $f_{H_2} = 0$ (SER). Consequently, the use of high pressures becomes advantageous after all due to the membrane effect.

3.1.3.2.4 Coke formation

The formation of coke was target of investigation as well, since it is an undesired product that may affect the performance of the catalyst, sorbent and membrane during actual operation of the SEMR. It was observed that the formation of coke in the TR increases with the decrease of temperature (and so a higher WGFR would be required to completely avoid coke formation) during GSR, however at 600 K and 1 atm a WGFR of 4 is high enough to completely avoid coke formation. When carbon dioxide or hydrogen were removed from the reaction medium, opposite effects were observed. While the formation of coke decreases comparatively to the TR when carbon dioxide is removed from the reaction medium, when hydrogen is removed more coke is produced. For a carbon dioxide removal of 99%, a WGFR of 1 is enough to completely avoid coke formation at temperatures between 600 and 800 K and 1 atm. On the other hand, when 99% of hydrogen is removed, a WGFR of 4.5 is necessary to avoid carbon formation in the same temperature range and atmospheric pressure.

Therefore, it allows us to conclude that most of coke is formed from methane through the reaction in Eq. (3.1.8) (the low WGFRs allow the formation of methane, even at hydrogen and carbon dioxide removals of 99%), being that the reactions in Eqs. (3.1.7), (3.1.9) and (3.1.10) are not compatible with the observed behavior and so they can be neglected.

It is therefore expected that when both products are removed from the reaction medium in the SEMR, an equilibrium between both opposite effects is reached. That was in fact observed, being that at $f_{CO_2} = 0.99$ and $f_{H_2} = 0.80$ a WGFR of 2.5 was enough to completely inhibit coke formation for all the range of temperatures and pressures tested. Even for a removal of 99% of both products, the stoichiometric WGFR of 3 was sufficient to avoid coke formation in all the temperature and pressure range. Therefore, it would be possible, from the thermodynamic point of view, to operate a SEMR for GSR under the temperature, WGFR and pressure ranges analyzed in this study without having any problems with coke formation.

3.1.4 Conclusions

A thermodynamic analysis was carried out on the GSR for hydrogen production in a SEMR with in situ hydrogen and carbon dioxide simultaneous removal. At 800 K, WGFR of 9, 1 atm and $f_{CO_2} = 0.99$ and $f_{H_2} = 0.80$, the hydrogen yield was 7 (maximum possible value). Regarding methane and carbon monoxide, no considerable production was observed under such conditions. Even though the SEMR presents higher hydrogen production than the SER and the MR and much higher hydrogen production than the TR, the difference is not very significative at higher temperatures compared to the two first configurations. However, this difference becomes much more meaningful with the decrease of temperature. At 600 K, a hydrogen production of 5 $\mathrm{mol}\cdot$

$\mathrm{mol}^{-1}_{\mathrm{converted\ glycerol}}$ was observed in the SEMR with $f_{CO_2} = 0.99$ and $f_{H_2} = 0.80$, while hydrogen productions of 1.83 and 2.62 $\mathrm{mol} \cdot \mathrm{mol}^{-1}_{\mathrm{converted\ glycerol}}$ were obtained in the SER and MR with the same removals, respectively. Therefore the advantages of the SEMR are more noticeable at lower temperatures and so, this new hybrid reactor configuration can be seen as a possible solution to lower the high operating temperatures necessary for the endothermic GSR. However, a proper judgement has to be done, because at lower temperatures longer reactors and longer and/or more permeable membranes would be necessary to compensate the decreased reaction kinetics and permeation rate.

In terms of WGFR and pressure effects, it is clear, from thermodynamic point of view, that higher WGFRs and lower pressures favor the production of hydrogen in the SEMR. Finnaly, it was observed that no coke was formed at WGFRs higher than 3.

Notation and Glossary

List of acronyms

GSR	Glycerol Steam Reforming
MR	Membrane Reactor
RWGS	Reverse Water-Gas-Shift
SER	Sorption-Enhanced Reactor
SEMR	Sorption-Enhanced Membrane Reactor
SRM	Steam Reforming of Methane
TR	Traditional Reactor
WGFR	Molar Water/Glycerol Feed Ratio
WGS	Water-Gas Shift

3.1.5 References

[1] Chen, H., T. Zhang, B. Dou, V. Dupont, P. Williams, M. Ghadiri, and Y. Ding, *Thermodynamic analyses of adsorption-enhanced steam reforming of glycerol for hydrogen production.* International Journal of Hydrogen Energy, 2009, 34(17), 7208-7222.

[2] Li, Y., W. Wang, B. Chen, and Y. Cao, *Thermodynamic analysis of hydrogen production via glycerol steam reforming with CO2 adsorption.* International Journal of Hydrogen Energy, 2010, 35(15), 7768-7777.

[3] Wang, X., N. Wang, M. Li, S. Li, S. Wang, and X. Ma, *Hydrogen production by glycerol steam reforming with in situ hydrogen separation: A thermodynamic investigation.* International Journal of Hydrogen Energy, 2010, 35(19), 10252-10256.

[4] Miguel, C.V., A. Mendes, S. Tosti, and L.M. Madeira, *Effect of CO and CO2 on H2 permeation through finger-like Pd–Ag membranes.* International Journal of Hydrogen Energy, 2012, 37(17), 12680-12687.

[5] Silva, J.M., M.A. Soria, and L.M. Madeira, *Challenges and strategies for optimization of glycerol steam reforming process.* Renewable and Sustainable Energy Reviews, 2015, 42, 1187-1213.

[6] Chang, A.C.C., W.-H. Lin, K.-H. Lin, C.-H. Hsiao, H.-H. Chen, and H.-F. Chang, *Reforming of glycerol for producing hydrogen in a Pd/Ag membrane reactor.* International Journal of Hydrogen Energy, 2012, 37(17), 13110-13117.

[7] Lin, K.-H., W.-H. Lin, C.-H. Hsiao, H.-F. Chang, and A.C.C. Chang, *Hydrogen production in steam reforming of glycerol by conventional and membrane reactors.* International Journal of Hydrogen Energy, 2012, 37(18), 13770-13776.

[8] Hanif, A., S. Dasgupta, S. Divekar, A. Arya, M.O. Garg, and A. Nanoti, *A study on high temperature CO2 capture by improved hydrotalcite sorbents.* Chemical Engineering Journal, 2014, 236(0), 91-99.

[9] Miguel, C.V., R. Trujillano, V. Rives, M.A. Vicente, A.F.P. Ferreira, A.E. Rodrigues, A. Mendes, and L.M. Madeira, *High temperature CO2 sorption with gallium-substituted and promoted hydrotalcites.* Separation and Purification Technology, 2014, 127, 202-211.

[10] Sutar, P.N., P.D. Vaidya, and A.E. Rodrigues, *Glycerol-reforming kinetics using a Pt/C catalyst.* Chemical Engineering and Technology, 2010, 33(10), 1645-1649.

[11] Cheng, C.K., S.Y. Foo, and A.A. Adesina, *Glycerol Steam Reforming over Bimetallic Co−Ni/Al2O3.* Industrial & Engineering Chemistry Research, 2010, 49(21), 10804-10817.

[12] Adhikari, S., S. Fernando, S.R. Gwaltney, S.D. Filip To, R. Mark Bricka, P.H. Steele, and A. Haryanto, *A thermodynamic analysis of hydrogen production by steam reforming of glycerol.* International Journal of Hydrogen Energy, 2007, 32(14), 2875-2880.

[13] Wang, X., S. Li, H. Wang, B. Liu, and X. Ma, *Thermodynamic analysis of glycerin steam reforming.* Energy and Fuels, 2008, 22(6), 4285-4291.

[14] Chen, H., Y. Ding, N.T. Cong, B. Dou, V. Dupont, M. Ghadiri, and P.T. Williams, *A comparative study on hydrogen production from steam-glycerol reforming: thermodynamics and experimental.* Renewable Energy, 2011, 36(2), 779-788.

[15] Adhikari, S., S. Fernando, and A. Haryanto, *A comparative thermodynamic and experimental analysis on hydrogen production by steam reforming of glycerin.* Energy and Fuels, 2007, 21(4), 2306-2310.

[16] Hajjaji, N., A. Chahbani, Z. Khila, and M.-N. Pons, *A comprehensive energy–exergy-based assessment and parametric study of a hydrogen production process using steam glycerol reforming.* Energy, 2014, 64(0), 473-483.

[17] Mendes, D., S. Sá, S. Tosti, J.M. Sousa, L.M. Madeira, and A. Mendes, *Experimental and modeling studies on the low-temperature water-gas shift reaction in a dense Pd–Ag packed-bed membrane reactor.* Chemical Engineering Science, 2011, 66(11), 2356-2367.

[18] Martunus, Z. Helwani, A.D. Wiheeb, J. Kim, and M.R. Othman, *Improved carbon dioxide capture using metal reinforced hydrotalcite under wet conditions.* International Journal of Greenhouse Gas Control, 2012, 7(0), 127-136.

[19] Slinn, M., K. Kendall, C. Mallon, and J. Andrews, *Steam reforming of biodiesel by-product to make renewable hydrogen.* Bioresource Technology, 2008, 99(13), 5851-5858.

3.2 Steam Reforming of Glycerol for Hydrogen Production - Modeling Study

- *A packed bed reactor model for glycerol steam reforming was validated.*
- *Model predicts both glycerol consumption and products/by-products formation.*
- *A parametric analysis was carried out for a wide range of conditions.*
- *A maximum H_2 production of 4.93 $mol \cdot mol_{fed\ glycerol}^{-1}$ was reached.*

A phenomenological model that predicts the operation of a packed bed reactor for glycerol steam reforming (GSR), in terms of glycerol conversion and products generation (first time to our knowledge), especially H_2, was built and used to perform a parametric analysis (range of conditions: 748-848 K, molar water/glycerol feed ratios (WGFRs) of 3-12 and 1-5 atm). First, the model was validated in terms of glycerol conversion, products yields and selectivities, having been observed very good agreement. Regarding the parametric study, higher temperatures, WGFRs and pressures were found to be more beneficial in terms of glycerol conversion. Moreover, the H_2 yield and selectivity are enhanced when higher temperatures and lower WGFRs and pressures are employed. Still, the maximum H_2 amount of 4.93 $mol \cdot mol_{fed\ glycerol}^{-1}$ was observed at 848 K, WGFR of 9 and 2 atm.

The contents of this chapter were adapted from: Silva, J.M., M.A. Soria, and L.M. Madeira, *Steam reforming of glycerol for hydrogen production: Modeling study.* International Journal of Hydrogen Energy, 2016, 41(3), 1408-1418.

3.2.1 Introduction

Nowadays hydrogen is seen by many authors as the energy carrier of the future due to its potential to fulfill many of our society needs without ignoring some of the environmental problems that fossil fuels, the main energy carriers of the present, cannot avoid. Therefore, several distinct processes for hydrogen production have been researched. While during the last century the focus was manly on using fossil fuels-based feedstock (e.g.: natural gas), in the last decades the interest has shifted towards cleaner raw materials such as methanol, ethanol and glycerol, among others. Glycerol, in particular, can be produced as a by-product during the biodiesel production process and converted into hydrogen through steam reforming (Eq. (3.2.1)).

$$C_3H_8O_3 + 3H_2O \rightarrow 7H_2 + 3CO_2 \quad (\Delta H_r^{298\,K} = 128\ \text{kJ·mol}^{-1}) \qquad \textbf{(3.2.1)}$$

However, the formation of secondary products of a more complex mechanism than Eq. (3.2.1), such as CO and CH_4, must be considered as well, according to some works reported in the literature regarding glycerol steam reforming (GSR) [1-4]. The use of glycerol as feedstock would prove itself advantageous compared to methanol or ethanol since it would decrease its disposal and associated costs, thus valorizing biodiesel.

Even though there has been done a huge amount of work regarding the search of GSR catalysts and there are several thermodynamic assessments that have been done [5], phenomenological models that allow describing the GSR reaction system in packed bed reactors, for example, are still too few. To the best of our knowledge there are only a couple of works where such models are reported [6-8]. Even though all these are 2D models that allow consequently to do an interesting analysis of the several variables profiles (e.g. contours over the 2D domain [8]), they only predict the consumption of glycerol. There is one work in which the generation of products (and by-products) is predicted; however, it

is for the sorption-enhanced GSR process and assumes theoretical yields [9], which is not realistic for conditions far from those employed by the authors. With the aim of covering up this hole, a phenomenological model capable of predicting accurately the real operation of a GSR packed bed reactor in terms of consumption of glycerol and production of the main products (H_2 and CO_2) and by-products (CO and CH_4), based on actual individual products generation kinetics, has been developed and will be target of analysis here. First a critical comparison between the model's predictions and the experimental results obtained by Cheng *et al.* [10] for a Co-Ni/Al_2O_3 catalyst is done, being then followed by a parametric analysis considering different temperatures (748-848 K), molar water/glycerol feed ratios (WGFRs) (3-12) and pressures (1-5 atm).

3.2.2 Phenomenological model

3.2.2.1 Model and governing equations

The pseudo-homogeneous model here proposed for describing the GSR reaction in a packed bed reactor considers the following assumptions:

- Steady state;
- Axially dispersed plug flow;
- Non-isothermal operation;
- Pressure drop along the bed described by the Ergun equation;
- Non-constant velocity along the bed;
- Ideal gas behavior.

The governing equations used to simulate such system are the following, being composed by 7 differential equations (one for each species - partial mass balances), 1 differential equation for the total mass balance (required due to the

non-constant velocity along the reactor bed), as well as 2 other differential equations to obtain temperature and total pressure profiles:

Partial mass balance

$$D_{ax}\frac{d^2C_i}{dx^2}-\frac{L}{\varepsilon_b}\frac{d(u_sC_i)}{dx}+\frac{W_{cat}L^2}{V_R\varepsilon_b}R_i=0 \quad \textbf{(3.2.2)}$$

Total mass balance

$$\frac{d(u_sC)}{dx}-\frac{W_{cat}L}{V_R}\sum_i R_i=0 \quad \textbf{(3.2.3)}$$

Energy balance

$$\frac{d^2T}{dx^2}-\frac{u_s\rho_f C_{p,f}L}{\lambda_{ax}}\frac{dT}{dx}+\frac{W_{cat}L^2}{V_R\lambda_{ax}}\sum_i\left(\left(-\Delta H_{f,i}\right)R_i\right)-2\frac{hL^2}{R_0\lambda_{ax}}(T-T_w)=0 \quad \textbf{(3.2.4)}$$

Momentum balance

$$\frac{dP}{dx}+150\frac{(1-\varepsilon_b)^2L\mu_f}{\varepsilon_b^3d_p^2}u_s+1.75\frac{(1-\varepsilon_b)L\rho_f}{\varepsilon_b^3d_p}{u_s}^2=0 \quad \textbf{(3.2.5)}$$

Since both partial mass balance and energy balance are second order differential equations, then two boundary conditions are required for each. The following boundary conditions were used:

$$x=0: \quad C_i=C_{i,in}\ ,\ T=T_{in}\ ,\ u_s=u_{s,in}\ ,\ P=P_{in} \quad \textbf{(3.2.6)}$$

$$x=1: \quad \frac{dC_i}{dx}=0,\ \frac{dT}{dx}=0 \quad \textbf{(3.2.7)}$$

where C_i is the molar concentration of compound i (i = $C_3H_8O_3$, H_2O, H_2, CO_2, CO, CH_4 and Ar), x is the dimensionless axial coordinate, D_{ax} is the mass axial dispersion coefficient, L is the reactor length, u_s is the superficial velocity, W_{cat} is the mass of catalyst in the reactor bed, V_R is the volume of the reactor bed (W_{cat}/V_R is the bulk density, ρ_b), ε_b is the void fraction of the catalyst bed and R_i is the consumption/formation rate of component i. C is the total concentration of species, T is the bed temperature, ρ_f is the gas mixture density, $C_{p,f}$ is the gas mixture heat capacity, λ_{ax} is the heat axial dispersion coefficient, $\Delta H_{f,i}$ is the heat of formation of species i, h is the convective wall-fluid heat transfer coefficient, R_0 is the reactor inner radius, T_w is the reactor wall temperature, P is the total reactor pressure, μ_f is the gas mixture viscosity and d_p is the catalyst particles diameter.

The void fraction of the catalyst bed was estimated with Eq. (3.2.8) [11]:

$$\varepsilon_b = \frac{A}{\left(2R_0/d_p\right)^n} + B \qquad \textbf{(3.2.8)}$$

where $A = 1.5$, $B = 0.35$ and $n = 1$ assuming that the catalyst particles are lumps of irregular shape.

Regarding the mass axial dispersion, it was calculated using the Edwards and Richardson correlation [12]:

$$D_{ax} = 0.73 D_{C_3H_8O_3,mix} + \frac{0.5 u_s d_p}{1 + 9.49 \frac{D_{C_3H_8O_3,mix}}{u_s d_p}} \qquad \textbf{(3.2.9)}$$

where $D_{C_3H_8O_3,mix}$ is the molecular diffusivity of glycerol in the reaction mixture, which can be estimated using the Wilke method [13]:

$$D_{C_3H_8O_3,mix} = \frac{1 - y_{C_3H_8O_3}}{\sum_{j=1}^{n} \frac{y_j}{D_{C_3H_8O_3,j}}} \qquad \textbf{(3.2.10)}$$

being $j \neq C_3H_8O_3$ and $D_{C_3H_8O_3,j}$ the binary diffusivity of glycerol when diffusing into species j. In order to calculate this last parameter the Fuller method [14] was used:

$$D_{C_3H_8O_3,j} = \frac{0.1013T^{1.75}\left(\frac{1}{M_{C_3H_8O_3}} + \frac{1}{M_j}\right)^{0.5}}{P\left[(\sum v)_i^{1/3} + (\sum v)_j^{1/3}\right]^2} \quad \textbf{(3.2.11)}$$

where $\sum v$ is the sum of the atomic diffusion volumes for each component (taken from [14]) and M_i is the molar mass of species i (in this case expressed in g·mol^{-1}).

In terms of heat axial dispersion coefficient, it was calculated using the Wakao and Funazkri correlation [15]:

$$\lambda_{ax} = 7\lambda_f + 0.5\rho_f u_s d_p C_{p,f} \quad \textbf{(3.2.12)}$$

where λ_f is the thermal conductivity of the gas mixture, calculated as detailed below. Both mass and heat axial dispersion coefficients were calculated at the inlet conditions in order to simplify the calculations and since no significant variation was observed along the bed.

The gas mixture density was calculated locally through Eq. (3.2.13):

$$\rho_f = \frac{P}{RT}\sum_{i=1}^{n} y_i M_i \quad \textbf{(3.2.13)}$$

where R is the ideal gases constant and y_i is the molar fraction of species i. Similarly, the viscosity of the gas mixture was calculated locally with the Wilke method [13]:

$$\mu_f = \sum_{i=1}^{n} \frac{y_i \mu_i}{\sum_{j=1}^{n} y_j \phi_{ij}} \quad \textbf{(3.2.14)}$$

being μ_i the viscosity of species i that is calculated using a polynomial equation (Eq. (3.2.15)) [16], except for Ar whose viscosity was calculated through Sutherland's equation (Eq. (3.2.16)) [17]:

$$\mu_i = A + BT + CT^2 \quad \textbf{(3.2.15)}$$

$$\mu_i = \frac{C_1 T^{3/2}}{T + S} \quad \textbf{(3.2.16)}$$

where *A*, *B* and *C* are constants that present specific values for each gas (taken from Ref. [16]), while C_1 and S are the Sutherlands constants for gas i ($C_1 = 2.08 \times 10^{-6}\ \mathrm{kg \cdot (m\ s\ K^{0.5})^{-1}}$ and $S = 191\ K$ for Ar). Parameter ϕ_{ij} is calculated with Eq. (3.2.17) [13]:

$$\phi_{ij} = \left[8\left(1 + \frac{M_i}{M_j}\right)\right]^{-0.5}\left[1 + \left(\frac{\mu_i}{\mu_j}\right)^{0.5}\left(\frac{M_i}{\mu_j}\right)^{-0.25}\right]^2 \quad \textbf{(3.2.17)}$$

where $j \neq i$. Similarly to the axial dispersion coefficients, the mass heat capacity of the gas mixture was calculated at feed conditions for the same reasons:

$$C_{p,f} = \frac{\sum_{i=1}^{n} y_i C_{p,i}}{\sum_{i=1}^{n} y_i M_i} \quad \textbf{(3.2.18)}$$

where $C_{p,i}$ is the molar heat capacity of species i and can be calculated with Eq. (3.2.19) [16]:

$$C_{p,i} = A + BT + CT^2 + DT^3 + ET^4 \quad \textbf{(3.2.19)}$$

being *A*, *B*, *C*, *D* and *E* constants that present specific values for each gas (taken from Ref. [16]).

The convective wall-fluid heat transfer coefficient was calculated using Leva's correlation [18]:

$$h = 0.813\left(\frac{\lambda_f}{2R_0}\right)\left(\frac{d_p\rho_f u_s}{\mu_f}\right)^{0.9} e^{-6d_p/(2R_0)} \quad \textbf{(3.2.20)}$$

λ_f was calculated using the Wassiljewa method [13]:

$$\lambda_f = \sum_{i=1}^{n} \frac{y_i\lambda_i}{\sum_{j=1}^{n} y_j A_{ij}} \quad \textbf{(3.2.21)}$$

where λ_i is the thermal conductivity of species i and was obtained through the correlation proposed by Eucken [13]:

$$\lambda_i = \mu_i\left(1.25\frac{R}{M_i} + \frac{C_{p,i}}{M_i}\right) \quad \textbf{(3.2.22)}$$

The parameter A_{ij} was obtained by the method of Lindsay and Bromley [14]:

$$A_{ij} = \frac{1}{4}\left\{1 + \left[\frac{\mu_i}{\mu_j}\left(\frac{M_j}{M_i}\right)^{3/4}\left(\frac{T+s_i}{T+s_j}\right)\right]^{1/2}\right\}^2\left(\frac{T+s_{ij}}{T+s_i}\right) \quad \textbf{(3.2.23)}$$

where s_{ij} is obtained from Eq. (3.2.24):

$$s_{ij} = F\sqrt{s_i s_j} \quad \textbf{(3.2.24)}$$

where F is a constant that takes the value of 1 except when either of both components i and j are very polar ($F = 0.73$). $s_{i,j}$ is a component temperature based parameter that takes the value of 79 K for H_2 and is expressed by Eq. (3.2.25) for the other components:

$$s_{i,j} = 1.5T_{bi,j} \quad \textbf{(3.2.25)}$$

being that $T_{bi,j}$ is the normal boiling temperature of component i or j (taken from Refs. [19, 20]).

3.2.2.2 Kinetics

An extensive literature review on GSR kinetics has been done. Most of the found kinetics are of the power-law type [3, 4, 6, 21-25] and refer to the glycerol consumption rather than to each of the reactions that normally take part in the GSR process (glycerol thermal decomposition, water-gas shift and methanation of carbon monoxide) or to each of the products that are formed (H_2, CO_2, CO and CH_4). More complex kinetics that take into consideration adsorption constants for glycerol and steam (of the Langmuir-Hinshelwood type) or several kinetic constants corresponding to several elementary steps of the GSR process were found as well [3, 10, 23]. However, and once again, they refer only to glycerol consumption. Therefore, in order to describe the GSR process, the power-law-type kinetics (Eq. (3.2.26)) proposed by Cheng *et al.* [10] for a Co-Ni/Al_2O_3 catalyst with estimated parameters not only for the consumption of glycerol but also for the generation of H_2, CO_2, CO and CH_4 was used:

$$R_i = (\nu_i) A e^{-E_a/RT} p_{C_3H_8O_3}^{\beta} p_{H_2O}^{\gamma} A_{metal\ surface} \quad \textbf{(3.2.26)}$$

being that ν_i takes the values of ±1, depending on if species i is being consumed (-1) or produced (+1). A is the pre-exponential factor, E_a stands for the activation energy, β and γ are the partial reaction orders for glycerol and steam, respectively, and $A_{metal\ surface}$ is the catalyst's metal surface area. The values for the kinetic parameters estimated by Cheng *et al.* [10] are presented in Table 3.2.1.

Table 3.2.1 - Kinetic parameters for the species consumption/formation [10].

Species	A **/ mol·m^{-2}·s^{-1}·kPa$^{-(\beta+\gamma)}$**	E_a **/ kJ·mol^{-1}**	β	γ
$C_3H_8O_3$	0.036	63.30	0.253	0.358
H_2	0.468	67.28	0.253	0.274
CO_2	0.074	64.06	0.281	0.403
CO	0.062	61.73	0.308	-0.065
CH_4	0.555	100.90	0.601	0.393

The metal surface area of the catalyst is 740 $\mathrm{m}^2 \cdot \mathrm{kg}_{\mathrm{cat}}{}^{-1}$. Since no kinetic parameters were presented for steam, its kinetics was estimated so that the error associated to the mass balance is very small (≤ 3%).

3.2.2.3 Numerical solution

The set of ordinary differential and algebraic equations previously described was solved using the bvp4c function of MATLAB software, a finite difference code which implements the three-stage Lobatto IIIa formula. The solutions were obtained at 200 equally spaced points along the column length and a value of 10^{-5} was considered for both absolute and relative tolerances.

3.2.3 Results and discussion

3.2.3.1 Reaction metrics

The reactor performance was evaluated in terms of glycerol conversion (Eq. (3.2.27)), products yields (Eq. (3.2.28)) and selectivities (Eq. (3.2.29)):

$$X_G = \frac{F_{C_3H_8O_3,in} - F_{C_3H_8O_3,out}}{F_{C_3H_8O_3,in}} \times 100 \quad \textbf{(3.2.27)}$$

$$Y_i = \frac{F_{i,out}}{F_{C_3H_8O_3,in} - F_{C_3H_8O_3,out}} \quad \textbf{(3.2.28)}$$

$$S_i = \frac{F_{i,out}}{F_{H_2,out} + F_{CO_2,out} + F_{CO,out} + F_{CH_4,out}} \times 100 \quad \textbf{(3.2.29)}$$

where F_i is the molar flux of species i; in stands for the reactor inlet while out stands for the reactor outlet. The experimental conversions obtained by Cheng *et al.* [10] were calculated based on the conversion into gaseous products. On the other hand, no further kinetics besides those shown in Table 3.2.1 were used. Therefore, neither liquid nor solid - e.g. coke - products formation is considered herein. Even though other definitions of selectivity are often used in the literature, the one of Eq. (3.2.29) is here adopted in order to match the one used by Cheng *et al.* [10]. It should be stressed that, according to this definition, even when no by-products are formed, CO_2 is always produced along with H_2. Thus, the maximum selectivities for the desired products are 70% and 30% for H_2 and CO_2, respectively.

3.2.3.2 Model validation

Before being used to perform a parametric analysis, the model must be validated so that we are sure that its outputs in terms of glycerol conversion and

products yields and selectivities are trustable. In Fig. 3.2.1 it is presented the comparison between the model predictions and the experimental results obtained by Cheng *et al.* [10] (results shown refer to different operating conditions, in the ranges 773-823 K, WGFRs between 3.4-11.9 and atmospheric pressure) for (a) the conversion of glycerol, (b) yields and (c) selectivities towards the different species.

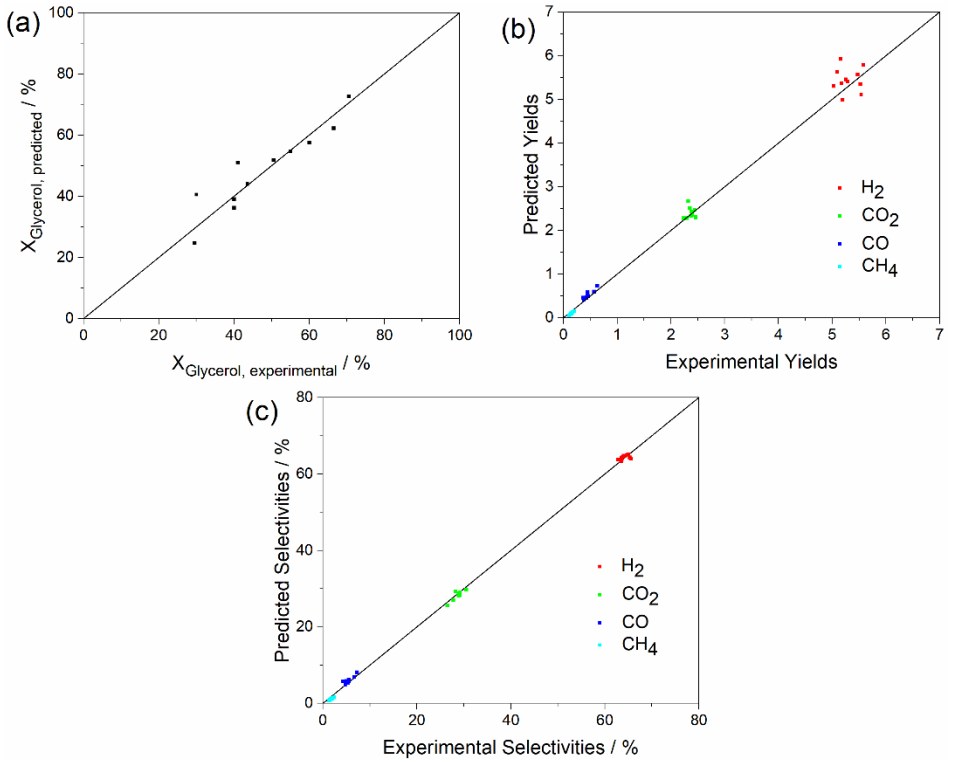

Fig. 3.2.1 - Parity plots for (a) glycerol conversion, (b) products yields and (c) selectivities for temperatures between 773 and 823 K, WGFRs between 3.4 and 11.9 and atmospheric pressure. Experimental yields and selectivities taken from Ref. [10], while conversion values were kindly provided by Doctor Chin Kui Cheng.

The parity plots show that there is in fact very good agreement between the model predictions and the experimental results, particularly for selectivites. It is also worth to notice that relatively high H_2 (and also CO_2 yields) were reached, although below the maximum theoretical value of 7 (cf. Eq. (3.2.1)).

Moreover, very low CO and CH_4 yields and selectivites are observed, which are desirable.

3.2.3.3 Profiles along the reactor bed

For the parametric study, a packed bed reactor with the characteristics presented in Table 3.2.2 was used (most of them similar to those used elsewhere [10]).

Table 3.2.2 - Parameters used during the simulations.

Parameter	Value	Units
L	0.12	m
R_0	5×10^{-3}	m
d_p	1.40×10^{-4}	m
W_{cat}	5×10^{-4}	kg
Gas hourly space velocity	9000	$L_N \cdot (kg_{cat} h)^{-1}$
$y_{C_3H_8O_{3,in}}$ [a]	0.05	
$y_{H_2O,in}$ [a]	0.15-0.60	

[a] Balanced with Argon.

Before going into the parametric analysis, it is important to understand how the species molar fractions and temperature vary along the packed bed length. For this the profiles obtained at 798 K, WGFR of 9 and 1 atm are presented in Fig. 3.2.2.

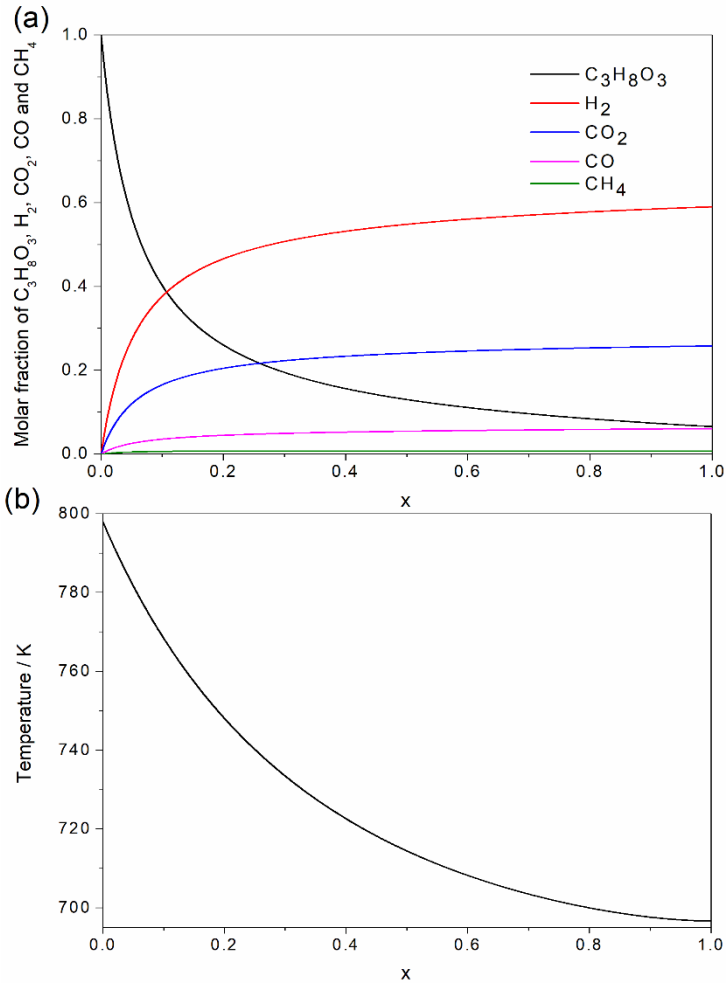

Fig. 3.2.2 - Simulated profiles of (a) molar fractions of $C_3H_8O_3$, H_2, CO_2, CO and CH_4 (dry basis and without carrier gas) and (b) temperature along the dimensionless length of the reactor bed at 798 K, WGFR of 9 and 1 atm.

Regarding the concentration profiles in Fig. 3.2.2 (a), it can be observed the existence of 2 distinct regions. In the first 10-15% of the reactor a rapid decrease of the glycerol concentration as well as a fast enhancement of the concentrations of particularly H_2 and CO_2 are observed. This happens because of the initial high glycerol and steam partial pressures and high temperature that result in a fast GSR kinetics. In the second region the concentrations of glycerol, H_2 and CO_2 vary much more slowly and start stabilizing due to the much smaller

partial pressures of glycerol and steam and the already diminished temperature. For CO and CH_4 this effect is much smaller since both present very small concentrations, especially CH_4 due to the low methanation selectivity of the Co-Ni/Al_2O_3 catalyst.

In terms of temperature profile, it can be seen that its shape is very similar to that normally observed in adiabatic reactors [18, 26]. However, the model here described takes into consideration the existence of heat transfer from the reactor wall (considered to be at the same temperature as the oven which on its side is considered to be equal to the inlet temperature) to the reaction mixture, which is at a lower temperature than the wall due to the endothermicity of the GSR reaction. Therefore, a non-adiabatic profile would be expectable. Nevertheless, it has been observed that the wall-fluid heat transfer coefficient obtained from Eq. (3.2.20) is very small and so heat transfer from the reactor wall to the reaction mixture only occurs up to a very limited extent.

Regarding total pressure, it presented a linear decrease along the bed length, as expected, being that an average pressure drop of approximately 12 kPa (~12%) was obtained.

3.2.3.4 Parametric analysis

In order to understand how the performance of a catalytic packed bed reactor for GSR can be enhanced, the effect of several operating conditions like temperature, WGFR and pressure was analyzed. In the parametric analysis, the ranges considered for temperature and partial pressures of the reactants in the reactor feed were slightly increased as compared to those used in the model validation. It was verified for all the range of simulated conditions that the glycerol conversion in the thermodynamic equilibrium (calculated with Aspen Plus software) was always higher or equal to the actual conversion obtained with the phenomenological model.

The first parameters to be target of analysis were temperature (748-848 K) and WGFR (3-12). The effect of both variables on the conversion of glycerol is presented in Fig. 3.2.3.

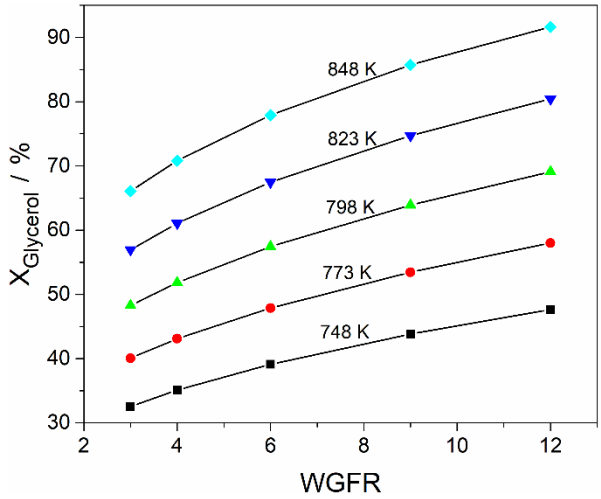

Fig. 3.2.3 - Effect of both temperature and WGFR on the conversion of glycerol at 1 atm.

Regarding temperature, it is clear that its increase at constant WGFR benefits the conversion of glycerol. This happens due to the enhancement of the reaction kinetics according to Eq. (3.2.26). It has also been verified that the increment in terms of glycerol conversion caused by the increase of temperature increases as the WGFR becomes higher, achieving a maximum absolute increment of approximately 44% when the temperature is increased from 748 K up to 848 K at WGFR of 12. Regarding the WGFR, its increase at constant temperature also results in an enhancement of the glycerol conversion. This happens because by increasing the amount of steam in the reaction mixture the glycerol consumption kinetics is enhanced since $\gamma > 0$ in Eq. (3.2.26). Also, it has been observed that the increment in terms of glycerol conversion caused by the increase of the amount of steam at constant temperature slightly increases as the WGFR gets close to 9. On the other hand, when it is varied from 9 to 12, this increment decreases slightly. This happens because the reaction rate

becomes approximately zero-order for water due to its excessive amount in the reaction media.

In terms of the products, their generation was evaluated in terms of yield and selectivity. The effect of both temperature and WGFR on the yields of H_2, CO_2, CO and CH_4 is presented in Fig. 3.2.4.

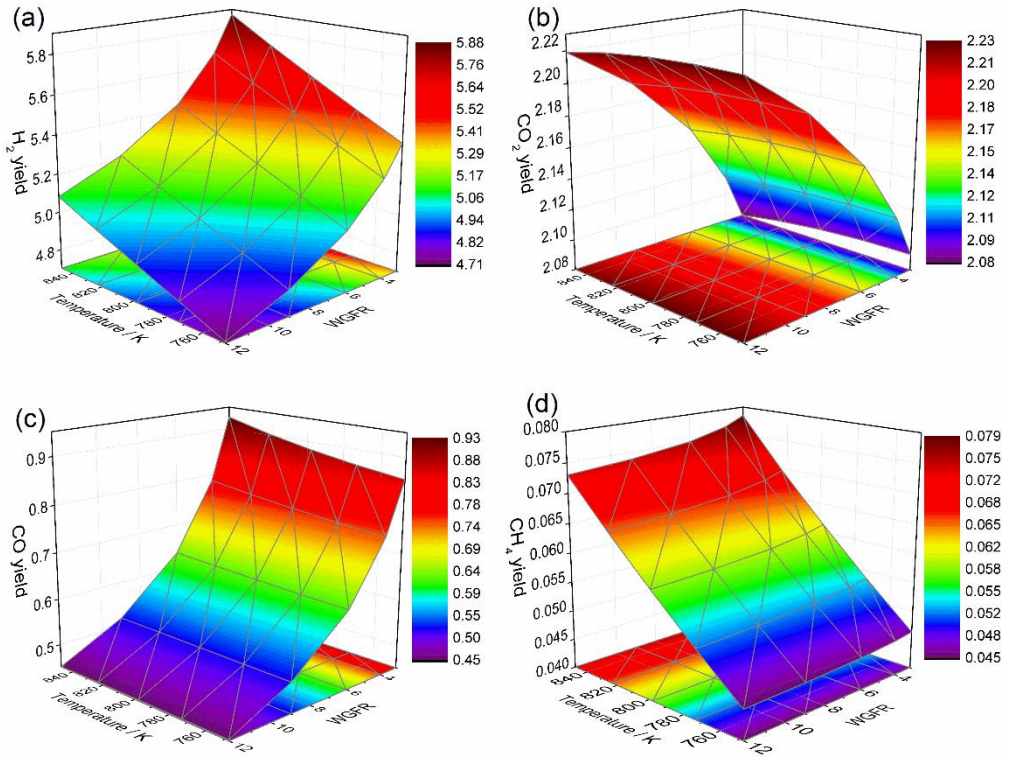

Fig. 3.2.4 - Effect of both temperature and WGFR on the yield of (a) H_2, (b) CO_2, (c) CO and (d) CH_4 at 1 atm.

By analyzing Fig. 3.2.4 (a) it can be seen that the yield of H_2 is positively influenced by the increase of temperature at constant WGFR. This happens because of the highly accelerated kinetics of H_2 formation at higher temperatures, according to Eq. (3.2.26). In other words, when the temperature is increased from 748 K up to 848 K, the rate of formation of H_2 increases more than the rate of consumption of glycerol and so higher H_2 yields are observed.

This is exclusively related to the difference between the values of activation energy presented in Table 3.2.1 for glycerol and H_2. Regarding the WGFR, its increase leads to a decrease of the H_2 yield. This means that when the steam content in the reaction mixture is increased the formation rate of H_2 increases less than the consumption rate of glycerol. This happens because the partial order of steam for the consumption of glycerol is higher than that for the production of H_2, as can be seen in Table 3.2.1. Regarding CO_2, it is observed that temperature has almost no effect on its yield. This is most probably due to the very close activation energy values presented in Table 3.2.1 for glycerol and CO_2. In terms of WGFR, a much more pronounced effect is observed as increasing WGFRs lead to the enhancement of the CO_2 yield. This is explained by the higher partial order of steam for the rate of CO_2 formation (0.403) than for the rate of glycerol consumption (0.358).

Concerning CO, Fig. 3.2.4 (c) shows that temperature has almost no effect on its yield at higher WGFRs. This is due to the very close activation energies of glycerol consumption and CO formation. However, at lower WGFRs a more pronounced effect of temperature is observed, being that the yield of CO increases with temperature, contrarily to what was expected based on the slightly lower activation energy of CO. In fact it was noticed that the decrease of both glycerol and steam partial pressures along the packed bed have a decisive role here. For a WGFR of 3, it was observed that the individual effect of increasing the inlet temperature from 748 K up to 848 K (assuming constant the glycerol and water partial pressures, and equal to the feed ones) led to an enhancement of the instantaneous CO yield (assessed based on reaction rates) of only 3%. On the other hand, when the individual effect of the reactants pressures decrease along the reactor bed for 748 K and 848K (Appendix B, Fig. B.1) was evaluated (assuming constant temperature, and equal to the feed one), an increase of the instantaneous CO yield from the inlet to the outlet reactor conditions of 53% and 22% was observed at 848 K and 748 K, respectively. This

happens because at 848 K the decrease of both glycerol and steam pressures is more pronounced, being that steam has an even more important role than glycerol here since its partial order for both glycerol and CO kinetics are very different (Table 3.2.1). The difference in terms of instantaneous CO yield enhancement is responsible for its overall increase when temperature is raised from 748 K up to 848 K (Fig. 3.2.4 (c)). Moreover, at a WGFR of 12 the same evaluation (Appendix B, Fig. B.1) led to a much smaller difference between 748 K and 848 K in terms of instantaneous CO yield enhancement along the reactor (7.9% and 8.7% at 848 K and 748 K, respectively). This much smaller difference is due to the much higher glycerol partial pressure relative reduction along the bed comparatively to the steam partial pressure reduction, which leads to a more emphasized negative effect of glycerol partial pressure decrease and a less important positive effect of steam partial pressure decline on the CO kinetics. Consequently there is almost no variation of the CO yield with temperature at WGFR of 12 (Fig. 3.2.4 (c)). Regarding the effect of the WGFR, it is clear that the decrease of the CO yield caused by the increase of the steam content shown in Fig. 3.2.4 (c) is related to the negative partial order of steam for the rate of CO formation.

Finally, in terms of CH_4 yield, the increase of temperature led to its big enhancement, as can be seen in Fig. 3.2.4 (d). This is due to the much higher activation energy for CH_4 formation. As for the WGFR, it presented almost no effect on the CH_4 yield (variation of 0.005 at 848 K), because γ is very similar for methane and glycerol.

The effect of both temperature and WGFR on the products selectivities was analyzed as well and is presented in Fig. 3.2.5 (a) and (b), respectively. As can be seen in Fig. 3.2.5 (a), while both H_2 and CH_4 selectivities increase with temperature, the selectivities of CO_2 and CO decrease. This is related to the respective activation energies for the rate of formation of each component, being that H_2 and CH_4 present higher activation energies than CO_2 and CO.

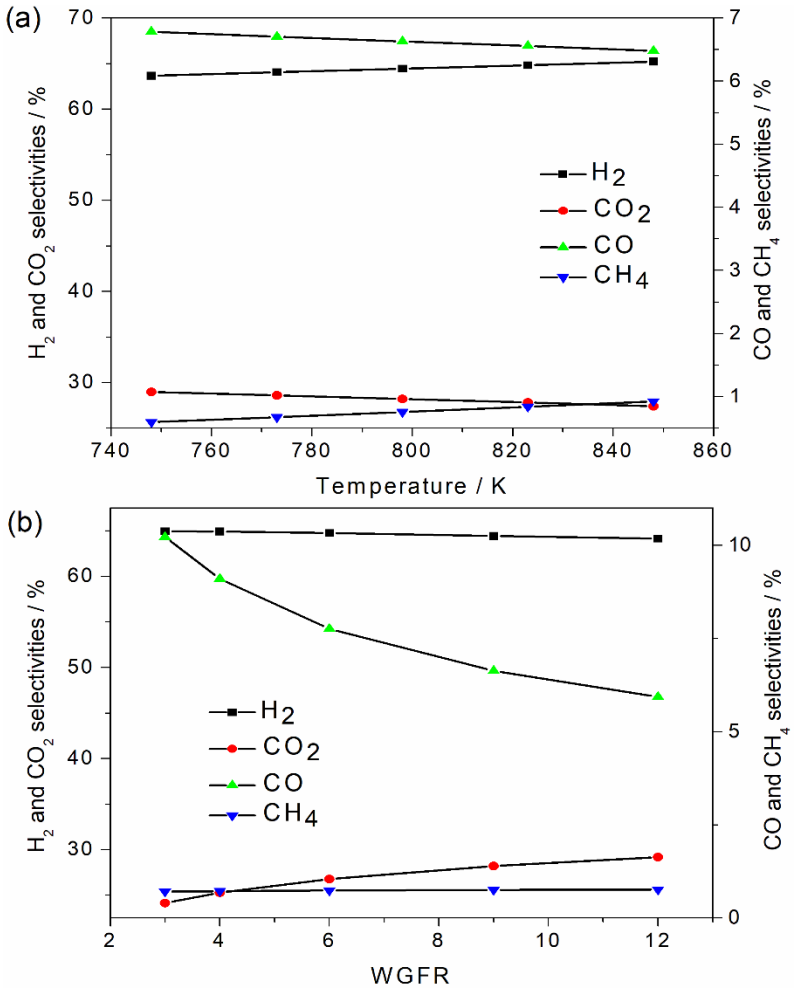

Fig. 3.2.5 - Effect of (a) temperature (WGFR = 9 and 1 atm) and (b) WGFR (798 K and 1 atm) on the selectivities of H_2, CO_2, CO and CH_4.

Also, since the activation energy for CH_4 formation is much higher than that for H_2, its selectivity suffers a much more pronounced relative increase (55%), while H_2 selectivity only suffers a slight relative increase (2.4%). On the other hand, since the activation energies for CO and CO_2 are very similar, both suffer very similar variations. Regarding the effect of WGFR (Fig. 3.2.5 (b)), while both CO_2 and CH_4 selectivities increase with the steam content, the selectivities of H_2 and CO show the opposite trend. This is due to the higher steam partial orders for the formation of both CO_2 and CH_4 or, for the case of CO, due to the negative

steam partial order, which results in a highly pronounced relative decrease of the CO selectivity (42%). On the other hand, the selectivity of H_2 only suffers a relative decrease of 1.2%. Also, since the steam partial order for CO_2 formation is higher than that for CH_4 formation, its selectivity enhancement caused by the increase of the steam content is also higher (21% and 8%, respectively). It is finally worth highlighting the completely different selectivities, with average values of 64.6% for H_2, 26.7% for CO_2, and far lower for CO (7.9%) and particularly CH_4 (0.8%), which were obtained.

By analyzing Fig. 3.2.6 it is possible to conclude that one benefits from the use of higher temperatures and WGFRs when intending to achieve higher H_2 production ($F_{H_2,out}/F_{Glycerol,in}$), being that at atmospheric pressure a maximum H_2 production of 4.66 $mol \cdot mol_{fed\ glycerol}^{-1}$ to the reactor was observed at 848 K and WGFR of 12.

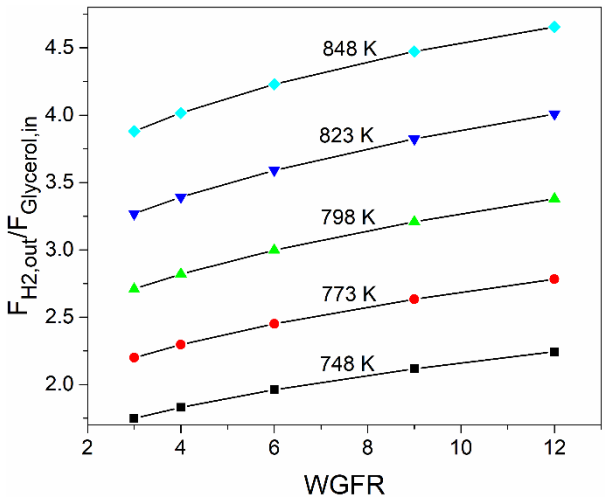

Fig. 3.2.6 - Effect of both temperature and WGFR on the amount of hydrogen produced per glycerol fed to the reactor at 1 atm.

The last parameter to be analyzed was the operating pressure. The effect of varying the operating pressure between 1 and 5 atm on the glycerol conversion at different temperatures and WGFR of 9 is presented in Fig. 3.2.7.

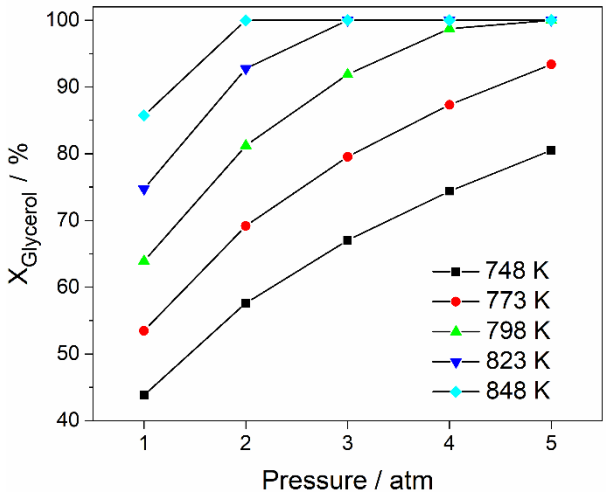

Fig. 3.2.7 - Effect of pressure on the conversion of glycerol at different temperatures and WGFR of 9.

It is possible to observe that higher pressures enhance the conversion of glycerol. This is explained by the positive values of the partial orders of glycerol and steam in its consumption rate (β and γ are both > 0). Moreover, even though increasing pressures have a more pronounced effect on glycerol conversion at lower temperatures (748-773 K), only at higher temperatures the glycerol conversion gets close and even reaches 100%. At 848 K, a pressure of 2 atm was observed to be already enough to allow glycerol to be completely converted.

A similar analysis was done for the products yields. Such effects are presented in Fig. 3.2.8. It can be seen in Fig. 3.2.8 (a) that as the pressure increases, at constant temperature, the yield of H_2 becomes lower. This happens because the same increase of pressure increases the glycerol consumption rate more than it increases the H_2 production rate, according to the respective partial orders presented in Table 3.2.1. Also, at higher temperatures such negative effect of the total pressure on hydrogen yield is less pronounced. It has also been observed that the initial temperature decrease along the reactor is more pronounced with increasing total pressure/glycerol conversions (Appendix B, Fig. B.2). However, after conversion of glycerol has reached completion, this

variation stops, as shown in Fig. B.2 (a) (Appendix B), leading to a higher average temperature in the reactor. This benefits slightly more the H_2 than the glycerol kinetics due to the higher H_2 formation activation energy, and that is why the H_2 yield does not decrease so much at higher temperatures. At lower temperatures this is not important because glycerol conversion never reaches completion, and so average reactor temperature is smaller for higher pressures (Appendix B, Fig. B.2 (b)).

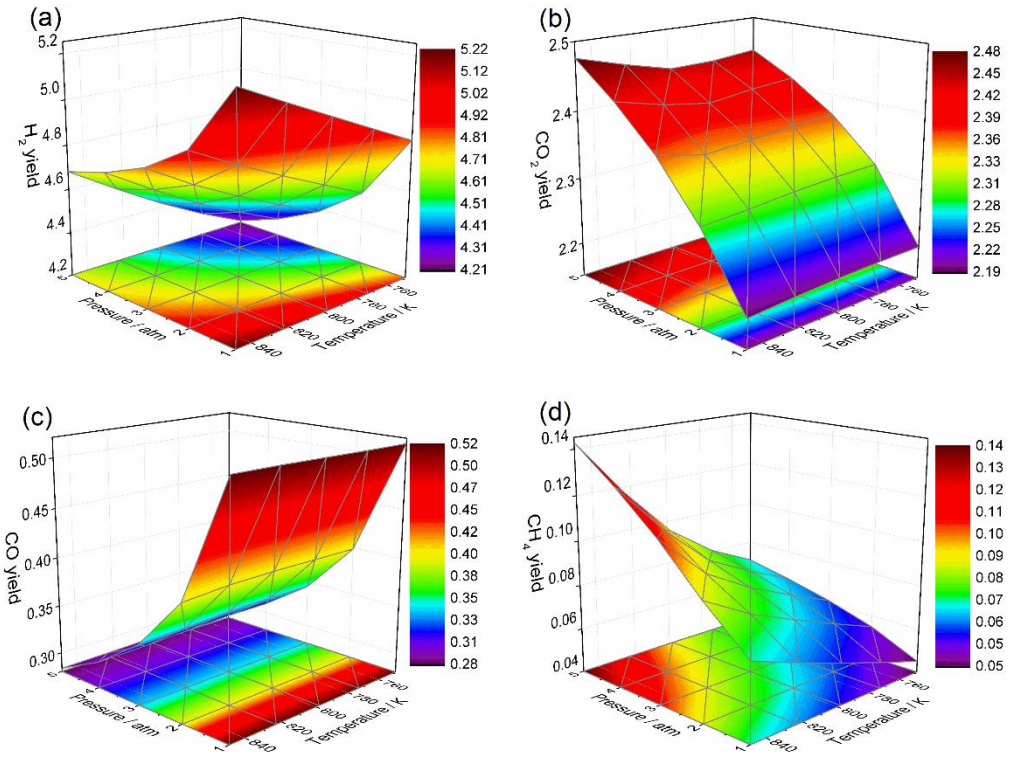

Fig. 3.2.8 - Effect of pressure on the yield of H_2 at different temperatures and WGFR of 9.

Regarding CO_2, higher pressures enhance its yield because of the higher glycerol and steam partial orders of CO_2 formation compared to glycerol kinetics. Also, it must be remarked that even though an apparent increase of the CO_2 yield with temperature at 5 atm is observed, it is almost negligible - < 0.03. As for CO, its yield is decreased when higher pressures are employed, as can be

seen in Fig. 3.2.8 (c), due to the negative partial order of steam for CO kinetics. Regarding CH_4, higher pressures exercise a positive effect on its yield, especially at higher temperatures. This once again occurs because of the higher partial orders of CH_4 formation compared to those of glycerol consumption. Also, the methane kinetics benefits much more than glycerol kinetics from the already mentioned progressively lower decrease of temperature in the reactor after the glycerol conversion is complete (higher temperatures and pressures) (Appendix B, Fig. B.2), due to its much higher activation energy. Therefore, CH_4 yield presents a considerably higher increase with pressure at higher temperatures.

A similar analysis was also done for the products selectivities as well, being that their variation with pressure at 798 K and WGFR of 9 is presented in Fig. 3.2.9.

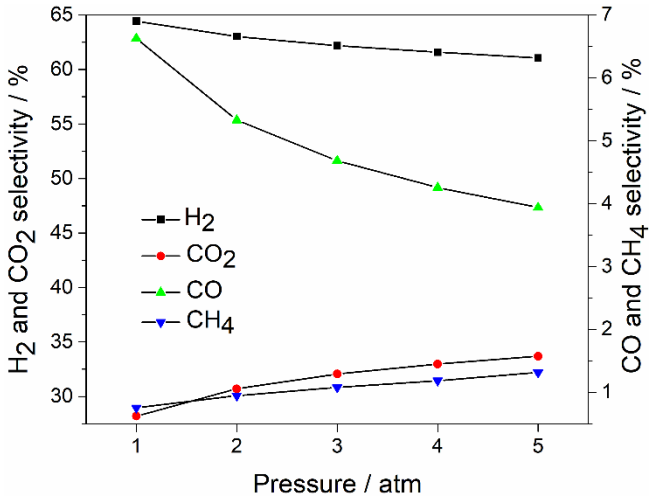

Fig. 3.2.9 - Effect of pressure on the selectivities of H_2, CO_2, CO and CH_4 at 798 K and WGFR of 9.

Regarding H_2 and CO, their selectivities decrease when higher pressures are employed due to their lower partial orders with respect to glycerol and steam compared to those for CO_2 and CH_4 (Table 3.2.1); this is particularly evident for CO due to its negative partial order for steam. Also, CH_4 selectivity increases much more than CO_2 selectivity due to its much higher glycerol partial order.

Finally, in terms of H_2 production, it can be seen in Fig. 3.2.10 that pressure positively affects the amount of hydrogen produced per glycerol fed to the reactor up to a certain point, being that afterwards it has a negative impact (mainly at higher temperatures). This happens since after glycerol conversion reaches 100% (Fig. 3.2.7), the selectivity towards H_2 production keeps decreasing. Ultimately, a maximum H_2 production of 4.93 $\mathrm{mol} \cdot \mathrm{mol}_{\mathrm{fed\ glycerol}}^{-1}$ was observed at 848 K, WGFR of 9 and 2 atm. In a recent work, Ebshish *et al.* [27] used response surface methodology to optimize process conditions through a non-phenomenological statistical approach (multiple regression analysis). In such study the ranges of conditions employed were similar to those reported by us. Ebshish *et al.* [27] have got to maximum experimental conversion of glycerol and H_2 production of 75% and 4.03 $\mathrm{mol} \cdot \mathrm{mol}_{\mathrm{fed\ glycerol}}^{-1}$, respectively, at 873 K, WGFR of 12 and atmospheric pressure while using a Ni/Al_2O_3 catalyst.

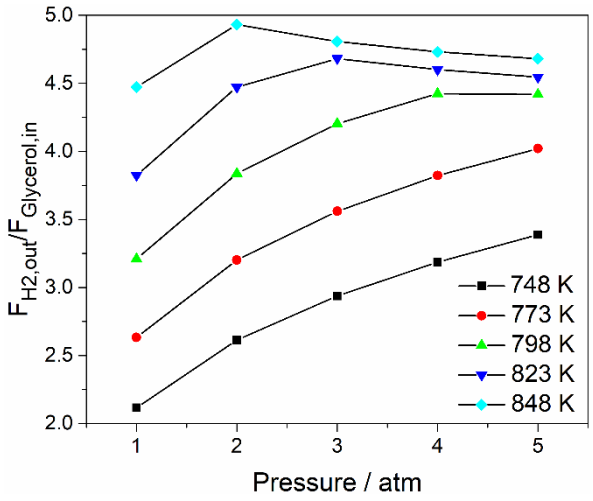

Fig. 3.2.10 - Effect of pressure on the amount of hydrogen produced per glycerol fed to the reactor at different temperatures and WGFR of 9.

3.2.4 Conclusions

The developed phenomenological model that describes the GSR reaction in a packed bed reactor, developed for the first time for predicting both glycerol consumption and products/by-products formation, presented quite good adherence with the experimental results. A parametric analysis was also performed, being that it was ultimately concluded that higher temperatures, higher WGFRs and higher pressures are more advantageous in terms of glycerol conversion and H_2 production ($\mathrm{mol} \cdot \mathrm{mol}_{\mathrm{fed\ glycerol}}^{-1}$). Even though higher WGFRs and pressures lead to lower H_2 yields and selectivities, its absolute production (produced flow rate) is increased until the total glycerol conversion reaches completion. After that, subsequent increments of these variables will decrease the absolute H_2 production due to their less positive effect on the H_2 kinetics compared to the other kinetics (except CO). Therefore, maximum H_2 production of 4.93 $\mathrm{mol} \cdot \mathrm{mol}_{\mathrm{fed\ glycerol}}^{-1}$ was observed at 848 K, WGFR of 9 and 2 atm. It is nonetheless necessary to remark that higher temperatures, WGFRs and pressures mean higher operation costs and so, alternatives that would allow the use of milder conditions without losing process efficiency, like membrane reactors or sorption-enhanced reactors, would be most welcome.

Notation and Glossary

A	Kinetics pre-exponential factor	$\mathrm{mol} \cdot \left(\mathrm{m}^2 \cdot \mathrm{s} \cdot \mathrm{kPa}^{(\beta+\gamma)}\right)^{-1}$
A_{ij}	Dimensionless parameter for the mixture of i and j	
$A_{metal\ surface}$	Metal surface area of the catalyst	$\mathrm{m}^2 \cdot \mathrm{kg}_{\mathrm{cat}}{}^{-1}$
C	Total concentration of species	$\mathrm{mol} \cdot \mathrm{m}^{-3}$
C_i	Molar concentration of compound i	$\mathrm{mol} \cdot \mathrm{m}^{-3}$

$C_{p,i}$	Molar heat capacity of species i	$\mathrm{J \cdot (mol \cdot K)^{-1}}$
$C_{p,f}$	Mass heat capacity of gas mixture	$\mathrm{J \cdot (kg \cdot K)^{-1}}$
C_1	Sutherland constant	$\mathrm{kg \cdot (m \cdot s \cdot K^{0.5})^{-1}}$
D_{ax}	Mass axial dispersion coefficient	$\mathrm{m^2 \cdot s^{-1}}$
$D_{C_3H_8O_3,j}$	Binary diffusivity of $C_3H_8O_3$ when diffusing into species j	$\mathrm{m^2 \cdot s^{-1}}$
$D_{C_3H_8O_3,mix}$	Molecular diffusivity of $C_3H_8O_3$ in the reaction mixture	$\mathrm{m^2 \cdot s^{-1}}$
d_p	Catalyst particles diameter	m
E_a	Activation energy	$\mathrm{J \cdot mol^{-1}}$
F	Dimensionless parameter	
F_i	Molar flux of species i	$\mathrm{mol \cdot (m^2 \cdot s)^{-1}}$
g	Dimensionless parameter of steam kinetics	
h	Convective wall-fluid heat transfer coefficient	$\mathrm{W \cdot (m^2 \cdot K)^{-1}}$
L	Reactor length	m
M_i	Molar mass of species i	$\mathrm{mol \cdot kg^{-1}}$
P	Reactor total pressure	Pa
p_i	Partial pressure of component $i = C_3H_8O_3$ and H_2O	kPa
R	Ideal gas constant	$\mathrm{J \cdot (K \cdot mol)^{-1}}$
R_i	Consumption/formation rate of component i	$\mathrm{mol \cdot (kg_{cat} \cdot s)^{-1}}$
R_0	Reactor inner radius	m
S	Sutherland temperature	K
S_i	Selectivity of species i	

s_i	Temperature based parameter for component i	K
T	Bed absolute temperature	K
T_{bi}	Normal boiling point of species i	K
$T_{i,0}$	Reference temperature for species i in Sutherland's equation	K
T_w	Reactor wall absolute temperature	K
u_s	Superficial velocity of the gas mixture	$\mathrm{m} \cdot s^{-1}$
V_R	Volume of the reactor bed	m^3
W_{cat}	Mass of catalyst in the reactor bed	$\mathrm{kg_{cat}}$
x	Dimensionless axial coordinate	
X_G	Conversion of $C_3H_8O_3$	
Y_i	Yield of species i	
y_i	Molar fraction of species i	

Greek letters

β	Partial reaction order for $C_3H_8O_3$	
$\Delta H_{f,i}$	Heat of formation of species i	$\mathrm{J} \cdot \mathrm{mol}^{-1}$
ε_b	Void fraction of the catalyst bed	$\mathrm{m}^3_{\mathrm{void}} \cdot \mathrm{m}^{-3}_{\mathrm{bed}}$
ϕ_{ij}	Dimensionless parameter for the mixture of i and j	
γ	Partial reaction order for H_2O	
λ_{ax}	Heat axial dispersion coefficient	$W \cdot (m\ K)^{-1}$
λ_i	Thermal conductivity of species i	$W \cdot (m\ K)^{-1}$
λ_f	Thermal conductivity for the gas mixture	$W \cdot (m\ K)^{-1}$

ρ_f	Gas mixture density	$kg \cdot m^{-3}$
μ_i	Viscosity of species i	$Pa\ s$
μ_f	Gas mixture viscosity	$Pa\ s$
v	Atomic diffusion volume	
ν_i	Unitary constant that indicates if i is consumed or produced	

List of acronyms

GSR	Glycerol Steam Reforming
WGFR	Molar Water/Glycerol Feed Ratio

3.2.5 References

[1] Silva, J.M., M.A. Soria, and L.M. Madeira, *Thermodynamic analysis of Glycerol Steam Reforming for hydrogen production with in situ hydrogen and carbon dioxide separation.* Journal of Power Sources, 2015, 273, 423-430.

[2] Dieuzeide, M.L. and N. Amadeo, *Thermodynamic analysis of Glycerol steam reforming.* Chemical Engineering and Technology, 2010, 33(1), 89-96.

[3] Sundari, R. and P.D. Vaidya, *Reaction Kinetics of Glycerol Steam Reforming Using a Ru/Al2O3 Catalyst.* Energy & Fuels, 2012, 26(7), 4195-4204.

[4] Pant, K.K., R. Jain, and S. Jain, *Renewable hydrogen production by steam reforming of glycerol over Ni/CeO2 catalyst prepared by precipitation deposition method.* Korean Journal of Chemical Engineering, 2011, 28(9), 1859-1866.

[5] Silva, J.M., M.A. Soria, and L.M. Madeira, *Challenges and strategies for optimization of glycerol steam reforming process.* Renewable and Sustainable Energy Reviews, 2015, 42, 1187-1213.

[6] Adhikari, S., S.D. Fernando, and A. Haryanto, *Kinetics and Reactor Modeling of Hydrogen Production from Glycerol via Steam Reforming Process over Ni/CeO2 Catalysts.* Chemical Engineering & Technology, 2009, 32(4), 541-547.

[7] Caglar, O.Y., C.D. Demirhan, and A.K. Avci, *Modeling and design of a microchannel reformer for efficient conversion of glycerol to hydrogen.* International Journal of Hydrogen Energy, 2015, 40(24), 7579-7585.

[8] Bakhtiari, M., M.A. Zahid, H. Ibrahim, A. Khan, P. Sengupta, and R. Idem, *Oxygenated hydrocarbons steam reforming over Ni/CeZrGdO2 catalyst: Kinetics and reactor modeling.* Chemical Engineering Science, 2015, 138, 363-374.

[9] Iliuta, I., H.R. Radfarnia, and M.C. Iliuta, *Hydrogen Production by Sorption-Enhanced Steam Glycerol Reforming: Sorption Kinetics and Reactor Simulation.* AIChE Journal, 2013, 59(6), 2105-2118.

[10] Cheng, C.K., S.Y. Foo, and A.A. Adesina, *Glycerol Steam Reforming over Bimetallic Co−Ni/Al2O3.* Industrial & Engineering Chemistry Research, 2010, 49(21), 10804-10817.

[11] Pushnov, A.S., *Calculation of average bed porosity.* Chemical and Petroleum Engineering, 2006, 42(1-2), 14-17.

[12] Edwards, M.F. and J.F. Richardson, *Gas dispersion in packed beds.* Chemical Engineering Science, 1968, 23(2), 109-123.

[13] B.E. Poling, J.M.P., J.P. O'Connell, *The Properties of Gases and Liquids.* 5 ed. 2001, New York: McGraw-Hill.

[14] Perry, R.H., Green, D.W. , *Perry's Chemical Engineer's Handbook.* 7 ed. 1999, New York: McGraw Hill.

[15] Wakao, N. and T. Funazkri, *Effect of fluid dispersion coefficients on particle-to-fluid mass transfer coefficients in packed beds: Correlation of sherwood numbers.* Chemical Engineering Science, 1978, 33(10), 1375-1384.

[16] Appendix C - *Physical Properties of Liquids and Gases*, in Ludwig's Applied Process Design for Chemical and Petrochemical Plants (Fourth Edition), A.K. Coker, Editor. 2010, Gulf Professional Publishing: Boston. p. 757-792.

[17] Sutherland, W., *The Viscosity of Gases and Molecular Force.* Phylosophical Magazine, 1893, 36, 507-531.

[18] Froment, B., De Wilde, *Chemical Reactor Analysis and Design.* 3 ed. 2011, New York: John Wiley & Sons.

[19] Smith, J.M., Van Ness, H.C., Abbott, M.M., *Introduction to Chemical Engineering Thermodynamics.* 7 ed. 2005, Singapore: McGraw-Hill.

[20] Rosaria, C., P.C. Della, R. Michele, and P. Mario, *Understanding the glycerol market.* European Journal of Lipid Science and Technology, 2014, 116(10), 1432-1439.

[21] Dave, C.D. and K.K. Pant, *Renewable hydrogen generation by steam reforming of glycerol over zirconia promoted ceria supported catalyst.* Renewable Energy, 2011, 36(11), 3195-3202.

[22] Wang, C., B. Dou, H. Chen, Y. Song, Y. Xu, X. Du, T. Luo, and C. Tan, *Hydrogen production from steam reforming of glycerol by Ni–Mg–Al based catalysts in a fixed-bed reactor.* Chemical Engineering Journal, 2013, 220(0), 133-142.

[23] Cheng, C.K., S.Y. Foo, and A.A. Adesina, *Steam reforming of glycerol over Ni/Al2O3 catalyst.* Catalysis Today, 2011, 178(1), 25-33.

[24] Cheng, C.K., S.Y. Foo, and A.A. Adesina, *H2-rich synthesis gas production over Co/Al2O3 catalyst via glycerol steam reforming.* Catalysis Communications, 2010, 12(4), 292-298.

[25] Sutar, P.N., P.D. Vaidya, and A.E. Rodrigues, *Glycerol-reforming kinetics using a Pt/C catalyst.* Chemical Engineering and Technology, 2010, 33(10), 1645-1649.

[26] Smith, J.M., *Chemical Engineering Kinetics.* 3 ed. 1981, Singapore: McGraw-Hill.

[27] Ebshish, A., Z. Yaakob, Y. Taufiq-Yap, and A. Bshish, *Investigation of the Process Conditions for Hydrogen Production by Steam Reforming of Glycerol over Ni/Al2O3 Catalyst Using Response Surface Methodology (RSM).* Materials, 2014, 7(3), 2257.

Chapter 4. Experimental Analysis of Modified Hydrotalcites During High Temperature CO_2 Sorption

This chapter presents the experimental analysis of several hydrotalcite-like materials during CO_2 sorption at high temperatures. In subchapter 4.1 several materials are studied under static conditions and the best one is selected. In subchapter 4.2 the performance of this material during breakthrough experiments is assessed.

4.1 High Temperature CO_2 Sorption over Modified Hydrotalcites

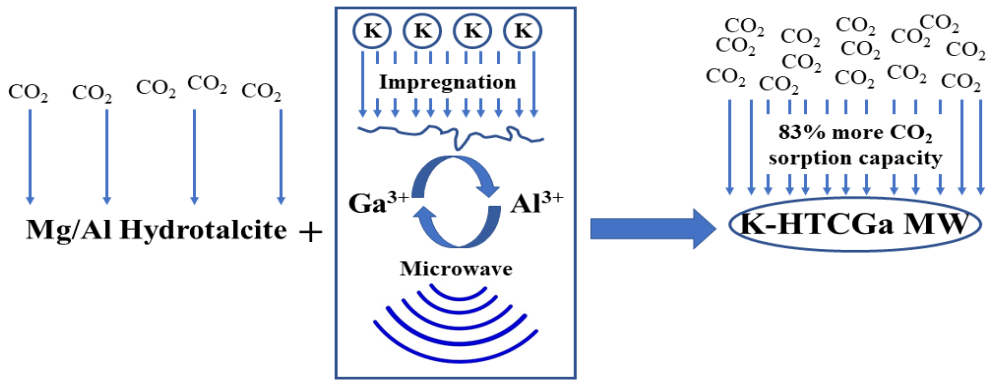

- *A K impregnated, Ga substituted microwave aged hydrotalcite was prepared.*
- *An astonishing CO_2 sorption capacity of 2.09 mol·kg^{-1} was achieved at 573 K.*
- *Two different kinetic contributions were identified during CO_2 uptakes.*

Hydrotalcite-like materials were prepared by the co-precipitation method, characterized by PXRD, FTIR, physical adsorption of N_2 at 77 K and SEM/EDS, and after calcination they were tested for CO_2 sorption at 573 K under dry conditions. The simultaneous effect of aluminum partial substitution with gallium, microwave aging of the precipitated gel and modification with potassium on their sorption capacity was assessed. Sorption isotherms were well described by the Freundlich model for all samples. A remarkable sorption capacity of 2.09 mol·kg^{-1} at 3.10 bar was obtained for the Ga-containing sample, aged under microwave irradiation and impregnated with 20 wt% of potassium. The sorption kinetics was analyzed from uptake measurements and two distinct contributions (related to fast and slow uptakes), which are considered by the proposed model, were observed. Despite the slower sorption kinetics on the potassium-modified samples, they showed sorption capacities considerably higher than those reported in the literature for commercial hydrotalcites under similar conditions, even for prolonged exposition to CO_2.

The contents of this chapter were adapted from: Silva, J.M., R. Trujillano, V. Rives, M.A. Soria, and L.M. Madeira, *High temperature CO2 sorption over modified hydrotalcites.* Chemical Engineering Journal, 2017, 325, 25-34.

4.1.1 Introduction

Increasing greenhouse gases (GHG) emissions are a major concern due to the changes that they are causing on our planet environment. Most of the countries are making a collective effort in order to implement measures that will hopefully, together with other initiatives, allow to keep the increase in global average temperature less than 2 ºC above pre-industrial levels. In fact, world governments have recently (December 2015) agreed at the Paris Climate Conference to aim to limit this increase to 1.5 ºC since it would considerably reduce the risks associated to impacts on climate change [1]. To achieve this target, release of carbon dioxide (one of the most emitted GHG) to the atmosphere should be sharply reduced. Moreover, and from an economical point of view, if recovered CO_2 can be used as feedstock for industrial production processes, the existing resource base would be broadened [2].

Regarding the pre-combustion capture of CO_2, several processes such as absorption, sorption, chemical looping combustion, membrane separation, hydrate based separation and cryogenic distillation, are possible [3]. Although absorption is the most widely used CO_2 separation technology due to its high efficiency and lower cost [3], it is not compatible with an intensified process where, for instance, both high temperature reaction (e.g., steam reforming, water-gas shift, etc.) and CO_2 separation occur simultaneously. However, capture of CO_2 through high temperature sorption on a solid material is highly compatible with such processes. In this regard, several materials such as CaO-based materials [4, 5], hydrotalcites [6, 7], lithium zirconates [8, 9] and lithium silicates [10, 11], among others, have been reported in the literature for high temperature CO_2 sorption. Among these materials, hydrotalcite-related materials have been observed to be the best option for temperatures between 573 and 773 K [6, 7, 12-14].

Hydrotalcite is a layered double hydroxide (LDH) which structure can be considered derived from that of brucite, $Mg(OH)_2$, and which general formula can be written as:

$$[M_{1-x}^{2+}M_x^{3+}(OH)_2]^{x+}\left[A_{x/n}^{n-}\cdot yH_2O\right]^{x-} \quad \textbf{(4.1.1)}$$

where M^{2+} and M^{3+} are divalent (e.g., Mg^{2+}, Ni^{2+}, Zn^{2+}, etc.) and trivalent (e.g., Al^{3+}, Ga^{3+}, Mn^{3+}, Y^{3+}, Fe^{3+}, etc.) metal cations within the brucite-like layers, A^{n-} is a charge compensating anion (e.g. CO_3^{2-}, Cl^-, SO_4^{2-}, etc.) located in the interlayer space and x is generally between 0.2 and 0.4 [15]. Regarding y, it represents the number of moles of water in the interlayer space. The mineral known as hydrotalcite possesses Mg^{2+}, Al^{3+} and CO_3^{2-} as divalent and trivalent cations and balancing anion, respectively. However, the properties of hydrotalcites can be tailored by combining adequate cations and anions [16, 17], by varying the M^{2+}/M^{3+} molar ratio (related to the value of x) [18], by modifying the hydrotalcite with alkaline metal cations (e.g. K^+, Cs^+, Na^+, etc.) [14, 19, 20], by changing the synthesis conditions such as pH [16, 21], aging process (e.g. conventional, microwave, ultrasonication, etc.) [6, 22], or calcination temperature [19, 23], among other parameters or conditions. Hydrotalcites have been reported to show good sorption capacity, stability and easy regeneration by temperature or pressure swing [14, 24-26]. Moreover, it is clear by now that the presence of steam, which is common in pre-combustion applications like sorption-enhanced steam reforming, highly benefits the sorption of CO_2 on these materials [14, 27, 28].

From the literature, it is concluded that potassium modified hydrotalcites showed the best performance among several alkali-modified hydrotalcites [13-14], and that partial substitution of aluminum with gallium [13, 26] also improved the performance for CO_2 sorption. On the other hand, the beneficial role of microwave treatment on the properties of hydrotalcites has been also reported [6, 22]. Taking into account these facts, a gallium substituted Mg-Al-hydrotalcite

aged under microwave irradiation and modified with potassium was evaluated in terms of CO_2 sorption capacity and compared to other formulations. In particular, the effects of the aluminum partial substitution with gallium, the microwave aging of the precipitated gel and the modification with potassium were separately assessed. Besides the physicochemical characterization of the synthetized materials, the sorption equilibrium isotherms at 573 K (typical temperature found in both pre- and post-combustion streams) were recorded. Finally, the sorption kinetics on the prepared materials was determined.

4.1.2 Experimental

4.1.2.1 Chemicals and gases

Aluminum nitrate 9-hydrate, magnesium nitrate 6-hydrate and gallium nitrate hydrate (Sigma Aldrich, highest purity degree available) were used as Al, Mg and Ga precursors, respectively. In order to assure that the charge compensating anion was carbonate and not nitrate, an excess of anhydrous sodium carbonate (Sigma Aldrich, highest purity degree available) was used. Sodium hydroxide (Sigma Aldrich, highest purity degree available) was used to maintain an alkaline pH during synthesis. Potassium carbonate (Sigma Aldrich, highest purity degree available) was used as chemical promoter to modify the prepared hydrotalcites. Carbon dioxide (99.99%), nitrogen (99.999%) and helium (99.999%) used were from L'Air Liquide.

4.1.2.2 Preparation of the materials

Two fresh base materials were prepared: $\mathrm{Mg_2Al(OH)_6(CO_3)_{0.5}\cdot}y\mathrm{H_2O}$ and $\mathrm{Mg_2(Al_{0.9}Ga_{0.1})(OH)_6(CO_3)_{0.5}\cdot}y\mathrm{H_2O}$, herein named as fHTC and fHTCGa,

respectively. For both materials, the Mg^{2+} / Al^{3+} and Mg^{2+} / $(Al^{3+} + Ga^{3+})$ molar ratios of 2 were used and an Al^{3+}/Ga^{3+} ratio of 9 was used to prepare sample fHTCGa. These ratios were chosen taking into account the results previously reported by Miguel *et al.* [13].

The materials were prepared via the co-precipitation method: a portion of 100 ml of a solution containing the salts of the divalent (1.93 M and 1.89 M for non-containing and containing gallium samples, respectively) and trivalent cations (0.97 M and 0.95 M for non-containing and containing gallium samples, respectively) was added drop-wise to a basic solution containing NaOH (1 M) and Na_2CO_3 (0.089 M). The final mixture was continuously stirred for approximately 20 h at room temperature. This allowed obtaining gels of the two aforementioned base materials. Then, half of the amount of fHTC and all fHTCGa suspensions were hydrothermally treated at 373 K in a Milestone Ethos Plus microwave furnace with a power of 600 W during 1 h, in sealed 100 ml Teflon reactors (fresh samples obtained are herein respectively called fHTC MW and fHTCGa MW). The heating ramp from room temperature up to 373 K was in all cases 10 $K \cdot min^{-1}$ and the heating process was programmed with Software Easywave. After this treatment the suspensions were centrifuged and the solids were washed with distilled water to remove nitrate and sodium counterions. The samples were dried at 313 K in air, crushed and a small amount of each sample was calcined at 673 K for 2 hours in air. The loss of mass during calcination of each sample was assessed in order to further prepare the potassium modified samples with a pre-determined stoichiometry. Then, half of the amount of the remaining fHTC, all fHTC MW and all fHTCGa MW were impregnated with a solution of potassium carbonate dissolved in the minimum possible amount of water with the aim of achieving a final potassium loading of 20 wt%, which is the percentage typically found in other works [6, 13, 29]. Finally, the samples were dried once again at 313 K, crushed, and calcined at 673 K for 2 h in air. It has been observed that calcination of hydrotalcite-based materials at 673 K allows

the attainment of higher sorption capacities [30]. A summary of the prepared calcined samples that were submitted to CO_2 sorption tests is given in Table 4.1.1.

Table 4.1.1 - Description of the prepared calcined samples that were submitted to CO_2 sorption tests.

Sample[a]	M^{2+}	M^{3+}	A^{n-}	Treatment	Promoter	K / wt%
cHTC	Mg^{2+}	Al^{3+}	CO_3^{2-}	-	-	-
cK-HTC	Mg^{2+}	Al^{3+}	CO_3^{2-}	-	K	20
cK-HTC MW	Mg^{2+}	Al^{3+}	CO_3^{2-}	Microwave	K	20
cK-HTCGa MW	Mg^{2+}	Al^{3+}, Ga^{3+}	CO_3^{2-}	Microwave	K	20

[a] The notation “c” stands for calcined samples.

4.1.2.3 Characterization of the materials

The powder X-ray diffraction (PXRD) patterns were recorded using non-oriented powder samples, in the 2 to 75° 2θ range, at a scanning speed of $2°\cdot min^{-1}$. The instrument used was a Siemens D-5000 diffractometer, operating at 40 kV and 30 mA, with filtered Cu Kα radiation (λ = 1.5418 Å). The Fourier Transformed Infrared (FTIR) spectra were recorded in the 4000–450 cm^{-1} range in a Perkin-Elmer Spectrum-One spectrometer. About 1 mg of sample and 300 mg of KBr were used in the preparation of the pellets. Nitrogen adsorption-desorption at 77 K were recorded, after degassing the samples for 2 h at 383 K in a FlowPrep 060 accessory (Micrometrics), in a Micrometrics, model Gemini II, apparatus. Scanning Electron Microscopy (SEM) coupled with Energy Dispersive Spectroscopy (EDS) was performed in a FEI Quanta 400 FEG ESEM/EDAX Pegasus X4M instrument. The samples were covered with an

approximately 10 nm thick conductive coating of PdAu through sputtering technique in a SPI module.

High temperature CO_2 sorption measurements were performed in a CI Microbalance. Before each test the microbalance was calibrated. Subsequently the samples were heated up to 573 K under vacuum (≈ 0.001 bar) and remained in such conditions until the measured mass was stable (variation lower than 0.030 mg in 5 h). The vacuum pump was turned off and CO_2 was introduced in the chamber until a given pressure was reached (first sorption equilibrium point). The equilibrium was assumed to be reached when a mass variation lower than 0.030 mg in 5 h was observed. After the equilibrium was reached, a new dose of CO_2 was introduced in the chamber until the next pursued pressure was reached. Since buoyancy caused by the gas in the microbalance chamber affects the measured mass of sorbent, buoyancy correction was done for each pressure according to the methodology used by Miguel *et al.* [13]. For screening purposes, the sorption equilibrium values were obtained for each sorbent at 573 K and CO_2 pressures of ca. 0.20, 0.50, 0.75, 1, 2 and 3 bar.

4.1.3 Results and discussion

4.1.3.1 Physicochemical characterization

4.1.3.1.1 PXRD

The PXRD patterns of the fresh (uncalcined) samples (Fig. 4.1.1 (a)) evidence the presence of the typical hydrotalcite structure. For each sample (with or without Ga), treatment under microwave irradiation increases the crystallinity of the sample, as concluded from the enhanced sharpness of the diffraction maxima, as it can be clearly observed for that corresponding to diffraction by planes (003). Also the doublet slightly above 60º is better defined

for samples submitted to microwave treatment. Such an increase in crystallinity upon microwave irradiation treatment has been related to Oswald ripening effect [31, 32]. Lattice parameter *c* was 22.59 Å for sample fHTC and 22.95 Å for samples fHTC MW, fHTCGa, and fHTCGa MW, that is, the values were almost coincident in all cases; the slightly smaller value obtained for sample fHTC is probably due to a somewhat lower water content in the interlayer. Concerning lattice parameter *a*, calculated from the positions of the diffraction maximum recorded just above 60º (2θ), its value was 3.04 ± 0.01 Å in all cases, indicating that incorporation of a small amount of gallium did not give rise to relevant distortions in the lattice.

The PXRD patterns of the samples calcined at 673 K (Fig. 4.1.1 (b)) correspond mostly to amorphous materials, and only weak and broad signals due to MgO were observed. The maxima due to the layered hydroxide structure completely disappeared for all samples, and some other very weak signals not associated to MgO can be observed. This behavior is due to the fact that calcination at 673 K is severe enough to destroy the layered structure, as concluded from TG results for similar materials [13, 33]. The weak peaks recorded in the K-containing samples might be probably due to formation of small amounts of potassium carbonate, which decomposes well above 1400 K. The main diffraction maxima recorded at values of 2θ close to 35.3, 42.85, and 61.95º correspond to the rock-salt structure of MgO. No differentiated diffraction maxima (in addition to these of MgO and K_2CO_3) due to any Al- or Ga-containing species are recorded, indicating that these cations are probably dispersed in a defective rock salt structure or even forming dispersed, non-crystalline, spinel-like domains, as when the calcination temperature is increased, spinel crystallizes [34].

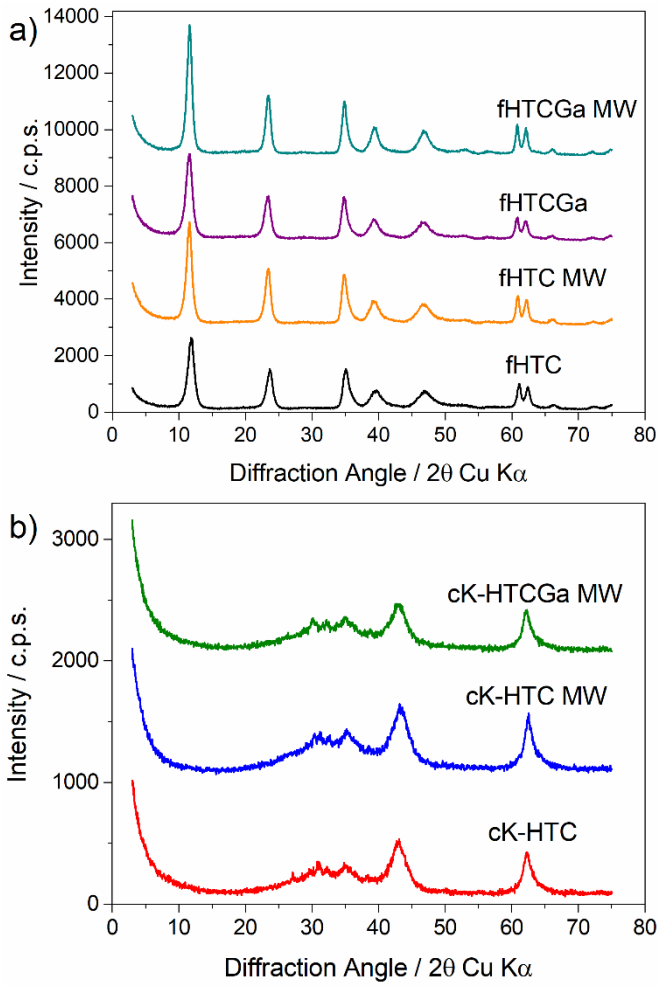

Fig. 4.1.1 - PXRD patterns of (a) fresh samples, and (b) freshly calcined samples at 673 K. The curves have been vertically displaced for clarity.

4.1.3.1.2 Physical adsorption of nitrogen at 77 K

For the determination of the specific surface areas (Table 4.1.2), adsorption-desorption isotherms of N_2 at 77 K were recorded. For the reasons detailed above, the study was restricted exclusively to the calcined samples tested for CO_2 sorption.

For all calcined materials, type II isotherms (IUPAC classification) were obtained (Fig. 4.1.2), meaning that these materials are

macroporous/mesoporous solids. The existence of micropores can be neglected since their volume is very low (< 0.007 $cm^3 \cdot g^{-1}$). It has also been observed that modification with potassium leads to much lower specific surface areas and the three samples impregnated with this alkaline metal show very similar specific surface area values. This is probably related to the pore blocking caused by the K_2CO_3 phase, which is observed in the SEM images (Fig. 4.1.4 below). Finally, neither the microwave treatment nor Ga incorporation had any significant effect on the specific surface areas of the samples.

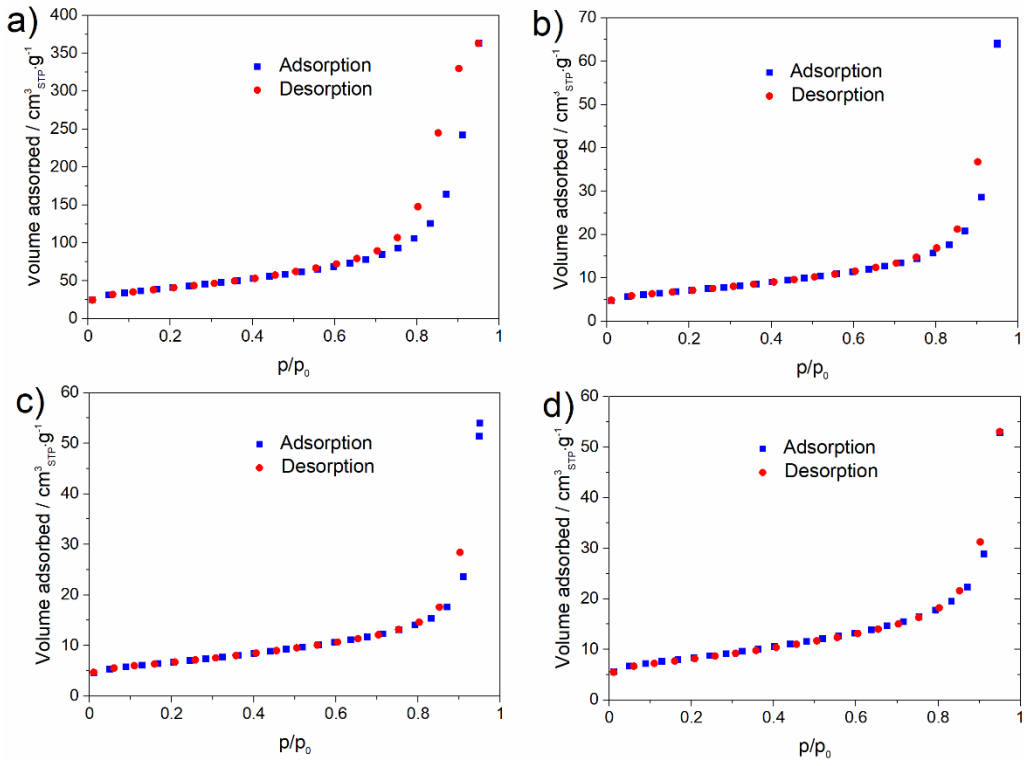

Fig. 4.1.2 - Adsorption/desorption isotherms of nitrogen over calcined samples: (a) cHTC, (b) cK-HTC, (c) cK-HTC MW and (d) cK-HTCGa MW.

Table 4.1.2 - BET specific surface areas of the prepared materials determined by physical adsorption of N_2 at 77 K.

Sample	S_{BET} / $m^2 \cdot g^{-1}$
cHTC	143
cK-HTC	24
cK-HTC MW	23
cK-HTCGa MW	28

4.1.3.1.3 FTIR

As the sorption experiments were carried out with the samples calcined at 673 K, only the FTIR spectra, Fig. 4.1.3, of the samples prepared at this temperature will be discussed. The spectra are very similar for all samples, and show an intense very broad band centered around 3450 cm^{-1}, which is due to the stretching mode of hydroxyl groups. This band is very broad, as it is the superposition of the bands of hydroxyl groups in different environments and so involved in hydrogen bonds with different strength. The shoulder usually recorded around 3000 cm^{-1} due to the stretching mode of hydroxyl groups hydrogen bonded to interlayer carbonate species is not recorded, as interlayer carbonate has been removed from the interlayer during the thermal treatment. The very weak bands slightly below 3000 cm^{-1} are due to the C-H stretching mode of alkane species, probably adsorbed on the surface of the materials, exposed to vapors in the laboratory. The medium intensity band at ca. 1630 cm^{-1} is due to the bending mode of water molecules, probably adsorbed on the external surface of the crystallites. This means that the samples, even after calcination at 673 K, were partially rehydrated/rehydroxylated and probably even recarbonated during storage and handling before recording the spectra;

however, as noticed from the PXRD patterns, the layered structure was not recovered and the absence of interlayer carbonate lost during calcination would account for the differences in the spectra between the uncalcined and calcined samples (not shown).

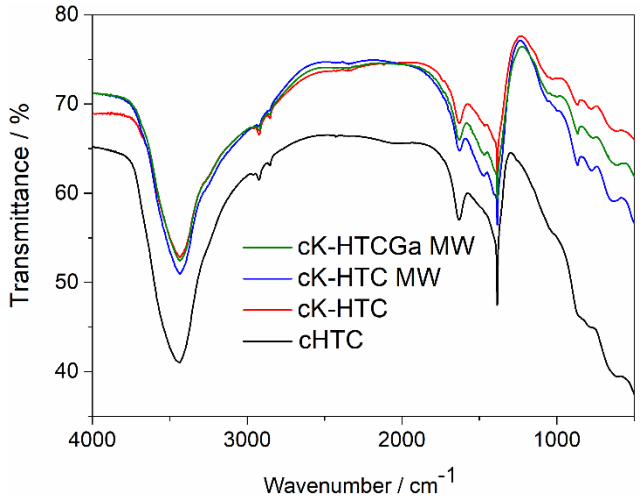

Fig. 4.1.3 - FTIR spectra of the samples calcined at 673 K.

The very sharp band at 1385 cm^{-1} is due to the presence of nitrate impurities, probably from the KBr used to prepare the discs to record the spectra. This band is clearly recorded on top of another, at a very close position, but broader band, usually ascribed to carbonate species. It should be noticed that the spectra for samples cK-HTC, cK-HTC MW, and CK-HTCGa MW show below ca. 1600 cm^{-1} some very weak bands, absent in the spectrum of sample cHTC. This difference can be due to the larger (see below, section 4.1.3.2) surface basicity of the former samples, probably because of the presence of added potassium. Such an increased surface basicity would favor further sorption of carbon dioxide from the environment, leading to the formation of a mixture of surface carbonate and hydrogencarbonate species, which can be bonded to the surface as monodentate, bidentate or even forming bridging species. The weakness of the bands and the closeness of the bands expected for these

different species makes rather doubtful a precise ascription of the bands to definitive surface adsorbed species. Nevertheless, formation of unidentate species can be discarded, as no intense band which could be ascribed to the stretching mode of C=O units is recorded above ca. 1600-1650 cm^{-1}. The weaker bands below 1000 cm^{-1} correspond mainly to vibrations of lattice bonds (Mg-OH, Al-OH, etc.) and also other carbonate-related vibrational modes.

4.1.3.1.4 SEM/EDS

The analysis of the SEM images of cHTC (Fig. 4.1.4 (a)) shows the exclusive existence of a not defined morphology, although the presence of thin slabs is clearly concluded. For the potassium impregnated samples, two additional patterns were identified: larger flat surfaces (Z1) and needle-like structures (Z3). The existence of such zones had already been reported for similar samples [13, 14]. EDS analysis (cf. Appendix C - Fig C.1) showed that the content of potassium is very large in both zones, especially in the flat surface zones (Z1) (34 - 44% in Z1 and 10 - 16% in Z3), where it was larger than in the irregular shape zones (Z2) (< 7%), meaning that potassium deposits preferentially on certain zones of the particles. Similarly, the cations precipitation did not occur homogeneously, being that the molar ratios of cations in the solids vary from zone to zone in the same material and do not coincide with the molar ratio(s) of cations in the starting solution, as previously observed [13, 14].

Rather surprisingly, Z2 zone was not identified in the unused cK-HTCGa MW (Fig. 4.1.4 (d)). It can be tentatively assumed that it was covered by the other two zones during impregnation. However, this same zone is not only clearly seen in the same sample after CO_2 sorption tests, but also shows high and similar amount of potassium (as compared to cK-HTC and cK-HTC MW samples).

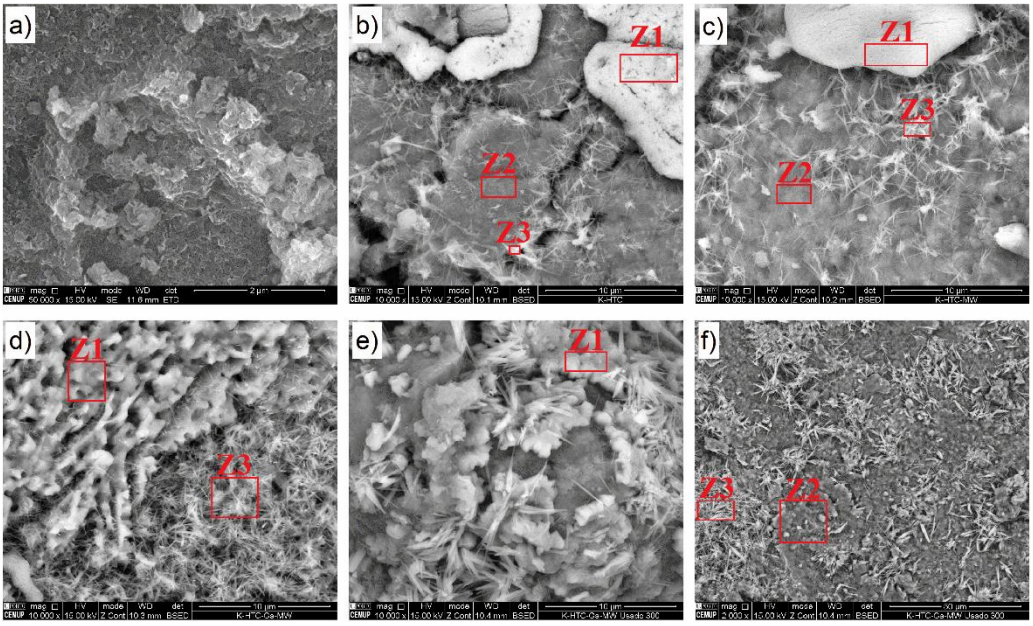

Fig. 4.1.4 - SEM images of the samples calcined at 673 K before CO_2 sorption tests (a) cHTC, (b) cK-HTC, (c) cK-HTC MW, (d) cK-HTCGa MW and after sorption tests at 573 K (e,f) cK-HTCGa MW.

4.1.3.2 CO_2 sorption experiments

4.1.3.2.1 Determination of sorption equilibrium isotherms at 573 K - sorbent screening

The sorption equilibrium isotherms were determined at 573 K under dry conditions for the four calcined samples, increasing the CO_2 partial pressure up to ca. 3 bar. It was verified that in general, the temperature inside the chamber varied less than 2 ºC during the uptake after the previous equilibrium stage has been reached. From the plot in Fig. 4.1.5, a gradual increase of the sorption capacity with the increasingly severe treatments can be observed. After impregnation with potassium, a considerable boost of more than 50% in the sorption capacity of the cHTC sample was observed. This beneficial effect of modification of calcined hydrotalcites with potassium on its sorption capacity is already very well known, being attributed to the increased surface basicity, which

enhances the acid base interaction between acidic CO_2 and the basic sites of the sorbent material [13, 14, 19, 27].

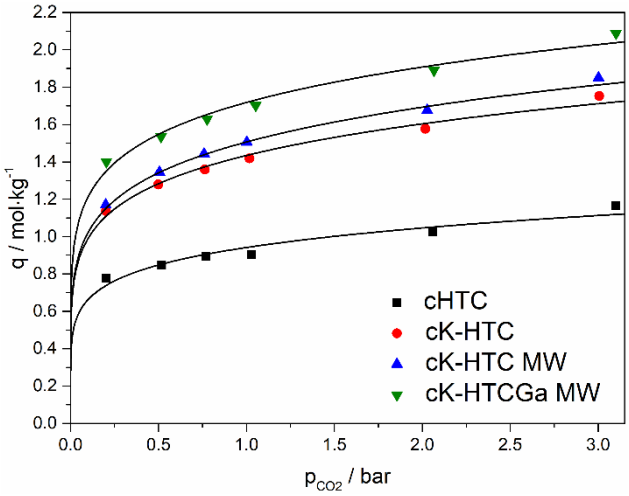

Fig. 4.1.5 - CO_2 sorption equilibrium isotherms at 573 K on the calcined hydrotalcites. The lines correspond to the fitting using the Freundlich equation.

When, in addition, the gel was treated under microwave irradiation, a further increase in the sorption capacity (around 5%) was observed. From microcalorimetric and spectroscopic measurements of CO_2 and CH_3CN sorption on Mg/Al mixed oxides obtained upon calcination of hydrotalcites, Tichit *et al.* [22] observed that the amount of basic and acid sites increased (higher amount of surface-defective sites) when the hydrotalcite had been aged under microwave irradiation. Finally, when the aluminum in the hydrotalcite structure was partially substituted with gallium, a further increase of around 14% in the sorption capacity was observed. It has been found that the amount and strength of the basic and acid sites depend, among other factors, on the nature of the trivalent cation. An increase in the basic character is usually observed when substituting Al by Ga. On the other hand, microwave irradiation of Ga-containing samples induces a higher surface segregation of Ga^{3+} [22]. In our potassium impregnated samples, with markedly lower BET specific surface areas (Table 4.1.2) than the potassium-free sample, the CO_2 sorption capacities are much

larger than for the potassium-free sample. This indicates that the sorption of CO_2 on these materials is not crucially influenced by the BET specific surface area, but, as previously reported [13, 14, 22, 35], rather by the chemical nature of the exposed surface. At 3.10 bar a large sorption capacity of 2.09 mol·kg^{-1} was measured. By comparing these results with other typically found in the literature under similar conditions (Table 4.1.3), those achieved in this study are markedly better in most of the cases than those previously reported.

Table 4.1.3 - Comparison of obtained CO_2 sorption equilibrium capacities for cK-HTCGa MW with values reported in the literature for other hydrotalcites.

Sorbent	T / K	p_{CO_2} / bar	q / mol·kg^{-1}	Shape of sorbent	Ref.
cK-HTCGa MW	573	1.05	1.70	Irregular lumps	This work
cK-HTCGa MW	573	0.51	1.54	Irregular lumps	This work
EXM696	573	1.00	0.50	Powder	[25]
KTI-K-Na	573	0.40[a]	1.11	Cylindrical pellets	[27]
HTA-MW-20K	573	1.00	1.46	n.d.	[6]
MG30-K	579	0.40[a]	0.48	Cylindrical pellets	[14]
MG30-K^N	608	0.50[a]	1.07	n.d.	[20]
K-HTC	673	0.50	0.28	Cylindrical pellets	[29]
K-HTC	673	0.50	0.59	Irregular lumps	[36]

[a] Wet conditions.
n.d. – not disclosed.

The sorption data obtained for each sample were fitted to the Freundlich equation (Eq. (4.1.2)), as usually reported to describe the sorption of CO_2 on hydrotalcites [13, 36, 37]:

$$q = K p_{CO_2}^{\frac{1}{n}} \quad \textbf{(4.1.2)}$$

where q is the CO_2 sorption capacity of the sorbent, and K and n are Freundlich equation parameters; p_{CO_2} stands for the carbon dioxide partial pressure. Parameter *n* is normally higher than 1 and as it gets larger than around 10 ($1/n < 0.1$) the sorption isotherm approaches the so-called irreversible isotherm (or rectangular isotherm), meaning that q remains nearly constant with increasing values of p_{CO_2}. When such state is reached, extremely low pressures are required so that the sorbate molecules start desorbing from the sorbent surface [38]. The fitting parameters of the Freundlich equation are included in Table 4.1.4.

Table 4.1.4 - Adjusted parameters of the Freundlich type isotherm to the experimental sorption data for each sample.

Sorbent	K / mol·kg^{-1} bar$^{(-1/n)}$	$1/n$	R^2
cHTC	0.94	0.15	0.9961
cK-HTC	1.43	0.16	0.9990
cK-HTC MW	1.51	0.17	0.9995
cK-HTCGa MW	1.72	0.15	0.9987

As it can be seen, the Freundlich model results in a very good fitting to the experimental data for all samples within the tested pressure range. This can also be concluded from the plots in Fig. 4.1.5. Regarding the values of n, they are very similar for all samples and below 10 ($1/n > 0.1$), meaning that for all cases

the isotherms were far from being irreversible. That can also be concluded by analyzing Fig. 4.1.5, in which it can be seen that the isotherms are not even close of being rectangular shaped.

Finally, it can be observed that the four equilibrium sorption isotherms obtained are quite steep, especially that for cK-HTCGa MW. If this material is used in cyclic operation (and according to the equilibrium theory for adsorption in fixed bed [39], which states that the velocity at which a specific concentration propagates is inversely proportional to the slope of the isotherm), lower concentrations would travel through the column more slowly and so the concentration front would be compressive and dispersive during the sorption and the desorption stages, respectively. The most crucial aspect here is that it is expected that the regeneration front for cK-HTCGa MW during cyclic CO_2 capture in a packed bed at high CO_2 pressures will be quite dispersive, mainly because of the considerable difference in the slope of the isotherm between low (ca. < 0.25 bar) and high (ca. > 1.0 bar) CO_2 pressures. Therefore, in order to save time and resources, a possibility would be to operate in the low pressure region during regeneration (pressure swing), which would allow a much lower difference in terms of isotherm slope and consequently a much less dispersive front.

4.1.3.2.2 Determination of CO_2 uptake mechanism

The kinetics of CO_2 sorption on the four calcined hydrotalcites was evaluated based on the findings reported by Ritter and co-workers [40], regarding the formation of different carbonate species during CO_2 sorption on hydrotalcite-like materials. These authors found, by *in situ* FTIR spectroscopic analysis, that four different carbonate species were formed: uni-, bi-, polydentate and bridged carbonate species. The formation of bridged, uni- and bidentate carbonates was associated to the fast reversible uptakes observed at short contact times, while the formation of polydentate species is related to the slow irreversible CO_2 uptake observed later on in the process. In a recent work [41],

it has been also observed that the sorption of CO_2 over hydrotalcite-based sorbents presents a very fast kinetics followed by a slower sorption. Moreover, Ritter and co-workers observed that bridged and unidentate carbonate species disappear after approximately 1 h, probably due to their transformation into polydentate carbonate [40]. More recently, Coenen *et al.* have concluded that irreversible formation of such carbonate species can actually be reverted in the presence of steam into a metal hydroxide, which can be reconverted into metal carbonate in the presence of CO_2 [42].

Following our previous findings [13] and considering the mechanism proposed by Ritter *et al.*, Eq. (4.1.3) was here used in order to describe the total amount of CO_2 entering the sorbent particle [43]:

$$F = \frac{q(t) - q(t=0)}{q(\infty) - q(t=0)}$$
$$= \left(1 - \frac{6}{\pi^2}\sum_{i=1}^{\infty}\frac{1}{i^2}e^{\left(-i^2\pi^2\frac{D_1}{r^2}t\right)}\right)\frac{q_1}{q_\infty} + \left(1 - \frac{6}{\pi^2}\sum_{i=1}^{\infty}\frac{1}{i^2}e^{\left(-i^2\pi^2\frac{D_2}{r^2}t\right)}\right)\frac{q_2}{q_\infty} \qquad \textbf{(4.1.3)}$$
$$= F_1\frac{q_1}{q_\infty} + F_2\frac{q_2}{q_\infty}$$

where F is the total CO_2 uptake fraction, F_1 and F_2 are the partial uptake fractions related to the fast and slow uptakes, respectively, $q(t)$ is the CO_2 sorption capacity measured at time t, $q(t=0)$ is the sorption capacity measured at the beginning of the sorption tests (null in the case of our experiments for the 1st uptake), $q(\infty)$ is the sorption capacity measured at the equilibrium and $\frac{D_1}{r^2}$, $\frac{D_2}{r^2}$ and q_1 (sorption capacity related to the fast uptake) are model parameters that were obtained through non-linear fitting of Eq. (4.1.3) to the experimental data. Regarding q_2, it is the sorption capacity related to the slow uptake and is the difference between $q(\infty)$ and q_1. Eq. (4.1.3) is therefore composed by two kinetic contributions, one related to the fast increase of sorption that occurs during the

first stages of the process and the other one related to the slow uptake that occurs at longer times; the kinetics of both contributions is characterized by the $\frac{D_i}{r^2}$ parameters.

Fig. 4.1.6 shows the experimental fractional uptakes at 0.20 bar CO_2 partial pressure for the different materials and the model curves fitted to the respective experimental data, bearing in mind that F is the sum of two terms which include curves F_1 and F_2 (see Appendix C, Fig. C.2 for the total and partial loading uptake curves). From Fig. 4.1.6 (or C.2) it is possible to conclude that the model predicts accurately the experimental CO_2 sorption uptake on these calcined hydrotalcites, which is in line with the very good fittings obtained by Miguel *et al.* [13] for a similar hydrotalcite. The fitted parameters are summarized in Table 4.1.5.

Table 4.1.5 - Parameters of Eq. (4.1.3) obtained through fitting of the experimental CO_2 uptakes for the four samples at 0.20 bar and 573 K.

Sorbent	$\frac{D_1}{r^2} \times 10^4$ **/ s^{-1}**	$\frac{D_2}{r^2} \times 10^6$ **/ s^{-1}**	$\frac{q_1}{q_\infty} \times 100$
cHTC	12.63	11.92	78
cK-HTC	6.90	9.18	62
cK-HTC MW	5.64	8.16	64
cK-HTCGa MW	7.66	6.34	63

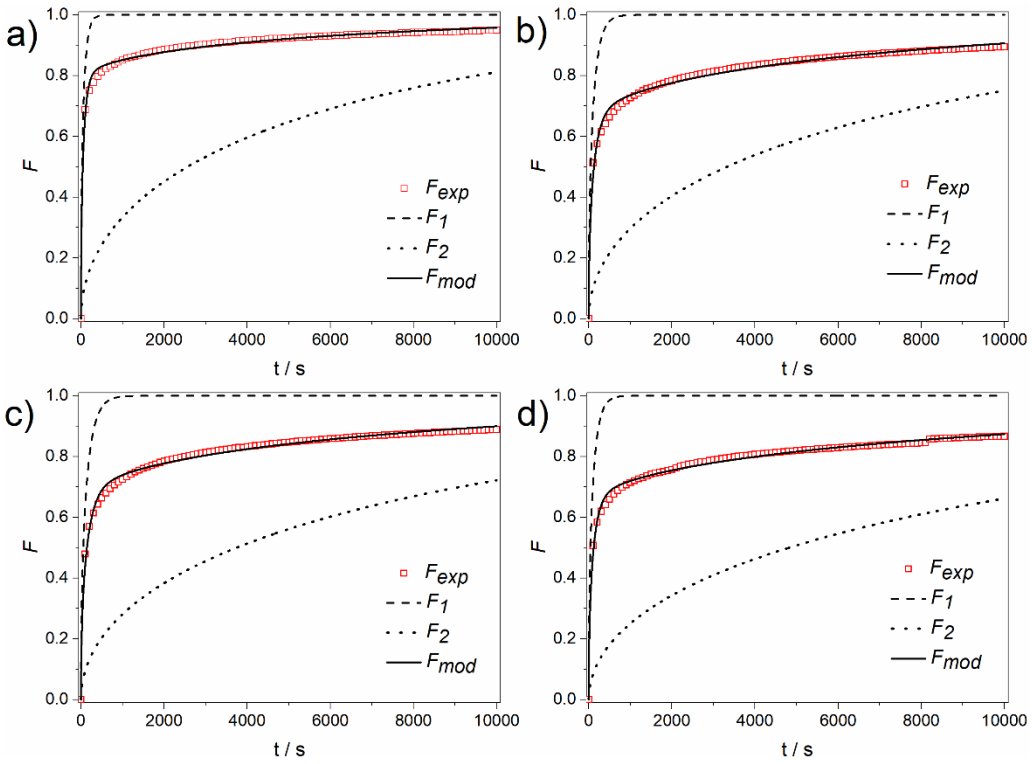

Fig. 4.1.6 - Uptake curves for CO_2 sorption at 0.20 bar and 573 K for (a) cHTC, (b) cK-HTC, (c) cK-HTC MW and (d) cK-HTCGa MW.

By comparing the parameters determined for the different samples, it is clearly observed that values for sample cHTC are larger than for the others. This basically means that cHTC shows a faster sorption kinetics than the other samples, both during the fast and the slow uptake steps. Moreover, a higher relative amount (as compared to the equilibrium amount) of CO_2 is adsorbed on sample cHTC (78 %) than for the other samples (62-64 %) during the fast uptake. This can be verified in Fig. 4.1.7, where these differences are clearly shown both for the fast and the slow uptakes. Also, the decreasing trend observed in general for both $\frac{D_1}{r^2}$ and $\frac{D_2}{r^2}$ in Table 4.1.5 as the treatment is more severe is similarly concluded from Fig 4.1.7 (a) and (b), respectively. Finally, when comparing the total uptake fraction calculated with Eq. (4.1.3) for the different samples (Fig. 4.1.7 (c)), it is confirmed that CO_2 adsorbs faster on cHTC than on the

potassium-loaded samples, this meaning that impregnation with potassium slows the sorption process, despite it enhances CO_2 sorption capacity. This might be related to the previously mentioned pore blocking caused by potassium impregnation, which probably slows the diffusion of CO_2 to the active sites. Regarding microwave aging and gallium incorporation, the first treatment does not seem to affect significantly the overall sorption kinetics, while the second treatment slows it slightly, as it can be seen in Fig. 4.1.7 (c). In any case, 70% of the total sorption capacity of cK-HTCGa MW at 0.20 bar and 573 K is achieved after only 10 min, which corresponds to a sorption capacity of 0.95 mol·kg^{-1}. This is more than what would be attained with any commercial hydrotalcite under similar conditions after equal or even longer periods of exposure to CO_2 [14, 25].

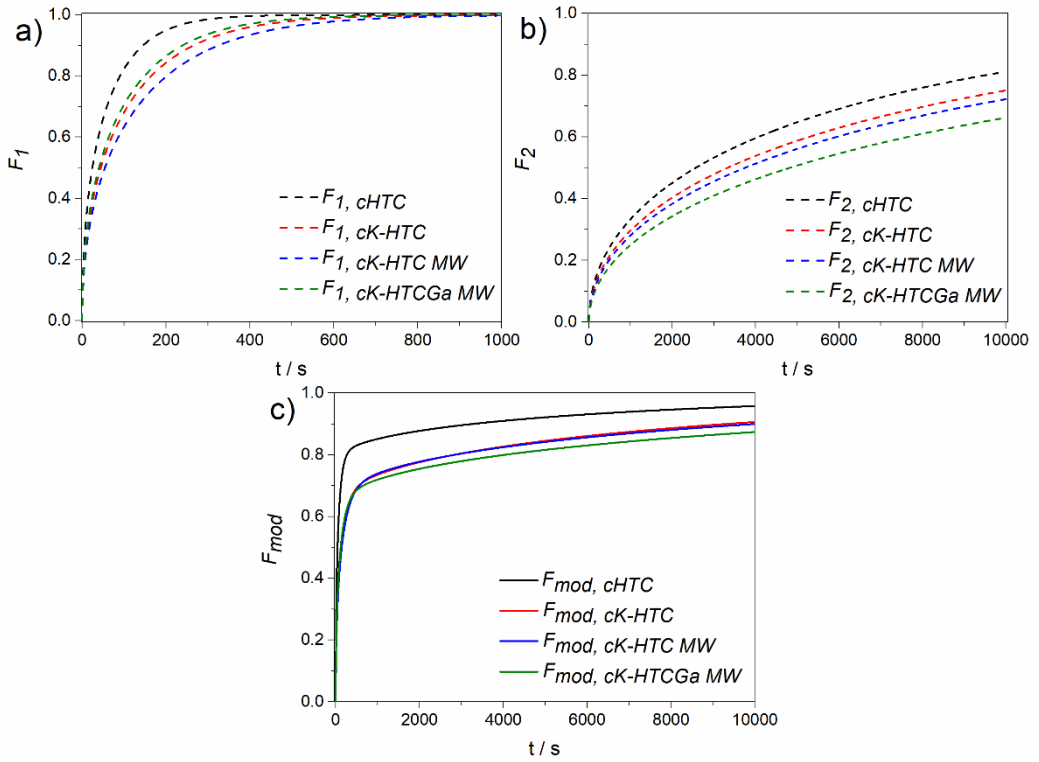

Fig. 4.1.7 - Comparison of the uptake curves at 0.20 bar obtained through non-linear fitting of Eq. (4.1.3) to the experimental data for the different samples: (a) F_1, (b) F_2 and (c) F_{mod}.

A similar analysis was done for the second CO_2 uptake (from 0.20 bar up to 0.51 bar) and is included in Appendix C (Figs. C.3-C.5 and Table C.1). Once again very good fittings were attained. For this second uptake, a decrease of the sorption kinetics was observed, especially for the potassium-doped materials which only reached 45-50% of the equilibrium sorption capacity after approximately 10 000 s (Appendix C, Fig. C.3) (more than 80% of the equilibrium sorption capacity was obtained by all the materials during the first uptake after the same period – Fig. 4.1.6). This decrease is probably related to the fact that the materials are not fresh anymore at the beginning of the new uptake, which also makes the sorption capacity increase lower (Appendix C, Fig. C.5). For this reason, the values attained for the parameters of Eq. (4.1.3) were lower as well (Appendix C, Table C.1). Finally, it was observed that the general kinetics' trend remained the same, i.e., CO_2 adsorbs faster on cHTC than on the potassium-loaded samples (Appendix C, Fig. C.4).

4.1.4 Conclusions

Different hydrotalcite-based materials were prepared and their calcined products were tested for CO_2 sorption. The samples showed CO_2 sorption capacities at 573 K well above the minimum value of 0.3 mol·kg^{-1} normally considered for their application in pre-combustion capture applications, particularly in sorption-enhanced reaction processes. The simultaneous modification with potassium and partial substitution of aluminum with gallium significantly enhanced the sorption capacity of the calcined hydrotalcites, especially the incorporation of potassium. Moreover, even though microwave aging did not lead to an enhancement of the CO_2 sorption capacity as notorious as the other changes did, it still contributed positively to the increase of the sorption capacity. For all the CO_2 pressure range studied, sample cK-HTCGa MW showed a sorption capacity much higher than those normally reported for

this kind of materials. A maximum CO_2 sorption capacity of 2.09 mol·kg^{-1} was achieved on sample cK-HTCGa MW at 573 K, 3.10 bar of CO_2 and dry conditions. The sorption equilibrium isotherms for all the materials were fitted using a Freundlich-type equation, reaching a very good adhesion to experimental data in all cases.

Finally, the sorption kinetics for all the samples was evaluated considering a model which encompasses two kinetic contributions (fast and slow contributions). The model predicted accurately the experimental CO_2 sorption uptake on these materials. It was also observed during the first uptake (up to 0.20 bar of CO_2) that the base formulation, cHTC, showed the fastest sorption kinetics both for the fast and slow uptakes, despite its considerably lower sorption capacity. The results indicate that modification of the hydrotalcites with potassium slows the sorption process, probably due to the limited diffusion of CO_2 to the active sites inside the partially blocked pores. A lower decrease of the sorption kinetics during the first uptake was attributed to both gallium incorporation and microwave aging. Furthermore, when the pressure of CO_2 was increased from 0.20 bar up to 0.51 bar, lower relative sorption uptakes with slower kinetics were observed. This was already expected since the material had already been submitted to an atmosphere of 0.20 bar of CO_2. Nevertheless, sample cK-HTCGa MW showed a much higher sorption capacity after only a few minutes than calcined commercial hydrotalcites would present after even hours of exposure to CO_2.

4.1.5 References

[1] Rodrigues, A.E., J.M. Calo, N.H. Sweed, *Scientific Basis for the Design of Two Phase Catalytic Reactors*, in *Multiphase Chemical Reactors*. 1981, NATO Advanced Study Institute Series; Sijthoff & Noordhoff: Alphen aan den Rijn: The Netherlands. p. 65-133.

[2] Naims, H., *Economics of carbon dioxide capture and utilization—a supply and demand perspective.* Environmental Science and Pollution Research, 2016, 23(22), 22226-22241.

[3] Leung, D.Y.C., G. Caramanna, and M.M. Maroto-Valer, *An overview of current status of carbon dioxide capture and storage technologies.* Renewable and Sustainable Energy Reviews, 2014, 39, 426-443.

[4] Sanchez-Jimenez, P.E., L.A. Perez-Maqueda, and J.M. Valverde, *Nanosilica supported CaO: A regenerable and mechanically hard CO2 sorbent at Ca-looping conditions.* Applied Energy, 2014, 118(0), 92-99.

[5] Zhang, X., Z. Li, Y. Peng, W. Su, X. Sun, and J. Li, *Investigation on a novel CaO-Y2O3 sorbent for efficient CO2 mitigation.* Chemical Engineering Journal, 2014, 243(0), 297-304.

[6] Hanif, A., S. Dasgupta, S. Divekar, A. Arya, M.O. Garg, and A. Nanoti, *A study on high temperature CO2 capture by improved hydrotalcite sorbents.* Chemical Engineering Journal, 2014, 236, 91-99.

[7] Maroño, M., Y. Torreiro, and L. Gutierrez, *Influence of steam partial pressures in the CO2 capture capacity of K-doped hydrotalcite-based sorbents for their application to SEWGS processes.* International Journal of Greenhouse Gas Control, 2013, 14(0), 183-192.

[8] Wang, S., C. An, and Q.-H. Zhang, *Syntheses and structures of lithium zirconates for high-temperature CO2 absorption.* Journal of Materials Chemistry A, 2013, 1(11), 3540-3550.

[9] Duan, Y., *Structural and electronic properties of Li8ZrO6 and its CO2 capture capabilities: an ab initio thermodynamic approach.* Physical Chemistry Chemical Physics, 2013, 15(24), 9752-9760.

[10] Mizunuma, M., M. Tsuda, Y. Maruo, and T. Nakagaki, *CO2 Capture System Using Lithium Silicate for Distributed Power Supply.* Energy Procedia, 2013, 37(0), 1194-1201.

[11] Seggiani, M., M. Puccini, and S. Vitolo, *Alkali promoted lithium orthosilicate for CO2 capture at high temperature and low concentration.* International Journal of Greenhouse Gas Control, 2013, 17(0), 25-31.

[12] Silva, J.M., M.A. Soria, and L.M. Madeira, *Challenges and strategies for optimization of glycerol steam reforming process.* Renewable and Sustainable Energy Reviews, 2015, 42, 1187-1213.

[13] Miguel, C.V., R. Trujillano, V. Rives, M.A. Vicente, A.F.P. Ferreira, A.E. Rodrigues, A. Mendes, and L.M. Madeira, *High temperature CO2 sorption with gallium-substituted and promoted hydrotalcites.* Separation and Purification Technology, 2014, 127, 202-211.

[14] Oliveira, E.L.G., C.A. Grande, and A.E. Rodrigues, *CO2 sorption on hydrotalcite and alkali-modified (K and Cs) hydrotalcites at high temperatures.* Separation and Purification Technology, 2008, 62(1), 137-147.

[15] A. de Roy, C.F., J.P. Besse, *in: V. Rives (Ed.), Layered Double Hydroxides: Synthesis and post synthesis modification*, in *Layered Double Hydroxides: Present and Future*. 2001, Nova Science Publishers Inc: New York. p. 1-39.

[16] Wang, Q., Z. Wu, H.H. Tay, L. Chen, Y. Liu, J. Chang, Z. Zhong, J. Luo, and A. Borgna, *High temperature adsorption of CO2 on Mg–Al hydrotalcite: Effect of the charge compensating anions and the synthesis pH.* Catalysis Today, 2011, 164(1), 198-203.

[17] Wang, Q., H.H. Tay, D.J.W. Ng, L. Chen, Y. Liu, J. Chang, Z. Zhong, J. Luo, and A. Borgna, *The Effect of Trivalent Cations on the Performance of Mg-M-CO3 Layered Double Hydroxides for High-Temperature CO2 Capture.* ChemSusChem, 2010, 3(8), 965-973.

[18] Kim, S., S.G. Jeon, and K.B. Lee, *High-Temperature CO2 Sorption on Hydrotalcite Having a High Mg/Al Molar Ratio.* ACS Applied Materials & Interfaces, 2016, 8(9), 5763-5767.

[19] Martunus, M.R. Othman, and W.J.N. Fernando, *Elevated temperature carbon dioxide capture via reinforced metal hydrotalcite.* Microporous and Mesoporous Materials, 2011, 138(1–3), 110-117.

[20] Wu, Y.J., P. Li, J.G. Yu, A.F. Cunha, and A.E. Rodrigues, *K-Promoted Hydrotalcites for CO2 Capture in Sorption Enhanced Reactions.* Chemical Engineering & Technology, 2013, 36(4), 567-574.

[21] Lee, J.-Y., G.-H. Gwak, H.-M. Kim, T.-i. Kim, G.J. Lee, and J.-M. Oh, *Synthesis of hydrotalcite type layered double hydroxide with various Mg/Al ratio and surface charge under controlled reaction condition.* Applied Clay Science, 2016, 134, Part 1, 44-49.

[22] Tichit, D., A. Rolland, F. Prinetto, G. Fetter, M. de Jesus Martinez-Ortiz, M.A. Valenzuela, and P. Bosch, *Comparison of the structural and acid-base properties of Ga- and Al-containing layered double hydroxides obtained by microwave irradiation and conventional ageing of synthesis gels.* Journal of Materials Chemistry, 2002, 12(12), 3832-3838.

[23] Hutson, N.D., S.A. Speakman, and E.A. Payzant, *Structural Effects on the High Temperature Adsorption of CO2 on a Synthetic Hydrotalcite.* Chemistry of Materials, 2004, 16(21), 4135-4143.

[24] Wang, Q., J. Luo, Z. Zhong, and A. Borgna, *CO2 capture by solid adsorbents and their applications: current status and new trends.* Energy & Environmental Science, 2011, 4(1), 42-55.

[25] Yong, Z., Mata, and A.E. Rodrigues, *Adsorption of Carbon Dioxide onto Hydrotalcite-like Compounds (HTlcs) at High Temperatures.* Industrial & Engineering Chemistry Research, 2001, 40(1), 204-209.

[26] Yavuz, C.T., B.D. Shinall, A.V. Iretskii, M.G. White, T. Golden, M. Atilhan, P.C. Ford, and G.D. Stucky, *Markedly Improved CO2 Capture Efficiency and Stability of Gallium Substituted Hydrotalcites at Elevated Temperatures.* Chemistry of Materials, 2009, 21(15), 3473-3475.

[27] Martunus, Z. Helwani, A.D. Wiheeb, J. Kim, and M.R. Othman, *Improved carbon dioxide capture using metal reinforced hydrotalcite under wet conditions.* International Journal of Greenhouse Gas Control, 2012, 7, 127-136.

[28] Soria, M.A., S. Tosti, A. Mendes, and L.M. Madeira, *Enhancing the low temperature water–gas shift reaction through a hybrid sorption-enhanced membrane reactor for high-purity hydrogen production.* Fuel, 2015, 159, 854-863.

[29] Boon, J., P.D. Cobden, H.A.J. van Dijk, C. Hoogland, E.R. van Selow, and M. van Sint Annaland, *Isotherm model for high-temperature, high-pressure adsorption of and on K-promoted hydrotalcite.* Chemical Engineering Journal, 2014, 248, 406-414.

[30] Ram Reddy, M.K., Z.P. Xu, G.Q. Lu, and J.C. Diniz da Costa, *Layered Double Hydroxides for CO2 Capture: Structure Evolution and Regeneration.* Industrial & Engineering Chemistry Research, 2006, 45(22), 7504-7509.

[31] Benito, P., M. Herrero, C. Barriga, F.M. Labajos, and V. Rives, *Microwave-Assisted Homogeneous Precipitation of Hydrotalcites by Urea Hydrolysis.* Inorganic Chemistry, 2008, 47(12), 5453-5463.

[32] Herrero, M., F.M. Labajos, and V. Rives, *Size control and optimisation of intercalated layered double hydroxides.* Applied Clay Science, 2009, 42(3–4), 510-518.

[33] Rives, V., *in: V. Rives (Ed.), Study of Layered Double Hydroxides by thermal methods*, in *Layered Double Hydroxides: Present and Future*. 2001, Nova Science Publishers Inc: New York. p. 127-151.

[34] Labajos, F.M., V. Rives, and M.A. Ulibarri, *Effect of hydrothermal and thermal treatments on the physicochemical properties of Mg-Al hydrotalcite-like materials.* Journal of Materials Science, 1992, 27(6), 1546-1552.

[35] Hutson, N.D. and B.C. Attwood, *High temperature adsorption of CO2 on various hydrotalcite-like compounds.* Adsorption, 2008, 14(6), 781-789.

[36] Halabi, M.H., M.H.J.M. de Croon, J. van der Schaaf, P.D. Cobden, and J.C. Schouten, *High capacity potassium-promoted hydrotalcite for CO2 capture in H2 production.* International Journal of Hydrogen Energy, 2012, 37(5), 4516-4525.

[37] Soares, J., G.L. Casarin, H.J. José, R.D.F.P.M. Moreira, and A.E. Rodrigues, *Experimental and Theoretical Analysis for the CO2 Adsorption on Hydrotalcite.* Adsorption, 2005, 11(1), 237-241.

[38] Do, D.D., *Adsorption Analysis: Equilibria and Kinetics*. 1998, London: Imperial College Press.

[39] DeVault, D., *The Theory of Chromatography.* Journal of the American Chemical Society, 1943, 65(4), 532-540.

[40] Du, H., C.T. Williams, A.D. Ebner, and J.A. Ritter, *In Situ FTIR Spectroscopic Analysis of Carbonate Transformations during Adsorption and Desorption of CO2 in K-Promoted HTlc.* Chemistry of Materials, 2010, 22(11), 3519-3526.

[41] Coenen, K., F. Gallucci, P. Cobden, E. van Dijk, E. Hensen, and M. van Sint Annaland, *Chemisorption working capacity and kinetics of CO2 and H2O of hydrotalcite-based adsorbents for sorption-enhanced water-gas-shift applications.* Chemical Engineering Journal, 2016, 293, 9-23.

[42] Coenen, K., F. Gallucci, G. Pio, P. Cobden, E. van Dijk, E. Hensen, and M. van Sint Annaland, *On the influence of steam on the CO2 chemisorption capacity of a hydrotalcite-based adsorbent for SEWGS applications.* Chemical Engineering Journal, 2017, 314, 554-569.

[43] Crank, J., *The Mathematics of Diffusion*. second ed. 1975, London: Oxford University Press.

4.2 Dynamic Behaviour of a K-doped Ga Substituted and Microwave Aged Hydrotalcite During CO_2 Sorption Experiments

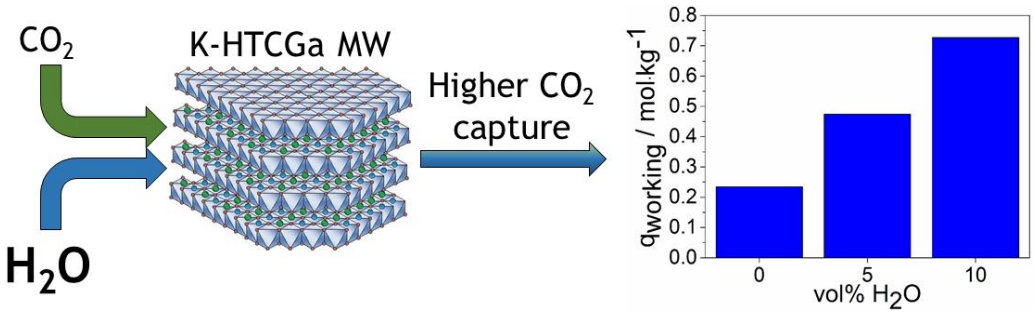

- *cK-HTCGa MW has a significant CO_2 capture working capacity.*
- *cK-HTCGa MW working capacity is 42% higher than that of commercial K-MG30.*
- *Higher pressures, temperatures and CO_2 and H_2O contents allowed better performance.*
- *The sorption working capacity increased by 200% when 10 vol% of H_2O was used.*
- *The presence of H_2O mobilized K and Ga basic sites towards c-KHTCGa MW's surface.*

A potassium impregnated magnesium-aluminum-gallium hydrotalcite, aged under microwave irradiation (K-HTCGa MW), was tested for CO_2 capture during a long term breakthrough experimental campaign for the very first time under different total pressures, CO_2 concentrations, temperatures and H_2O contents. Higher total pressures, concentrations of CO_2 in the feed stream and temperatures resulted in higher outstanding sorption capacities. The presence of H_2O during both sorption and desorption was considerably advantageous for promoting a supplementary increase in CO_2 capture by the hydrotalcite. The calcined material (cK-HTCGa MW) presented a sorption working capacity after 7-8 cycles of around 0.7 $mol \cdot kg^{-1}$ at 6 bar, 673 K, 15 vol% CO_2 and under dry conditions, which is considerably higher (almost 2-fold increase) than the approximately 0.4 $mol \cdot kg^{-1}$ attained with the commercial K-MG30 material, under the same conditions. Finally, it was observed that higher total pressures, temperatures and H_2O contents allowed higher bed usage efficiencies. EDS elemental distribution mapping showed that both potassium and gallium (basic sites) were mobilized towards the sorbent surface in the presence of H_2O, which could have contributed to the observed enhanced behavior of the sorbent under wet conditions. Furthermore, PXRD and FTIR evidenced that the used hydrotalcite (uK-HTCGa MW) kept a stable structure after more than 300 hours of utilization.

The contents of this chapter were adapted from: Silva, J.M., R. Trujillano, V. Rives, M.A. Soria, and L.M. Madeira, *Dynamic behaviour of a K-doped Ga substituted and microwave aged hydrotalcite during CO_2 sorption experiments.* Submitted for publication.

4.2.1 Introduction

Layered double hydroxides (LDHs), also known as hydrotalcites-like materials, are anionic clays with at least two kinds of metallic cations in the main layers and anionic species in the interlayers. These brucite-like layered materials present as general formula $[M^{2+}_{1-x}M^{3+}_{x}(OH)_2]^{x+}\left[A^{n-}_{x/n}\cdot yH_2O\right]^{x-}$, where M^{2+} and M^{3+} are divalent (e.g., Mg^{2+}, Ni^{2+}, Zn^{2+}, etc.) and trivalent (e.g., Al^{3+}, Ga^{3+}, Mn^{3+}, Y^{3+}, Fe^{3+}, etc.) metal cations within the brucite-like layers, A^{n-} is a charge balancing anion (e.g. CO_3^{2-}, Cl^-, SO_4^{2-}, etc.) located in the interlayer space and x, the trivalent metal molar fraction, is generally between 0.2 and 0.4 [1]. These materials have been reported for almost a century but only in the last decades attention has been focused on their capacity for CO_2 capture; more specifically, because of their unique stable behavior during CO_2 capture at temperatures between 573 and 773 K [2-6], which makes them very good candidates for pre-combustion CO_2 capture applications.

The performance of these materials during high temperature CO_2 sorption can be significantly enhanced by combining adequate cations in the brucite-like layers [7, 8], by using appropriate charge balancing anions in the interlayer [9], by varying the trivalent metal molar fraction [10] or by modifying the material with alkaline metal cations, such as K^+, Na^+ or Cs^+ [2, 5]. Changes regarding the synthesis process and pH [9, 11], aging process of the precipitated gels, such as microwave irradiation, ultrasonication or conventional [12, 13], calcination temperature [5, 14], among others, also play an important role in determining the performance of hydrotalcites during high temperature CO_2 capture. On the other hand, the dynamic behavior of hydrotalcites during high temperature CO_2 sorption will also be considerably dependent on the process conditions used, such as sorption and desorption temperature, sorption and desorption total pressure, CO_2 concentration present in the feed stream during sorption, total flow rate, among others. The use of pressure and/or temperature swing has

been frequently reported as advantageous in this kind of processes [2, 15, 16]. Moreover, the presence of H_2O during sorption and/or desorption of CO_2 over hydrotalcites has been commonly reported as advantageous [2, 17-20], which is highly convenient as H_2O is often present in pre-combustion processes such as sorption-enhanced steam reforming and water-gas shift.

It has been concluded in a previous work [8] that simultaneous modification with potassium, partial substitution of aluminum with gallium and aging the precipitated gel under microwave irradiation resulted in a hydrotalcite with outstanding CO_2 sorption capacity at 573 K under static conditions in a microbalance. It was observed that this new hydrotalcite was able to retain even more CO_2 than some of the most active hydrotalcites reported in the literature under similar conditions. In fact, this hydrotalcite was able to capture considerably more CO_2 in the first minutes of exposure than commercial materials would do even after hours [8]. However, the material was only submitted to a set of 6 CO_2 uptakes in a microbalance that allowed the determination of the CO_2 sorption isotherm at 573 K. In order to understand how such promising material behaves during dynamic continuous operation, namely in terms of sorption capacity and sorption kinetics, several breakthrough tests were carried out for more than 300 h under different total pressures, sorption temperatures, CO_2 concentrations and H_2O contents in the feed. The most favorable conditions within the selected ranges were determined. Also, the fraction of sorbent bed that was efficiently used and which conditions maximize this usage were determined for the several conditions tested. In order to better understand the obtained results, the effect of submitting the hydrotalcite to more than 300 h of CO_2 sorption/desorption cycles on its structure and surface composition was assessed by means of several characterization techniques.

4.2.2 Experimental

4.2.2.1 Chemicals and gases

Aluminum nitrate 9-hydrate, magnesium nitrate 6-hydrate and gallium nitrate hydrate (all from Sigma Aldrich, highest purity degree available) were used as Al, Mg and Ga precursors, respectively. In order to assure that the charge balancing anion was carbonate and not nitrate, an excess of anhydrous sodium carbonate (Sigma Aldrich, highest purity degree available) was used. Sodium hydroxide was used to maintain an alkaline pH during synthesis. Potassium carbonate (Sigma Aldrich, highest purity degree available) was used as chemical promoter to modify the prepared hydrotalcites.

Carbon dioxide (99.998%) and nitrogen (99.9995%), both from L'Air Liquide, were used in the breakthrough experiments. Deionized water was also used during some of the sorption tests.

4.2.2.2 Preparation of the material

A fresh base material, $Mg_2(Al_{0.9}Ga_{0.1})(OH)_6(CO_3)_{0.5} \cdot yH_2O$, herein named as fHTCGa, was prepared with a Mg^{2+} / $(Al^{3+} + Ga^{3+})$ molar ratio of 2 and a Al^{3+}/Ga^{3+} molar ratio of 9. These ratios were chosen taking into account the results previously reported by Miguel *et al.* [21] and used in our previous work [8].

The procedure used to prepare first fHTCGa and then fHTCGa MW (fHTCGa aged under microwave irradiation) is described elsewhere [8]. Then, the sample was dried at 313 K for 48 h in an oven, crushed and a small amount was calcined at 673 K for 2 h in air in a NETZSCH STA 449 F3 Jupiter thermobalance. The loss of mass during calcination was assessed through thermogravimetric analysis in order to further prepare the potassium modified sample with a pre-determined stoichiometry. Then, fHTCGa MW was

impregnated with a solution of potassium carbonate in water and under vigorous stirring to achieve a final potassium loading of 20 wt% (sample called fK-HTCGa MW), which is the percentage typically found in other studies [12, 21, 22] and also used in our previous work [8]. Finally, the samples were dried once again at 313 K for 48 h in an oven and crushed.

4.2.2.3 Characterization of the materials

Thermogravimetric and differential scanning calorimetry (TG-DSC) analysis of fK-HTCGa MW was performed in a NETZSCH SSA 449F3 Jupiter thermobalance; the Differential Thermogravimetric (DTG) curve was also analyzed. Approximately 20 mg of sample were placed in an alumina basket and heated up to the desired temperature at a rate of 10 $K \cdot min^{-1}$ under a N_2 flow rate of 60 $mL_N \cdot min^{-1}$. All data analyses were performed using NETZSCH Proteus Thermal Analysis software. The powder X-ray diffraction (PXRD) patterns were recorded using non-oriented powder samples, in the 3-70° 2θ range, at a scanning speed of 2° min^{-1}. The instrument used was a Siemens D-5000 diffractometer, operating at 40 kV and 30 mA, with filtered Cu Kα radiation (λ = 1.5418 Å). The Fourier Transformed Infrared (FTIR) spectra were recorded in the 4000–450 cm^{-1} range in a Perkin-Elmer Spectrum-One spectrometer. About 1 mg of sample and 300 mg of KBr were used in the preparation of the pellets. Nitrogen adsorption-desorption isotherms at 77 K were recorded, after degassing the samples for 2 h at 383 K in a FlowPrep 060 accessory (Micrometrics), in a Micrometrics, model Gemini II, apparatus. Scanning Electron Microscopy (SEM) coupled with Energy Dispersive Spectroscopy (EDS) was performed in a FEI Quanta 400 FEG ESEM/EDAX Pegasus X4M equipment. The samples were covered with an approximately 10 nm thick conductive coating of PdAu through the sputtering technique in a SPI module.

4.2.2.4 Experimental setup for the CO_2 sorption experiments

A stainless steel column (120 mm of height and 7.2 mm of inner diameter) was attached to the experimental setup (Fig. 4.2.1), placed inside a tubular oven (model Split from Termolab, Fornos Eléctricos, Lda.) equipped with a 3-zone PID temperature controller (model MR13 from Shimaden). The type-K thermocouples used to measure and control the oven temperature were placed in the same radial position of the oven and close the column wall.

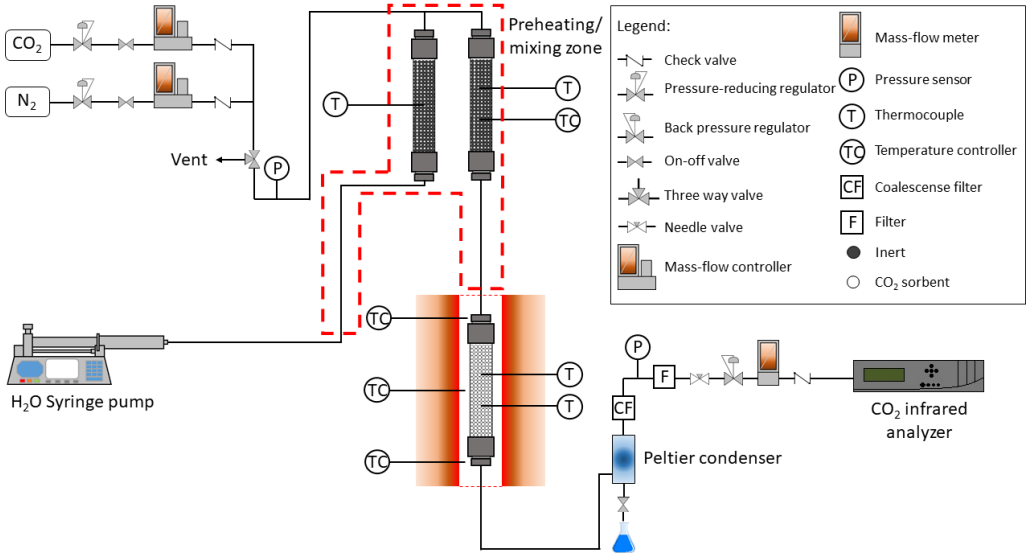

Fig. 4.2.1 - Scheme of the experimental setup.

Both CO_2 and N_2 were fed by mass flow controllers (model F201 from Bronkhorst High-Tec) while water was fed by a syringe pump (Chemyx, Nexus 6000) and evaporated before entering the column. The pressure in the system was monitored by means of 2 pressure transducers (model PMP 4010 from Druck) placed before and after the sorption bed.

The evolution of the CO_2 outlet dry composition was monitored by an online infrared based CO_2 analyser (Servomex, model 4210). For the cases in which steam was utilized, a Peltier based cold-trap was used between the sorption column and the analyser in order to condense water vapor.

The stainless steel column, closed in both ends with two stainless steel mesh (10-15 μm) discs, was filled with 2.8 g of fK-HTCGa MW. Two type-K thermocouples inserted laterally and radially centred (40 and 80 mm of the column length) were used with the aim of continuously monitoring the bed temperature. The temperature difference along the column length under inert atmosphere was negligible (< 1 K). In order to minimize pressure drop along the bed, sorbent particles with diameters between 354-600 μm were used.

4.2.2.5 Breakthrough experiments

At the beginning of the experimental campaign the sorbent was heated up to 673 K at a rate of 5 $K \cdot min^{-1}$ under a N_2 flow rate of 200 $mL_N \cdot min$ and it was kept under such conditions overnight in order to calcine the material (cK-HTCGa MW, see below), as it has been observed that hydrotalcite-based materials calcined at 673 K retain more CO_2 [23]. After this, the CO_2 breakthrough experiments were performed. The sequential experimental plan summarized in Table 4.2.1 was followed. First, several CO_2 sorption cycles were performed at 673 K, total pressure of 6 bar, total flow rate of 200 $mL_N \cdot min^{-1}$, CO_2 volume fraction of 0.15 (balanced with N_2) under dry conditions until the sorption working capacity was reached (i.e., no significant deactivation between cycles). Afterwards, in order to assess if further deactivation occurred between cycles at different conditions, the initial test at 673 K, total pressure of 6 bar, CO_2 volume fraction of 0.15 (balanced with N_2) under dry conditions was repeated periodically. Regeneration was always done at 673 K, total pressure of 1.3 bar and under pure dry N_2 atmosphere. Finally, it is worth mentioning that all dry sorption-desorption cycles lasted exactly the same time, 12 h (4 h of sorption and 8 h of desorption). In this way it was possible to carry out all dry tests consecutively in different days while keeping them comparable. If a more practical approach is prioritized in detriment of results comparability, much shorter sorption-desorption cycles would have certainly been adopted (e.g. sorption only until the breakthrough time followed

by regeneration until no significant amount of CO_2 is present in the outlet stream). For comparison purposes, the conditions used during the first 11 cycles (Table 4.2.1) were repeated for a K_2CO_3 promoted (17 wt%) hydrotalcite (Mg/Al molar ratio of 0.5) supplied by Sasol and here labelled as K-MG30, which is a reference commercial hydrotalcite that has been widely reported in the literature [2, 3, 18, 24].

The sorption-desorption cycles in the presence of steam were carried out over 45 min each. Also, to have higher steam feed stability, a total pressure of 6 bar was used during both sorption and desorption. Since the sorbent had to be regenerated overnight under dry N_2 atmosphere (total pressure of 1.3 bar), 4 dry sorption-desorption cycles of 45 min each were carried out in order to verify if the sorption working capacity under dry conditions was the same before doing the wet breakthrough tests. Then, for each steam composition, 6 sorption-desorption cycles were done. This set of experiments was designed with the aim of further understanding how cKHTCGa MW would behave under different conditions (total pressure, temperature and CO_2 and H_2O volume fraction in the feed) during sorption-enhanced processes.

Table 4.2.1 - Set of experiments adopted to study the effect of temperature, total pressure, CO_2 composition and steam presence on the sorption capacity of the cK-HTCGa MW material.

Experiment Number	Nº of Cycles	Sorption Temperature / K	Sorption Pressure / bar	y_{CO_2}/y_{H_2O} - Sorption[a]	y_{N_2}/y_{H_2O} - Desorption	Sorption-Desorption duration / h
1-11[b]	11	673	6	0.15/0	1/0	4-8
12	1	673	3	0.15/0	1/0	4-8
13	1	673	1.3	0.15/0	1/0	4-8
14	1	673	1.3	0.10/0	1/0	4-8
15	1	673	1.3	0.05/0	1/0	4-8
16-18	3	673	6	0.15/0	1/0	4-8
19	1	623	6	0.15/0	1/0	4-8
20	1	573	6	0.15/0	1/0	4-8
21	1	673	6	0.15/0	1/0	4-8
22[c]	1	673	1.3	-	1/0	Overnight

Table 4.2.1 - Set of experiments adopted to study the effect of temperature, total pressure, CO_2 composition and steam presence on the sorption capacity of the cK-HTCGa MW material (cont.).

Experiment Number	Nº of Cycles	Sorption Temperature / K	Sorption Pressure / bar	y_{CO_2}/y_{H_2O} - Sorption[a]	y_{N_2}/y_{H_2O} - Desorption	Sorption-Desorption duration / h
23-26	4	673	6	0.15/0	1/0	0.25-0.5
27[c]	1	673	6	-	0.95/0.05	2
28-33	6	673	6	0.15/0.05	0.95/0.05	0.25-0.5
34[c]	1	673	1.3	-	1/0	Overnight
35-38	4	673	6	0.15/0	1/0	0.25-0.5
39[c]	1	673	6	-	0.90/0.10	2
40-45	6	673	6	0.15/0.10	0.90/0.10	0.25-0.5
46[c]	1	673	1.3	-	1/0	Overnight

[a] Balanced with N_2.
[b] Stabilization cycles.
[c] Regeneration procedures carried out without CO_2 sorption.

4.2.2.6 Process metrics

The breakthrough time (t_{bp}) was defined as the moment at which 5% of the feed CO_2 concentration was reached in the outlet stream. Regarding the stoichiometric time, t_{st}, it was defined as follows [25]:

$$t_{st} = \int_0^{t_{test}} \left(1 - \frac{y_{CO_2}^{out}}{y_{CO_2}^{in}}\right) dt \quad \textbf{(4.2.1)}$$

where $y_{CO_2}^{out}$ and $y_{CO_2}^{in}$ are the volume fractions (dry basis) of CO_2 in the outlet and in the feed stream, respectively, and t_{test} is the total test time. The total sorption capacity, q_{tot}, can be calculated as:

$$q_{tot} = \frac{F_{CO_2}^{in} t_{st}}{m_{sorb}} \quad \textbf{(4.2.2)}$$

where $F_{CO_2}^{in}$ is the molar flow rate of CO_2 fed to the sorption column and m_{sorb} is the mass of sorbent after calcination (cK-HTCGa MW). The amount of CO_2 in the bed interparticle voids was found to be negligible. Blank experiments were performed in the same operational conditions as in Table 4.2.1, but replacing the sorption column with a 1/8" tube. In this way it was possible to determine the setup tubing space time, to correct both breakthrough and stoichiometric times and thus the total sorption capacity.

The sorbent bed usage efficiency (η) was calculated as:

$$\eta(\%) = \frac{q_{bp}}{q_{tot}} \times 100 = \frac{\int_0^{t_{bp}} \left(1 - \frac{y_{CO_2}^{out}}{y_{CO_2}^{in}}\right) dt}{\int_0^{t_{test}} \left(1 - \frac{y_{CO_2}^{out}}{y_{CO_2}^{in}}\right) dt} \times 100 \quad \textbf{(4.2.3)}$$

where q_{bp} is the sorption capacity until the breakthrough.

4.2.3 Results and discussion

4.2.3.1 Physicochemical characterization

4.2.3.1.1 TG/DTG/DSC analysis

Fig. 4.2.2 shows the TG/DTG/DSC profiles for sample fK-HTCGa MW. A total mass loss of 44% was observed, with three DTG peaks below 650 K and a less pronounced peak slightly above 1000 K. The first peak at 378 K should correspond to the removal of H_2O adsorbed on the external surface of the crystallites. As the temperature is increased, a series of partially overlapped peaks is recorded, which are usually ascribed to removal of water (from condensation of hydroxyl groups from the brucite-like layers) and of CO_2 from decomposition of the interlayer carbonate anions [26, 27]. The final peak above 1000 K could be possibly related to removal of residual carbonate anions trapped firmly in the calcined material [28]. Another possibility is that this peak is associated to the decomposition of bulk K_2CO_3 deposited on the surface of the material [29]. Based on this and on the findings of Reddy *et al.* [23] regarding the optimum calcination temperature, 673 K was used as the calcination temperature. Moreover, isothermal TG at this temperature showed that two hours of calcination are enough (see Appendix D, Fig. D.1), as mass loss is negligible for prolonged calcination times.

The analysis of the DSC profile clearly confirms the presence of the four already identified mass losses (TG), also identified as DTG peaks, and indicates that these mass losses are endothermic processes. Moreover, the amount of energy required for each species removal seems proportional to the mass loss as both DTG and DSC curves are approximately mirrors of each other.

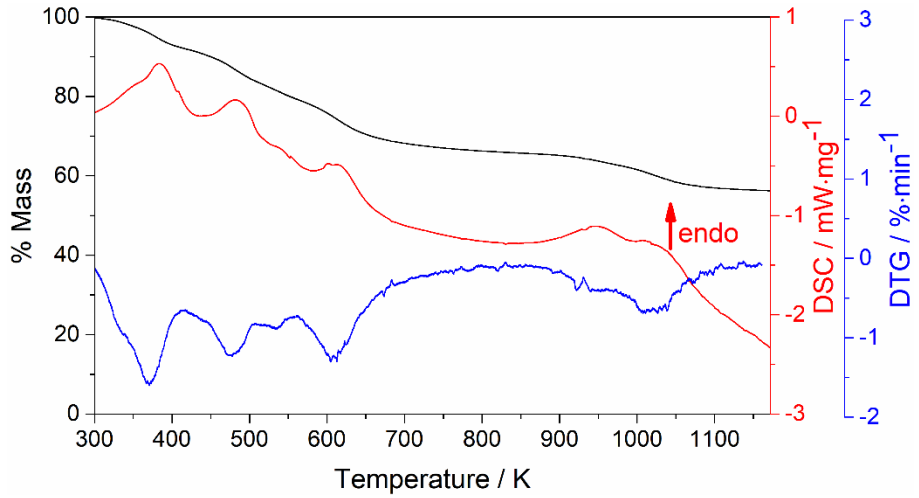

Fig. 4.2.2 - TG/DTG/DSC profiles for sample fK-HTCGa MW.

4.2.3.1.2 PXRD

The PXRD pattern of fK-HTCGa MW in Fig. 4.2.3 is clearly in line with the typical pattern observed for a hydrotalcite structure. The high intensity and sharpness of the (003) peak recorded right after 10º shows how highly crystalline the fresh sample is. For the calcined (cK-HTCGa MW) and used (after CO_2 breakthrough experiments; uK-HTCGA MW) samples this peak, as well as most of the characteristic peaks of the layered double hydroxide structure, disappear; this is attributed to the calcination at 673 K and the cyclic sorption-desorption tests at the same temperature that completely disrupt the crystalline layered double hydroxide structure into amorphous oxides, as suggested by the TG analysis and in previous works as well [8, 21, 30].

For both the calcined and the used samples, very similar PXRD patterns were recorded, the observed peaks corresponding mostly to MgO and small amounts of K_2CO_3. The presence of the rock salt structure of MgO is proved by the presence of diffraction maxima recorded at approximately 32.7, 43.2 and 62.5 º. The other weak peaks might be associated to the presence of K_2CO_3. As observed in a previous work [8] no diffraction maxima related to Al- or Ga-containing species is observed. This probably means that these cations became

dispersed in a defective rock salt structure or even formed dispersed non-crystalline spinel-like domains [31]. By comparing the patterns for both the calcined and the used samples a slight sharpening of the maxima is observed for the last sample. This is probably related to the fact that the use of this material on multiple dry and wet sorption-desorption cycles led to a slight increase in the crystallinity of the particles, as the heating time is markedly increased from the calcined to the used sample. In fact, it has been recently observed the occurrence of sintering at similar temperatures for MgO-based salts [32].

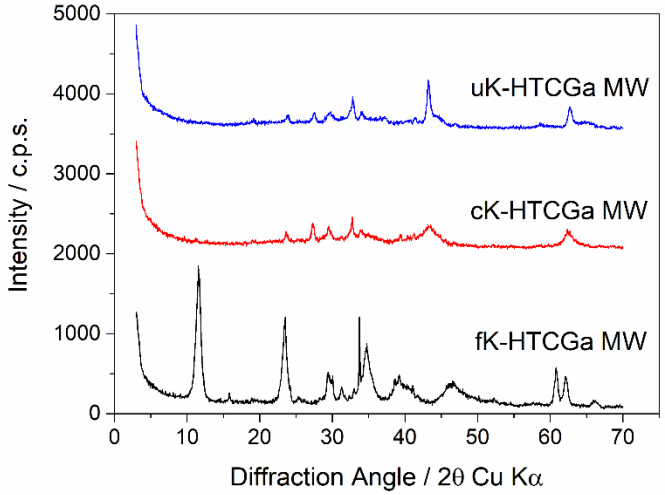

Fig. 4.2.3 - PXRD patterns of samples fK-HTCGa MW, cK-HTCGa MW and uK-HTCGa MW.

4.2.3.1.3 Physical adsorption of nitrogen at 77 K

For the determination of the specific surface areas (Table 4.2.2), adsorption-desorption isotherms of N_2 at 77 K were recorded for the three samples.

Table 4.2.2 - BET specific surface areas of the different samples determined by physical adsorption of N_2 at 77 K.

Sample	S_{BET} / $m^2 \cdot g^{-1}$
fK-HTCGa MW	28
cK-HTCGa MW	20
uK-HTCGa MW	8

Type II isotherms (IUPAC classification [33]) were observed for all the samples (Fig. 4.2.4; the scale in Fig. 4.2.4 (c)) is different as the observed slight hysteresis might be important), meaning that these materials are macroporous/mesoporous solids. The existence of micropores can be neglected since their volume is very low. In terms of BET specific surface areas, the fresh material (fK-HTCGa MW) already possesses a rather small surface area, as shown in Table 4.2.2. Calcination to prepare sample cK-HTCGa MW reduces the specific surface area by 28 % (similar to that obtained in our previous work [8]). For a pure hydrotalcite an increase of BET surface area with calcination would be expected. However, it is not expected that the hydrotalcite here used, which suffered several modifications (e.g. Al substitution by Ga and K impregnation) and high temperature thermal treatment, behaves as a pure hydrotalcite. It is possible that sintering has occurred during calcination at 673 K [32], justifying the surface area decline. Multiple CO_2 sorption-desorption cycles caused a considerable decrease in the BET surface area. This finding can be partially related to the slight increase in the crystallinity suggested by the PXRD diagrams, and so it can be also related to the significant morphological changes observed by SEM in the uK-HTCGa MW sample that are discussed below. Also, multiple high temperature sorption-desorption cycles might have given rise to fragmentation and blocking of the pores, which is supported by the SEM/EDS

results for uK-HTCGa MW. Furthermore, the above-mentioned sintering might have kept occurring up to higher extent.

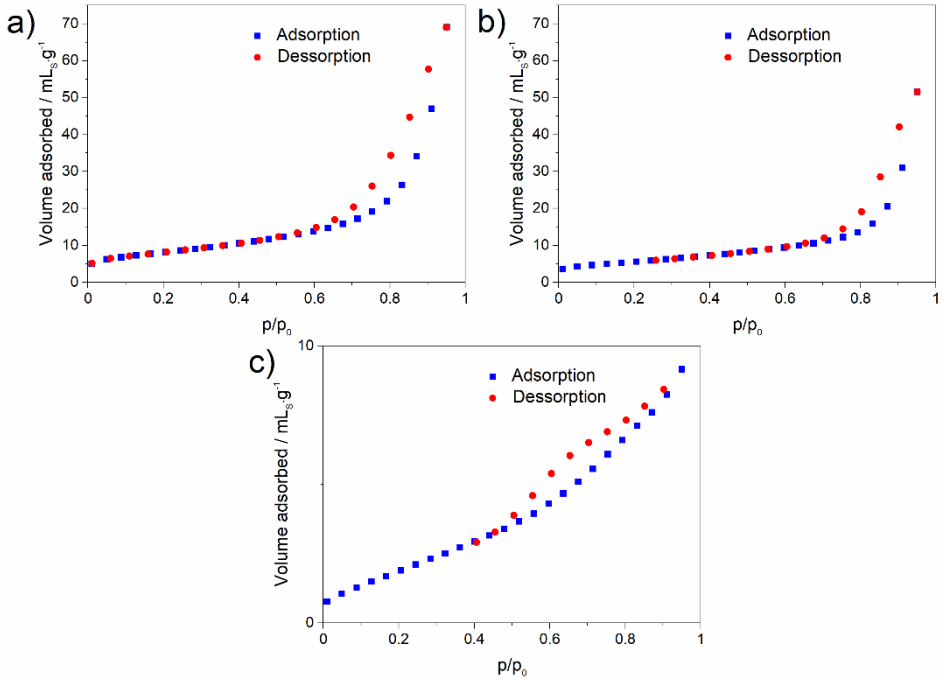

Fig. 4.2.4 - Adsorption/desorption isotherms of nitrogen over samples (a) fK-HTCGa MW, (b) cK-HTCGa MW and (c) uK-HTCGa MW.

4.2.3.1.4 FTIR

To further understand how calcination and multiple CO_2 sorption/desorption cycles structurally affected the hydrotalcite structure, the three samples were studied by FTIR spectroscopy (Fig. 4.2.5). The spectra in the 4000-1000 cm^{-1} are rather similar to each other. The band recorded above 3000 cm^{-1} (3140 and 3440 cm^{-1}) corresponds to the stretching mode of hydroxyl groups; this band is very broad because of the hydrogen bonds established between these surface hydroxyl groups and the water molecules, both in the interlayers and adsorbed on the external surface of the crystallites. There is a small difference, as the spectrum for the original sample shows a shoulder around 2927 cm^{-1} which has been ascribed [34] to the stretching mode of

hydroxyl groups hydrogen bonded to the interlayer carbonate anions; as these anions are absent in the other two samples, the shoulder is missing in their spectra. The weak feature around 2500-2200 cm^{-1} (2320 and 2427 cm^{-1}) is due to the miscancellation of the band due to atmospheric CO_2. The medium intensity band close to 1630 cm^{-1} (1640 cm^{-1} for both calcined and used sample) is due to the bending mode of water molecules, and the intense band at ca. 1370 cm^{-1} is due to mode ν_3 of carbonate species. It should be stressed that carbonate species are not expected to exist in the calcined and used samples, but because of the strong basicity of these solids, their exposure to atmosphere has probably led to sorption of CO_2 from the air, forming adsorbed CO_3^{2-} species responsible for this band; this phenomenon would obviously account for the bands due to the hydroxyl groups and water molecules recorded in the spectra of the calcined and used samples.

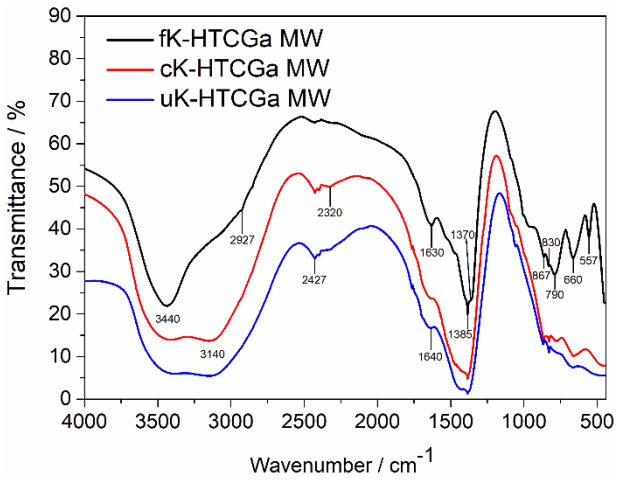

Fig. 4.2.5 - FTIR spectra of the three samples.

Below 1000 cm^{-1} some differences can be found. This is very important, as these bands (557, 660, 790, 830 and 867 cm^{-1}) are mostly due to vibrations involving metal-oxygen bonds, and the structure and spatial disposition of these bonds is very different in the hydrotalcite structure and in the oxides formed upon calcination.

A very sharp band is observed at 1385 cm^{-1} and is ascribed to the presence of nitrate impurities, ascribed to the KBr used to prepare the discs to record the spectra (also seen in blank discs containing only KBr).

4.2.3.1.5 SEM/EDS

SEM/EDS analyses of the three samples were carried out (Fig. 4.2.6) to further assess how calcination at 673 K and long term sorption/desorption cycles (around 300 hours) affected both surface morphology and its elemental composition.

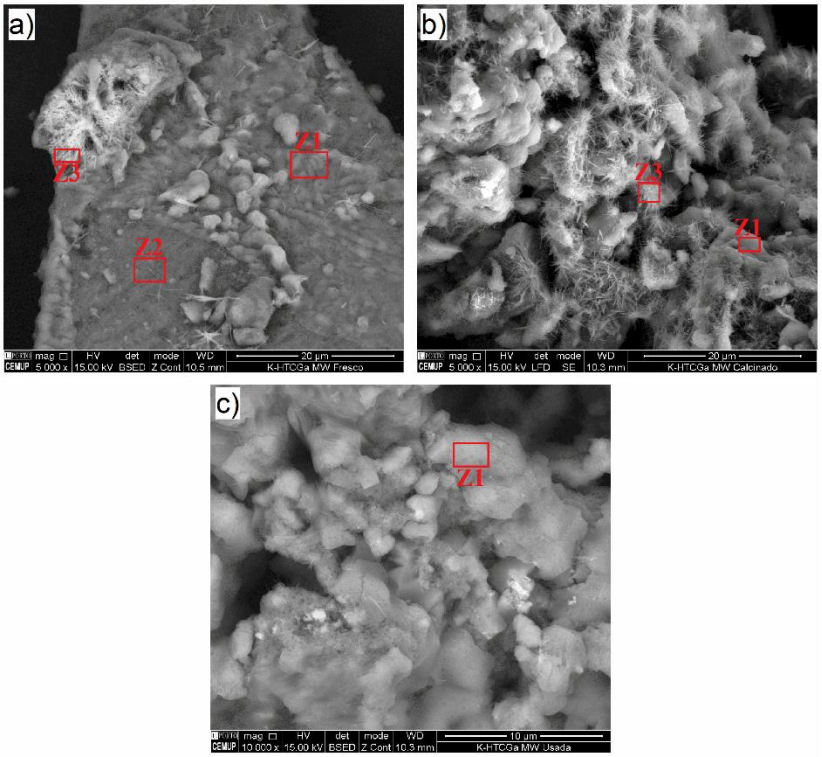

Fig. 4.2.6 - SEM images of samples (a) fK-HTCGa MW, (b) cK-HTCGa MW and (c) uK-HTCGa MW.

Three distinct zones were observed in the fK-HTCGa MW sample: large flat surfaces (Z1), irregular shaped zones (Z2) and needle-like structures (Z3). Those zones had already been identified in our previous work [8]. In the calcined

sample, cK-HTCGa MW, only zones Z1 and Z3 were found, while Z2 was absent, as previously found [8]. Finally, after the sorption experiments (sample uK-HTCGa MW), only Z1 was observed. Regarding the potassium rich needle-like structures (Z3), even though they are not found in the surface of the material, as observed in previous works [2, 21, 35], they can be noticed under the surface structures. In a previous work [8] it has been observed that the morphologies found on this material after dry CO_2 sorption (Z1, Z2 and Z3) are considerably more shape defined than the one found in this work on the same material but after wet CO_2 sorption, thus suggesting that the presence of steam significantly influenced the material surface morphology. In fact, the surface morphology that was dominant in uK-HTCGa MW, Z1, was highly rich in potassium, as observed by EDS (not shown).

In order to further understand the changes that the material underwent in terms of elemental composition, EDS elemental distribution maps were obtained for K, Mg, Al, Ga and O and are shown in Fig. 4.2.7.

By analyzing the oxygen maps (red) for the three samples, it can be observed that some areas are brighter than others and also that there are some completely dark areas. Since oxygen is all over the sample, the different intensities of red must be associated to something else. If it is considered that the EDS detector is not positioned exactly above the sample but in one of the corners of the analysis chamber and that the oxygen X-ray photons, produced through the interaction of the electron beam with surface oxygen, have relatively low energy, than it can be understood that the oxygen X-ray photons in the lower regions will not have enough energy to pass through the higher surfaces and reach the detector. On the other hand, the higher the region in which these photons are produced the lower the probability that they will have to go through other surfaces before reaching the analyzer. Therefore, the differences in brightness can be attributed to surface topography of the analyzed region for

each sample: the darker areas correspond to deeper regions while the bright red areas correspond to the higher regions, closer to the detector.

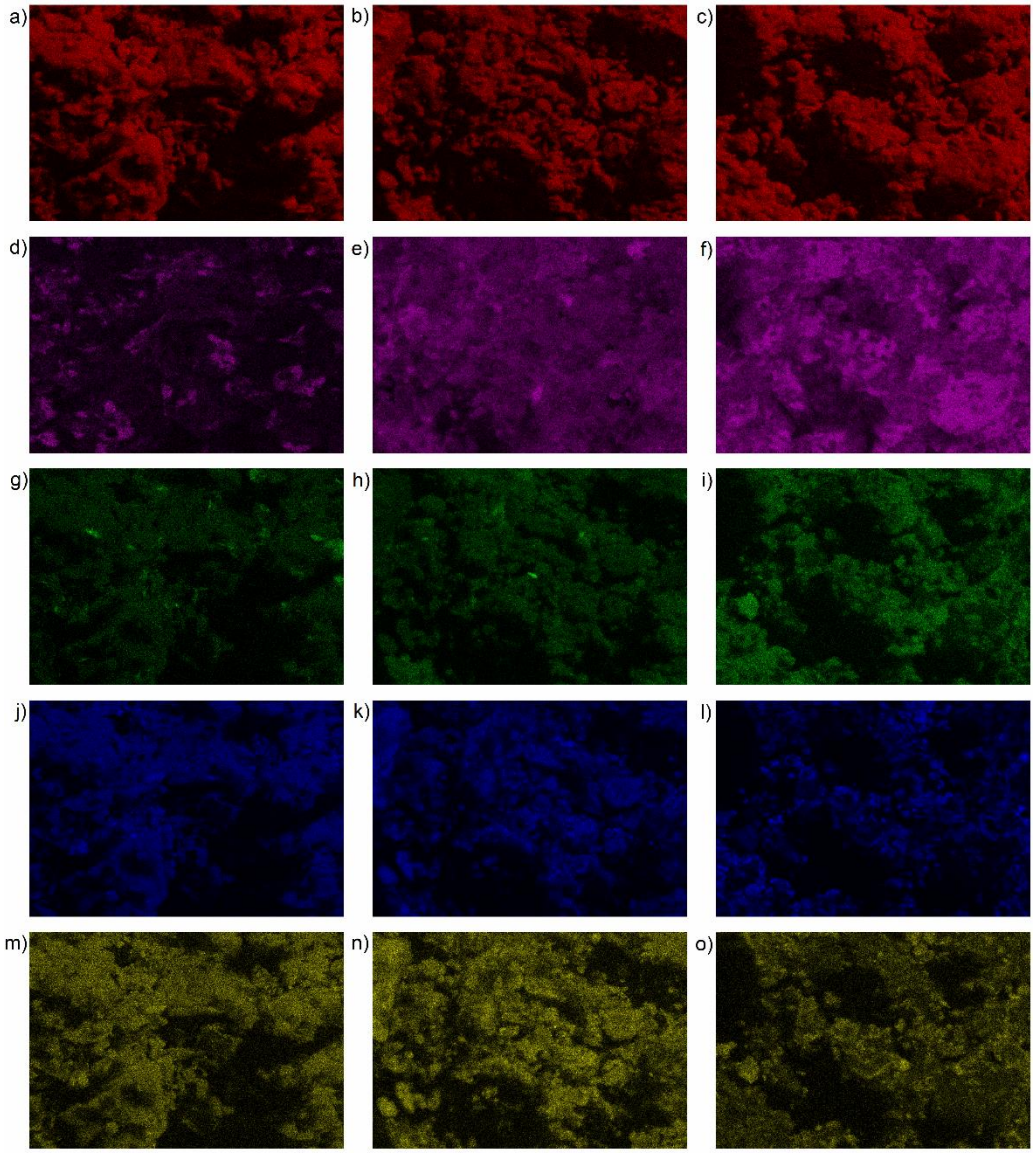

Fig. 4.2.7 - EDS elemental distribution maps (127 × 99 μm) of oxygen (a-c), potassium (d-f), gallium (g-i), magnesium (j-l) and aluminum (m-o) for samples fK-HTCGa MW (first column), cK-HTCGa MW (second column) and uK-HTCGa MW (third column).

The distribution of potassium across the surface is not homogeneous, especially in the fresh sample, as it had already been observed above and in

other works [2, 8, 21]. This might be related to non-homogeneous potassium impregnation. As it can be seen, the fresh sample shows poorer potassium distribution with high concentration in specific regions (brighter pink zones). On the other hand, a better surface potassium distribution is observed after calcination. Moreover, after wet sorption tests it appears that the hydrotalcite surface is covered by layers especially rich in potassium (the zones that are even brighter than in the calcined sample). Something very similar seems to happen to gallium. However, gallium is much better distributed in the fresh sample than potassium, probably because it was co-precipitated during synthesis instead of being impregnated after the material had been prepared. Since gallium X-ray photons are much more sensitive to surface topography than those of potassium, the surface topography has to be especially taken into consideration for this case. In fact, most of the dark regions identified in each sample for oxygen mapping can also be observed for the respective gallium maps. This can also be observed for both magnesium and aluminum, whose X-ray photons have similar energies. Therefore, the darker regions in the maps of these elements do not necessarily indicate the absence of those elements but the non-detection of their respective X-ray photons due to surface topography. Regarding magnesium and aluminum, they seem to be more homogeneously distributed (considering topography) in both the fresh and the calcined samples than potassium and gallium. Once again, this might be due to the fact that they co-precipitated during preparation. Nevertheless, variations in the Mg/(Al+Ga) ratio were quantitatively observed meaning that even co-precipitation did not occur homogeneously, as reported elsewhere [2, 8, 21]. After wet sorption tests, lower amounts of both magnesium and aluminum seem to exist. However, this may not be associated to a loss of these elements but instead to the mentioned partial surface rearrangement and coverage of those by the potassium and gallium rich layers.

4.2.3.2 CO_2 breakthrough experiments

4.2.3.2.1 Dry conditions

Several sorption-desorption tests were performed over the cK-HTCGa MW sample for ca. 300 hours. The first set of experiments was carried out under dry conditions at 673 K, 15 vol% of CO_2 balanced with N_2 and total pressure of 6 bar, and consisted of several cycles in order to lead the sorbent to reach its sorption working capacity. Although eleven stabilization cycles were carried out (see also Table 4.2.1), a stable sorption capacity was already reached after 7-8 cycles (Fig. 4.2.8 (a)). After these eleven cycles, other conditions were tested and in order to verify if the sorption working capacity remained constant, further stability verification cycles were performed. As observed in Fig. 4.2.8 (a), a slight loss of sorption capacity was observed between the 11^{th} cycle and the first verification cycle. During the second and third verification cycles there is a small recovery of the sorption capacity, although total recovery was not reached. In the fourth verification cycle a very similar capacity is observed meaning that no further deactivation was sustained during the lower temperature tests (see discussion below).

The temperature profiles for the several sorption-desorption cycles (see Appendix D, Fig. D.2) are coherent with the evolution of the sorption capacity throughout the several cycles since the higher the sorption capacity, the higher the maximum temperature. Moreover, these profiles show that regeneration of this sorbent is considerably slower than sorption. This had already been foressen in a previous work [8] due to the high steepness of the equilibrium isotherm measured for this material and the consequent highly dispersive regeneration front. For this reason atmospheric pressure was always used during regeneration (pressure swing in this case).

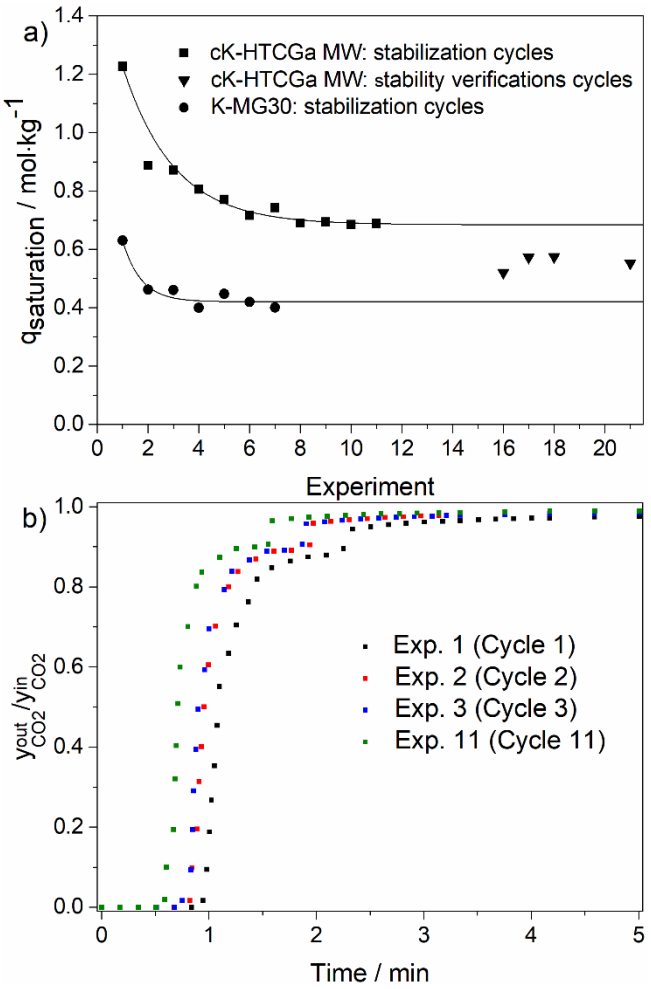

Fig. 4.2.8 - Stability analysis at 673 K, 15 vol% CO_2 balanced with N_2, under dry conditions and total pressure of 6 bar (a) in terms of sorption capacity for both cK-HTCGa MW and commercial K-MG30 and (b) in terms of breakthrough curves obtained during the stabilization cycles for cK-HTCGa MW.

The breakthrough curves shown in Fig. 4.2.8 (b) are also in line with the variation of sorption capacity during the stabilization cycles. The breakthrough time decreased more significantly from the first to the second cycle, while a much smaller decay was observed from the second to the third cycle. In fact, the breakthrough curves obtained in these two cycles are almost coincident. For this reason, besides these data only the breakthrough curve obtained in the last stabilization cycle is shown. Even though a considerable decrease of the

breakthrough time is observed between the third and the eleventh cycle, this difference resulted from slight cumulative decreases during the seven intermediate cycles. Moreover, a slight progressive increase of breakthrough curve steepness can be noticed throughout the cycles.

For comparison purposes, tests under the same conditions were carried out for the commercial K-MG30 material, used as reference. As it can be seen in Fig. 4.2.8 (a), while c-KHTCGa MW showed a first cycle capacity of 1.23 $mol \cdot kg^{-1}$, commercial K-MG30 only captured 0.63 $mol \cdot kg^{-1}$ in the first cycle. On the other hand, commercial K-MG30 reached its sorption working capacity faster than cK-HTCGa MW. Moreover, K-MG30 lost around 34% of sorption capacity between the first cycle and the last cycle while cK-HTCGa MW lost approximately 44% during the first 11 cycles. Nonetheless, the sorption working capacity for cK-HTCGa MW is approximately 65% higher than that of K-MG30.

The effect of the system total pressure during sorption was studied as well in terms of both sorption working capacity and stoichiometric time. As it can be seen in Fig. 4.2.9 (a) an increase in the total pressure increases both the sorption working capacity and the stoichiometric time. This increase of the stoichiometric time is also seen in Fig. 4.2.9 (b), where it is observed that at higher pressures the concentration front started exiting the reactor progressively later. Moreover, at higher pressures the concentration front became steeper, especially in the breakthrough tail region (above 1.5 min).

On the other hand, an increase of the CO_2 content in the feed (at 1.3 bar) also leads to an increase of the sorption working capacity but to a decrease of the stoichiometric time (Fig 4.2.10 (a)). This is also observed in Fig. 4.2.10 (b), being that this increase of the stoichiometric time with decreasing CO_2 contents in the feed is accompanied by the dispersion of the concentration front, especial at 5 vol%. Since the sorption equilibrium of cK-HTCGa MW is described by a favorable isotherm [8], the decrease of CO_2 content corresponds to an increase of the isotherm slope.

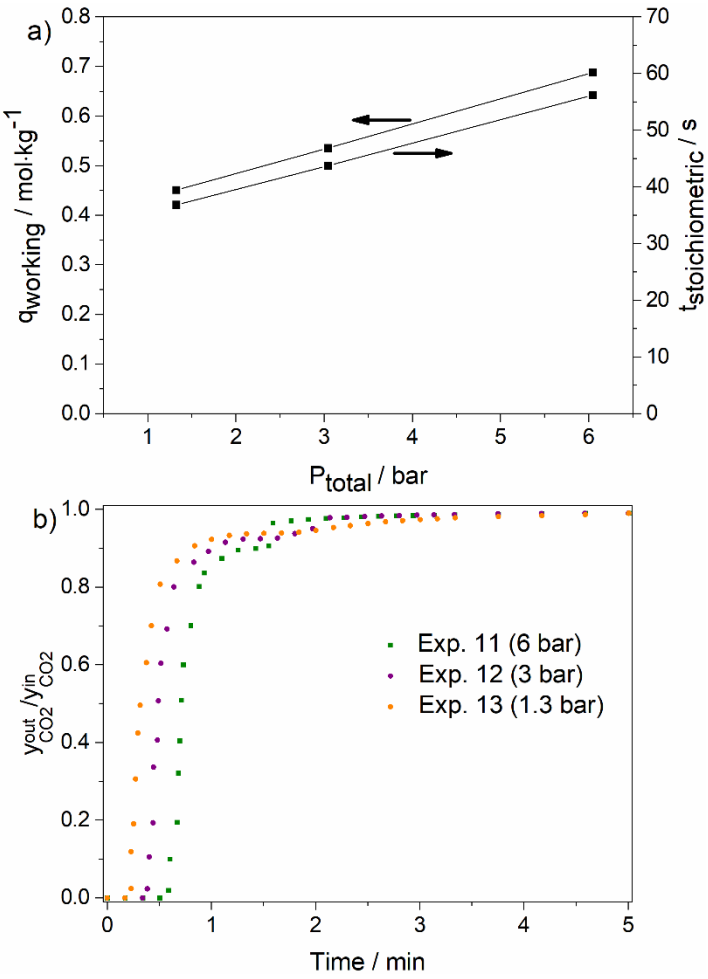

Fig. 4.2.9 - Effect of total pressure (experiments 11-13) on (a) the sorption working capacity and stoichiometric time and on (b) the breakthrough curves of cK-HTCGa MW at 673 K, 15 vol% CO_2 balanced with N_2 and under dry conditions.

Therefore, according to DeVault's equation [36], lower CO_2 contents imply lower concentration front velocities and, consequently, higher breakthrough (or stoichiometric) times and more dispersed concentration fronts, as can be seen in Fig. 4.2.10 (b). At higher total pressures the concentration front takes more time to reach the column outlet, as already discussed. Therefore, increasing the partial pressure of CO_2 during sorption leads to different results depending on the method used (increasing the total pressure of the system or increasing the

concentration of CO_2 in the feed stream), as previously observed [18]. The temperature profiles for these tests (see Appendix D, Fig. D.3 and D.4) are in line with the behavior observed for these runs, i.e., the higher the sorption capacities, the more significant will be the temperature increase.

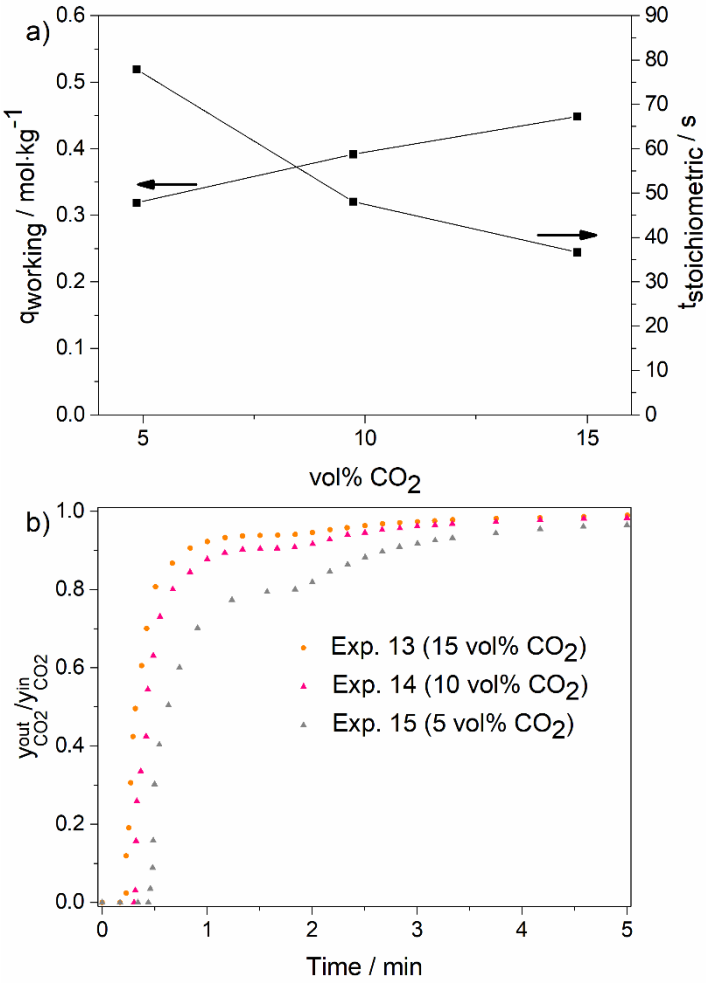

Fig. 4.2.10 - Effect of CO_2 content (experiments 13-15) on (a) the sorption working capacity and stoichiometric time and on (b) the breakthrough curves of cK-HTCGa MW at 673 K, 1.3 bar and under dry conditions.

After these tests at lower total pressures and lower CO_2 contents (experiments 12-15), three verification cycles at 673 K, 15 vol% of CO_2 balanced with N_2, total pressure of 6 bar and under dry conditions (experiments 16-18) were performed; it was observed that deactivation of the sorbent had occured (Fig. 4.2.8). Since the CO_2 capture that occured during these last 4 tests at lower total pressures and lower CO_2 contents was considerably lower than that observed during the last stabilization cycles at 6 bar, this deactivation cannot be attributed to a higher CO_2 coverage of the hydrotalcite active sites. However, it might be related to the different CO_2 sorption dynamics that might take place at lower total pressures and/or lower CO_2 contents. A fourth verification test (experiment 21) was carried out after the different temperature tests and a sorption capacity very similar to those obtained during the previous verification cycles was observed. Therefore, it can be concluded that varying the sorption temperature did not cause any further deactivation.

On the other hand, varying the temperature did affect both sorption working capacity and breakthrough/stoichiometric time as it can be observed in Fig. 4.2.11. For total sorption pressure of 6 bar, higher temperatures led to higher CO_2 capture and stoichiometric times, in agreement with the respective temperature profiles (Appendix D, Fig. D.5). In this case, the breakthrough curves are practically parallel during the full duration of the test (Fig. 4.2.11 (b)). In terms of sorption capacity tendency, these results are in line with other reports in the literature for similar materials in similar temperature ranges [2, 3, 37]. Since regeneration was always performed at 673 K for 8 h, these variations in CO_2 uptake are only due to the variation of temperature during sorption.

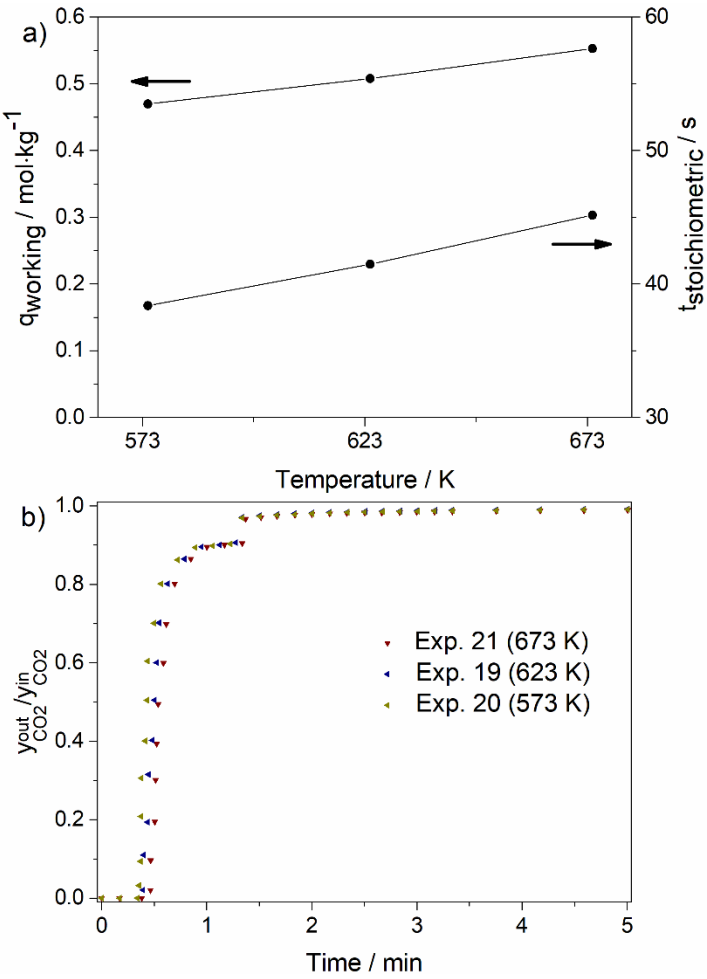

Fig. 4.2.11 - Effect of temperature on (a) the sorption working capacity and stoichiometric time and on (b) the breakthrough curves of cK-HTCGa MW at 15 vol% of CO_2 balanced with N_2, under dry conditions and at total pressure of 6 bar (experiments 19-21).

4.2.3.2.2 Wet conditions

The beneficial effect of steam on the performance of hydrotalcites during CO_2 capture has been reported in the literature [17-20]. For this reason and in order to better assess its effect with cK-HTCGa MW, breakthrough tests under different steam contents were performed and both CO_2 sorption capacity and stoichiometric time were compared.

Before the short breakthrough tests (15 min of sorption and 30 min of regeneration) under wet conditions and for comparison reasons, equally short dry breakthroughs (experiments 23-26) were carried out. From data in Fig. 4.2.12 it can be observed that an increase of the steam content up to 10 vol% considerably enhances the performance of cK-HTCGa MW by increasing the stoichiometric time and consequently the sorption capacity, a conclusion that can be also reached from the corresponding temperature profiles (see Appendix D, Fig. D.7). Even only 5 vol% of steam already increased the sorption working capacity in almost 90%. When 10 vol% of steam was used the sorption working capacity further increased 60% approximately, resulting a total increase of 200% in the sorption capacity when 10 vol% of steam was used instead of dry conditions. In fact, the CO_2 sorption capacity attained with 10 vol% of steam during the 45 minutes cycles is very similar to those attained during the last 4 hours stabilization cycles performed at the beginning of the experimental campaign under dry conditions (experiments 8-11), 0.7 $mol \cdot kg^{-1}$. However, besides the considerable difference in cycle duration, wet desorption was performed at 6 bar instead of 1.3 bar for practical reasons. For the dry conditions it would probably be negative to regenerate the sorbent at 6 bar since it would make the process even slower. However, in the presence of steam it may not be completely true. It has been observed in previous works [20, 38, 39] that some sorption sites can only be regenerated in the presence of steam since the strongly bonded bidentate carbonate species can only be removed through hydroxylation. Therefore, even if higher regeneration pressures slowed down the removal of CO_2 that normally occurs under dry conditions, it probably accelerated the hydroxylation of the sites, during wet desorption, where strongly bonded carbonates where formed. From this point of view, to perform wet regeneration at 6 bar could have been positive.

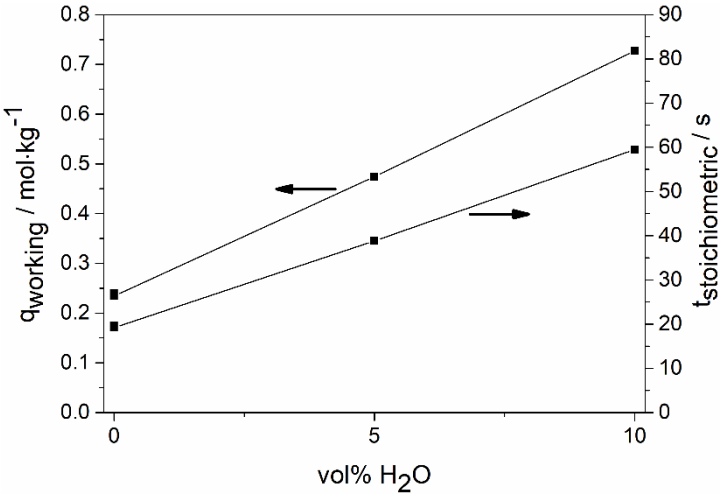

Fig. 4.2.12 - Effect of H_2O content during both sorption and regeneration on the CO_2 sorption working capacity and stoichiometric time of cK-HTCGa MW after 6 cycles at 673 K, 6 bar and 15 vol% of CO_2 balanced with N_2 (experiments 26, 33, 38 and 45).

A final consideration about these results having in mind the SEM/EDS analysis performed might be helpful. As observed, uK-HTCGa MW showed different surface morphologies and surface elemental composition. Specifically, a mobilization of potassium and gallium to the sorbent surface took place, leading to partial coverage of magnesium and aluminum. These changes that occurred during the experimental campaign are likely to be mainly attributed to the use of steam, as observed elsewhere [35], since previously [8] studied dry CO_2 sorption over this same material did not result in such morphological and compositional surface changes. Therefore, these phenomena suggest a changing in the accessibility of CO_2 to the different active sites. In other words, sites that were previously of more difficult access to CO_2 might have become more accessible and vice versa. This could have implications in terms of sorption capacity and sorption kinetics, which could have contributed to the higher CO_2 capture under wet conditions.

4.2.3.2.3 Bed usage efficiency

Knowing which conditions allow the maximization of bed usage is of great importance as well [25]. In other words, it is relevant identifying the conditions that maximize the amount of captured CO_2 before breakthrough, highly important for continuous operation processes such as sorption-enhanced processes [40], relatively to the total amount of CO_2 that might be retained (Eq. (4.2.3)). This ratio will be higher under conditions that allow steeper concentration fronts, meaning narrower mass transfer zones [25]. The bed usage efficiency was calculated for the tests performed under dry conditions and it is included in Fig. 4.2.13 by the same order as in Table 4.2.1.

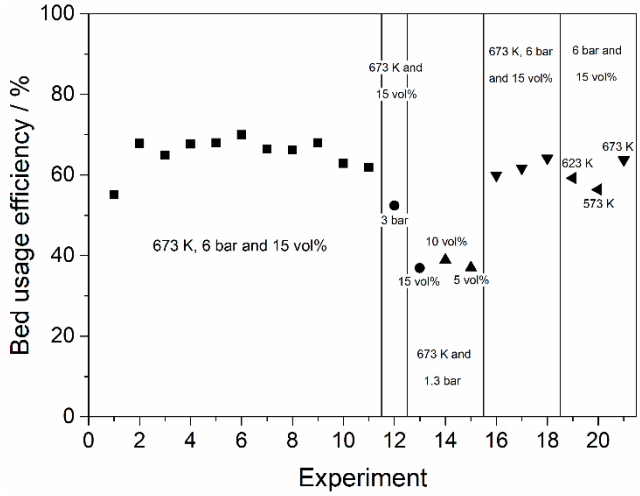

Fig. 4.2.13 - Bed usage efficiency for the several sorption tests performed under dry conditions on sample cK-HTCGa MW (meaning of symbols as in Figs. 4.2.8-11).

A bed usage of 55% was obtained during the first sorption cycle on sample cK-HTCGa MW, increasing to 60-70% during the following stabilization cycles. Even though the breakthrough time during the first cycle is considerably higher than in the subsequent stabilization cycles, as observed in Fig. 4.2.8, the post-breakthrough curve is more extended as well and that is the reason for the slightly lower bed usage efficiency. As for the stabilization cycles (i.e., until experiment 11), a progressively slight decrease in efficiency is observed, as the

breakthrough time decreases more than the mass transfer zone width (stoichiometric time). Regarding the stability verification cycles (runs 16-18 and 21), they showed very similar bed usage efficiencies.

As already discussed, when the total pressure is decreased (experiments 12-13) the mass transfer zone becomes broader, and consequently the bed usage efficiency drops significantly down to 37% at 1.3 bar. The progressively more extended breakthrough tails observed with decreasing total pressures (above 1.5 min in Fig. 4.2.9 (b)) were the main responsible for this broadening of the mass transfer zone and consequent decrease of bed usage efficiency. Regarding the CO_2 content (experiments 14-15), it did not affect significantly the sorbent bed usage, as lower CO_2 concentrations result not only in longer breakthroughs but also in a more dispersed concentration fronts (Fig. 4.2.10 (b)). Finally, efficiencies for different temperatures at 6 bar were determined as well, being that a progressive increase with temperature (experiments 20, 19 and 21, in order of increasing temperature) from around 56% up to around 64% was observed. In this case, as already mentioned, this difference is mostly associated to the increasing breakthrough times with higher temperatures and much less associated to differences in terms of mass transfer zone width.

Finally, the effect of steam on the efficiency of bed usage was studied as well. However, since the duration of these sorption cycles was only 15 minutes these efficiencies are only comparable among themselves and not with the efficiencies obtained during the 4 h dry cycles. It was observed that higher bed usages can be obtained under wet conditions. While under 5 vol% H_2O the bed usage efficiency varied between 55-58%, under 10 vol% H_2O efficiencies between 68-78% were attained. This means that the relative amount of CO_2 that is retained before the breakthrough increases in the presence of steam. The higher sorption capacities measured under wet conditions would mean a higher slope of the isotherm for the same CO_2 concentration, thus resulting in a lower compression of the concentration front and lower bed usage efficiencies. The

opposite trend is observed for the efficiency. Considering once more the surface structural changes observed by SEM/EDS, these changes might have resulted in a higher fraction of fast CO_2 sorption, which would result in a compressed concentration front, leading, consequently, to the higher bed usage efficiencies observed under wet conditions. In any case, this would only be known for sure if a deeper mechanistic analysis was done.

4.2.4 Conclusions

It was observed for the first time that cK-HTCGa MW presented a sorption working capacity 65% higher than that of K-MG30 and of most hydrotalcites reported in the literature. As expected, higher total pressures allowed to reach higher sorption working capacities and stoichiometric times. Moreover, they also allowed the compression of the concentration front, which resulted in higher bed usage efficiencies. Lower CO_2 concentration in the feed resulted in lower sorption capacities. Also, the increase of both breakthrough time and mass transfer zone counterbalance each other and the bed usage efficiency remains practically constant regardless the concentration of CO_2 fed to the sorption column.

On varying the sorption temperature between 573 K and 673 K at 6 bar it was clear that higher temperatures led to higher sorption capacities and stoichiometric times. Regarding the bed usage efficiency, it decreased linearly with the decrease of temperature. Thus, it was shown that operating at 673 K was benefitial for CO_2 sorption over cK-HTCGa MW.

Finally, it was observed for the first time that cK-HTCGa MW benefits from the presence of H_2O during both sorption and desorption in terms of sorption capacity and stoichiometric time. Compared to dry conditions, the use of 5 vol% and 10 vol% H_2O increased the sorption capacity ca. 90% and 200%, respectively. A sorption working capacity of 0.73 $mol \cdot kg^{-1}$ was obtained in the

presence of 10 vol% H_2O, which is outsanding considering that wet sorption-desorption cycles only lasted 45 min, 15 min of sorption and 30 min of regeneration. The presence of steam even enhanced the bed usage efficiency, which might be associated to the mechanism of CO_2 capture on sample cK-HTCGa MW under wet conditions; it is also possible that these wet conditions during sorption favor the fast sorption of CO_2 in detriment of the slower CO_2 retention. In fact, EDS elemental distribution mapping showed that both potassium and gallium were mobilized towards the sorbent surface under wet conditions, which made these basic sites more easily acessible.

It can be concluded that cK-HTCGa MW is significantly advantageous in several aspects when compared to commercial materials, being the most notorious one its remarkable sorption capacity. Furthermore, it is very adequate for pre-combustion CO_2 capture applications such as sorption-enhanced steam reforming, as its multicycle performance is enhanced under high pressures and temperatures and even more in the presence of H_2O, which are very common conditions in this kind of processes.

4.2.5 References

[1] A. de Roy, C.F., J.P. Besse, *in: V. Rives (Ed.), Layered Double Hydroxides: Synthesis and post synthesis modification*, in *Layered Double Hydroxides: Present and Future*. 2001, Nova Science Publishers Inc: New York. p. 1-39.

[2] Oliveira, E.L.G., C.A. Grande, and A.E. Rodrigues, *CO2 sorption on hydrotalcite and alkali-modified (K and Cs) hydrotalcites at high temperatures.* Separation and Purification Technology, 2008, 62(1), 137-147.

[3] Coenen, K., F. Gallucci, P. Cobden, E. van Dijk, E. Hensen, and M. van Sint Annaland, *Chemisorption working capacity and kinetics of CO2 and H2O of hydrotalcite-based adsorbents for sorption-enhanced water-gas-shift applications.* Chemical Engineering Journal, 2016, 293, 9-23.

[4] Silva, J.M., M.A. Soria, and L.M. Madeira, *Challenges and strategies for optimization of glycerol steam reforming process.* Renewable and Sustainable Energy Reviews, 2015, 42, 1187-1213.

[5] Martunus, M.R. Othman, and W.J.N. Fernando, *Elevated temperature carbon dioxide capture via reinforced metal hydrotalcite.* Microporous and Mesoporous Materials, 2011, 138(1–3), 110-117.

[6] Hutson, N.D. and B.C. Attwood, *High temperature adsorption of CO2 on various hydrotalcite-like compounds.* Adsorption, 2008, 14(6), 781-789.

[7] Wang, Q., H.H. Tay, D.J.W. Ng, L. Chen, Y. Liu, J. Chang, Z. Zhong, J. Luo, and A. Borgna, *The Effect of Trivalent Cations on the Performance of Mg-M-CO3 Layered Double Hydroxides for High-Temperature CO2 Capture.* ChemSusChem, 2010, 3(8), 965-973.

[8] Silva, J.M., R. Trujillano, V. Rives, M.A. Soria, and L.M. Madeira, *High temperature CO2 sorption over modified hydrotalcites.* Chemical Engineering Journal, 2017, 325(Supplement C), 25-34.

[9] Wang, Q., Z. Wu, H.H. Tay, L. Chen, Y. Liu, J. Chang, Z. Zhong, J. Luo, and A. Borgna, *High temperature adsorption of CO2 on Mg–Al hydrotalcite: Effect of the charge compensating anions and the synthesis pH.* Catalysis Today, 2011, 164(1), 198-203.

[10] Kim, S., S.G. Jeon, and K.B. Lee, *High-Temperature CO2 Sorption on Hydrotalcite Having a High Mg/Al Molar Ratio.* ACS Applied Materials & Interfaces, 2016, 8(9), 5763-5767.

[11] Lee, J.-Y., G.-H. Gwak, H.-M. Kim, T.-i. Kim, G.J. Lee, and J.-M. Oh, *Synthesis of hydrotalcite type layered double hydroxide with various Mg/Al ratio and surface charge under controlled reaction condition.* Applied Clay Science, 2016, 134, Part 1, 44-49.

[12] Hanif, A., S. Dasgupta, S. Divekar, A. Arya, M.O. Garg, and A. Nanoti, *A study on high temperature CO2 capture by improved hydrotalcite sorbents.* Chemical Engineering Journal, 2014, 236, 91-99.

[13] Tichit, D., A. Rolland, F. Prinetto, G. Fetter, M. de Jesus Martinez-Ortiz, M.A. Valenzuela, and P. Bosch, *Comparison of the structural and acid-base properties of Ga- and Al-containing layered double hydroxides obtained by microwave irradiation and conventional ageing of synthesis gels.* Journal of Materials Chemistry, 2002, 12(12), 3832-3838.

[14] Hutson, N.D., S.A. Speakman, and E.A. Payzant, *Structural Effects on the High Temperature Adsorption of CO2 on a Synthetic Hydrotalcite.* Chemistry of Materials, 2004, 16(21), 4135-4143.

[15] Wang, Q., J. Luo, Z. Zhong, and A. Borgna, *CO2 capture by solid adsorbents and their applications: current status and new trends.* Energy & Environmental Science, 2011, 4(1), 42-55.

[16] Yong, Z., Mata, and A.E. Rodrigues, *Adsorption of Carbon Dioxide onto Hydrotalcite-like Compounds (HTlcs) at High Temperatures.* Industrial & Engineering Chemistry Research, 2001, 40(1), 204-209.

[17] Martunus, Z. Helwani, A.D. Wiheeb, J. Kim, and M.R. Othman, *Improved carbon dioxide capture using metal reinforced hydrotalcite under wet conditions.* International Journal of Greenhouse Gas Control, 2012, 7, 127-136.

[18] Soria, M.A., S. Tosti, A. Mendes, and L.M. Madeira, *Enhancing the low temperature water–gas shift reaction through a hybrid sorption-enhanced membrane reactor for high-purity hydrogen production.* Fuel, 2015, 159, 854-863.

[19] Coenen, K., F. Gallucci, G. Pio, P. Cobden, E. van Dijk, E. Hensen, and M. van Sint Annaland, *On the influence of steam on the CO2 chemisorption capacity of a hydrotalcite-based adsorbent for SEWGS applications.* Chemical Engineering Journal, 2017, 314, 554-569.

[20] Coenen, K., F. Gallucci, B. Mezari, E. Hensen, and M. van Sint Annaland, *An in-situ IR study on the adsorption of CO2 and H2O on hydrotalcites.* Journal of CO2 Utilization, 2018, 24, 228-239.

[21] Miguel, C.V., R. Trujillano, V. Rives, M.A. Vicente, A.F.P. Ferreira, A.E. Rodrigues, A. Mendes, and L.M. Madeira, *High temperature CO2 sorption with gallium-substituted and promoted hydrotalcites.* Separation and Purification Technology, 2014, 127, 202-211.

[22] Boon, J., P.D. Cobden, H.A.J. van Dijk, C. Hoogland, E.R. van Selow, and M. van Sint Annaland, *Isotherm model for high-temperature, high-pressure adsorption of and on K-promoted hydrotalcite.* Chemical Engineering Journal, 2014, 248, 406-414.

[23] Ram Reddy, M.K., Z.P. Xu, G.Q. Lu, and J.C. Diniz da Costa, *Layered Double Hydroxides for CO2 Capture: Structure Evolution and Regeneration.* Industrial & Engineering Chemistry Research, 2006, 45(22), 7504-7509.

[24] Maroño, M., Y. Torreiro, and L. Gutierrez, *Influence of steam partial pressures in the CO2 capture capacity of K-doped hydrotalcite-based sorbents for their application to SEWGS processes.* International Journal of Greenhouse Gas Control, 2013, 14(0), 183-192.

[25] W.L. McCabe, J.C.S., P. Harriot *Unit Operations of Chemical Engineering*. fifth ed. 1993: McGraw-Hill.

[26] Rives, V., *Characterisation of layered double hydroxides and their decomposition products.* Materials Chemistry and Physics, 2002, 75(1), 19-25.

[27] Rives, V., *Comment on "Direct Observation of a Metastable Solid Phase of Mg/Al/CO3-Layered Double Hydroxide by Means of High-Temperature in Situ Powder XRD and DTA/TG"1.* Inorganic Chemistry, 1999, 38(2), 406-407.

[28] Hibino, T., Y. Yamashita, K. Kosuge, and A. Tsunashima, *Decarbonation behavior of Mg-Al-CO3 hydrotalcite-like compounds during heat treatment.* Clays and Clay Minerals, 1995, 43(4), 427-432.

[29] Walspurger, S., L. Boels, P.D. Cobden, G.D. Elzinga, W.G. Haije, and R.W.v.d. Brink, *The Crucial Role of the K+–Aluminium Oxide Interaction in K+- Promoted Alumina- and Hydrotalcite- Based Materials for CO2 Sorption at High Temperatures.* ChemSusChem, 2008, 1(7), 643-650.

[30] Rives, V., *in: V. Rives (Ed.), Study of Layered Double Hydroxides by thermal methods*, in *Layered Double Hydroxides: Present and Future*. 2001, Nova Science Publishers Inc: New York. p. 127-151.

[31] Labajos, F.M., V. Rives, and M.A. Ulibarri, *Effect of hydrothermal and thermal treatments on the physicochemical properties of Mg-Al hydrotalcite-like materials.* Journal of Materials Science, 1992, 27(6), 1546-1552.

[32] Jin, S., K. Ho, A.-T. Vu, and C.-H. Lee, *Salt-Composition-Controlled Precipitation of Triple-Salt-Promoted MgO with Enhanced CO2 Sorption Rate and Working Capacity.* Energy & Fuels, 2017, 31(9), 9725-9735.

[33] Brunauer, S., L.S. Deming, W.E. Deming, and E. Teller, *On a Theory of the van der Waals Adsorption of Gases.* Journal of the American Chemical Society, 1940, 62(7), 1723-1732.

[34] Kloprogge, J.T. and R.L. Frost, *Fourier Transform Infrared and Raman Spectroscopic Study of the Local Structure of Mg-, Ni-, and Co-Hydrotalcites.* Journal of Solid State Chemistry, 1999, 146(2), 506-515.

[35] Miguel, C.V., M.A. Soria, A. Mendes, and L.M. Madeira, *A sorptive reactor for CO2 capture and conversion to renewable methane.* Chemical Engineering Journal, 2017, 322, 590-602.

[36] DeVault, D., *The Theory of Chromatography.* Journal of the American Chemical Society, 1943, 65(4), 532-540.

[37] Coenen, K., F. Gallucci, P. Cobden, E. van Dijk, E. Hensen, and M. van Sint Annaland, *Influence of material composition on the CO2 and H2O adsorption capacities and kinetics of potassium-promoted sorbents.* Chemical Engineering Journal, 2018, 334, 2115-2123.

[38] Ram Reddy, M.K., Z.P. Xu, and J.C. Diniz da Costa, *Influence of Water on High-Temperature CO2 Capture Using Layered Double Hydroxide Derivatives.* Industrial & Engineering Chemistry Research, 2008, 47(8), 2630-2635.

[39] Ding, Y. and E. Alpay, *Equilibria and kinetics of CO2 adsorption on hydrotalcite adsorbent.* Chemical Engineering Science, 2000, 55(17), 3461-3474.

[40] Rodrigues, A.E., L.M. Madeira, R. Faria, and Y.J. Wu, *Sorption Enhanced Reaction Processes*. 2017: World Scientific Publishing Company Pte Limited.

Chapter 5. Experimental Analysis of Glycerol Steam Reforming for H_2 Production

This chapter includes the experimental assessment of glycerol steam reforming. In subchapter 5.1 the glycerol steam reforming is studied in a traditional reactor. In subchapter 5.2 both sorption-enhanced reactor and sorption-enhanced membrane reactor are applied to glycerol steam reforming.

5.1 Low Temperature Glycerol Steam Reforming Over a Rh-based Catalyst Combined with Oxidative Regeneration

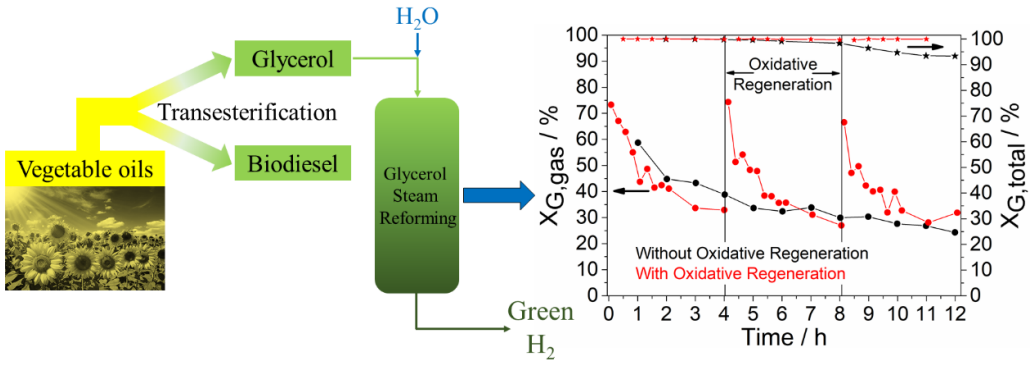

- *Low temperature GSR was combined with oxidative regeneration of the Rh catalyst.*
- *Oxidative regeneration allowed almost full recovery of the catalytic activity.*
- *Cyclic oxidative regeneration allowed to keep total glycerol conversions above 99%.*
- *Superior H_2 production was observed when oxidative regeneration was performed.*

A Rh on alumina catalyst was tested for glycerol steam reforming at 673 K, 4.5 bar and molar water/glycerol feed ratio (WGFR) of 19. Even though a conversion of glycerol into carbon-containing gaseous products of around 73% was observed at the beginning of the reaction, a progressive deactivation was noticed afterwards, less than 40% of glycerol being converted into carbon-containing gas products after 4 h of time-on-stream. On the other hand, the total glycerol conversion remained above 99% during the same period, thus indicating the increasing formation of coke and/or liquid products over time. The total glycerol conversion started to decrease more pronouncedly only after 6 h, reaching a value of approximately 92% after 13 h. SEM/EDS analysis of the used catalyst showed the presence of carbon deposits, Raman spectroscopy evidencing the dominant presence of ordered carbon, probably graphitic. Therefore, oxidative regeneration with air at 773 K was carried out. This temperature proved to be enough to gasify all removable coke (according to temperature-programmed oxidation results). After regeneration, almost complete recovery of catalytic performance was observed. In fact, maximum H_2 yields between 2.1 and 2.6 $mol \cdot mol_{fed\ glycerol}^{-1}$ were observed for the reaction cycles performed with intermediate oxidative regenerations. By combining glycerol steam reforming with periodic oxidative regeneration of the catalyst, superior average performance, compared to the case where no oxidative regeneration was used, was attained.

The contents of this chapter were adapted from: Silva, J.M., L.S. Ribeiro, J.J.M. Órfão, M.A. Soria, and L.M. Madeira, *Low temperature glycerol steam reforming over a Rh-based catalyst combined with oxidative regeneration.* Submitted for publication.

5.1.1 Introduction

Worldwide glycerol production has been on a massively increasing trend over the last decades and the main reason for that has been the global growth of the biodiesel industry [1]. While in 1999 the main glycerol supplier was the oleochemicals industry, in 2009 the biodiesel industry had become the main glycerol supplier [2]. Biodiesel worldwide production went from 774 thousand metric tons in 2000 up to approximately 30 000 thousand metric tons in 2016 [3], representing an increase of almost 40-fold. The use of biodiesel-derived glycerol not only has the potential of reducing society's dependence on non-renewable resources, as it would promote both commercialization and further development of biodiesel production, as well as the development of integrated biorefineries [4].

Hydrogen is a clean energy source whose demand is expected to greatly increase in the future due to the technological advances in the fuel cell industry [1], driven by the growing environmental concerns associated to the use of fossil fuels; the amount of hydrogen that can be produced from glycerol is considerable, as 1 glycerol molecule contains 8 hydrogen atoms. The use of biodiesel-derived glycerol in H_2 production would not only benefit the economic competitiveness of biodiesel, but would also be advantageous in several ways when compared to the use of non-renewable feedstocks, such as methane or naphtha. These advantages are not only environmental, but also processual. While steam reforming of CH_4 leads to the production of 4 moles of H_2 per mole of reacted CH_4, glycerol steam reforming (GSR) allows the generation of 7 moles of H_2 per mole of converted glycerol. This process consists of 2 major steps: glycerol decomposition into syngas – CO and H_2 (Eq. (5.1.1)) – followed by the water-gas shift (WGS) reaction (Eq. (5.1.2)).

$$C_3H_8O_3 \rightarrow 3CO + 4H_2 \quad (\Delta H_r^{298\,K} = 251\ kJ \cdot mol^{-1}) \qquad \textbf{(5.1.1)}$$

$$CO + H_2O \rightleftharpoons H_2 + CO_2 \quad (\Delta H_r^{298\,K} = -41\ kJ \cdot mol^{-1}) \qquad \textbf{(5.1.2)}$$

The GSR process is therefore described by the global reaction shown in Eq. (5.1.3).

$$C_3H_8O_3 + 3H_2O \rightarrow 7H_2 + 3CO_2 \quad (\Delta H_r^{298\,K} = 128\ kJ \cdot mol^{-1}) \qquad \textbf{(5.1.3)}$$

Methanation of both CO (Eq. (5.1.4)) and CO_2 (Eq. (5.1.5)) are probably the main secondary reactions (apart from coke deposition), especially the one making use of CO:

$$CO + 3H_2 \rightleftharpoons CH_4 + H_2O \quad (\Delta H_r^{298\,K} = -206\ kJ \cdot mol^{-1}) \qquad \textbf{(5.1.4)}$$

$$CO_2 + 4H_2 \rightleftharpoons CH_4 + 2H_2O \quad (\Delta H_r^{298\,K} = -165\ kJ \cdot mol^{-1}) \qquad \textbf{(5.1.5)}$$

It is known from the literature [1, 5-8] that high temperatures (e.g. above 773 K) are normally more favorable for GSR.

The formation of coke during GSR is not so uncommon. Pompeo *et al.* [9] observed the formation of heavy compounds such as 2-methyl-2-cyclopentanone, phenol and 5-hydroxyl-2-methyl-1,3-dioxane, which could have been formed by dehydration, hydrogenolysis and condensation reactions; these compounds could have been coke precursors. On the other hand carbon-containing gaseous products, such as CO, CO_2 and CH_4, can also be coke precursors, according to Eqs. (5.1.6-9) [10].

$$2CO \rightleftharpoons CO_2 + C \quad (\Delta H_r^{298\,K} = -172\ kJ \cdot mol^{-1}) \qquad \textbf{(5.1.6)}$$

$$CH_4 \rightleftharpoons 2H_2 + C \quad (\Delta H_r^{298\,K} = 75\ kJ \cdot mol^{-1}) \qquad \textbf{(5.1.7)}$$

$$CO + H_2 \rightleftharpoons H_2O + C \quad (\Delta H_r^{298\,K} = -131\ kJ \cdot mol^{-1}) \qquad \textbf{(5.1.8)}$$

$$CO_2 + 2H_2 \rightleftharpoons 2H_2O + C \quad (\Delta H_r^{298\,K} = -90\ kJ \cdot mol^{-1}) \qquad \textbf{(5.1.9)}$$

The use of Rh-based catalysts for GSR has only been reported in a few works [5-7, 11-14]. Chiodo *et al.* [5] concluded that Rh/Al_2O_3 is more active and stable during GSR than Ni-based catalyst. In other work, Senseni *et al.* [12] observed a very similar behavior of a $Rh/MgAl_2O_3$ catalyst in terms of catalytic activity and stability during GSR. In this case, the Rh-based catalyst was found to be more suitable for GSR than Pt, Ir and even Ru, on the same support. It has been reported that the presence of Rh favors the gasification of carbon deposits formed during GSR, due to its capacity to activate H_2O [7]. Moreover, its presence favors the conversion of glycerol into gas products at the expense of liquid products [14]. However, since high temperatures and low pressures lead to better GSR performance, these works focused mainly on temperatures above 773 K and atmospheric pressure. Therefore, in order to address that gap, a Rh-based catalyst was tested at 673 K and 4.5 bar aiming also, in future works, to test it in multifunctional reactors where such conditions are preferred or even required for materials compatibility reasons (e.g. due to the use of hydrotalcites for CO_2 capture and/or H_2-permselective membranes). The catalytic performance was evaluated in terms of total glycerol conversion, gas products generation, gas products yields and selectivities, and H_2 purity. Moreover, the formation of coke under such conditions was analyzed, and a coke removal procedure to be used in parallel with GSR was carried out.

5.1.2 Experimental

5.1.2.1 Chemicals, gases and materials

Nitrogen (99.999%), reconstituted air (99.999%) and hydrogen (99.999%), all from Linde, were used as carrier gas in the reaction tests, as oxidant agent during temperature programmed oxidation (TPO) and oxidative catalyst

regeneration, and as reducing agent during catalyst reduction, respectively. Helium from Linde (99.999%) was used as carrier gas in the gas chromatograph. An aqueous solution of glycerol (JMGS, 99.95%) with a molar water/glycerol feed ratio (WGFR) of 19 was used in all reaction tests.

During all catalytic tests a Rh on rare earth promoted theta-alumina catalyst supplied by Johnson Matthey was used. Inert silicon carbide (SiC, Alfa Aesar) was adopted as catalyst bed diluting agent during all experiments.

5.1.2.2 Characterization of the materials

In situ (TPO) was carried out after a preliminary reaction run where 200 mg of catalyst were used. After the preliminary reaction run the system was flushed with N_2 and the reactor was cooled down to room temperature. Then 100 $mL_N \cdot min^{-1}$ of reconstituted air passed through the catalyst bed and the reactor was heated up to 1023 K at 10 $K \cdot min^{-1}$.

Scanning Electron Microscopy (SEM) coupled with Energy Dispersive Spectroscopy (EDS) was performed in a FEI Quanta 400 FEG ESEM/EDAX Pegasus X4M equipment. The analyzed samples were covered with an approximately 10 nm thick conductive coating of PdAu through the sputtering technique in a SPI module.

The Raman spectra were obtained using a Horiba Jobin-Yvon XploRA™ with 100x objective lens apparatus, equipped with an excitation wavelength of 532 nm from a Nd:YAG laser at a power of 25 mW and diffraction gratings with 1200 lines mm^{-1}. A density filter was used to avoid the thermal decomposition of carbon by the laser. The incident beam perpendicular to the plane of the sample was focused through the microscope lens, which also collected the Raman scattered radiation in back-scattering geometry. A highly sensitive CCD camera was used to collect the Raman spectra.

5.1.2.3 Experimental setup

A stainless steel column (120 mm of height and 7.2 mm of inner diameter) was attached to the experimental setup (Fig. 5.1.1), placed inside a tubular oven (model Split from Termolab, Fornos Eléctricos, Lda.) divided in 3-zones, which is equipped with a PID temperature controller (model MR13 from Shimaden). The type-K thermocouples used to measure and control the oven temperature were placed in each zone and in the same radial position of the oven and close to the column wall.

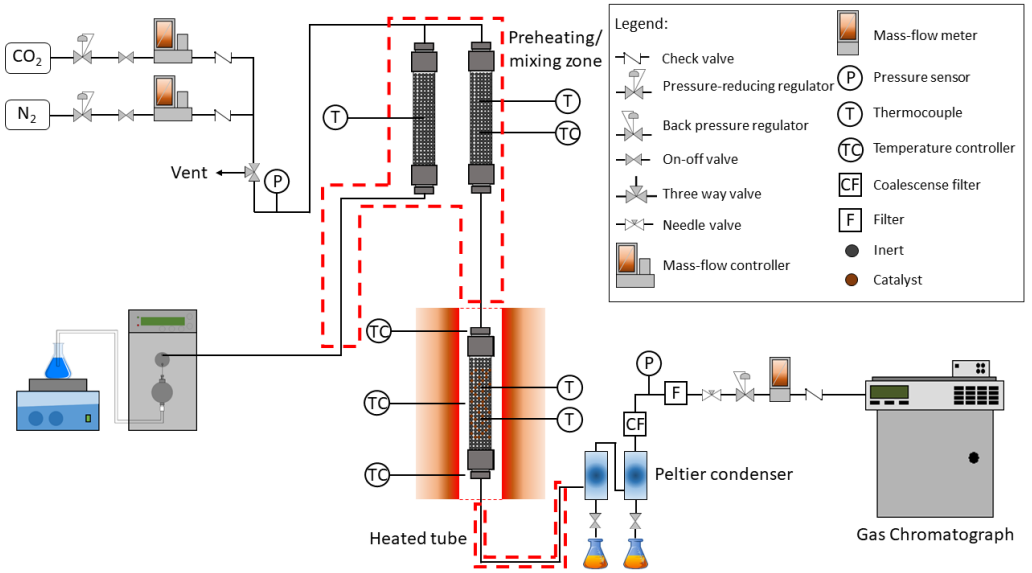

Fig. 5.1.1 - Scheme of the experimental setup.

Nitrogen was fed by a mass flow controller (model F201 from Bronkhorst High-Tec) while the glycerol aqueous solution was fed by an HPLC pump (Eldex, 1LMP) and forced to pass through an evaporation/mixing zone at 623 K before entering the reactor. The tube between the reactor outlet and the first Peltier condenser was kept at 423 K. The pressure in the system was monitored by means of two pressure transducers (model PMP 4010 from Druck) placed before and after the reactor.

During the reaction tests small samples of the dry outlet streams containing N_2, H_2, CO_2, CO and CH_4 were periodically collected in a single loop and the concentrations of the different gases were determined on-line in a gas chromatograph (Dani, model 1000). The chromatograph was equipped with a micro-TCD detector (VICI, model TCD-C-220) and a capillary column (Supelco, carboxen 1010 plot). A system of two Peltier based cold-traps, a coalescence filter and a filter was used between the reactor and the analysis system in order to retain all condensable species. The condensed samples were collected periodically and analyzed in terms of glycerol concentration by high performance liquid chromatography in a chromatograph (Elite LaChrom HITACHI) equipped with a refractive index detector. The liquid products were separated using an Alltech OA-1000 ion exclusion column (300 × 6.5 mm), with a 0.005 mol·L^{-1} H_2SO_4 solution as mobile phase at a flowrate of 0.5 mL·min^{-1}. Glycerol was determined quantitatively based on the calibration curve of the standard compound. The CO and CO_2 outlet concentrations obtained during TPO and regenerative oxidation were monitored by an online infrared-based analyser (Servomex, model 4210).

5.1.2.4 Catalytic tests

The stainless steel reactor, closed in both ends with two stainless steel mesh (10-15 μm) discs, was filled with 800 mg of catalyst (350-600 μm) homogeneously diluted with SiC (241-559 μm; 4.7 g). The reactor ends were filled with SiC (inert material). Two type-K thermocouples inserted laterally and radially centred were used with the aim of continuously monitoring the bed temperature. The temperature profile along the column length under inert atmosphere was uniform (differences < 1 K).

Before the GSR tests, the reactor was heated up to the desired temperature under N_2 atmosphere (80 $mL_N \cdot min^{-1}$) and pressurized by means of a back pressure valve up to 4.5 bar. When the pressure was stable, 0.1 $mL \cdot min^{-1}$ (WHSV of 7.8 h^{-1}, excluding the inert) of an aqueous solution of glycerol with a WGFR of 19 was fed to the reactor in order to minimize coke formation. These experiments were carried out at 673 K and 4.5 bar. A blank run, herein called Exp. 1, in which the reactor was filled with only SiC was carried out for 4 h. Afterwards, three catalytic experimental runs were carried out. First, a 13 h test was performed during two days (8 h in the first day and 5 h in the second day), the catalyst bed being kept under N_2 atmosphere overnight (Exp. 2). The effect of both oxidative catalyst regeneration with air and catalyst reduction with H_2 was evaluated in Exp. 3. The regenerative oxidation during these tests consisted of flowing 100 $mL_N \cdot min^{-1}$ of reconstituted air through the catalyst bed at 773 K until no CO_2 nor CO were detected (around 30 min). Reduction was carried out by flowing 50 $mL_N \cdot min^{-1}$ of H_2 through the catalyst bed at 773 K for 30 min.

The last test, here designated Exp. 4 and carried out using fresh catalyst, consisted of a 16 h test carried out over 4 days, 4 h each day, being that after each 4 h reaction the catalyst was kept under N_2 atmosphere overnight. Before starting the next 4 h reaction, the reactor temperature was increased to 773 K and regenerative oxidation of the used catalyst took place under 100 $mL_N \cdot min^{-1}$ of reconstituted air for 30 min. During regenerative oxidation the CO_2 and CO produced were measured by the online infrared based analyser described above. After regenerating the catalyst the system was cooled back to 673 K and flushed with N_2 for another 30 min before starting the following reaction. These experiments are summarized in Table 5.1.1.

Table 5.1.1 - Catalytic tests performed at 673 K, 4.5 bar and WGFR of 19.

Experiment	Total Duration / h	Mass of catalyst / mg	Frequency of oxidative regeneration	Frequency of reduction
Exp. 1	4	-	-	-
Exp. 2	13	800	-	-
Exp. 3	24	800[a]	Every 6 h except at 24 h	At 18 h
Exp. 4	16	800	Every 4 h except at 16 h	-

[a] Catalyst previously used during 13 h in an experiment equal to Exp. 2 (not shown).

5.1.2.5 Process metrics

The conversion of glycerol during GSR was calculated in two different ways: glycerol conversion into carbon-containing gaseous products $(X_{G,gas})$ and total glycerol conversion $(X_{G,Total})$. The conversion of glycerol into carbon-containing gaseous products was defined as follows:

$$X_{G,gas}(\%) = \frac{F_{CO_2}^{out} + F_{CO}^{out} + F_{CH_4}^{out}}{3 \times F_G^{in}} \times 100 \quad \textbf{(5.1.10)}$$

where $F_{CO_2}^{out}$, F_{CO}^{out} and $F_{CH_4}^{out}$ are the molar flow rates of CO_2, CO and CH_4 at the reactor outlet and F_G^{in} is the molar flow rate of glycerol fed to the reactor. The total glycerol conversion was calculated as:

$$X_{G,Total}(\%) = \frac{F_G^{in} - F_G^{out}}{F_G^{in}} \times 100 \quad \textbf{(5.1.11)}$$

where F_G^{out} is the molar flow rate of unreacted glycerol at the reactor outlet. The yields of all gaseous products (Y_i) and selectivities of carbon-containing gaseous products $(S_{C,i})$ were defined as:

$$Y_i = \frac{F_i^{out}}{F_G^{in}} \quad \textbf{(5.1.12)}$$

$$S_{C,i}(\%) = \frac{F_i^{out}}{F_{CO_2}^{out} + F_{CO}^{out} + F_{CH_4}^{out}} \times 100 \quad \textbf{(5.1.13)}$$

in which i corresponds to H_2, CO_2, CO or CH_4 in Eq. (5.1.12) and corresponds to CO_2, CO or CH_4 in Eq. (5.1.13). Regarding the selectivity of H_2 comparatively to carbon-containing gaseous products(S_{H_2}), it was calculated according to Eq. (5.1.14).

$$S_{H_2}(\%) = \frac{F_{H_2}^{out}}{F_{CO_2}^{out} + F_{CO}^{out} + F_{CH_4}^{out}} \times \frac{3}{7} \times 100 \quad \textbf{(5.1.14)}$$

where $F_{H_2}^{out}$ is the molar flow rate of H_2 at the reactor outlet. The $(3/7)$ factor is related to the stoichiometry of the GSR reaction (Eq. (5.1.3)) in which 7 moles of H_2 and 3 moles of CO_2 are ideally produced for each mole of reacted glycerol. Finally, the purity (Pur_{H_2}) of the produced H_2 was evaluated through Eq. (5.1.15):

$$Pur_{H_2}(\%) = \frac{F_{H_2}^{out}}{\sum F_i^{out}} \times 100 \quad \textbf{(5.1.15)}$$

where here *i* represents H_2, CO_2, CO and CH_4. Dry basis was always considered and N_2 was not taken into consideration (used merely as diluting/inert species) in all process metrics defined in this section. These definitions are identical to those reported in several works in the literature on GSR [5, 8].

5.1.3 Results and discussion

5.1.3.1 Physicochemical characterization of spent catalyst

5.1.3.1.1 Temperature programmed oxidation

In order to determine if carbon deposits were formed on the catalyst during GSR reaction, in situ TPO was performed, as described in section 5.1.2.2. The molar fractions of both CO_2 and CO produced in the combustion of deposited coke as well as the temperature profile along time are presented in Fig. 5.1.2.

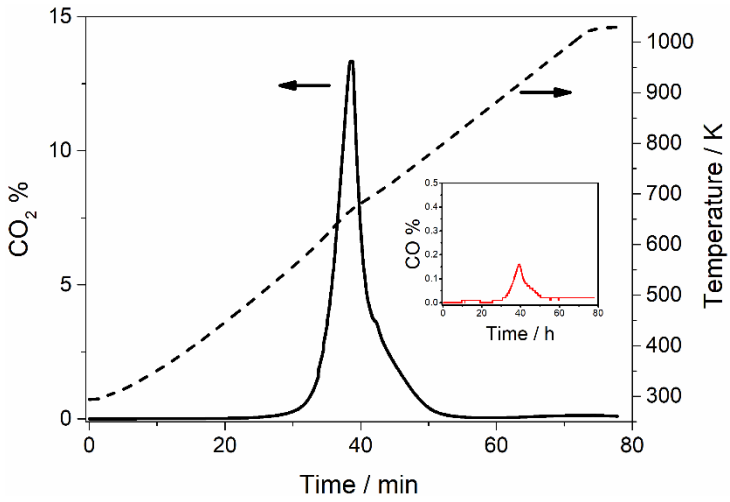

Fig. 5.1.2 - Concentration profiles of CO_2 and CO (inset) obtained during TPO of spent catalyst under 100 $mL_N \cdot min^{-1}$ of reconstituted air.

TPO confirms that coke deposition on the catalyst occurred during GSR. Furthermore, most of the coke was converted into CO_2 and only a small amount of CO was produced (see inset in Fig. 5.1.2). It was observed that coke deposits are gasified between approximately 500 and 800 K, with a CO_2 peak maximum at around 670 K. According to TPO results, regenerative oxidation of the catalyst in subsequent runs was carried out at 773 K.

5.1.3.1.2 SEM/EDS

In order to better understand the changes that the catalyst went through during reaction, namely in terms of formation of coke deposits, SEM/EDS analyses were carried out. Even though the catalyst suffered visual changes in terms of color, no major changes were observed in the SEM images between the fresh and the used catalyst samples. Some localized morphological changes were observed and are depicted in Fig. 5.1.3. As can be seen in Fig. 5.1.3 (a), only poorly defined structures are observed in the fresh catalyst. However, the used catalyst (Fig. 5.1.3 (b) and (c)) presented a different morphology in some regions of its surface. This new morphology, more easily observed in Fig. 5.1.3 (c), is similar to a clearer capsule around some kind of darker nucleus. It was concluded by EDS that these capsules are rich in carbon.

Since only small visual changes were detected by SEM, the surface of the materials was analyzed by EDS with the aim of comparing their carbon content. For the catalyst samples used during Exp. 2 and 4 (see section 5.1.2.4 with further details), the carbon content was analyzed in three different regions.

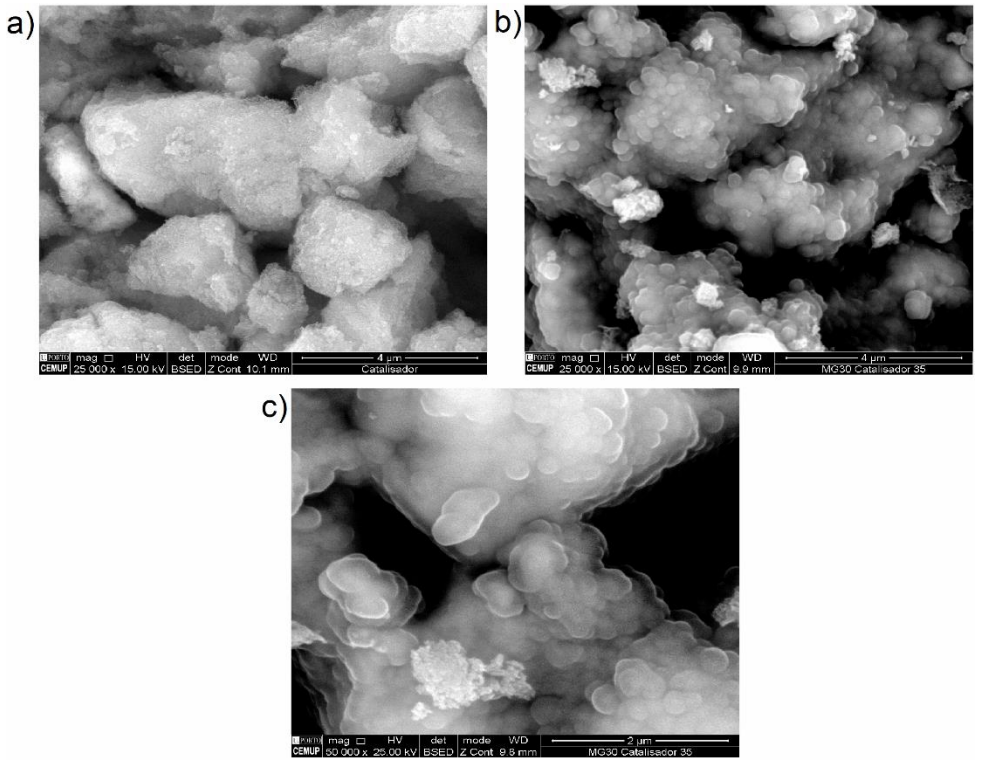

Fig. 5.1.3 - SEM images of (a) fresh catalyst and of (b,c) used catalyst.

The results are summarized in Table 5.1.2, taking into consideration that the carbon contents obtained for the different samples were subtracted by the average carbon contents obtained for the fresh catalyst (herein called additional carbon contents). The results in Table 5.1.2 confirm once more the occurrence of coke deposition on the catalyst during the experiments. Moreover, considerably more coke was observed in the catalyst used in Exp. 2 than in the catalyst used in Exp. 4. This was already expected as the first sample was submitted to GSR for 13 h without oxidative regeneration, while the second sample was regenerated with reconstituted air every 4 h, except after the last 4 h of reaction; therefore, most of the coke detected in the catalyst used in Exp. 4 was formed during the last 4 h of reaction.

Table 5.1.2 - Average additional carbon contents and respective standard deviations (wt%) obtained by EDS for the catalyst used in the different experiments.

Experiment	Additional Carbon Content / wt%
Exp. 2	9.5 ± 1.3
Exp. 4	4.5 ± 0.3

5.1.3.1.3 Raman

Raman spectroscopy was used with the aim of better understanding the structure of the formed coke. Fig. 5.1.4 shows the Raman spectra of the catalyst used in Exp. 2 in the range of 1000-1800 cm^{-1}.

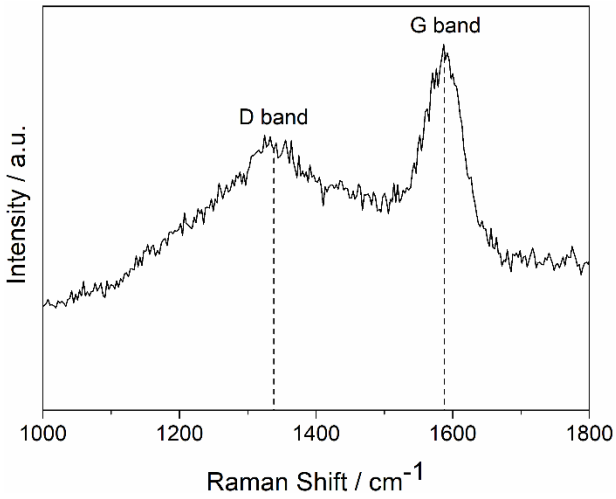

Fig. 5.1.4 - Raman spectra of the catalyst used in Exp. 2.

Two peaks were identified, the first centered around 1338 cm^{-1}, the so-called D band, and the second at around 1588 cm^{-1}, the so-called G band. The first is normally associated to allotropic carbon forms, such as amorphous carbon, defective filamentous carbon or carbon nanotubes, while the G band is associated to the presence of ordered carbon [15-17]. This is supported by the

relative peak width, since broader peaks are usually associated to less ordered carbon structures [18, 19]. The ratio between the areas of both peaks (D/G) is approximately 1.6, which suggest a predominant formation of amorphous carbon structures in detriment of organized carbon deposits.

5.1.3.2 Steam reforming of glycerol tests

In order to understand how the Rh-based catalyst performs under GSR reaction, three sets of experiments were carried out. However, before those experiments a blank test in which the reactor was filled exclusively with inert SiC took place. A change in colour from the fed aqueous glycerol solution (colourless) to the liquid effluent (yellow) was clearly observed, meaning that glycerol conversion into condensable products occurred. It has been reported that such conversion occurs mainly through thermal decomposition of glycerol [20, 21]. Moreover, according to some works [8, 22] a temperature as low as 673 K favors considerably the formation of such condensable products than higher temperatures. Even though a thorough analysis of such products was not undertaken, it is possible that condensable compounds such as acetol, acetone, acrolein, acetaldehyde, acetic acid and allyl alcohol were formed [8, 21, 22]. However, the concentration of glycerol present in the condensed effluent was analyzed and total glycerol conversions below 10% were observed. Still, none of the converted glycerol or of the condensable products formed were steam reformed and so gaseous products (H_2, CO_2, CO and CH_4) were not produced.

The evolution of both total conversion of glycerol and conversion of glycerol into carbon-containing gaseous products over 13 h during Exp. 2 is presented in Fig. 5.1.5. As can be seen, almost complete total conversion of glycerol (above 99%) was obtained during the first reaction hours; in addition approximately 60% of the fed glycerol was being converted into carbon-containing gaseous products after the first hour of reaction. However, loss of activity was observed throughout the experiment and although after 13 h of

reaction more than 90% of glycerol was still being converted, the conversion into carbon-containing gaseous products was only 22%. This means that the amount of glycerol converted into condensable products and coke increased over time, which was visually noticed in the liquid samples periodically removed. The characterization of the used catalyst confirmed that carbon deposits were formed during reaction (cf. section 5.1.3.1), thus becoming clear the reason for the loss of the activity over time. Assuming that part of the gaseous products are not formed directly from glycerol, but from intermediate liquids produced from glycerol [7, 20], it could be that coke deposited preferentially on the active sites that catalyzed the conversion of intermediate liquids into gaseous products. The high loss of activity towards carbon-containing gaseous products could also be associated to their direct conversion into coke (see Eqs. (5.1.6-9)), which would also target the active sites where gaseous products are generated. In fact, Bobadilla *et al.* [20] mentioned that besides being formed from polymerization of unsaturated carbonaceous species, carbon deposits can also be formed directly from carbon-containing gaseous products through, mainly, CH_4 decomposition (Eq. (5.1.7)) and CO disproportionation (Boudouard reaction – Eq. (5.1.6)).

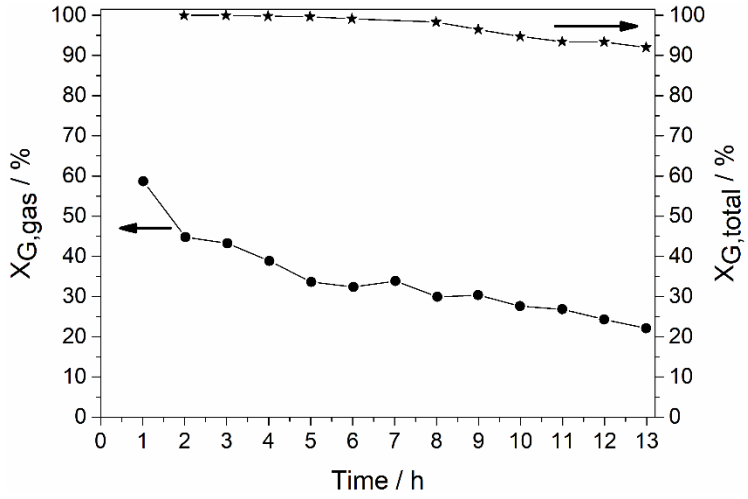

Fig. 5.1.5 - Evolution of both total glycerol conversion and glycerol conversion into carbon-containing gaseous products during Exp. 2 (conditions provided in Table 5.1.1).

The yields of H_2, CO_2, CO and CH_4 are depicted in Fig. 5.1.6 (a). For all four gases a decrease of the respective yield is observed throughout time, being that after 1 h of reaction an H_2 yield of approximately 2 $\mathrm{mol} \cdot \mathrm{mol}_{\mathrm{fed\ glycerol}}^{-1}$ was obtained.

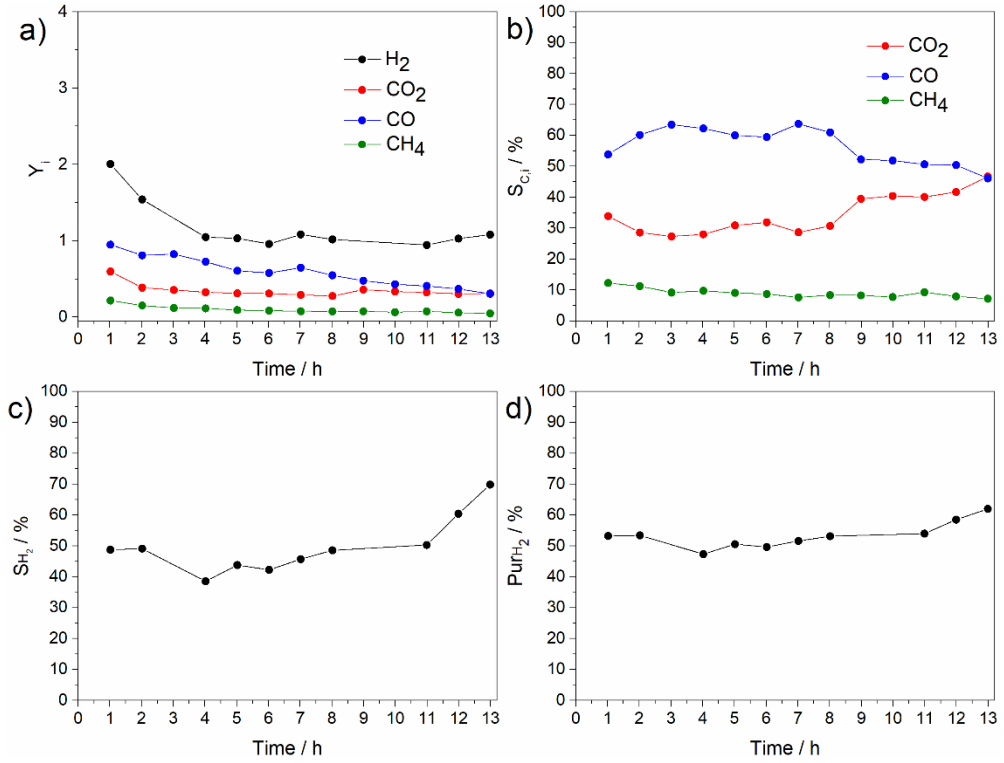

Fig. 5.1.6 - Evolution during Exp. 2 of (a) the yields of gaseous products, (b) the selectivities towards carbon-containing gaseous products, (c) H_2 selectivity and (d) H_2 purity (conditions provided in Table 5.1.1).

Moreover, values of 1, 0.6 and 0.2 $\mathrm{mol} \cdot \mathrm{mol}_{\mathrm{fed\ glycerol}}^{-1}$ were obtained for the yields of CO, CO_2 and CH_4, respectively. After 13 h these values decreased to approximately 1.1 for H_2, 0.3 for both CO and CO_2 and below 0.1 $\mathrm{mol} \cdot \mathrm{mol}_{\mathrm{fed\ glycerol}}^{-1}$ for CH_4. It is worth noticing that CH_4 was produced, meaning that exothermic methanation occurred since low temperatures were used (see Eqs. (5.1.4-5)). Furthermore, the yield of CO was higher than that of CO_2 during almost all the reaction time. This could be associated to WGS reaction inhibition.

In other words, even though CO was produced during decomposition of glycerol (Eq. (5.1.1)), it was not fully converted into CO_2 through WGS (Eq. (5.1.2)). As the reaction proceeded the yields of both CO and CO_2 became closer, mainly due to CO yield decrease, meaning that CO production via glycerol decomposition probably started being more affected by catalyst deactivation and/or CO was being converted into coke, for example by the Boudouard reaction (Eq. (5.1.6)). Probably for this reason the selectivity towards CO_2 increased over time while the selectivity of CO decreased (Fig. 5.1.6 (b)). Furthermore, progressive inhibition of H_2-consuming methanation was observed over time, which could have contributed to the increase of H_2 selectivity (Fig. 5.1.6 (c)).

Finally, the purity of the dry gas stream in terms of H_2 is a very important criterion when evaluating the efficiency of steam reforming processes. In this case the purity of produced H_2 remained approximately constant throughout the first 11 h of reaction and between 47-54% (Fig. 5.1.6 (d)), increasing to around 62% during the last 2 h. Even though the amount of H_2 produced decreased over time, the production of the other gases decreased as well. The gradually lower overall gas flow rate was induced by catalyst deactivation, and so avoiding such deactivation to maintain a high glycerol conversion into gaseous products over time is vital.

Therefore, regenerating the catalyst with air by burning the carbon deposits could be a possibility for recovering the catalyst activity, as observed by TPO and also done elsewhere in Ni-based catalyst for GSR [23]. However, this procedure could oxidize the catalyst active phase and affect its catalytic performance. The catalyst used in an experiment equal to Exp. 2 (not shown here) was regenerated with air according to the procedure previously described in section 5.1.2.4 (see also Table 5.1.1) and then GSR reaction was carried out for 6 h. This procedure was repeated four times, being that the fourth repetition also included exposure of the catalyst to a reducing atmosphere (H_2), as

previously described, after oxidative regeneration (Exp. 3). Regenerative oxidation allowed a partial recovery of glycerol conversion into carbon-containing gaseous products from 26 % (similar to Exp. 2; Fig. 5.1.5) up to 44 % (data not shown). The following regenerations performed at 6 h and 12 h allowed to keep very similar conversions, 42% and 39%, respectively, meaning that the coke formed in the reaction periods 0-6 h and 6-12 h was almost completely gasified during the respective oxidative regenerations. The oxidative regeneration performed at 18 h was followed by exposure of the Rh-based catalyst to reducing atmosphere (H_2), as previously described, and the glycerol conversion into carbon-containing gaseous products obtained afterwards was approximately 35%. Therefore, it can be concluded that exposing the noble metal catalyst to a reducing atmosphere did not affect the catalytic activity of the material, as the slightly decreasing trend that was being observed for the conversions into carbon-containing gaseous products after the previous regenerations remained.

For this reason, another catalytic test (Exp. 4) was carried out for 16 h and oxidative regeneration (without reduction) was performed every 4 h. Moreover, since in Exp. 2 the first analysis was only done after 1 h of reaction time and considering it is now known that the catalyst deactivates considerably, especially during the first hours, analyses of the gas products were performed every 15 minutes during the first 2 h of reaction and every hour afterwards. The conversion of glycerol into carbon-containing gaseous products as well as the total conversion of glycerol over time are presented in Fig. 5.1.7. The total conversion of glycerol remained above 99% during the first 4 h of reaction, which is in agreement with the behavior observed in Exp. 2. As for the conversion into carbon-containing gaseous products, the initial value was 73%; during the first hour a decrease (absolute) of approximately 30% was observed and in the subsequent 3 h a further decrease smaller than 15% occurred. Afterwards, oxidative regeneration was carried out as already described. After regeneration,

another 4 h cycle was performed and the initial conversion into carbon-containing gaseous products was very close to that obtained at nearly the same reaction time in the first cycle.

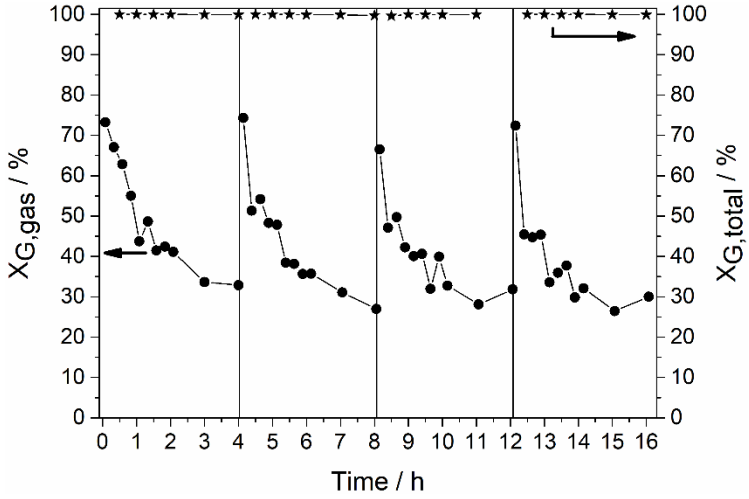

Fig. 5.1.7 - Evolution of both total glycerol conversion and glycerol conversion into carbon-containing gaseous products during Exp. 4 (conditions provided in Table 5.1.1). The vertical solid lines represent the moments at which oxidative regeneration with air during 30 min was performed.

In fact, the oxidative regeneration was so effective that the initial conversion to carbon-containing gaseous products was 67% and 72% in the third and fourth cycles, respectively. As for the conversion into carbon-containing gases after 4 h of reaction, very similar values were obtained compared to that observed in the first cycle. Moreover, the total conversion of glycerol was higher than 99% during all the reaction time. This means that the oxidation procedure used allowed approximately complete removal of the coke deposits formed during the 4 h reaction runs, restoring the catalytic performance.

The concentrations of CO_2 and CO produced during the oxidative regenerations along Exp. 4 are depicted in Fig. 5.1.8 and, upon integration, the amounts of gasified carbon in the three oxidative regenerations were obtained, and are summarized in Table 5.1.3.

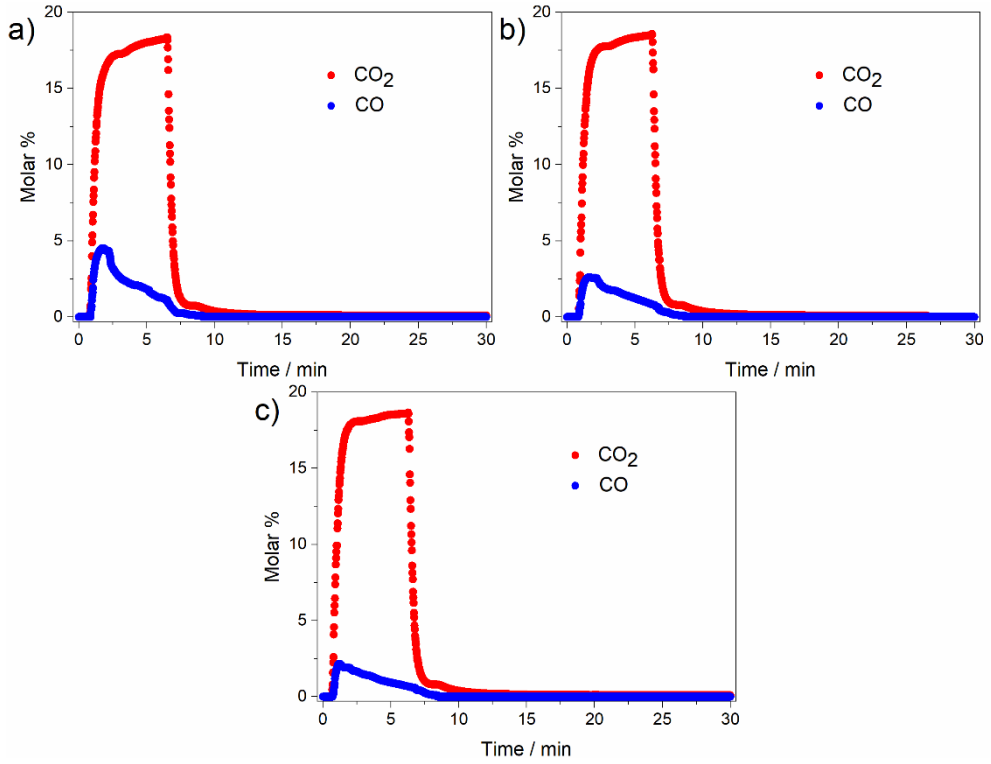

Fig. 5.1.8 - Evolution of CO_2 and CO concentrations during oxidative regeneration performed at 773 K during Exp. 4 at the end of (a) 1st cycle, (b) 2nd cycle and (c) 3rd cycle.

Table 5.1.3 - Amount of carbon deposited on the catalyst used in Exp. 4 that was gasified during each oxidative regeneration.

Oxidative regeneration at the end of / h	**Gasified carbon** $/\ mg_C \cdot g_{cat}^{-1}$
1st cycle	74.1
2nd cycle	68.8
3rd cycle	70.2

As can be seen from Table 5.1.3 the amount of carbon gasified was very similar for the three regenerations; only a slightly higher amount of carbon deposits seems to have been removed in the first regeneration.

During the three oxidative regenerations along Exp. 4, temperature increase in the reactor due to heat release was observed, and maximum temperatures between 856 and 889 K were observed (Fig. 5.1.9). According to Fig. 5.1.2, these temperatures assure complete coke gasification. Since probably there was coke being burned across all bed, it means that heat was accumulating at higher reactor lengths and that is why the temperature peak at 80 mm was higher than that at 40 mm.

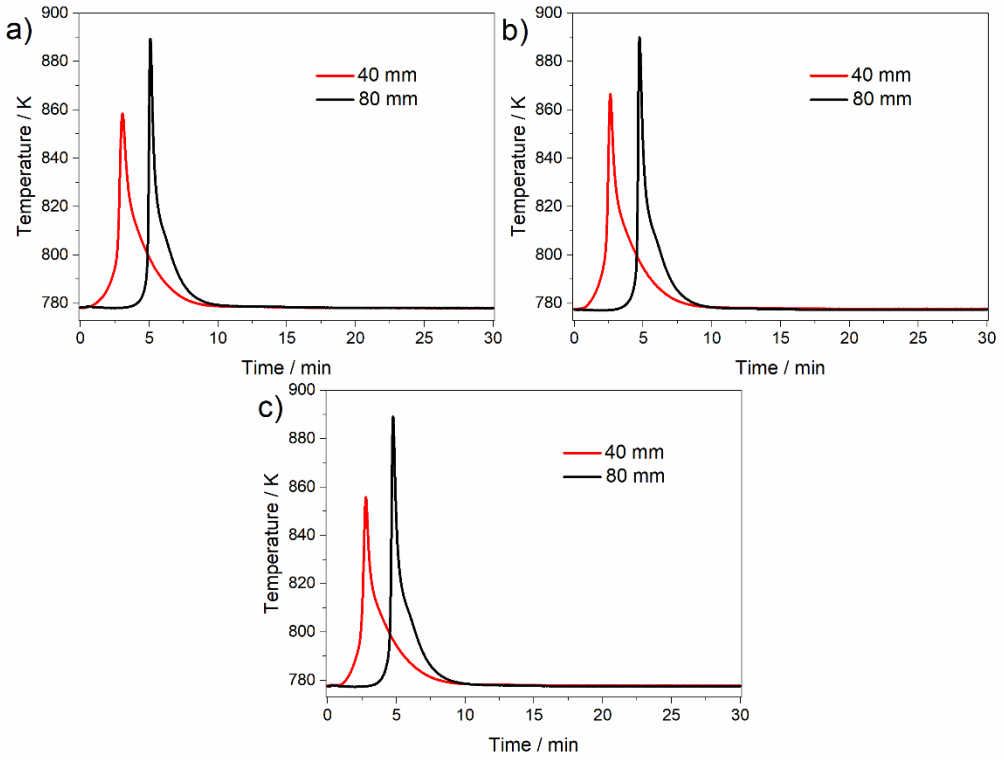

Fig. 5.1.9 - Temperature histories at 40 and 80 mm of the reactor length obtained during the oxidative regenerations performed during Exp. 4 at the end of (a) 1st cycle, (b) 2nd cycle and (c) 3rd cycle.

Coming back to Exp. 4, it is worth noting that an increase of the H_2 yield (Fig. 5.1.10 (a)) was observed during the first 30 min of reaction, a maximum value of approximately 2.3 $\mathrm{mol} \cdot \mathrm{mol}_{\mathrm{fed\ glycerol}}^{-1}$ being observed at that time.

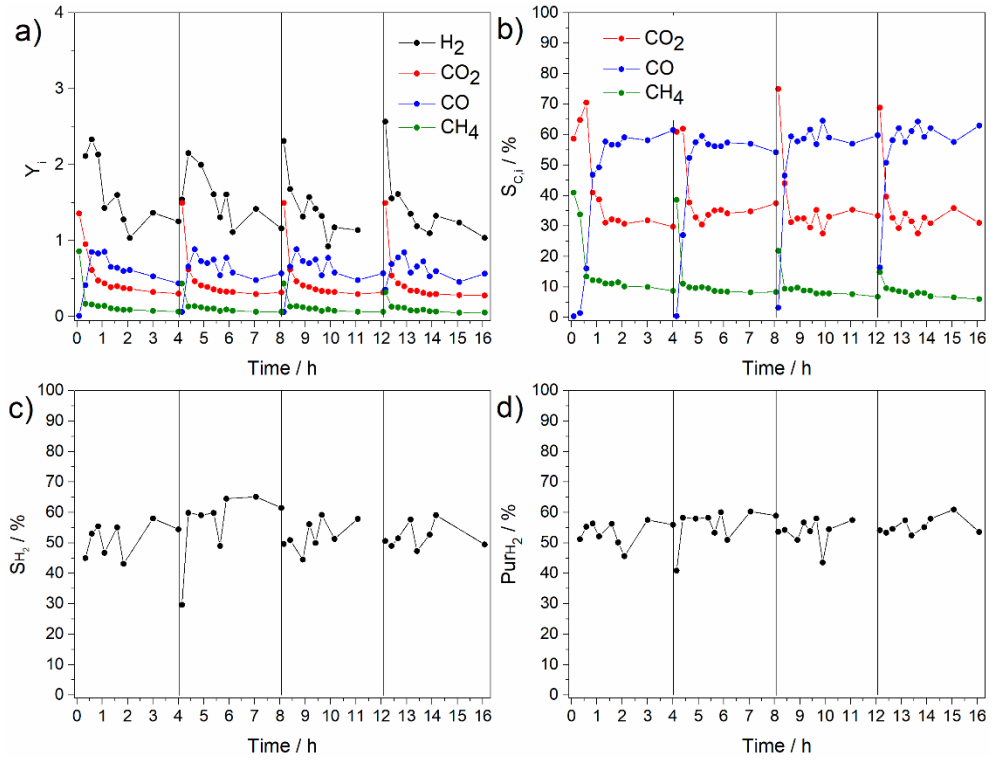

Fig. 5.1.10 - Evolution during Exp. 4 of (a) the yields of gaseous products, (b) the selectivities towards carbon-containing gaseous products, (c) H_2 selectivity and (d) H_2 purity (conditions provided in Table 5.1.1). The vertical solid lines represent the moments at which oxidative regeneration was performed.

Afterwards, the amount of H_2 produced started decreasing during the reaction period of 4 h. After oxidative regeneration the yield of H_2 started increasing, reached a maximum of 2.1 $\mathrm{mol} \cdot \mathrm{mol}_{\mathrm{fed\ glycerol}}^{-1}$ and then decreased again until the end of the reaction. Besides the similar H_2 yield maximum obtained in the second cycle, the tendency after the maximum is very similar to that observed in the first cycle. The initial increase in H_2 yield after regeneration was also observed for the third and fourth reaction cycles, but the maximum was reached

even more rapidly than in the second reaction cycle. On the other hand, the maximum H_2 yield obtained increased from approximately 2.1 $\mathrm{mol} \cdot \mathrm{mol}_{\mathrm{fed\ glycerol}}^{-1}$ in the second cycle to approximately 2.3 $\mathrm{mol} \cdot \mathrm{mol}_{\mathrm{fed\ glycerol}}^{-1}$ in the third cycle and then to around 2.6 $\mathrm{mol} \cdot \mathrm{mol}_{\mathrm{fed\ glycerol}}^{-1}$ in the fourth cycle. To understand the reason for this behavior the evolution of the other gaseous products throughout time has to be analyzed too.

The evolution over time of the other WGS product (CO_2) follows a very similar trend to that described for H_2 for the four reaction cycles, but less pronounced in terms of variation of the maximum value (Fig. 5.1.10 (a)). An advantage of monitoring the gaseous products during the first hour is that it was possible to observe that no CO was detected during the first moments. This occurred because CO was being totally consumed through both WGS and methanation. This is supported by the high yields of H_2, CO_2 and CH_4 attained in the first moments, whose subsequent decrease is accompanied by a symmetric increase in the yield of CO in all four reaction cycles. Moreover, a temperature increase (4-8 K) was observed inside the reactor bed during the first moments of each cycle (Fig. 5.1.11), which is in agreement with the exothermic nature of both WGS and CO methanation, followed by a decrease to a temperature below 673 K (< 4 K), which is probably mainly related to the endothermic glycerol decomposition that becomes thermally dominant. A final stabilization in the range 671-673 K was observed (Fig. 5.1.11). First, this clearly indicates, as already observed in Exp. 2, that an initial loss of WGS activity occurred during every cycle, while apparently glycerol decomposition's activity was not so affected. Also, the maximum of CH_4 attained at the beginning of each cycle decreased with passing cycles, contrary to what occurred with the maximum H_2 yield. This suggests that the increase of the latter throughout reaction cycles is probably associated to its lower initial consumption through methanation.

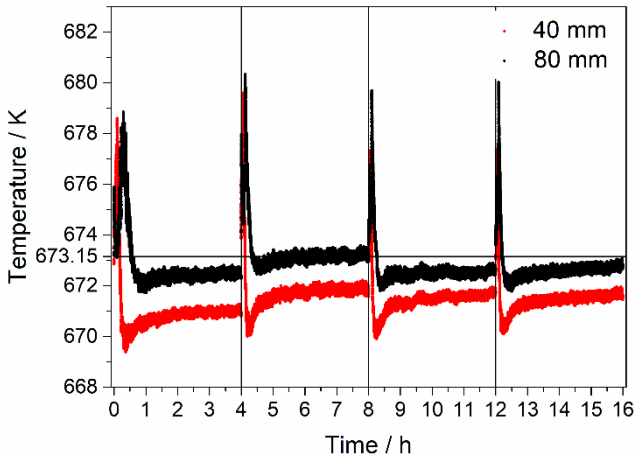

Fig. 5.1.11 - Temperature histories at 40 and 80 mm of the reactor length obtained during Exp. 4. The vertical solid lines represent the moments at which oxidative regeneration was performed. The horizontal solid line represents the temperature set point of the oven controller.

As for the much smoother increase of the CO_2 maximum yield with passing cycles, it could be related to inhibition of CO_2 methanation that could eventually be occurring to a lower extension. Due to this progressive inhibition of CH_4 production and also due to some WGS inhibition that could have built up, CO was detected at the reactor outlet progressively earlier in the reaction cycles. Since an increase of the initial maximum H_2 yield was observed over the cycles, this progressively earlier CO appearance should be mainly related to the inhibition of CH_4 production. This is supported by the narrowing of the initial temperature peak over cycles, especially from the first to the second cycle (see Fig. 5.1.11). The reason for such CH_4 inhibition is not clear but it could be related to deposition of carbon on methanation sites, which possibly might not be completely gasified during oxidative regeneration and that consequently accumulated on these sites. It has been reported for Ni-based catalysts that graphitic like carbon is less reactive to O_2 than less ordered carbon [24, 25], which could be the case here as observed by Raman spectroscopy (Fig. 5.1.4), where the band attributed to graphitic carbon is more intense. If coke formation on the methanation sites really occurred and CO methanation was the main CH_4

production route, those carbon deposits would probably be formed from CO or CH_4, either through Boudouard reaction (Eq. (5.1.6)) and/or CH_4 cracking (Eq. (5.1.7)), respectively. Guo *et al.* [18] observed for a Ni-based catalyst that CH_4 cracking led preferentially to the formation of ordered carbon deposits, which could be the reason for the irreversible loss of CH_4 production activity. In principle, both CO and CO_2 reductions (Eq. (5.1.8) and (5.1.9), respectively) were not considerably involved in the formation of coke as the high amounts of steam here used probably inhibited these reactions. As for the initial WGS deactivation, it could be related to either CO disproportionation and/or CO and/or CO_2 reductions. However, since both reductions should not be thermodynamically favored here, Boudouard reaction could have been a considerable cause of WGS active sites deactivation. The loss of activity could also be related to the presence of condensable products, as already mentioned. In principle, the reason for this deactivation is not sintering as it is not common for the catalyst here used under the temperatures adopted [5]. Furthermore, if sintering (irreversible phenomenon) had occurred, oxidative regeneration would not allow the observed full recovery of the catalytic activity.

Very similar trends over time were observed for the gaseous products containing carbon and H_2 selectivities in the four reaction cycles (Fig 5.1.10 (b) and (c)). The slightly increasing trend observed at around 7 h for the H_2 selectivity in Exp. 2 was not observed here as each reaction cycle only lasted 4 h. Moreover, the values obtained were similar to those obtained for the same reaction period during Exp. 2. Finally, in terms of purity of the gas stream in H_2 (Fig. 5.1.10 (d)), the maintenance of an approximately constant value between 50-60% was once again observed during most part of the reaction cycles.

5.1.4 Conclusions

A Rh on alumina catalyst was tested during GSR at 673 K, 4.5 bar and WGFR of 19, conditions that have never been much explored for this kind of catalyst in GSR. High deactivation due to coke formation was observed; the conversion of glycerol into carbon-containing gaseous products decreased from around 60 % after 1 h to around 22% after 13 h of reaction. On the other hand, the total glycerol conversion remained above 99% for 6 h and then started decreasing more rapidly, and aproximately 92% of glycerol was being converted after 13 h. This means that the production of carbon-containing gaseous products is more affected than the conversion of glycerol into liquid products; so, the production of liquids increased over time and/or the higher decrease observed for the carbon-containing gaseous products is related to their direct conversion into carbon.

Due to the observed coke formation, a 16 h test was carried out with intermediate oxidative regenerations every 4 h in air atmosphere and 773 K. This allowed to reach a much better average performance of the catalytic system, since approximately full recovery of the catalytic activity was observed after each oxidative regeneration. On the other hand, the total glycerol conversion remained above 99% for the full duration of the test. Maximum H_2 yields between 2.1 and 2.6 $\mathrm{mol} \cdot \mathrm{mol}_{\mathrm{fed\ glycerol}}^{-1}$ were observed in the first minutes, followed by a rapid decrease to values between 1.0-1.3 $\mathrm{mol} \cdot \mathrm{mol}_{\mathrm{fed\ glycerol}}^{-1}$ after 4 h. In addition, the purity of produced H_2 remained between 50-60%. A very similar trend was observed for CO_2 as well, which could indicate rapid initial deactivation of WGS sites. The results also suggest that methanation occured during the first moments of each cycle, followed by deactivation of the methanation sites. Moreover, the initial formation of CH_4 was less and less observed throughout the reaction cycles, thus indicating that a progressive deactivation of the CO methanation sites could be occuring. This loss of activity towards CO methanation over the reaction cycles could be associated to incomplete

gasification of the coke deposits on those sites. Raman spectroscopy showed that the formation of organized carbon deposits, which are known to be less reactive to O_2, was dominant on the used catalyst. Moreover, it is possible that Boudouard reaction and/or CH_4 cracking were involved in the formation of carbon deposits on the CO methanation sites while only Boudouard reaction was responsible for the initial deactivation of WGS sites.

The combination of GSR with oxidative regeneration allowed to perform equally long GSR reaction periods with better average performance compared to the case where no oxidative regeneration was performed. Nevertheless, the initial fast deactivation observed is quite limiting and should preferably be minimized. One possible way of increasing the selectivity towards H_2 in detriment of CO, CH_4, condensable products and coke, without having to change catalyst, could be to remove CO_2 and/or H_2 from the reaction medium in a sorption and/or membrane reactor; this will be addressed in the second part of this work.

Notation and Glossary

F_G^{in}	Molar flow rate of glycerol fed to the reactor
F_G^{out}	Molar flow rate of unreacted glycerol at the reactor outlet
F_i^{out}	Molar flow rate of species i at the reactor outlet
Pur_{H_2}	Purity of produced H_2
$S_{C,i}$	Selectivity towards carbon-containing gaseous products
S_{H_2}	Selectivity towards H_2 comparatively to carbon-containing gaseous products
$X_{G,gas}$	Glycerol conversion into carbon-containing gaseous products
$X_{G,total}$	Total glycerol conversion
Y_i	Yield of species i

Greek letters

$\Delta H_r^{298\ K}$	Reaction enthalpy at 298 K

List of acronyms

EDS	Energy Dispersive Spectroscopy
GSR	Glycerol Steam Reforming
SEM	Scanning Electron Microscopy
TPO	Temperature Programmed Oxidation
WGFR	Molar Water/Glycerol Feed Ratio
WGS	Water-Gas Shift

5.1.5 References

[1] Silva, J.M., M.A. Soria, and L.M. Madeira, *Challenges and strategies for optimization of glycerol steam reforming process.* Renewable and Sustainable Energy Reviews, 2015, 42, 1187-1213.

[2] Rosaria, C., P.C. Della, R. Michele, and P. Mario, *Understanding the glycerol market.* European Journal of Lipid Science and Technology, 2014, 116(10), 1432-1439.

[3] *U.S. Energy Information Administration*. [cited 2018 23-06]; Available from: http://www.eia.gov/cfapps/ipdbproject/iedindex3.cfm?tid=79&pid=81&aid=1&cid=ww,r1,r2,r3,r4,r5,r6,r7,&syid=2001&eyid=2011&unit=TBPD.

[4] Yang, F., M.A. Hanna, and R. Sun, *Value-added uses for crude glycerol--a byproduct of biodiesel production.* Biotechnology for Biofuels, 2012, 5(1), 13.

[5] Chiodo, V., S. Freni, A. Galvagno, N. Mondello, and F. Frusteri, *Catalytic features of Rh and Ni supported catalysts in the steam reforming of glycerol to produce hydrogen.* Applied Catalysis A: General, 2010, 381(1), 1-7.

[6] Martínez T, L.M., M. Araque, J.C. Vargas, and A.C. Roger, *Effect of Ce/Zr ratio in CeZr-CoRh catalysts on the hydrogen production by glycerol steam reforming.* Applied Catalysis B: Environmental, 2013, 132-133, 499-510.

[7] Araque, M., L.M. Martínez T, J.C. Vargas, M.A. Centeno, and A.C. Roger, *Effect of the active metals on the selective H2 production in glycerol steam reforming.* Applied Catalysis B: Environmental, 2012, 125, 556-566.

[8] Goula, M.A., N.D. Charisiou, K.N. Papageridis, and G. Siakavelas, *Influence of the synthesis method parameters used to prepare nickel-based catalysts on the catalytic performance for the glycerol steam reforming reaction.* Chinese Journal of Catalysis, 2016, 37(11), 1949-1965.

[9] Pompeo, F., G. Santori, and N.N. Nichio, *Hydrogen and/or syngas from steam reforming of glycerol. Study of platinum catalysts.* International Journal of Hydrogen Energy, 2010, 35(17), 8912-8920.

[10] Silva, J.M., M.A. Soria, and L.M. Madeira, *Thermodynamic analysis of Glycerol Steam Reforming for hydrogen production with in situ hydrogen and carbon dioxide separation.* Journal of Power Sources, 2015, 273, 423-430.

[11] Zarei Senseni, A., F. Meshkani, S.M. Seyed Fattahi, and M. Rezaei, *A theoretical and experimental study of glycerol steam reforming over Rh/MgAl2O4 catalysts.* Energy Conversion and Management, 2017, 154, 127-137.

[12] Zarei Senseni, A., M. Rezaei, and F. Meshkani, *Glycerol steam reforming over noble metal nanocatalysts.* Chemical Engineering Research and Design, 2017, 123, 360-366.

[13] Kunkes, E.L., R.R. Soares, D.A. Simonetti, and J.A. Dumesic, *An integrated catalytic approach for the production of hydrogen by glycerol reforming coupled with water-gas shift.* Applied Catalysis B: Environmental, 2009, 90(3), 693-698.

[14] Araque, M., L.M. Martínez T, J.C. Vargas, and A.C. Roger, *Hydrogen production by glycerol steam reforming over CeZrCo fluorite type oxides.* Catalysis Today, 2011, 176(1), 352-356.

[15] Osorio-Vargas, P., C.H. Campos, R.M. Navarro, J.L.G. Fierro, and P. Reyes, *Improved ethanol steam reforming on Rh/Al2O3 catalysts doped with CeO2 or/and La2O3: Influence in reaction pathways including coke formation.* Applied Catalysis A: General, 2015, 505, 159-172.

[16] Tuinstra, F. and J.L. Koenig, *Raman Spectrum of Graphite.* The Journal of Chemical Physics, 1970, 53(3), 1126-1130.

[17] Soria, M.A., C. Mateos-Pedrero, I. Rodríguez-Ramos, and A. Guerrero-Ruiz, *Catalytic steam reforming of methane under conditions of applicability with Pd membranes over supported Ru catalysts.* Catalysis Today, 2011, 171(1), 126-131.

[18] Guo, J., H. Lou, and X. Zheng, *The deposition of coke from methane on a Ni/MgAl2O4 catalyst.* Carbon, 2007, 45(6), 1314-1321.

[19] Jawhari, T., A. Roid, and J. Casado, *Raman spectroscopic characterization of some commercially available carbon black materials.* Carbon, 1995, 33(11), 1561-1565.

[20] Bobadilla, L.F., A. Penkova, F. Romero-Sarria, M.A. Centeno, and J.A. Odriozola, *Influence of the acid–base properties over NiSn/MgO–Al2O3 catalysts in the hydrogen production from glycerol steam reforming.* International Journal of Hydrogen Energy, 2014, 39(11), 5704-5712.

[21] Tran, N.H. and G.S.K. Kannangara, *Conversion of glycerol to hydrogen rich gas.* Chemical Society Reviews, 2013, 42(24), 9454-9479.

[22] Kousi, K., D.I. Kondarides, X.E. Verykios, and C. Papadopoulou, *Glycerol steam reforming over modified Ru/Al2O3 catalysts.* Applied Catalysis A: General, 2017, 542, 201-211.

[23] Veiga, S., R. Faccio, D. Segobia, C. Apesteguia, and J. Bussi, *Hydrogen production by crude glycerol steam reforming over Ni–La–Ti mixed oxide catalysts.* International Journal of Hydrogen Energy, 2017, 42, 30525-30534.

[24] An, L., C. Dong, Y. Yang, J. Zhang, and L. He, *The influence of Ni loading on coke formation in steam reforming of acetic acid.* Renewable Energy, 2011, 36(3), 930-935.

[25] Guo, J., H. Lou, H. Zhao, D. Chai, and X. Zheng, *Dry reforming of methane over nickel catalysts supported on magnesium aluminate spinels.* Applied Catalysis A: General, 2004, 273(1), 75-82.

5.2 From Sorption-Enhanced Reactor to Sorption-Enhanced Membrane Reactor: a Step towards H_2 Production Optimization through Glycerol Steam Reforming

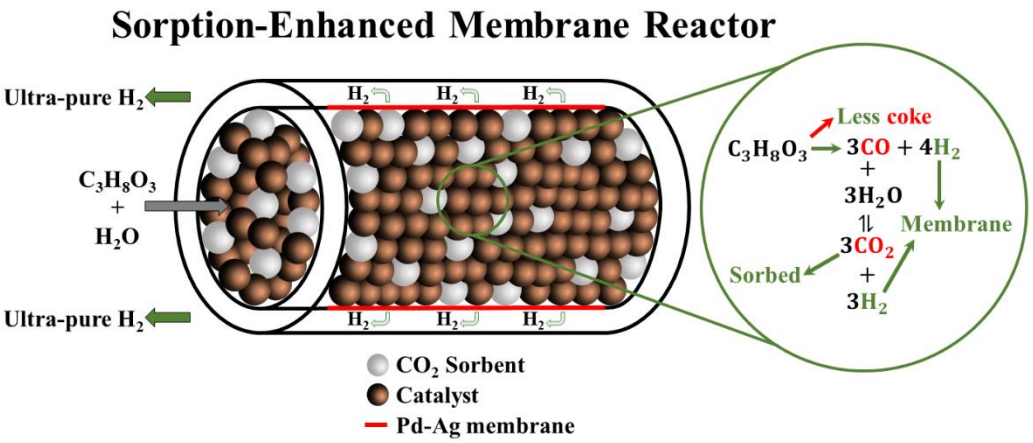

- *The GSR was performed in a multifunctional sorption-enhanced membrane reactor.*
- *Removal of both CO_2 and H_2 instead of only CO_2 increased the H_2 yield in 125%.*
- *In the pre-breakthrough, H_2 was mostly obtained in the permeate side as ultra-pure.*
- *Highly pure H_2 was obtained in the retentate stream during pre-breakthrough.*

The main goal of this work is to assess the benefits of using a sorption-enhanced membrane reactor (SEMR) comparatively to a sorption-enhanced reactor (SER) and a traditional reactor (TR) for H_2 production through glycerol steam reforming (GSR). A SER, where a hydrotalcite (K-MG30) was used to capture the CO_2 produced during GSR on an alumina supported Rh catalyst, was tested. Enhancement of H_2 production was observed not only during the pre- and breakthrough of CO_2 but also during the post-breakthrough comparatively to the TR. While the initial enhancement was mostly due to CO_2 sorption and affected more directly the water-gas shift (WGS) reaction, the catalytic activity of K-MG30 towards glycerol decomposition and manly WGS reaction was responsible for the improved performance during post-breakthrough. Still, considerably higher H_2 purity was obtained in the first moments. A significant improvement in terms of H_2 production was observed in the SEMR, where a Pd-Ag membrane separated selectively the hydrogen from the other gases. An increment of the maximum H_2 yield in the pre- and breakthrough regions from 1.6, in the SER, up to 3.6 $mol \cdot mol_{fed\ glycerol}^{-1}$ was obtained. Simultaneous removal of H_2 and CO_2 significantly benefited the WGS reaction. Consequently, only H_2 was obtained in the gas phase of the retentate stream during the pre-breakthrough period. Moreover, ultra-pure H_2 was obtained in the permeate side of the dense Pd-Ag membrane, meaning that if the SEMR is continuously operated in the pre-breakthrough region, pure H_2 would continuously be obtained in both retentate and permeate streams.

The contents of this chapter were adapted from: Silva, J.M., L.S. Ribeiro, J.J.M. Órfão, S. Tosti, M.A. Soria, and L.M. Madeira, *From sorption-enhanced reactor to sorption-enhanced membrane reactor: A step towards H_2 production optimization through glycerol steam reforming.* Submitted for publication.

5.2.1 Introduction

The production of H_2 through biodiesel-derived glycerol steam reforming (GSR) has been a growing target of research during the last decade not only due to its potential to benefit the economic competitiveness of biodiesel, but also due to the environmental and processual advantages of such process [1, 2]. The GSR reaction consists of two major steps: a first irreversible decomposition of glycerol into syngas, Eq. (5.2.1), followed by the upgrade of CO to CO_2 and more H_2 through the water-gas shift (WGS) reaction (Eq. (5.2.2)).

$$C_3H_8O_3 \rightarrow 3CO + 4H_2 \qquad (\Delta H_r^{298\,K} = 251\ kJ \cdot mol^{-1}) \qquad \textbf{(5.2.1)}$$

$$CO + H_2O \rightleftharpoons H_2 + CO_2 \qquad (\Delta H_r^{298\,K} = -41\ kJ \cdot mol^{-1}) \qquad \textbf{(5.2.2)}$$

This process is described by the global reaction shown in Eq. (5.2.3) (sum of Eq. (5.2.1) and Eq. (5.2.2)):

$$C_3H_8O_3 + 3H_2O \rightarrow 7H_2 + 3CO_2 \qquad (\Delta H_r^{298\,K} = 128\ kJ \cdot mol^{-1}) \qquad \textbf{(5.2.3)}$$

The GSR is normally accompanied by secondary methanation reactions of CO and CO_2, as described in Eqs. (5.2.4) and (5.2.5), respectively, which could significantly decrease the hydrogen yield.

$$CO + 3H_2 \rightleftharpoons CH_4 + H_2O \qquad (\Delta H_r^{298\,K} = -206\ kJ \cdot mol^{-1}) \qquad \textbf{(5.2.4)}$$

$$CO_2 + 4H_2 \rightleftharpoons CH_4 + 2H_2O \qquad (\Delta H_r^{298\,K} = -165\ kJ \cdot mol^{-1}) \qquad \textbf{(5.2.5)}$$

It has been highly reported that temperatures around 673 K highly favor both CO and CO_2 methanation [3-5], namely over noble metal-based catalysts similar to the Rh-based catalyst here used. Besides methane, other even less desired secondary products such as liquid compounds and coke can also be formed [6-9], the last being associated to catalyst deactivation. The formation of carbon deposits might be promoted by the formation of liquid compounds [6, 10,

11] and/or by carbon-containing gaseous products, according to Eqs. (5.2.6-9) [7, 12, 13].

$$2\mathrm{CO} \rightleftharpoons \mathrm{CO_2} + \mathrm{C} \quad (\Delta H_r^{298\,K} = -172\ kJ \cdot mol^{-1}) \tag{5.2.6}$$

$$\mathrm{CH_4} \rightleftharpoons 2\mathrm{H_2} + \mathrm{C} \quad (\Delta H_r^{298\,K} = 75\ kJ \cdot mol^{-1}) \tag{5.2.7}$$

$$\mathrm{CO} + \mathrm{H_2} \rightleftharpoons \mathrm{H_2O} + \mathrm{C} \quad (\Delta H_r^{298\,K} = -131\ kJ \cdot mol^{-1}) \tag{5.2.8}$$

$$\mathrm{CO_2} + 2\mathrm{H_2} \rightleftharpoons 2\mathrm{H_2O} + \mathrm{C} \quad (\Delta H_r^{298\,K} = -90\ kJ \cdot mol^{-1}) \tag{5.2.9}$$

The use of intensified reaction-separation process concepts with the aim of surpassing both thermodynamic and kinetic limitations has been considered in general for steam reforming of several H_2-containing feedstocks. Since the main products of steam reforming processes are normally CO_2 and H_2, the removal of one of them is normally carried out either in a sorption-enhanced reactor (SER) through CO_2 removal or in a membrane reactor (MR) through H_2 recovery [1, 12]. The removal of CO_2 in a SER can be carried out by combining in the same bed the steam reforming catalyst and a CO_2 sorbent, such as a hydrotalcite [14-16], CaO-based materials [17-19], lithium zirconates and silicates [20-22], among other materials. Since the temperature that will be used here is 673 K, for the reasons mentioned above and also due to the restrictions of materials compatibility (CO_2 sorbent and H_2-permselective membrane), the best option for in site CO_2 capture are hydrotalcites; both sorption and regeneration can be carried out at such temperature while maintaining reasonable sorption capacities and kinetics [1, 23]. Regarding the removal of H_2, it can be carried out by using a H_2-permselective membrane, being that dense metallic membranes have been the most widely studied for H_2 separation [24]. Pd-based membranes have been found as the most promising ones, and particularly the Pd-Ag membranes have been extensively researched due to

their higher permeability and stability against poisoning by CO_2, CO or H_2S [25-29]. Moreover, they are compatible with the conditions here adopted.

Even though several works have reported the use of these reactor concepts for several reactions, only in a few cases GSR was studied in a SER [30-34] or in a MR [35-38]. Furthermore, most of GSR studies in SER are carried out at temperatures above 773 K where CaO-based sorbents are used, being that up to the author's knowledge only one work [34] reported the use of a hydrotalcite in such a reactor configuration and for this application. Moreover, the experimental analysis of a combined sorption-enhanced membrane reactor (SEMR) system has only been reported a few times [39-42] and up the author's knowledge it has never been reported for GSR. In this work, the GSR reaction was carried out in both SER and SEMR, where a Rh supported on alumina catalyst was combined with a commercial hydrotalcite, K-MG30, in the SER, and a dense Pd-Ag membrane, in the SEMR. The obtained results were not only compared for the two reactor concepts here tested, but also with the results obtained in our previous work for a traditional reactor (TR) [43].

5.2.2 Experimental

5.2.2.1 Chemicals, gases and materials

Nitrogen (99.999%), reconstituted air (99.999%) and hydrogen (99.999%), all from Linde, were used as carrier gas in the reaction tests, as oxidant agent during oxidative regeneration of the catalyst, sorbent and membrane, and during both membrane activation and permeation tests, respectively. Helium from Linde (99.999%) was used as carrier gas in the gas chromatograph. An aqueous solution of glycerol (JMGS, 99.95%) with a molar water/glycerol feed ratio (WGFR) of 19 was used in all reaction tests.

During all catalytic tests a Rh supported on alumina catalyst supplied by Johnson Matthey was used. A 17 wt% K_2CO_3 promoted hydrotalcite, here labelled K-MG30, supplied by Sasol, with a Mg/Al molar ratio of 0.5, was utilized as CO_2 sorbent. Inert silicon carbide (SiC, Alfa Aesar) was adopted as catalyst and sorbent bed diluting agent during all experiments. A tube made of Pd-Ag with 25 wt% silver and wall thickness of 100 μm, length of 120 mm and diameter of 10 mm, was used as hydrogen selective membrane during the SEMR tests. The membrane tube was brazed at its ends to two stainless steel joints and located in a stainless steel shell where the permeate stream (pure hydrogen) was collected.

5.2.2.2 Characterization of the materials

Scanning Electron Microscopy (SEM) coupled with Energy Dispersive Spectroscopy (EDS) was performed in a FEI Quanta 400 FEG ESEM/EDAX Pegasus X4M equipment. The samples were covered with an approximately 10 nm thick conductive coating of PdAu through the sputtering technique in a SPI module.

5.2.2.3 Experimental setup

Two different stainless steel columns (120 mm and 220 mm of height, and both with 7.2 mm of inner diameter) were attached to the experimental setup (Fig. 5.2.1), one a time depending on the experiments to be carried out, as detailed below. The columns were placed inside a tubular oven (model Split from Termolab, Fornos Eléctricos, Lda.) equipped with a 3-zone PID temperature controller (model MR13 from Shimaden) for the SER tests. During the SEMR tests the stainless steel column was replaced by a reactor module containing the Pd-Ag membrane inside as described in section 5.2.2.4.2. The type-K

thermocouples used to measure and control the oven temperature were placed in the same radial position of the oven and close to the column wall.

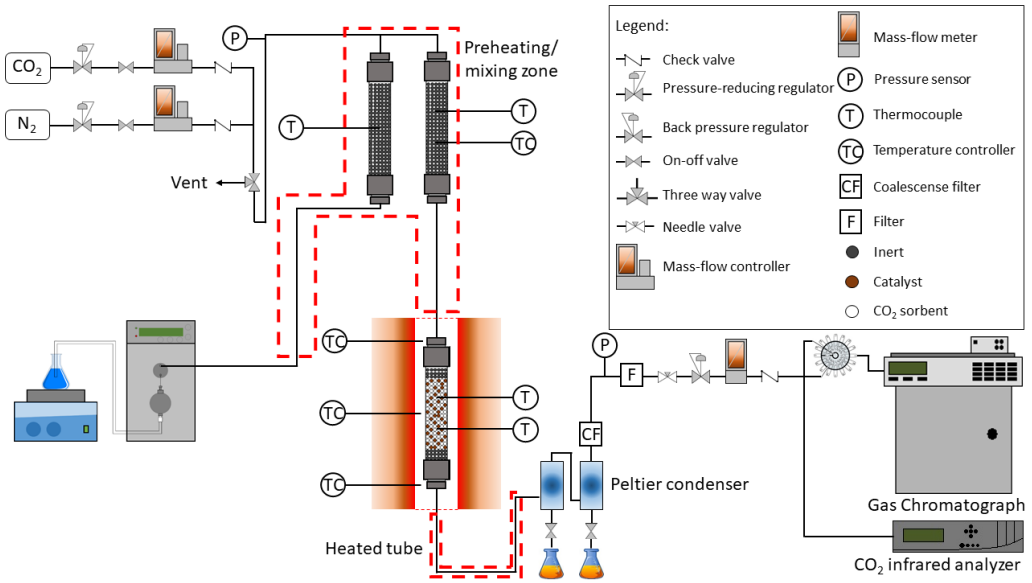

Fig. 5.2.1 - Scheme of the experimental setup.

N_2 was fed by a mass flow controller (model F201 from Bronkhorst High-Tec) while the glycerol aqueous solution was fed by an HPLC pump (Eldex, 1LMP) and forced to pass through an evaporation/mixing zone at 623 K before entering the reactor – cf. Fig. 5.2.1. The tube between the reactor outlet and the first Peltier condenser was kept at 423 K. The pressure in the system was monitored by means of 2 pressure transducers (model PMP 4010 from Druck) placed before and after the reactor. The N_2 sweep gas flow rate in the SEMR was controlled by a mass flow controller (model F201 from Bronkhorst High-Tec); counter-current configuration was adopted. The permeate outlet flow rate was measured by a mass flow meter (model F111 from Bronkhorst High-Tec).

During the reaction tests small samples of the dry outlet stream containing N_2, H_2, CO_2, CO and CH_4 were collected along time using a 16-loop valve (VICI, model ST) and the concentrations of the different gases were determined in a gas chromatograph (Dani, model 1000). The chromatograph was equipped with

a micro-TCD detector (VICI, model TCD-C-220) and a capillary column (Supelco, carboxen 1010 plot). Moreover, the CO_2 and CO outlet dry composition was monitored by an online infrared-based CO_2 analyser (Servomex, model 4210). A system of two Peltier based cold-traps, a coalescence filter and a filter was used between the reactor and the analysis system in order to retain all condensable species. The condensed samples were collected periodically and analyzed in terms of glycerol concentration by high performance liquid chromatography in an apparatus (Elite LaChrom HITACHI) equipped with a refractive index detector. The liquid products were separated using an Alltech OA-1000 ion exclusion column (300 × 6.5 mm), with a 0.005 $mol \cdot L^{-1}$ H_2SO_4 solution as mobile phase at a flowrate of 0.5 $mL \cdot min^{-1}$. Glycerol was determined quantitatively based on the calibration curve of the standard compound.

5.2.2.4 Catalytic tests

5.2.2.4.1 Sorption-enhanced reactor

The catalytic tests performed are described in Table 5.2.1. The 120 mm long stainless steel reactor, closed in both ends with two stainless steel mesh (10-15 μm) discs, was filled with an homogeneous mixture of 800 mg of catalyst (350-600 μm) and 1.6 g of K-MG30 (350-600 μm), which corresponds to a sorbent/catalyst weight ratio of 2. As for the longer 220 mm reactor, it was filled with the same amount of catalyst but diluted in 4.7 g of K-MG30 (350-600 μm), which corresponds to a sorbent/catalyst weight ratio of approximately 5.9. The reactor ends were in both cases filled with SiC (inert material). Two type-K thermocouples, inserted laterally and radially centred, were used in both reactors with the aim of continuously monitoring the bed temperature. The temperature profile along the column length under inert atmosphere was negligible (< 1 K).

Table 5.2.1 - Catalytic tests performed at 673 K, 4.5 bar and WGFR of 19 in different reactor configurations.

Experiment	Reactor Length / mm	Total Duration / h	Mass of catalyst / mg	Mass of sorbent / g	Frequency of oxidative regeneration	Frequency of sorbent regeneration with N_2
TR short blank[a]	120	4	-	-	-	-
TR short 1[a]	120	13	800	-	-	-
TR short 2[a]	120	16	800	-	Every 4 h except at 16 h	-
TR long 1	220	1	800	-	-	-
SER long 1	220	1	800	4.7	-	-
SER long 2	220	20	800	4.7	Every 4 h except at 16 and 20 h	Every 4 h

Table 5.2.1 - Catalytic tests performed at 673 K, 4.5 bar and WGFR of 19 in different reactor configurations (cont.).

Experiment	Reactor Length / mm	Total Duration / h	Mass of catalyst / mg	Mass of sorbent / g	Frequency of oxidative regeneration	Frequency of sorbent regeneration with N_2
SER short blank	120	6	-	1.6	-	-
SER short 1	120	12	800	1.6	-	Every 2 h
SER short 2	120	13	800	1.6	-	At 6 h
SER short 3	120	16	800	1.6	Every 4 h except at 16 h	Every 4 h
SEMR	120	8	800	1.6	Every 4 h[b]	At 4 h

[a] TR short blank, TR short 1 and 2 correspond to Exp. 1, 2 and 4 of our previous work [43], respectively.
[b] Isothermal oxidative regeneration performed at 673 K.

Before the GSR tests, the reactor was heated up to 673 K under N_2 atmosphere (80 $mL_N \cdot min^{-1}$) and pressurized by means of a back pressure valve up to 4.5 bar. When the pressure was stable, 0.1 $mL \cdot min^{-1}$ (WHSV of 7.8 h^{-1}, excluding the sorbent and the inert) of an aqueous solution of glycerol with a WGFR of 19 was fed to the reactor.

The SER experiments were divided in two main sets: a first set of experiments using the 220 mm long reactor and a second stage in which the shorter 120 mm long reactor was used, as indicated in Table 5.2.1. Regarding the long reactor, a first 1 h experiment was carried out, herein named SER long 1. For comparison purposes, the same experiment was repeated but without the CO_2 sorbent (TR, run TR long 1 in Table 5.2.1). A longer SER experiment, herein named SER long 2, consisted of a 20 h experiment performed over 5 days, 4 h a day. Since it was observed in our previous work that regenerative oxidation (used for coke gasification) allowed almost full recovery of the catalytic activity [43], after the first 3 individual 4 h reaction cycles regenerative oxidation of both catalyst and sorbent was carried out overnight. The adopted procedure for the oxidative regeneration was the following: 25 $mL_N \cdot min^{-1}$ of reconstituted air diluted with 75 $mL_N \cdot min^{-1}$ of N_2 was passed through the reactor, being that the temperature was kept at 673 K for 3 h; then, the reactor temperature was increased to 773 K, remained at this temperature for 1 h and was then decreased back to 673 K. During these oxidative regenerations the air fed was diluted with N_2 in order to avoid the temperature gradients observed during oxidative regenerations in TR short 2 experiment [43], which could damage K-MG30. Before the following 4 h reaction stage, the system was flushed with N_2 for 30 min. After the fourth and before the fifth reaction cycle (16 h), regenerative oxidation was not carried out, and only sorbent regeneration (CO_2 desorption) with 100 $mL_N \cdot min^{-1}$ of N_2 was performed overnight.

In order to establish a comparison with the TR experiments previously performed in the 120 mm long reactor [43] and with the SEMR experiments that

where performed inside a 120 mm long membrane, different SER experiments were carried out in the smaller reactor as well. Before those experiments, a blank test (entitled SER short blank – cf. Table 5.2.1) in which the reactor was filled with 1.6 g of K-MG30 (homogeneously diluted with SiC) was performed to assess the catalytic activity of the hydrotalcite. Afterwards 3 different experiments were carried out. A first 12 h test consisting of 6 separate 2 h reactions was carried out, the sorbent being regenerated with 100 $mL_N \cdot min^{-1}$ of N_2 for 3 h between reactions (run SER short 1). A second 13 h test (SER short 2) consisted of 2 separate reactions of 6 h and 7 h performed in different days with the catalyst having been kept under N_2 atmosphere overnight (for sorbent regeneration). In both cases no regenerative oxidation was carried out. The third test, herein named SER short 3, was carried out very similarly to SER long 2, but with oxidative regeneration during which the reactor temperature remained at 773 K for 2 h instead of 1 h, in order to assure that maximum coke removal was attained.

5.2.2.4.2 Sorption-enhanced membrane reactor

The lower section of the tube was filled with SiC until reaching the permeable Pd-Ag membrane wall – cf. Fig. 5.2.2. Then the membrane zone was filled with an homogeneous mixture of 800 mg of catalyst (350-600 μm) and 1.6 g of K-MG30 (350-600 μm), which corresponds to a sorbent/catalyst weight ratio of 2. Finally, the superior section was also filled with SiC and was closed with glass wool. The membrane was then joined to the reactor module (Fig. 5.2.2), which was attached to the experimental setup in Fig. 5.2.1. The membrane tube is assembled in the reactor module in a finger-like configuration where the feed stream is sent into the membrane lumen through a small stainless tube while the sweeping gas (N_2) is sent counter-currently in the shell side.

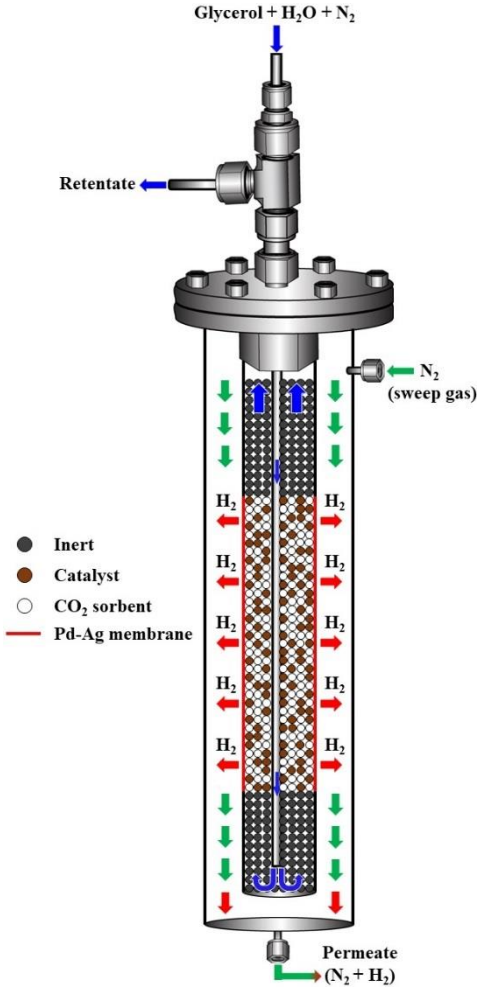

Fig. 5.2.2 - Scheme of the hybrid sorption-enhanced membrane reactor.

The reactor was heated up to 673 K under N_2 atmosphere (80 $mL_N \cdot min^{-1}$) and membrane activation was carried out under approximately 5 bar of H_2 (200 $mL_N \cdot min^{-1}$) while the permeating H_2 was swept by 200 $mL_N \cdot min^{-1}$ of N_2. Atmospheric pressure was maintained in the permeate side. The permeation tests were carried out with pure H_2 under different driving forces. Finally, a catalytic test was carried out in the SEMR at 673 K and 4.5 bar, similarly to SER short 3 for comparison purposes. However, the test was performed over 8 h (2 days) instead of 16 h. During this test 200 $mL_N \cdot min^{-1}$ of N_2 were used as sweep

gas in counter-current mode. Moreover, oxidative regeneration of the catalyst, sorbent and membrane (performed after 4 h of reaction) was carried out under 2.5 $mL_N \cdot min^{-1}$ of reconstituted air diluted with 97.5 $mL_N \cdot min^{-1}$ of N_2 for 15 h and always at 673 K. Such procedure was used in order to avoid significant temperature gradients that could damage the membrane (thus requiring a longer regeneration at a lower temperature). After oxidative regeneration, the system was flushed with N_2 for 30 min before the membrane was reactivated for 24 h under the initial activation conditions. Finally, before the second 4 h reaction cycle the system was once again flushed with N_2 for another 30 min.

5.2.2.5 Process metrics

The conversion of glycerol was calculated in 2 different ways: glycerol conversion into carbon-containing gaseous products $(X_{G,gas})$ and total glycerol conversion $(X_{G,total})$. The conversion of glycerol into carbon-containing gaseous products was defined as follows:

$$X_{G,gas}(\%) = \frac{F_{CO_2}^{out} + F_{CO}^{out} + F_{CH_4}^{out}}{3 \times F_G^{in}} \times 100 \quad \textbf{(5.2.10)}$$

where $F_{CO_2}^{out}$, F_{CO}^{out} and $F_{CH_4}^{out}$ are the molar flow rates of CO_2, CO and CH_4 at the reactor outlet and F_G^{in} is the molar flow rate of glycerol fed to the reactor. The total glycerol conversion was calculated as:

$$X_{G,Total}(\%) = \frac{F_G^{in} - F_G^{out}}{F_G^{in}} \times 100 \quad \textbf{(5.2.11)}$$

where F_G^{out} is the molar flow rate of unreacted glycerol at the reactor outlet. The yields of all gaseous products (Y_i) and selectivities towards carbon-containing gaseous products $(S_{C,i})$ were defined as:

$$Y_i = \frac{F_i^{out}}{F_G^{in}} \quad \textbf{(5.2.12)}$$

$$S_{C,i}(\%) = \frac{F_i^{out}}{F_{CO_2}^{out} + F_{CO}^{out} + F_{CH_4}^{out}} \times 100 \quad \textbf{(5.2.13)}$$

in which i corresponds to H_2, CO_2, CO and CH_4 in Eq. (5.2.12) and corresponds to CO_2, CO and CH_4 in Eq. (5.2.13). Regarding the selectivity towards H_2 comparatively to carbon-containing gaseous products (S_{H_2}), it was calculated according to Eq. (5.2.14).

$$S_{H_2}(\%) = \frac{F_{H_2}^{out}}{F_{CO_2}^{out} + F_{CO}^{out} + F_{CH_4}^{out}} \times \frac{3}{7} \times 100 \quad \textbf{(5.2.14)}$$

where $F_{H_2}^{out}$ is the molar flow rate of H_2 at the reactor outlet. The $(3/7)$ factor is related to the stoichiometry of the GSR reaction in which 7 mol of H_2 and 3 mol of CO_2, are ideally produced for each mole of reacted glycerol (Eq. 5.2.3). Finally, the purity (Pur_{H_2}) of the produced H_2 was evaluated through Eq. (5.2.15):

$$Pur_{H_2}(\%) = \frac{F_{H_2}^{out}}{\sum F_i^{out}} \times 100 \quad \textbf{(5.2.15)}$$

being that here i represents H_2, CO_2, CO and CH_4. In all process metrics defined in this section, dry basis was always considered and N_2 was not taken into consideration (used merely as diluting/inert species). The recovery of H_2 (Re_{H_2}) in the permeate side of the membrane during GSR reaction in the SEMR was defined as:

$$Re_{H_2}(\%) = \frac{F_{H_2}^{permeate}}{F_{H_2}^{permeate} + F_{H_2}^{retentate}} \times 100 \quad \textbf{(5.2.16)}$$

where $F_{H_2}^{permeate}$ and $F_{H_2}^{retentate}$ represent the molar flow rate of produced H_2 that permeates through the membrane and the flow rate of H_2 that exits the SEMR in the retentate side, respectively.

5.2.3 Results and discussion

5.2.3.1 Physicochemical characterization

5.2.3.1.1 EDS

In order to better understand the changes that both catalyst and sorbent went through during the reaction runs in the different reactor configurations, namely in terms of formation of coke deposits, SEM/EDS analyses were carried out. Regarding the catalyst, some localized morphological changes, similar to those observed in the catalyst used in the TR short tests [43], were noticed. The extent of coke formation during each of the performed experiments was assessed by analyzing the surface of the used materials (both sorbent and catalyst) by EDS. For each material the carbon content was analyzed in three different regions. The results are summarized in Table 5.2.2, being that the carbon contents obtained for the different samples were subtracted by the carbon contents obtained for the fresh samples (herein called additional carbon contents).

Table 5.2.2 - Average additional carbon contents and respective standard deviations (wt%) obtained by EDS for both catalyst and K-MG30 used in the different experiments.

Experiment	Additional Carbon Content / wt%	
	Catalyst	**K-MG30**
TR short 1	9.5 ± 1.3[a]	-
TR short 2	4.5 ± 0.3[a]	-
TR long 1	1.4 ± 0.8	-
SER long 1	7.3 ± 1.6	0.5 ± 1
SER long 2	19.3 ± 8.3	3.5 ±0.3
SER short blank	-	8.7 ± 0.2
SER short 1	39.1 ± 18.7	12.3 ± 1.8
SER short 2	17.6 ± 9.2	9.5 ± 1.2
SER short 3	11.3 ± 1.8	3.6 ± 0.6

[a] Results taken from our previous work [43].

By comparing the additional carbon content of the catalyst used in TR long 1 and SER long 1 runs (Table 5.2.2), it is observed that higher amounts of carbon were formed in the SER. This is supported by the higher amounts of deposited carbon observed in the catalyst samples used during tests SER short 1, 2 and 3 and SER long 2 as compared to those observed in the catalyst samples used during TR short 1 and 2. In fact, even the catalyst used during SER long 1, which was only submitted to 1 h of reaction, presented higher carbon deposits than the catalyst used during TR short 2 of our previous work [43], which was submitted to 4 h of reaction after the last oxidative regeneration. By comparing the amounts

of carbon measured in the catalyst samples used in SER short 1, 2 and 3, higher carbon deposits were measured in the catalyst samples used during SER short 1 and 2. This occurs because while in SER short 3 regenerative oxidation was carried out every 4 h, except after the last 4 h reaction, during both SER short 1 and 2 no regenerative oxidation was performed (Table 5.2.1).

Higher amounts of carbon where obtained for the catalyst used during SER short 1 as compared to that used in SER short 2 (Table 5.2.2). The differences between SER short 1 and 2 are the total duration of the tests, 12 h and 13 h respectively, and the frequency of sorbent regeneration (cf. Table 5.2.1). Clearly, the difference in the total duration of the tests is not the cause of the differences in carbon deposition. If that was the case, the catalyst used during SER short 1 would at most present similar or even lower amounts of carbon compared to those observed in the catalyst used in SER short 2. Therefore, the cause of such difference in carbon deposition should be associated to the more frequent sorbent regenerations performed in SER short 1 run. These more frequent regenerations allowed the reactor to be operated in the sorption-enhanced mode more often and consequently for a longer total period. This suggests that the longer the reactor is operated in sorption-enhanced mode, the more coke deposition occurs on the used catalyst. In other words, most of the observed coke could have been formed during the first moments of reaction (pre- and breakthrough). Such conclusion also agrees with the significant increase in the carbon content from the catalyst samples used in the TR to those employed in the SER. This will be further discussed later on.

Regarding K-MG30, the formation of carbon deposits on this material was observed for the different SER runs. Furthermore, during the SER short reactor experiments the formation of carbon deposits on K-MG30 increased similarly to that on the catalyst (Table 5.2.2). However, considerably lower amounts of coke were formed on K-MG30 as compared to the catalyst samples. Similar carbon deposits were observed in the sorbent samples used during both SER long 2

and SER short 3 (the only tests where oxidative regeneration was carried out). However, while the sorbent used in SER long 2 was submitted to 8 h of reaction after the last oxidative regeneration, the sorbent used in SER short 3 was only submitted to 4 h of reaction after the last oxidative regeneration. This means that lower carbon deposition per mass of sorbent occurred in the long reactor. This does not mean that the total amount of carbon that deposited over K-MG30 in the long reactor is lower. This will also be further discussed below.

5.2.3.2 Steam reforming of glycerol tests

5.2.3.2.1 Sorption-enhanced reactor

5.2.3.2.1.1 Effect of CH_4 production

With the aim of reducing the shortcomings observed during the TR tests in our previous work [43], namely in terms of limited H_2 production and deactivation due to coke formation, a SER was used, the only difference being the inclusion of K-MG30, a commercial hydrotalcite for CO_2 capture, on the bed together with the catalyst. Preliminary, 1 h reaction cycles (not shown) were carried out with intermediate oxidative regenerations. Surprisingly, for all reaction cycles the yields of H_2 obtained during the CO_2 pre-breakthrough were lower than those obtained during the breakthrough and in the post-breakthrough.

In order to understand such behavior, a longer reactor (described above) was used, aiming to increase the CO_2 breakthrough time. Firstly, the SER long 1 run was carried out (Fig. 5.2.3 (a)), being that in this case a maximum H_2 yield was observed in the pre-breakthrough region, followed by a subsequent slight decrease and stabilization. However, after approximately 25 min the yield of H_2 started increasing again, considerably surpassed the maximum observed at the end of the pre-breakthrough and stabilized until the end of the experiment.

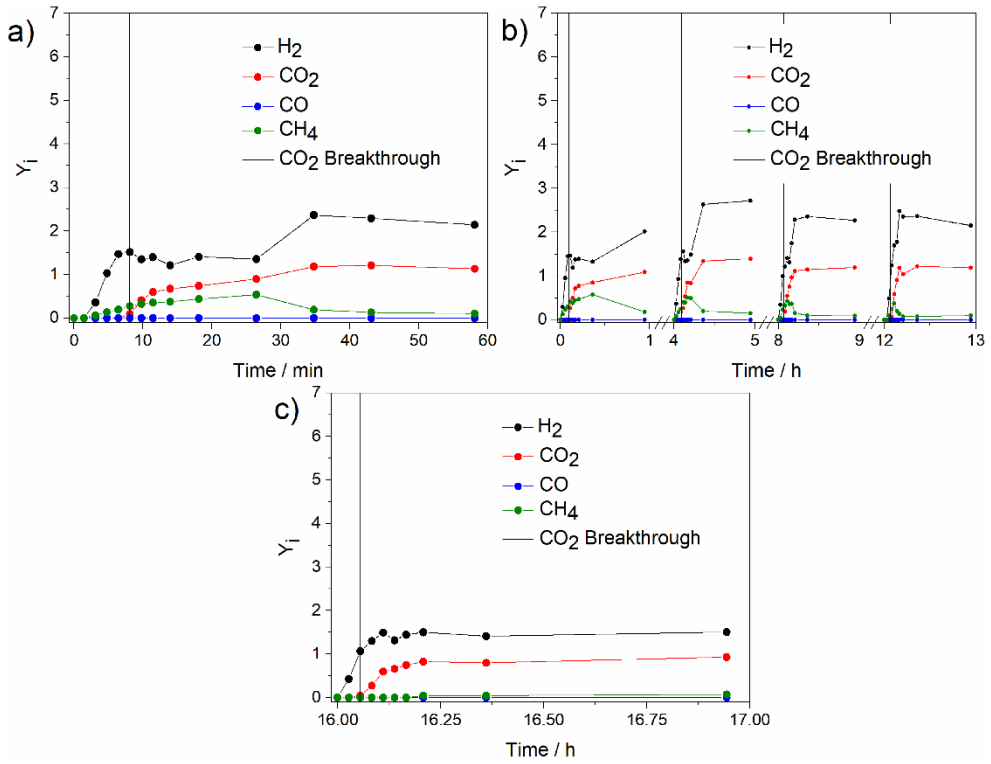

Fig. 5.2.3 - Evolution over time of the yields of gaseous products during (a) SER long 1, (b) the first hour of each 4 initial cycles of SER long 2 and (c) the first hour of the fifth cycle of SER long 2 experiments (conditions provided in Table 5.2.1).

To better understand the H_2 yield behavior, SER long 2 test was performed (with oxidative regenerations every 4 h as described in Table 5.2.1). Besides the behavior already described for SER long 1 test, it was observed that the H_2 yield remained surprisingly stable until the end of the 4 h cycle (Fig. 5.2.3 (b)); not shown after the first hour). During the 4 reaction cycles the H_2 yields were always higher during the post-breakthrough, thus suggesting that this behavior is not mainly related to the duration of CO_2 breakthrough. On the other hand, the maximum of H_2 yield in the post-breakthrough zone was observed progressively earlier as the reaction cycles were carried out, and in the fourth cycle that maximum was observed exactly at the end of the CO_2 breakthrough.

Symmetrically, it was noticed that CH_4 production was progressively inhibited from cycle to cycle, so that in the fourth cycle not only less CH_4 was initially produced, but also its production was almost completely inhibited earlier, similarly to the behavior observed in our previous work [43].

A fifth 4 h reaction cycle was carried out for a better comprehension of this behavior, but this time without being preceded by regenerative oxidation, only by CO_2 sorbent regeneration with N_2. In this case the H_2 yield reached its maximum during the breakthrough, stabilized and a slow deactivation after 17 h on-stream (not shown) was observed (Fig. 5.2.3 (c)). Since the catalyst was not regenerated, not only were the H_2 yields lower, but also very low CH_4 yields were observed during the whole test. The initial production of CH_4 noticed in the first four cycles (Figure 5.2.3 (b)) was not observed in this case probably because the methanation sites were inhibited by carbon deposits.

It can be concluded that the initial occurrence of H_2-consuming methanation was the main responsible for the hindered effect of CO_2 capture on H_2 production. Since a comparison is to be established between the different reactor configurations, all SER tests discussed below were carried out in the 120 mm long reactor (due to limitations of the membrane length used in the SEMR). Before that, a comparison between SER long 1 and TR long 1 in terms of the evolution over time of both H_2 yield and purity is presented in Fig. 5.2.4. The H_2 yield obtained in TR long 1 during the CO_2 pre-breakthrough period of SER long 1 was below that reached in the latter. Afterwards an increase was also observed, but earlier as compared to SER long 1. In terms of H_2 purity, significantly higher H_2 purity was attained in the SER, especially in the pre-breakthrough region due to CO_2 removal.

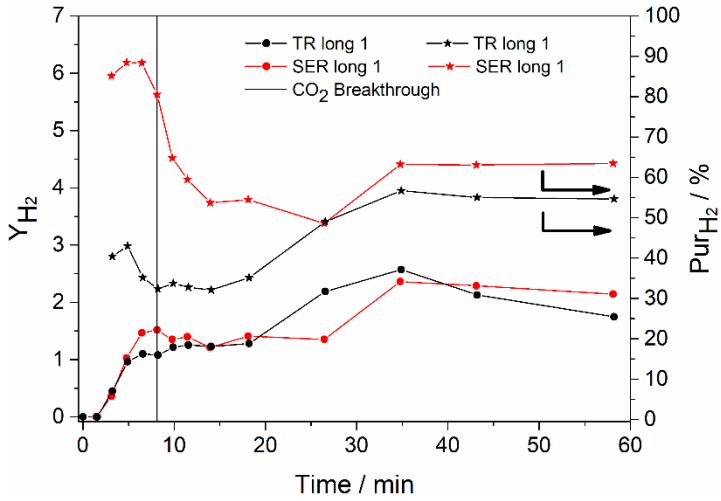

Fig. 5.2.4 - Evolution over 1 h of the H_2 yield and purity during SER long 1 and TR long 1 experiments (conditions provided in Table 5.2.1).

5.2.3.2.1.2 Blank test with K-MG30

Regarding the short reactor tests, a blank test in which the reactor was filled with 1.6 g of K-MG30 homogeneously diluted with SiC was firstly performed over 6 h. The production of gaseous products was observed over the full duration of the experiment (Fig. 5.2.5). It has been previously reported that K-MG30 catalyzes the WGS reaction in the temperature range 573-673 K [39, 44]. However, here only glycerol and water are fed and not CO. As seen before in the TR short blank experiment, conversion of glycerol into condensable products occurred, but not into carbon-containing gaseous products [43]. Therefore, it is likely that the hydrotalcite catalyzed to some extent the decomposition of glycerol into syngas (Eq. (5.2.1)). Afterwards, WGS reaction must have taken place as well. During the whole test, total conversion of glycerol was always above 99% (Fig. 5.2.5 (a)). As for the conversion into carbon-containing gaseous products, since some of the produced CO_2 was captured by the sorbent, it was only calculated after the end of the first hour (all gas produced exits the reactor). The conversion into carbon-containing gases remained between 11-13%. This means that all the remaining glycerol was converted into condensable products

and coke and/or part of the formed carbon-containing gaseous products were converted into coke.

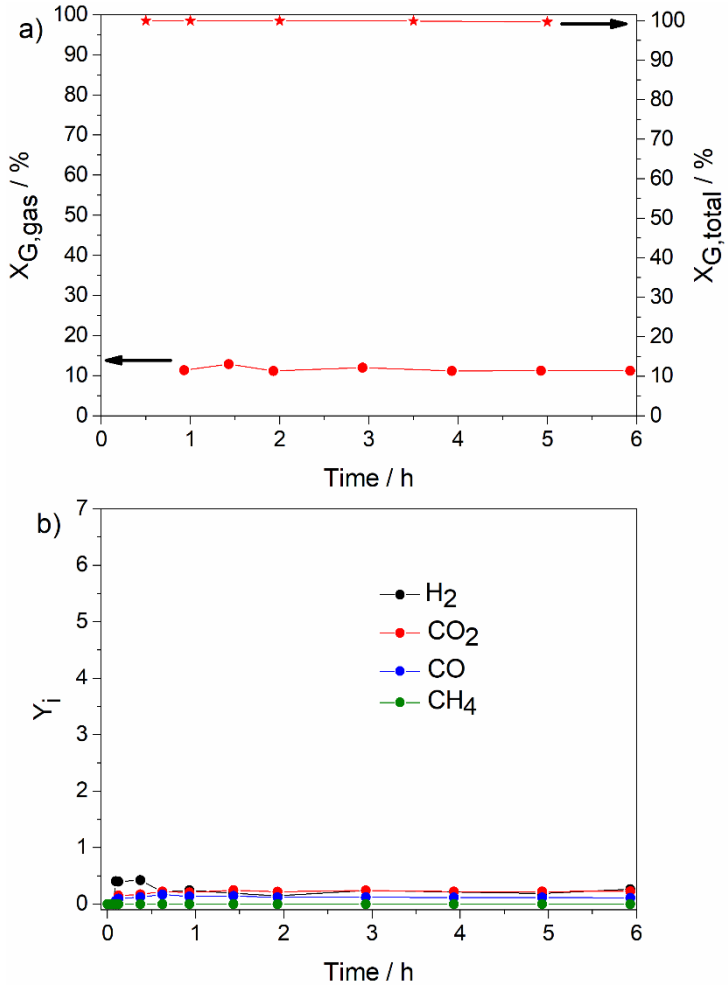

Fig. 5.2.5 - Evolution during the SER short blank experiment of (a) both total glycerol conversion and glycerol conversion into carbon-containing gaseous products and of (b) the yields of gaseous products (experimental conditions provided in Table 5.2.1).

Since only less than 10% of glycerol was decomposed into liquid products during the TR short blank experiment [43], the additional total glycerol conversion here observed must have been catalyzed by the hydrotalcite. Di Cosimo *et al.* [45] observed that calcined hydrotalcites with similar Mg/Al ratio as K-MG30 presented catalytic activity towards ethanol dehydrogenation to acetaldehyde.

In another work [46] it was found that similar calcined hydrotalcites catalyzed acetone oligomerization, which could have occurred here as well. Moreover, coke formation was observed during acetone oligomerization on potassium promoted MgO [47]. This could explain the considerable carbon deposits observed in the K-MG30 used in this test (See Table 5.2.2).

The yields of H_2, CO and CO_2 over time are presented in Fig. 5.2.5 (b). A maximum H_2 yield of approximately 0.4 $\mathrm{mol} \cdot \mathrm{mol}_{\mathrm{fed\ glycerol}}^{-1}$ was attained at the beginning of the test, followed by a subsequent decrease and stabilization until the end of the test. Regarding CO and CO_2, they presented a very similar behavior, the yield of CO_2 being always higher than that of CO. Moreover, after the CO_2 breakthrough (ca. 0.6 h) the yield of H_2 remained very similar to that of CO_2, which confirms the occurrence of WGS. No CH_4 was observed meaning that the sorbent was not active towards methanation reactions.

5.2.3.2.1.3 Long term operation with frequent sorbent regeneration

A first 12 h test consisting of 6 reaction periods of 2 h in the SER was carried out, being that between each reaction stage the sorbent was regenerated with N_2. Both total conversion of glycerol and post-breakthrough (during the second hour of each cycle) glycerol conversion into carbon-containing gaseous products are presented in Fig. 5.2.6, as well as a comparison with the results attained under the same conditions in the TR. While complete conversion of glycerol was observed during the whole test in the SER, a decrease started being observed at around 8 h in the TR. The post-breakthrough conversion into carbon-containing gaseous products started at around 50-55% and suffered an absolute decrease below 20% during the six 2 h reaction cycles in the SER. Even though similar post-breakthrough glycerol conversions into carbon-containing gaseous products were initially observed in both TR and SER, a more pronounced loss of activity over time was observed in the TR.

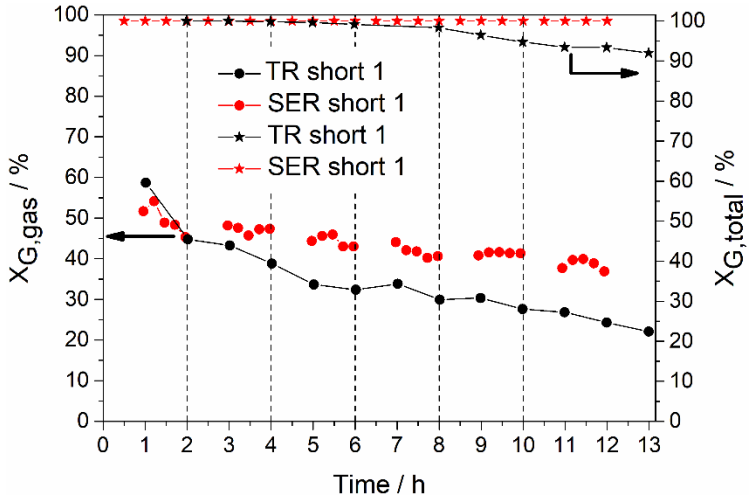

Fig. 5.2.6 - Comparison of the evolution of both total glycerol conversion and post-breakthrough glycerol conversion into carbon-containing gaseous products over time between TR short 1 and SER short 1 experiments (conditions provided in Table 5.2.1). The vertical dashed lines represent the moments at which sorbent regeneration with N_2 was performed.

The yields of H_2, CO, CH_4 and CO_2 (observed at the SER outlet) are presented in Fig. 5.2.7. In the first cycle, the yields of both H_2 and CH_4 started increasing simultaneously in the pre-breakthrough region, being that the increase of CH_4 ceased during the CO_2 breakthrough. In that moment the yield of CH_4 decreased drastically from around 0.7 to around 0.3 $\mathrm{mol} \cdot \mathrm{mol}_{\mathrm{fed\ glycerol}}^{-1}$ and the yield of H_2 increased from 2 to 3 $\mathrm{mol} \cdot \mathrm{mol}_{\mathrm{fed\ glycerol}}^{-1}$, once more indicating that in the latter period H_2-consuming methanation was inhibited. At the same time the observed outlet CO_2 yield reached its maximum of approximately 1.5 $\mathrm{mol} \cdot \mathrm{mol}_{\mathrm{fed\ glycerol}}^{-1}$, and started decreasing until the end of the reaction stage; the same was observed for both H_2 and CH_4. In opposition to what occurred in the TR, there was no CO exiting the SER for more than 1 h and when it started being detected at the reactor outlet, its yield remained below 0.1 $\mathrm{mol} \cdot \mathrm{mol}_{\mathrm{fed\ glycerol}}^{-1}$. This means that all or almost all CO that was being produced in the decomposition of glycerol was being consumed either through WGS or methanation (Eq. (5.2.4)). However, since CH_4 production dropped significantly

at around 30 min and CO remained almost undetected, it means that WGS became its major route of conversion. Moreover, since after the saturation of the sorbent high conversion of CO remains, it implicates that the enhanced conversion of CO was not only due to the removal of CO_2 from the reaction medium (therefore shifting the WGS equilibrium), but probably also due to the catalytic activity of K-MG30 in WGS. Maroño *et al.* [44] observed that K-MG30 could convert more than 90% of CO at 673 K and 15 bar for at least 3 h. CO could also be consumed in coke production, but this will be discussed later.

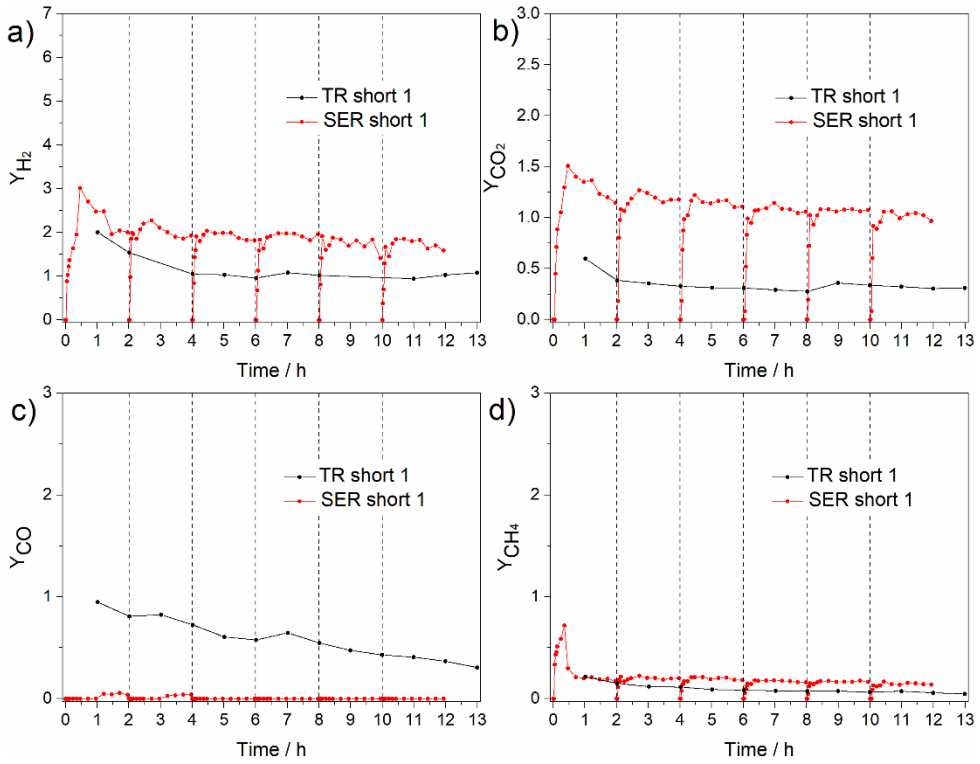

Fig. 5.2.7 - Comparison of the evolution of the yields of (a) H_2, (b) CO_2, (c) CO and (d) CH_4 over time between TR short 1 and SER short 1 experiments (conditions provided in Table 5.2.1). The vertical dashed lines represent the moments at which sorbent regeneration with N_2 was performed.

As for the reaction cycles performed afterwards with intermediate regeneration of the sorbent (but no catalyst regeneration), a decrease of the

initial maximum of H_2 yield was observed from the first to the second cycle. Then, a much smaller decrease is progressively observed throughout the cycles. Moreover, the H_2 yield maximum appeared progressively earlier, as progressively lower amounts of CH_4 were being produced. Regarding CO, the behavior observed in the first 2 h was also observed in the second cycle, but in the subsequent cycles no CO was registered. It could be anticipated that the slight deactivation that is observed throughout the cycles leads to a slightly lower production of CO from glycerol, but does not affect as much its conversion through WGS as the sorbent was regenerated every 2 h. Nevertheless, the difference is small. As for the yield of CO_2 in the post breakthrough region, a high decrease was observed during the first cycle while a smoother decrease was observed in the following cycles, similarly to what occurred with H_2. This similar behavior of both H_2 and CO_2 indicates once again the dominance of WGS reaction over secondary reactions such as methanation or coking reactions.

Regarding the selectivities towards H_2, CO_2, CO and CH_4, their evolution with time is presented in Fig. E.1 of Appendix E. Since these selectivities depend on the outlet CO_2 molar flow rate, for the SER they were only estimated during the second hour of each reaction cycle where no CO_2 sorption is occurring anymore.

Finally, the purity of H_2 was analyzed (Fig. 5.2.8). As expected, the maximum H_2 purity in the first reaction cycle, around 70%, was observed in the pre-breakthrough region when all CO_2 was being retained by the sorbent. Afterwards it decreased down to around 50%, stabilized and when the production of CH_4 started being inhibited, less hydrogen was consumed by such parallel reaction and inherently the purity of H_2 increased again, reaching a new value around 60%. For the other cycles, a very similar behavior was observed. The only difference as compared to the first cycle is that after the initial maximum due to the capture of CO_2, the purity of H_2 decreased directly to the final steady-

state value around 60%, as almost no CH_4 was produced during these cycles, contrarily to what occurred at the beginning of the first cycle.

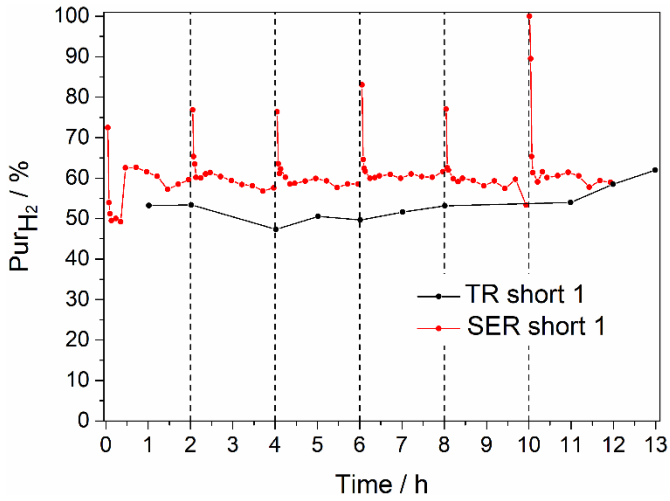

Fig. 5.2.8 - Comparison of the evolution of the purity of H_2 over time between TR short 1 and SER short 1 experiments (conditions provided in Table 5.2.1). The vertical dashed lines represent the moments at which sorbent regeneration with N_2 was performed.

When comparing the results obtained in the SER short 1 and TR short 1 experiments, several advantages of the SER can be highlighted. The first advantage is the considerably higher yields obtained during the whole duration of the test and post-breakthrough selectivities of both WGS products, H_2 and CO_2 (Figs. 5.2.7 and 1). Probably due do the significant extension of this reaction, CO was practically absent for the complete duration of the SER short 1 test, in opposition to the high amounts detected when using the conventional TR. As for CH_4, a very similar behavior was observed for both reactors. Even though very similar conversions into carbon-containing gaseous products were observed during the first 2 h for both reactors, from that point on they started diverging, and while in the TR that conversion after 12 h was around 22%, in the SER it was around 37% (Fig. 5.2.6). Moreover, the total glycerol conversion was always 100% in the SER, on contrary to the observed decrease in the TR. The H_2 purity of the outlet stream was in general around 10% higher in the SER,

except before and during the breakthrough where that difference was considerably higher (Fig. 5.2.8). Therefore, it can be concluded that the SER showed not only to be advantageous in the pre-breakthrough and breakthrough regions, but also during the post breakthrough, probably due to the already mentioned catalytic activity of K-MG30 towards both glycerol decomposition and, more importantly, WGS.

5.2.3.2.1.4 Long term operation without frequent sorbent regeneration

Considering the post-breakthrough advantage of the SER compared to the TR, a second experiment (SER short 2) was performed in the SER for 13 h (6 h + 7h), but this time the sorbent was only regenerated overnight after 6 h of reaction. The main goal of this test was to assess the effect of performing longer GSR cycles on the process performance. No significant differences as compared to SER short 1 run were observed (Fig. 5.2.9-11 and Fig. E.2 vs. Figs. 5.2.6-8 and Fig. E.1).

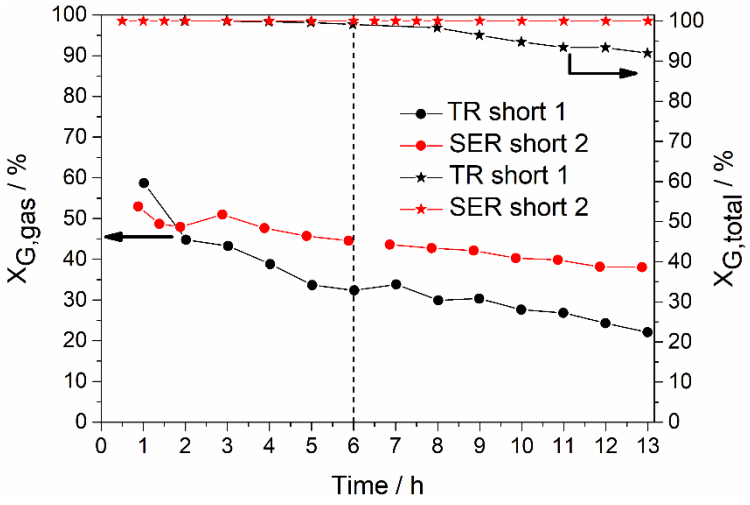

Fig. 5.2.9 - Comparison of the evolution of both total glycerol conversion and post-breakthrough glycerol conversion into carbon-containing gaseous products over 13 h between TR short 1 and SER short 2 experiments (conditions provided in Table 5.2.1). The vertical dashed line represents the moment at which sorbent regeneration with N_2 was performed.

Even though K-MG30 was only regenerated once during SER short 2 test, the loss of activity over time was very similar to that obtained in SER short 1.

Regarding the presence of CO in the reactor outlet, a small difference between both experiments was observed. While in SER short 1 during the first 2 cycles unreacted CO was detected during the second hour of each cycle, in SER short 2 the detection of unreacted CO started occurring at approximately the same time but lasted until the end of 6 h (Fig. 5.2.10).

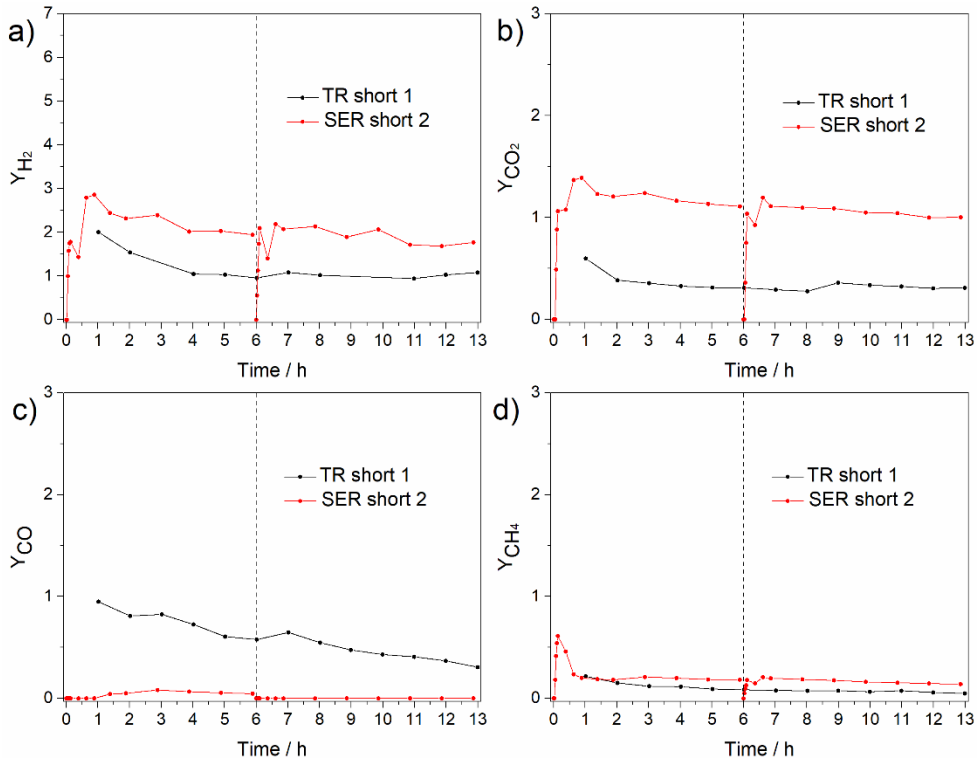

Fig. 5.2.10 - Comparison of the evolution of the yields of a) H_2, b) CO_2, c) CO and d) CH_4 over 13 h between TR short 1 and SER short 2 experiments (conditions provided in Table 5.2.1). The vertical dashed line represents the moment at which sorbent regeneration with N_2 was performed.

This probably occurred because in SER short 2 the sorbent was not regenerated every two hours and it is possible that such regeneration contributed to a slightly higher catalytic performance of the sorbent towards CO

consumption through WGS. The more frequent regenerations during SER short 1 could have also allowed a generally higher activity of the sorbent towards the formation of liquid precursors of coke, which could have contributed to the higher coke formation observed during SER short 1. During the second cycle, no CO was detected at the reactor outlet, similarly to what occurred during SER short 1 experiment. Since the sorbent was not regenerated every 2 h, the other identified difference was that the higher purities of the outlet stream in H_2 before and during the breakthrough were not observed so often, but only at the beginning of the test and at 6 h, after sorbent regeneration (Fig. 5.2.11).

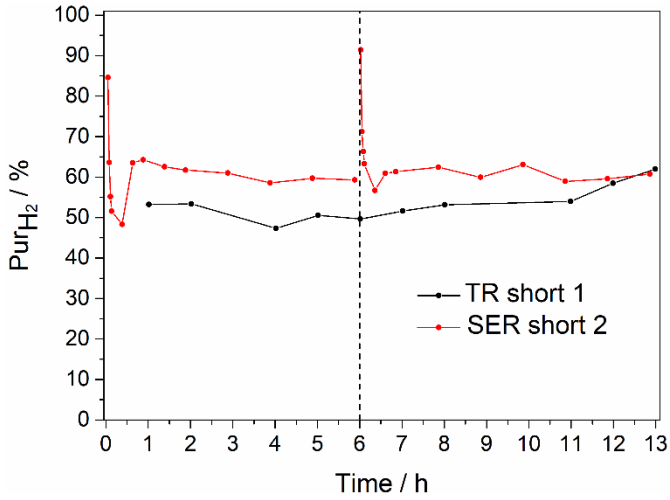

Fig. 5.2.11 - Comparison of the evolution of the purity of H_2 over 13 h between TR short 1 and SER short 2 experiments (conditions provided in Table 5.2.1). The vertical dashed line represents the moment at which sorbent regeneration with N_2 was performed.

5.2.3.2.1.5 Long term operation with frequent catalyst and sorbent oxidative regeneration

Even though it has been observed in SER long 2 that regenerating the catalyst partially hid the CO_2 capture effect at the beginning of the process, due to regeneration of the methanation sites, it was also observed in SER short 1 and 2 experiments that the post-breakthrough region is also very important, as the catalytic activity of the sorbent towards mainly WGS leads to a higher

performance of the SER as compared to the TR. Moreover, it has been observed in TR short 2 run that a considerable enhancement of the process performance was obtained when periodic oxidative regeneration was performed [43]. For that reason, a third 16 h test (SER short 3) consisting of four 4 h cycles with intermediate regenerative oxidation was performed.

Once again full total glycerol conversion was observed throughout the experiment (Fig. 5.2.12), similarly to what occurred during TR short 2. In terms of conversion of glycerol into carbon-containing gaseous products in the post-breakthrough region, a very similar behavior was observed throughout the cycles, similarly to what was observed in TR short 2 test. Moreover, once again the initial post-breakthrough glycerol conversion into carbon-containing gaseous products was in general similar to that obtained in the TR and for higher reaction times the conversions obtained in the SER decreased less than in the TR.

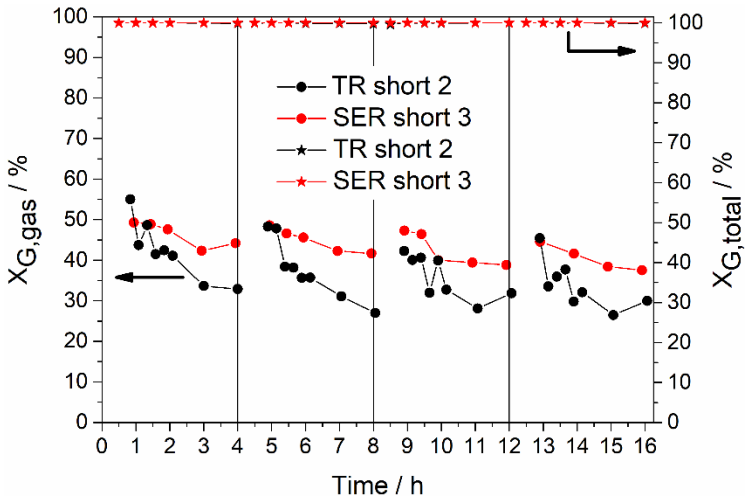

Fig. 5.2.12 - Comparison of the evolution of both total glycerol conversion and post-breakthrough glycerol conversion into carbon-containing gaseous products over 16 h between TR short 2 and SER short 3 experiments (conditions provided in Table 5.2.1). The vertical solid lines represent the moments at which oxidative regeneration was performed.

Regarding the products yields, Fig. 5.2.13, the behavior observed here during the first 4 h reaction cycle was very similar to what was observed during

the first 4 h of SER short 2 (Fig. 5.2.10). The main difference occurs in the subsequent cycles, where the yields of the first cycle are almost completely recovered. Namely in terms of H_2, CO_2 and CO, their yields varied very similarly during the 4 reaction cycles. The maximum of H_2 observed during cycles 2-4 may have been missed between loops in cycle 1 as it was not observed. As for CH_4, on the other hand, the maximum initially observed slightly decreased throughout the reaction cycles.

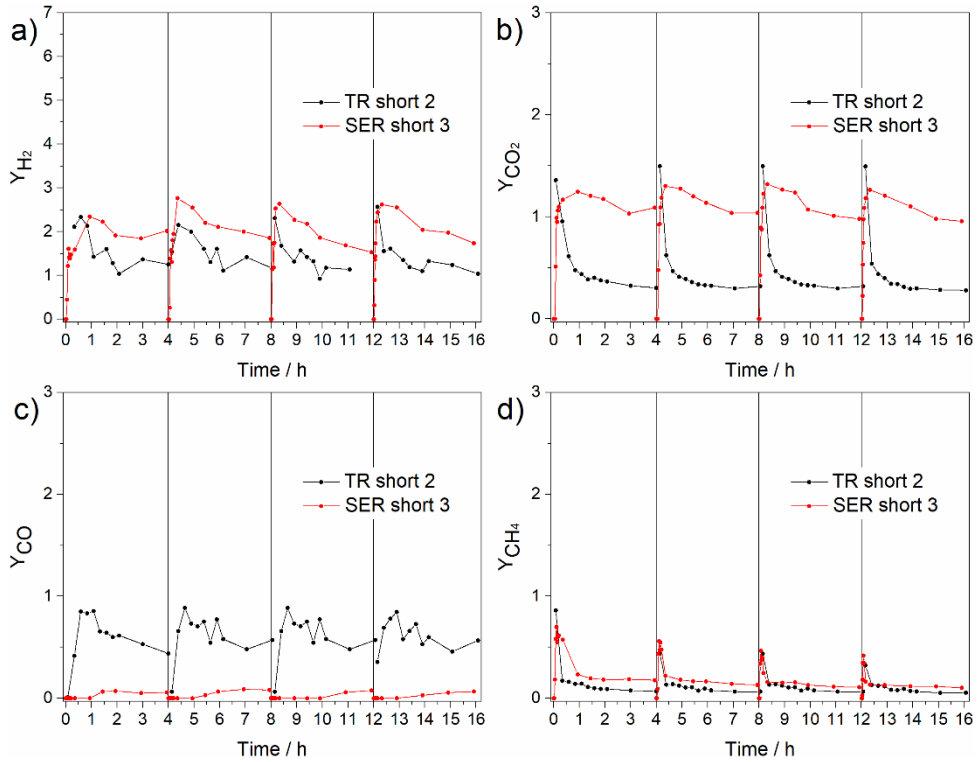

Fig. 5.2.13 - Comparison of the evolution of the yields of (a) H_2, (b) CO_2, (c) CO and (d) CH_4 over 16 h between TR short 2 and SER short 3 experiments (conditions provided in Table 5.2.1). The vertical solid lines represent the moments at which oxidative regeneration was performed.

The particular behavior observed for CO during the 3 tests performed in the SER might help to better understand how coke formation selectively affected the catalytic activity towards the desired reactions, i.e. glycerol decomposition and WGS. While in SER short 1 experiment CO was observed only during the

second hour of the first 2 cycles, in SER short 2 it was observed, only in the first cycle, after the first hour of reaction and remained until 6 h. In SER short 3 (the only one where oxidative regeneration has been employed), CO was observed after the first hour of each reaction cycle; after 16 h CO was still being detected at the reactor outlet. As observed in TR short 2 test, while high WGS inhibition occurred during the first moments, during the rest of reaction time CO concentration decreased gradually, meaning that glycerol decomposition sites suffered a more progressive deactivation over time. Therefore, during the post-breakthrough in the SER the catalyst should be mainly active towards glycerol decomposition into syngas and K-MG30 should contribute significantly to the conversion of CO through WGS. The appearance of CO in SER short 3 run probably means that K-MG30 was not active enough to convert all CO being produced by the catalyst. In other words, K-MG30 was probably deactivating faster than the catalyst. This probably occurs because K-MG30 is used for CO_2 sorption and, consequently, less active sites are used for catalyzing the WGS reaction. Since in SER short 1 run the sorbent was regenerated every 2 h with N_2, it was able to recover part of its catalytic activity, possibly at the expense of the decrease in CO_2 sorption capacity, and so all CO was once again fully consumed. At the same time the catalyst kept deactivating and a point was reached in which the activity of K-MG30 towards WGS during the 2 h cycles remained higher than the catalyst activity towards CO production. On the other hand, during SER short 2 experiment K-MG30 was only regenerated with N_2 at 6 h and that is why CO was observed for 6 h during this test. After sorbent regeneration, partial recovery of the WGS activity of K-MG30 probably occurred, thus remaining more active towards CO consumption than the catalyst towards CO generation. Finally, in SER short 3 experiment, since both catalyst and K-MG30 were oxidatively regenerated, both recovered their respective catalytic activities and assuming that K-MG30 deactivates faster than the catalyst, CO was always observed after the first hour of each reaction cycle.

In terms of post-breakthrough selectivity towards H_2 production (Appendix E, Fig. E.3), a slight decrease over time was observed for the different cycles in the SER, being that these were once again in average between 50-75%. As for the selectivity towards CO_2, very similar values to those obtained during both SER short 1 and 2 were observed throughout all the test. In terms of CO and CH_4, their selectivities were also very similar to those observed during SER short 1 and 2 except that for CO, whose selectivity started increasing after the first hour of every reaction cycle and was noticeable even after 16h. This is related to what was discussed above. In terms of H_2 purity (Fig. 5.2.14) initial process peaks were observed at the beginning of each cycle once again due to CO_2 capture. In general, overall performance during the four reaction cycles in the SER was similar, evidencing the effectiveness of the oxidative regeneration.

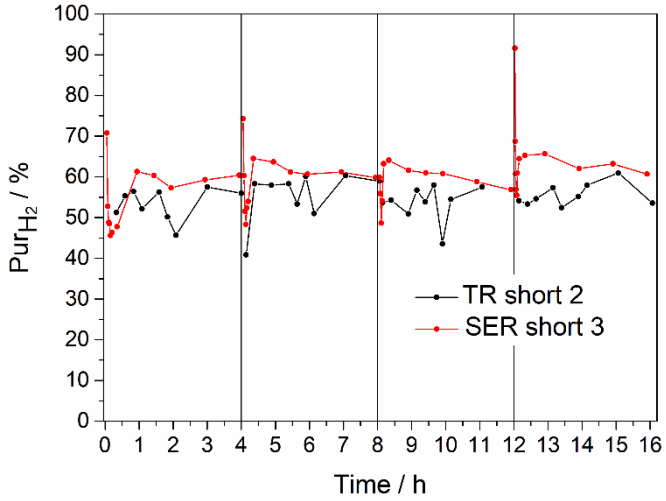

Fig. 5.2.14 - Comparison of the evolution of the purity of H_2 over 16 h between TR short 2 and SER short 3 experiments (conditions provided in Table 5.2.1). The vertical solid lines represent the moments at which oxidative regeneration was performed.

For SER short 3 experiment, the amounts of carbon burned during the three oxidative regenerations are summarized in Table 5.2.3, while the CO_2 and CO profiles obtained during such regenerations are presented in Fig. E.4 (Appendix E). More carbon deposits were observed during these experiments,

in accordance with the superior carbon content in SER short 3 run compared to TR short 2 measured through EDS (Table 5.2.2). This could mean that the removal of CO_2, during sorption-enhanced, might have enhanced the formation of carbon in the catalyst, for example through Boudouard reaction (Eq. (5.2.6)), where CO_2 is the co-product. In fact such strongly exothermal reaction could be favored by the low temperature used [48] and it has been described as one of the main sources of deactivation in GSR [49]. Since this was not observed in our previous thermodynamic analysis [12], this result could be more influenced by the catalyst selectivity towards coke formation than by the process thermodynamics. Moreover, if the formation of coke deposits was enhanced by CO_2 sorption, a considerable portion of the observed coke should have been formed during the pre- and breakthrough periods. This could be the reason for the similar conversion of glycerol into carbon-containing gaseous products observed in the SER at 1 h of each cycle. Afterwards, as both catalyst and K-MG30 worked as catalysts, the formation of coke was distributed by both, as observed in the EDS results, and this might be the reason for the lower loss of catalytic activity towards gaseous products. Also it was observed during SER short blank that K-MG30 possessed some activity towards glycerol decomposition into CO and H_2. This could have also contributed to the higher production of gaseous products in the SER, despite the higher coke formation. In case Boudouard reaction occurred significantly, it also contributed to the lower amounts of CO measured in the SER.

This higher formation of gaseous products and carbon deposits implies that the intermediate liquid products formed were converted to a higher extent in the SER. Furthermore, the higher coke formation could be associated to a more selective production of intermediate liquid products that are potential coke precursors. As already discussed, the presence of K-MG30 could have promoted oligomerization reactions that lead to the formation of coke promoters. If these compounds are not reformed to produce gaseous products, the acid-

base sites of K-MG30 could have kept promoting the dehydrogenation of these species, ultimately leading to the formation of carbon deposits [50]. This could mean that such coke precursors will be formed when hydrotalcite-like materials contact with glycerol under conditions similar to those here adopted, regardless of the catalyst used. Considering that hydrotalcites are the best option for CO_2 sorption at around 673 K, a possible alternative could be to use, before the mixed catalyst/sorbent bed, a catalyst bed where glycerol would be converted into syngas. That way the hydrotalcite would not promote such undesired reactions, besides CO_2 sorption and WGS. Another possibility would be to use modified hydrotalcites that are less selective towards the formation of coke precursors.

Table 5.2.3 - Amount of carbon deposited on both catalyst and sorbent used in SER short 3 experiment that was gasified during each oxidative regeneration.

Moment of oxidative regeneration / h	Gasified carbon / $mg_C \cdot g_{cat+sorb}^{-1}$
4	90.5
8	104.4
12	108.4

5.2.3.2.2 Sorption-enhanced membrane reactor

Before being used, an initial membrane activation procedure was carried out and permeation tests were performed, as detailed in Appendix E. Afterwards, two 4 h GSR experiments with intermediate oxidative regeneration were carried out in the SEMR. A comparison between the SER and SEMR in terms of both total glycerol conversion and glycerol conversion into carbon-containing gaseous products is established in Fig. 5.2.15. The results obtained during SER short 3 experiment are used for this comparison.

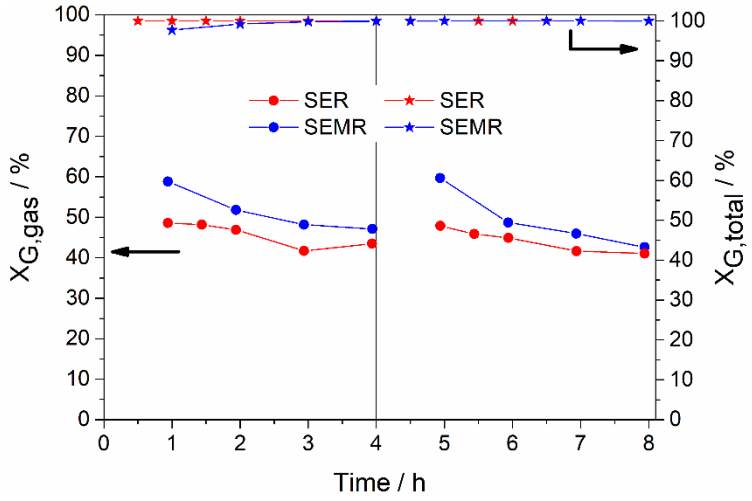

Fig. 5.2.15 - Comparison of the evolution of both total glycerol conversion and post-breakthrough glycerol conversion into carbon-containing gaseous products over 8 h between the SER and SEMR (conditions provided in Table 5.2.1). The vertical solid line represents the moment at which oxidative regeneration was performed.

Total glycerol conversion above 99% was obtained in the SER during the whole test, as already observed previously, and the same was observed in the SEMR. Regarding glycerol conversion into carbon-containing gaseous products, after the first hour of each reaction cycle (post-breakthrough region), an increase was observed from the SER to the SEMR. Therefore, it can be concluded that the addition of the membrane increased the production of carbon-containing gases. In other words, since the total glycerol conversion is the same in both reactors, the conversion of glycerol into liquid products and coke decreased.

For a more precise understanding of the effect of the membrane, the evolution over time of the yields of H_2, CO_2 CO and CH_4 is presented in Fig. 5.2.16 for both the SER and SEMR. More H_2 was produced in the SEMR than in the SER during both reaction cycles. During the pre-breakthrough, maximum H_2 yields of approximately 3.6 $\mathrm{mol} \cdot \mathrm{mol}_{\mathrm{fed\ glycerol}}^{-1}$ were attained for both cycles when using the Pd-Ag membrane, while the maximum H_2 yields obtained in the SER during the pre- and breakthrough were around 1.6 $\mathrm{mol} \cdot \mathrm{mol}_{\mathrm{fed\ glycerol}}^{-1}$. This corresponds to an enhancement of 125%.

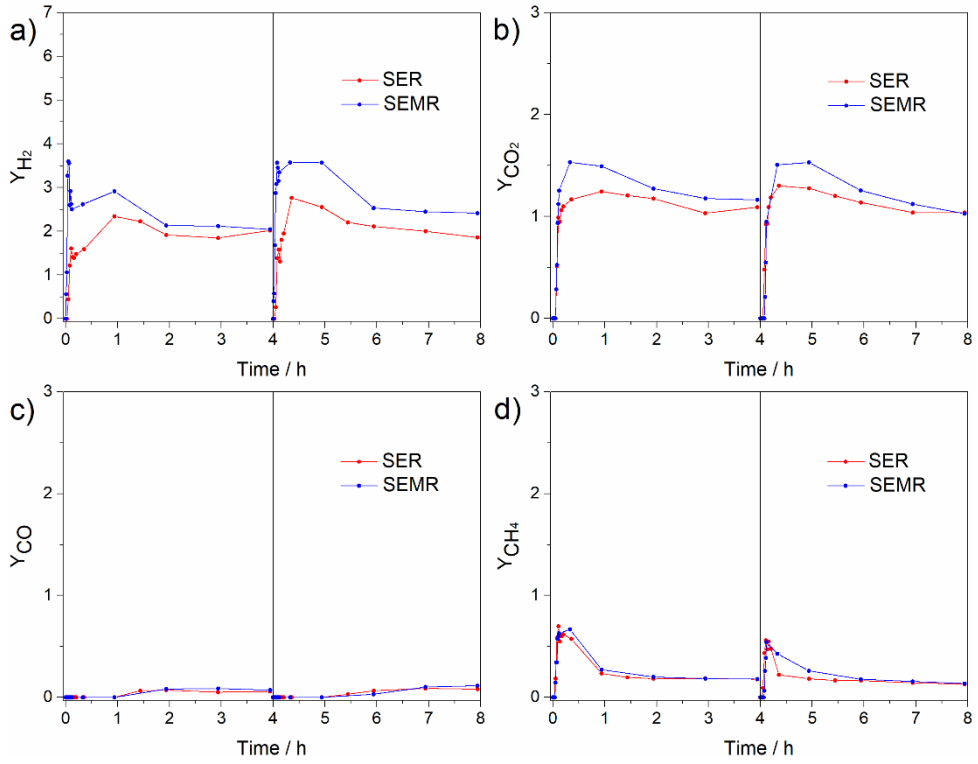

Fig. 5.2.16 - Comparison of the evolution of the yields of (a) H_2, (b) CO_2, (c) CO and (d) CH_4 over 8 h between the SER and SEMR (conditions provided in Table 5.2.1). The vertical solid line represents the moment at which oxidative regeneration was performed.

Moreover, in the SEMR, CH_4 only started being observed at the reactor outlet at the beginning of CO_2 breakthrough (Fig. 5.2.17). Methanation inhibition occurred during the breakthrough and post-breakthrough periods, which resulted in a new increase of the H_2 yield. However, the yield of H_2 during methanation inhibition did not increase to values above those observed during the pre-breakthrough, contrarily to what was observed in the SER. The difference is that while in the SER simultaneous production of H_2 and CH_4 was observed in the pre-breakthrough region, more noticeable in Fig. 5.2.3 (a), which certainly avoided the attainment of higher H_2 yields, in the SEMR only H_2 was produced in the same region and so no H_2 was consumed for CH_4 production. This can be more clearly seen in Fig. 5.2.17. While H_2 removal from the gas phase by the permselective membrane directly affects methanation reactions, CO_2 removal

by the hydrotalcite might only have an indirect influence on it (assuming CO methanation, Eq. (5.2.4), was the main CH_4 production path, also according to our previous observations [43]). The combination of both might be the responsible for the retarded CH_4 production in the SEMR as WGS was probably the most favored reaction with both its products being removed.

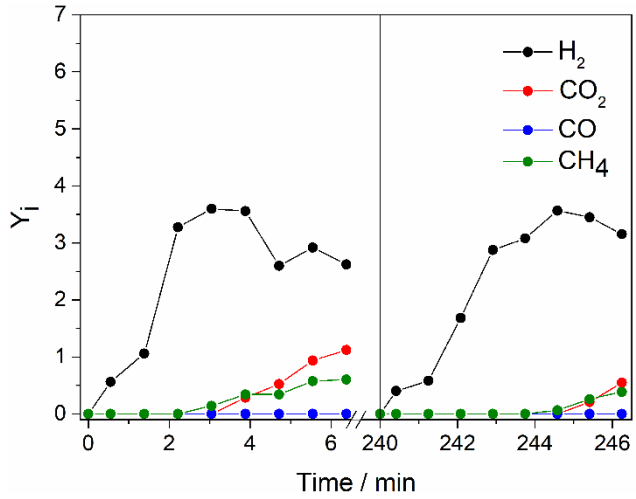

Fig. 5.2.17 - Evolution over time of the yields of gaseous products during the first minutes of each reaction cycle in the SEMR (conditions provided in Table 5.2.1). The vertical solid line represents the moment at which oxidative regeneration was performed.

The yields of CO_2 observed after the breakthrough in the SEMR were also higher than those obtained in the SER, which is clearly associated to an enhanced WGS due to the presence of the membrane. As the reaction in the SEMR proceeded, the difference between both SEMR and SER decreased, which might be related to membrane deactivation, potentially due to coke formation [36] and poisoning by mainly CO [25, 29].

Even though higher H_2 yields were observed during both reaction cycles in the SEMR, the same was not observed for the selectivity towards H_2, as only during the second reaction cycle the beneficial effect of using the SEMR on the H_2 selectivity was observed (Appendix E, Fig. E.6). During the first cycle reaction, the difference between the H_2 yields obtained in the SER and SEMR

after the first hour of reaction was not significant, and inherently selectivities were rather similar. On the other hand, the production of the carbon-containing gaseous products was not so affected, and for that reason the post-breakthrough selectivity towards H_2 was similar in both reactor configurations during the first 4 h. As for the other post-breakthrough gaseous products selectivities, no significant changes from the SER to the SEMR were observed (Appendix E, Fig. E.6).

Finally, one of the main advantages of the SEMR is the purity of the obtained H_2. First of all it was possible to obtain 100% pure H_2 in the permeate side during the whole experiment due to the nearly infinite selectivity of the used Pd-based membrane towards H_2. The percentage of H_2 recovered in the permeate side during the experiment is depicted in Fig. 5.2.18.

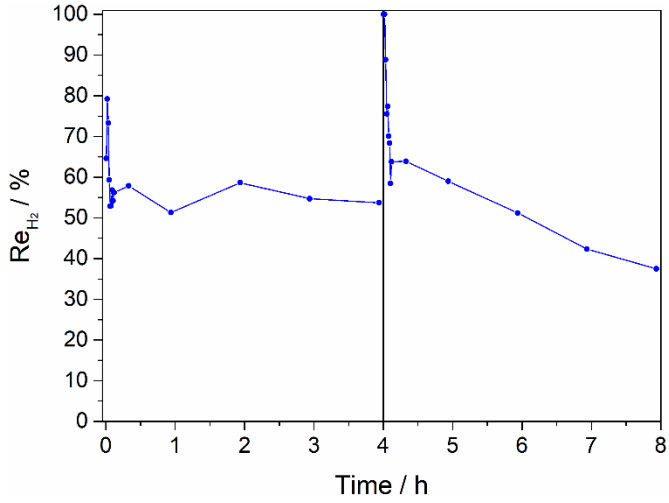

Fig. 5.2.18 - Evolution of H_2 recovery in the permeate side over 8 h in the SEMR. The vertical solid line represents the moment at which oxidative regeneration was performed.

It can be noticed that higher H_2 recoveries were obtained in the pre-breakthrough region, with values in the range of 70-100%. Moreover, during most of the pre-breakthrough period no other gaseous products besides H_2 were detected in the retentate stream, meaning that approximately 100% pure H_2 was also being obtained in the retentate side. In other words, if this process was carried out in

a multi column system that would allow to continuously operate in the pre-breakthrough region, highly pure H_2 would be continuously obtained in both retentate and permeate sides. The application of the simulated moving bed membrane reactor concept employing a mixed catalyst/sorbent bed [51] could be an even more attractive solution for the continuous operation in the pre-breakthrough region. Another advantage of working continuously in the pre-breakthrough region is the fact that CO and CO_2 are not present, thus avoiding the poisoning of the membrane.

During the post-breakthrough less H_2 was recovered, as seen in Fig. 5.2.18. In fact, during the second reaction cycle an almost linear decrease of H_2 recovery was observed over time, which could be associated to poisoning of the membrane caused by mostly CO, and coke that could have been depositing on the membrane, as well as on the catalyst and on the sorbent (for the case of coke), as already discussed. Furthermore, the production of H_2 decreased over time in detriment of other species, which resulted in a decrease of the H_2 permeation driving force, thus contributing to the decrease of H_2 recovery. In order to understand how much carbon deposits were formed during the SEMR operation, the concentration profiles of CO_2 obtained during the 2 oxidative regenerations performed (Appendix E, Fig. E.7) were used to estimate the amounts of coke gasified in each case, which are summarized in Table 5.2.4. In this case the CO_2 profiles are considerably more flat than those obtained in the SER (Appendix E, Fig. E.4) since air was considerably more diluted with N_2 in order to avoid significant temperature gradients that could potentially damage the membrane. Consequently, the oxidative regenerations lasted between 13-15 h in the SEMR instead of 5-6 h in the SER. No significant CO was observed.

Slightly more carbon was gasified during the second oxidative regeneration in the SEMR (see also Table 5.2.4). Still, the amounts of deposited carbon that was gasified were lower than those obtained in the SER. In fact, the total amount of gasified carbon obtained during the second and third oxidative

regenerations in the SER short 3 experiment (Table 5.2.3) are considerably higher than those observed in Table 5.2.4 for the SEMR. However, the average amount of carbon gasified during oxidative regeneration only at 673 K in the SER was 87.1 ± 3.5 $\mathrm{mg_C \cdot g_{cat+sorb}^{-1}}$. Therefore, the combination of both CO_2 sorption and H_2 permeation through the Pd-Ag membrane led to a slight decrease of the formation of coke in the SEMR comparatively to the SER. Moreover, some of the gasified carbon was possibly deposited on the membrane, meaning that the actual amount of gasified carbon that was deposited on both catalyst and sorbent should be lower than that reported in Table 5.2.4. The fact that both WGS products were removed at the beginning of the process in the SEMR instead of only CO_2 could have played an important role in reducing the selectivity towards coke formation through CH_4 decomposition (methanation was probably inhibited during that period) and liquid products that could be potential coke precursors. In the post breakthrough region, since only H_2 was removed, CH_4 decomposition should have been thermodynamically favored [12]. Boudouard reaction could have also taken place since only very small amounts of CO were observed. As for both CO and CO_2 reduction, they were not thermodynamically favored as excessive amounts of steam were present and since the reducing agent, H_2, was being removed from the reaction medium.

Even though the SEMR would only be operated in the pre-breakthrough region, coke formation would probably still be observed. Therefore, in order to avoid coke formation and consequently the need of regenerative oxidation, catalysts that are more selective towards the formation of gaseous products at such low temperatures should be integrated and contact between glycerol and the hydrotalcite should be minimized and/or hydrotalcites less selective towards coke precursors should be used (as discussed in section 5.2.3.2.1.5). Furthermore, thinner membranes should be employed, as they would considerably increase hydrogen permeation fluxes and decrease the initial

process costs, thus making the SEMR a better candidate to replace conventional reformers.

Table 5.2.4 - Amount of carbon deposited on the catalyst used in SEMR that was gasified during each oxidative regeneration.

Moment of oxidative regeneration / h	Gasified carbon / $mg_C \cdot g_{cat+sorb}^{-1}$
4	77.3
8	83.6

5.2.4 Conclusions

Two different reaction-separation intensified concepts, SER and SEMR, were tested for GSR using a Rh-based catalyst and a commercial hydrotalcite-like material (K-MG30) as CO_2 sorbent. The occurrence of H_2-consuming methanation in the pre- and breakthrough regions limited the production of H_2 in that period, being that when such reaction was inhibited, during the CO_2 post-breakthrough, the amount of H_2 produced increased. Moreover, it was observed that K-MG30 was catalytically active towards glycerol decomposition into liquid products, into CO and H_2 and WGS. EDS analysis suggest that CO_2 removal from the reaction medium in the SER enhanced the formation of coke, which could have happened if the major coke formation route during the pre- and breakthrough periods was Boudouard reaction. Consequently, the better performance observed for the SER in the post-breakthrough comparatively to the conventional TR was probably due to a synergism between the catalyst and the sorbent: while the catalyst mainly promoted glycerol decomposition into CO and H_2, K-MG30 was probably the main responsible for converting CO through

WGS and also for some glycerol decomposition too. The presence of K-MG30 could have also led to a more selective production of liquid coke precursors.

Further enhancement of H_2 production was obtained by combining both catalyst and CO_2 sorbent with an H_2-permselective membrane in a SEMR. The removal of both WGS products, CO_2 and H_2, avoided the occurrence of methanation in the pre-breakthrough region, which allowed to reach higher H_2 yields during that period comparatively to the SER. This allowed a simultaneous production of highly pure H_2 in the retentate and ultra-pure H_2 in the permeate. Moreover, since there was no CO in the pre-breakthrough, poisoning of the membrane due to its presence probably did not occur. Therefore, if the SEMR is applied in a multi column system or even in a simulated moving bed system (thinner membranes would be required) that allows continuous operation in the pre-breakthrough region, ultra-pure (depending on the thinner membranes selectivites) and highly pure H_2 would be continuously obtained in the permeate and retentate streams, respectively, and at higher flow rates than in the SER. After the CO_2 breakthrough a decrease in performance was observed, but higher H_2 and carbon-containing gaseous products production in comparison to the SER was still observed due to continuous H_2 removal (operation as a MR). Slightly lower formation of carbon deposits was observed in the SEMR, which could be associated to CH_4 decomposition inhibition and/or to the partial inhibition of the reactions that lead to the formation of liquid coke precursors.

Notation and Glossary

F_G^{in}	Molar flow rate of glycerol fed to the reactor
F_G^{out}	Molar flow rate of unreacted glycerol at the reactor outlet
$F_{H_2}^{permeate}$	Molar flow rate of H_2 permeating through the membrane

$F_{H_2}^{retentate}$	Molar flow rate of H_2 at the retentate side
F_i^{out}	Molar flow rate of species i at the reactor outlet
Pur_{H_2}	Purity of produced H_2
Re_{H_2}	Recovery of H_2 in the permeate side
$S_{C,i}$	Selectivity towards carbon-containing gaseous products
S_{H_2}	Selectivity towards H_2 comparatively to carbon-containing gaseous products
$X_{G,gas}$	Glycerol conversion into carbon-containing gaseous products
$X_{G,total}$	Total glycerol conversion
Y_i	Yield of species i

Greek letters

$\Delta H_r^{298\,K}$	Reaction enthalpy at 298 K

List of acronyms

EDS	Energy Dispersive Spectroscopy
GSR	Glycerol Steam Reforming
MR	Membrane Reactor
TR	Traditional Reactor
SEM	Scanning Electron Microscopy
SEMR	Sorption-Enhanced Membrane Reactor
SER	Sorption-Enhanced Reactor
WGFR	Molar Water/Glycerol Feed Ratio
WGS	Water-Gas Shift

5.2.5 References

[1] Silva, J.M., M.A. Soria, and L.M. Madeira, *Challenges and strategies for optimization of glycerol steam reforming process.* Renewable and Sustainable Energy Reviews, 2015, 42, 1187-1213.

[2] Avasthi, K.S., R.N. Reddy, and S. Patel, *Challenges in the production of hydrogen from glycerol – A biodiesel byproduct via steam reforming process.* Procedia Engineering, 2013, 51, 423-429.

[3] Jiménez, V., P. Sánchez, P. Panagiotopoulou, J.L. Valverde, and A. Romero, *Methanation of CO, CO2 and selective methanation of CO, in mixtures of CO and CO2, over ruthenium carbon nanofibers catalysts.* Applied Catalysis A: General, 2010, 390(1), 35-44.

[4] Miguel, C.V., M.A. Soria, A. Mendes, and L.M. Madeira, *A sorptive reactor for CO2 capture and conversion to renewable methane.* Chemical Engineering Journal, 2017, 322, 590-602.

[5] Panagiotopoulou, P., D.I. Kondarides, and X.E. Verykios, *Selective methanation of CO over supported noble metal catalysts: Effects of the nature of the metallic phase on catalytic performance.* Applied Catalysis A: General, 2008, 344(1), 45-54.

[6] Pompeo, F., G. Santori, and N.N. Nichio, *Hydrogen and/or syngas from steam reforming of glycerol. Study of platinum catalysts.* International Journal of Hydrogen Energy, 2010, 35(17), 8912-8920.

[7] Goula, M.A., N.D. Charisiou, K.N. Papageridis, and G. Siakavelas, *Influence of the synthesis method parameters used to prepare nickel-based catalysts on the catalytic performance for the glycerol steam reforming reaction.* Chinese Journal of Catalysis, 2016, 37(11), 1949-1965.

[8] Chiodo, V., S. Freni, A. Galvagno, N. Mondello, and F. Frusteri, *Catalytic features of Rh and Ni supported catalysts in the steam reforming of glycerol to produce hydrogen.* Applied Catalysis A: General, 2010, 381(1), 1-7.

[9] Araque, M., L.M. Martínez T, J.C. Vargas, M.A. Centeno, and A.C. Roger, *Effect of the active metals on the selective H2 production in glycerol steam reforming.* Applied Catalysis B: Environmental, 2012, 125, 556-566.

[10] Corma, A., G.W. Huber, L. Sauvanaud, and P. O'Connor, *Biomass to chemicals: Catalytic conversion of glycerol/water mixtures into acrolein, reaction network.* Journal of Catalysis, 2008, 257(1), 163-171.

[11] Tran, N.H. and G.S.K. Kannangara, *Conversion of glycerol to hydrogen rich gas.* Chemical Society Reviews, 2013, 42(24), 9454-9479.

[12] Silva, J.M., M.A. Soria, and L.M. Madeira, *Thermodynamic analysis of Glycerol Steam Reforming for hydrogen production with in situ hydrogen and carbon dioxide separation.* Journal of Power Sources, 2015, 273, 423-430.

[13] Nahar, G., V. Dupont, M.V. Twigg, and E. Dvininov, *Feasibility of hydrogen production from steam reforming of biodiesel (FAME) feedstock on Ni-supported catalysts.* Applied Catalysis B: Environmental, 2015, 168-169, 228-242.

[14] Silva, J.M., R. Trujillano, V. Rives, M.A. Soria, and L.M. Madeira, *High temperature CO2 sorption over modified hydrotalcites.* Chemical Engineering Journal, 2017, 325, 25-34.

[15] Miguel, C.V., R. Trujillano, V. Rives, M.A. Vicente, A.F.P. Ferreira, A.E. Rodrigues, A. Mendes, and L.M. Madeira, *High temperature CO2 sorption with gallium-substituted and promoted hydrotalcites.* Separation and Purification Technology, 2014, 127, 202-211.

[16] Coenen, K., F. Gallucci, P. Cobden, E. van Dijk, E. Hensen, and M. van Sint Annaland, *Chemisorption working capacity and kinetics of CO2 and H2O of hydrotalcite-based adsorbents for sorption-enhanced water-gas-shift applications.* Chemical Engineering Journal, 2016, 293, 9-23.

[17] Chi, C., Y. Li, X. Ma, and L. Duan, *CO2 capture performance of CaO modified with by-product of biodiesel at calcium looping conditions.* Chemical Engineering Journal, 2017, 326, 378-388.

[18] Li, Z.-H., Y. Wang, K. Xu, J.-Z. Yang, S.-B. Niu, and H. Yao, *Effect of steam on CaO regeneration, carbonation and hydration reactions for CO2 capture.* Fuel Processing Technology, 2016, 151, 101-106.

[19] Hu, Y., W. Liu, J. Sun, M. Li, X. Yang, Y. Zhang, X. Liu, and M. Xu, *Structurally improved CaO-based sorbent by organic acids for high temperature CO2 capture.* Fuel, 2016, 167, 17-24.

[20] Amorim, S.M., M.D. Domenico, T.L.P. Dantas, H.J. José, and R.F.P.M. Moreira, *Lithium orthosilicate for CO2 capture with high regeneration capacity: Kinetic study and modeling of carbonation and decarbonation reactions.* Chemical Engineering Journal, 2016, 283, 388-396.

[21] Seggiani, M., E. Stefanelli, M. Puccini, and S. Vitolo, *CO2 sorption/desorption performance study on K2CO3-doped Li4SiO4-based pellets.* Chemical Engineering Journal, 2018, 339, 51-60.

[22] Wang, K., Z. Yin, P. Zhao, Z. Zhou, Z. Su, and J. Sun, *Development of metallic element-stabilized Li4SiO4 sorbents for cyclic CO2 capture.* International Journal of Hydrogen Energy, 2017, 42(7), 4224-4232.

[23] Sunho, C., D.J. H., and J.C. W., *Adsorbent Materials for Carbon Dioxide Capture from Large Anthropogenic Point Sources.* ChemSusChem, 2009, 2(9), 796-854.

[24] Gallucci, F., E. Fernandez, P. Corengia, and M. van Sint Annaland, *Recent advances on membranes and membrane reactors for hydrogen production.* Chemical Engineering Science, 2013, 92, 40-66.

[25] Miguel, C.V., A. Mendes, S. Tosti, and L.M. Madeira, *Effect of CO and CO2 on H2 permeation through finger-like Pd–Ag membranes.* International Journal of Hydrogen Energy, 2012, 37(17), 12680-12687.

[26] Tosti, S., A. Basile, L. Bettinali, F. Borgognoni, F. Chiaravalloti, and F. Gallucci, *Long-term tests of Pd–Ag thin wall permeator tube.* Journal of Membrane Science, 2006, 284(1), 393-397.

[27] Tosti, S., A. Adrover, A. Basile, V. Camilli, G. Chiappetta, and V. Violante, *Characterization of thin wall Pd–Ag rolled membranes.* International Journal of Hydrogen Energy, 2003, 28(1), 105-112.

[28] Tosti, S., L. Bettinali, and V. Violante, *Rolled thin Pd and Pd–Ag membranes for hydrogen separation and production.* International Journal of Hydrogen Energy, 2000, 25(4), 319-325.

[29] Pérez, P., C.A. Cornaglia, A. Mendes, L.M. Madeira, and S. Tosti, *Surface effects and CO/CO2 influence in the H2 permeation through a Pd–Ag membrane: A comprehensive model.* International Journal of Hydrogen Energy, 2015, 40(20), 6566-6572.

[30] Dou, B., B. Jiang, Y. Song, C. Zhang, C. Wang, H. Chen, B. Du, and Y. Xu, *Enhanced hydrogen production by sorption-enhanced steam reforming from glycerol with in-situ CO2 removal in a fixed-bed reactor.* Fuel, 2016, 166, 340-346.

[31] Ni, Y., C. Wang, Y. Chen, X. Cai, B. Dou, H. Chen, Y. Xu, B. Jiang, and K. Wang, *High purity hydrogen production from sorption enhanced chemical looping glycerol reforming: Application of NiO-based oxygen transfer materials and potassium promoted Li2ZrO3 as CO2 sorbent.* Applied Thermal Engineering, 2017, 124, 454-465.

[32] Sánchez, N., J.M. Encinar, and J.F. González, *Sorption Enhanced Steam Reforming of Glycerol: Use of La-Modified Ni/Al2O3 as Catalyst.* Industrial & Engineering Chemistry Research, 2016, 55(13), 3736-3741.

[33] Wang, C., Y. Chen, Z. Cheng, X. Luo, L. Jia, M. Song, B. Jiang, and B. Dou, *Sorption-Enhanced Steam Reforming of Glycerol for Hydrogen Production over a NiO/NiAl2O4 Catalyst and Li2ZrO3-Based Sorbent.* Energy & Fuels, 2015, 29(11), 7408-7418.

[34] Dewoolkar, K.D. and P.D. Vaidya, *Sorption-Enhanced Steam Reforming of Glycerol over Ni–hydrotalcite: Effect of Promotion with Pt.* ChemCatChem, 2016, 8(22), 3499-3509.

[35] Chang, A.C.C., W.-H. Lin, K.-H. Lin, C.-H. Hsiao, H.-H. Chen, and H.-F. Chang, *Reforming of glycerol for producing hydrogen in a Pd/Ag membrane reactor.* International Journal of Hydrogen Energy, 2012, 37(17), 13110-13117.

[36] Iulianelli, A., T. Longo, S. Liguori, and A. Basile, *Production of hydrogen via glycerol steam reforming in a Pd-Ag membrane reactor over Co-Al2O3 catalyst.* Asia-Pacific Journal of Chemical Engineering, 2010, 5(1), 138-145.

[37] Lin, K.-H., W.-H. Lin, C.-H. Hsiao, H.-F. Chang, and A.C.C. Chang, *Hydrogen production in steam reforming of glycerol by conventional and membrane reactors.* International Journal of Hydrogen Energy, 2012, 37(18), 13770-13776.

[38] Iulianelli, A., P.K. Seelam, S. Liguori, T. Longo, R. Keiski, V. Calabrò, and A. Basile, *Hydrogen production for PEM fuel cell by gas phase reforming of glycerol as byproduct of bio-diesel. The use of a Pd–Ag membrane reactor at middle reaction temperature.* International Journal of Hydrogen Energy, 2011, 36(6), 3827-3834.

[39] Soria, M.A., S. Tosti, A. Mendes, and L.M. Madeira, *Enhancing the low temperature water–gas shift reaction through a hybrid sorption-enhanced membrane reactor for high-purity hydrogen production.* Fuel, 2015, 159, 854-863.

[40] Park, B.-G., *A hybrid adsorbent-membrane reactor (HAMR) system for hydrogen production.* Korean Journal of Chemical Engineering, 2004, 21(4), 782-792.

[41] Park, B.-G. and T.T. Tsotsis, *Models and experiments with pervaporation membrane reactors integrated with an adsorbent system.* Chemical Engineering and Processing: Process Intensification, 2004, 43(9), 1171-1180.

[42] García-García, F.R., M. León, S. Ordóñez, and K. Li, *Studies on water–gas-shift enhanced by adsorption and membrane permeation.* Catalysis Today, 2014, 236, 57-63.

[43] Silva, J.M., L.S. Ribeiro, J.J.M. Órfão, M.A. Soria, and L.M. Madeira, *Low temperature glycerol steam reforming over a Rh-based catalyst combined with oxidative regeneration.* Chemical Engineering Journal, 2018, Submitted for publication.

[44] Maroño, M., Y. Torreiro, D. Cillero, and J.M. Sánchez, *Experimental studies of CO2 capture by a hybrid catalyst/adsorbent system applicable to IGCC processes.* Applied Thermal Engineering, 2015, 74, 28-35.

[45] Di Cosimo, J.I., V.K. Díez, M. Xu, E. Iglesia, and C.R. Apesteguía, *Structure and Surface and Catalytic Properties of Mg-Al Basic Oxides.* Journal of Catalysis, 1998, 178(2), 499-510.

[46] Di Cosimo, J.I., V.K. Díez, and C.R. Apesteguía, *Synthesis of α,β-unsaturated ketones over thermally activated Mg–Al hydrotalcites.* Applied Clay Science, 1998, 13(5), 433-449.

[47] Di Cosimo, J.I. and C.R. Apesteguía, *Study of the catalyst deactivation in the base-catalyzed oligomerization of acetone.* Journal of Molecular Catalysis A: Chemical, 1998, 130(1), 177-185.

[48] Carlsson, M., *Carbon Formation in Steam Reforming and Effect of Potassium Promotion.* Johnson Matthey Technology Review, 2015, 59(4), 313-318.

[49] de Rezende, S.M., C.A. Franchini, M.L. Dieuzeide, A.M. Duarte de Farias, N. Amadeo, and M.A. Fraga, *Glycerol steam reforming over layered double hydroxide-supported Pt catalysts.* Chemical Engineering Journal, 2015, 272, 108-118.

[50] Lin, Y.-C., *Catalytic valorization of glycerol to hydrogen and syngas.* International Journal of Hydrogen Energy, 2013, 38(6), 2678-2700.

[51] Silva, V.M.T.M., C.S.M. Pereira, A.E. Rodrigues, Simulated Moving Bed Membrane Reactor, New Hybrid Separation Process and Uses Thereof. PCT/IB2010/051510, April 2010. US Patent 20120108841 A1, January 2012. EU Patent 2418009, October 2011, granted August 2015. Portuguese Patent 104496, April 2009, granted March 2009.

Chapter 6. Conclusions and Future Work

6.1 Conclusions

This thesis focused on the energetic valorization of the main biodiesel by-product, glycerol, by means of H_2 production through glycerol steam reforming (GSR), and how it could be ultimately enhanced by applying a hybrid reaction-separation sorption-enhanced membrane reactor (SEMR) system. In this sense, an initial theoretical thermodynamic and phenomenological analysis of the GSR was carried out, a thorough experimental assessment of high temperature CO_2 capture over hydrotalcite-like materials was performed, and the process was experimentally evaluated in a traditional reactor (TR), sorption-enhanced reactor (SER) and SEMR.

Aiming to better understand the thermodynamic boundaries of the GSR process performed in different reactor configurations, a thermodynamic analysis was performed. For all cases considered and in the whole range of the study, full glycerol conversion was obtained, which could be a strong indicator of the irreversibility of the glycerol decomposition into syngas reaction. Higher undesired CH_4 production was attained in the TR and a progressive decrease was obtained in the order: SER, membrane reactor (MR) and SEMR. As for the other undesired by-product, coke, the results suggest that in the thermodynamic equilibrium most coke is formed through methane cracking. It was also concluded that the SEMR led to a much more significant enhancement of H_2 production, comparatively to the SER, MR and TR, at lower temperatures (c.a. 600-700 K) as compared to the higher temperatures studied (c.a. 800 K). Still, higher temperatures, molar water/glycerol feed ratios (WGFRs) and lower pressures favor H_2 production in the SEMR. Ultimately, the maximum theoretical

H_2 yield of 7 $\mathrm{mol} \cdot \mathrm{mol}^{-1}_{\mathrm{converted\ glycerol}}$ was obtained in the SEMR at 800 K, WGFR of 9 and 1 atm.

In order to complement this thermodynamic assessment by simulating more realistic reaction conditions, a phenomenological model describing the GSR process in a TR was developed and validated. Contrarily to what was observed in the thermodynamic equilibrium, incomplete glycerol conversion was observed under most of the simulated conditions. Moreover, it was concluded that higher temperatures and WGFRs led to higher glycerol conversions and H_2 production, but this time because they favoured both glycerol consumption and H_2 production kinetics. However, on contrary to what was observed in the thermodynamic analysis, even though higher pressures resulted in lower hydrogen yields (moles of H_2 produced per mole of glycerol converted), they led to higher total glycerol conversions and hydrogen production (moles of H_2 produced per mole of glycerol fed). The absolute production of H_2 increased until full total glycerol conversion was reached. From that point on, subsequent increments of pressure decreased the flow rate of produced H_2 as the kinetics of H_2 production was less favoured than those of CO_2 and CH_4. Consequently, a maximum H_2 production of 4.93 $\mathrm{mol} \cdot \mathrm{mol}^{-1}_{\mathrm{fed\ glycerol}}$ was reached at 848 K, WGFR of 9 and 2 atm.

Considering that the operation of both SER and SEMR is significantly dependent on the CO_2 sorbent that is integrated in the hybrid reactor, an experimental assessment of several hydrotalcite-like materials was performed under static conditions. Four materials were prepared and calcined at 673 K, having been concluded that the modification with potassium and partial substitution of aluminum with gallium enhanced considerably the CO_2 sorption capacity of the calcined hydrotalcites, especially potassium incorporation. Microwave again also contributed positively to the increase of the sorption capacity. The prepared cK-HTCGa MW sample presented an outstanding CO_2 capture of 2.09 $\mathrm{mol \cdot kg^{-1}}$ at 573 K, 3.10 bar of CO_2 and under dry conditions. The

sorption kinetics was also evaluated assuming two kinetic contributions: an initial fast contribution followed by a slower one. The model predicted accurately the experimental CO_2 uptakes of the four materials, having been observed that the modification of the hydrotalcites with potassium slowed both fast and slow sorption contributions, possibly due to limited diffusion of CO_2 to the active sites inside the partially blocked pores; in fact, a considerable BET surface area decrease was observed upon impregnation of the hydrotalcites with potassium. Nevertheless, cK-HTCGa MW still presents considerably higher sorption capacities after just a few minutes than commercial hydrotalcites would after hours of CO_2 exposure.

For that reason, cK-HTCGa MW was submitted to long term dynamic CO_2 sorption experiments, where the sorbent was under conditions more similar to those typically employed during sorption-enhanced processes. After 7-8 sorption-desorption cycles cK-HTCGa MW reached a sorption working capacity of around 0.70 $mol \cdot kg^{-1}$ at 6 bar, 673 K, 15 vol% CO_2 and under dry conditions, which represents an almost 2-fold increase in comparison to commercial K-MG30 hydrotalcite from Sasol, commonly used as reference. Moreover, higher total pressures, higher CO_2 contents in the feed and higher temperatures (in the range 573 - 673 K) benefited CO_2 capture on cK-HTCGa MW. Also, higher pressures and temperatures allowed better bed usage efficiencies. Sorption experiments under wet conditions were also carried out with the cK-HTCGa MW, having been observed that the material benefited with the presence of steam in terms of CO_2 sorption capacity and bed usage efficiency. Increments in sorption working capacity of 90% and 200%, comparatively to dry conditions, were observed when 5 and 10 vol% of H_2O were employed in the feed. This enhancement of the hydrotalcite performance could be partially associated to the mobilization of both potassium and gallium towards the sorbent surface during the wet tests that was observed through Energy dispersive spectroscopy (EDS) elemental distribution mapping.

Finally, the experimental analysis of the catalytic GSR process was carried out using a Rh supported on alumina catalyst, provided by Johnson Matthey. Firstly, the process was carried out in a TR at 673 K, 4.5 bar and WGFR of 19. Due to the observed coke formation, which resulted in the decrease over time of both total glycerol conversion and mainly glycerol conversion into carbon-containing gaseous products, the GSR was combined with periodic oxidative regeneration of the catalyst. This resulted in a much better average catalytic performance over time as compared to the previous reaction runs, since almost full recovery of the catalytic activity was observed after each oxidative regeneration. This way, the total glycerol conversion remained above 99% during the whole 16 h test. Also, maximum initial glycerol conversions into carbon-containing gaseous products and H_2 yields between 67 and 74% and 2.1 and 2.6 $\mathrm{mol} \cdot \mathrm{mol}_{\mathrm{fed\ glycerol}}^{-1}$, respectively, were obtained in the four cycles. Moreover, the purity of H_2 remained between 50 and 60% during the reaction runs.

In order to further enhance GSR performance, namely in terms of H_2 yield and purity, both SER and SEMR where tested. The SER enhanced the production of H_2 not only in the CO_2 pre- and breakthrough region, but also in the post-breakthrough period. While in the first case CO_2 sorption plays an important role in such enhancement, in the later the enhanced behaviour of the SER as compared to the TR is attributed to the catalytic activity of the sorbent, K-MG30 hydrotalcite, towards glycerol decomposition into syngas and mainly to water-gas shift (WGS) reaction. EDS results suggest that longer operation in both pre- and breakthrough regions resulted in higher coke formation, thus implying that Boudouard reaction could have been enhanced by CO_2 sorption, in opposition to the prediction of the thermodynamic analysis. The catalytic activity of K-MG30 towards the formation of liquid coke precursors could have also contributed to this higher coke formation. This clearly indicates that the SER

operates in the kinetic regime, where the results are highly dependent on the reaction path.

A much more significant improvement of the H_2 yield was obtained in the SEMR, where an increase of the H_2 yield in the CO_2 pre- and breakthrough region from 1.6, in the SER, up to 3.6 $\mathrm{mol} \cdot \mathrm{mol}_{\mathrm{fed\ glycerol}}^{-1}$ was reached. Since in the SEMR CH_4 formation was completely inhibited during the pre-breakthrough, on contrary to what was observed in the SER, not only more H_2 was produced (because it was not consumed in the parallel methanation reaction(s)), but also the H_2 obtained in the retentate side was highly pure since no other gaseous products were detected. Moreover, the H_2 recovered in the permeate side, which was most of the produced H_2 during pre- and breakthrough, was ultra-pure due to high Pd-Ag membrane selectivity. Also, since CO was not observed during the pre-breakthrough, membrane poisoning due to its presence probably did not occur. Therefore, if the SEMR is operated only in the pre-breakthrough region, two streams of highly pure and ultra-pure H_2 would be continuously obtained.

6.2 Limitations

Modeling the GSR process is quite challenging, as several reaction pathways involving not only the formation of gas products (e.g. H_2, CO_2, CO and CH_4), but also the formation of liquid products (e.g. through dehydration; hydrogenolysis; polymerization) [1] and carbon deposits are possible [2,3]. Even though the kinetics used in subchapter 3.2 was taken from the literature [4] and considered as the most complete at the time, it only considered the involvement of gas products in GSR and not the presence of liquid products nor coke. Therefore, such kinetics and, consequently, the phenomenological model would not be adequate to describe a GSR system as complex as the one experimentally studied in chapter 5. Also, since the thermodynamic equilibrium

was not taken into consideration by the used kinetics, it did not allow simulating equilibrium dislocating reactor concepts such as SER, MR and SEMR.

In chapter 4 it was observed that the potassium-doped gallium substituted and microwave aged hydrotalcite presented higher overall performance than most hydrotalcites reported in the literature, especially commercial materials. However, the amount of such material that can be prepared per cycle in the facilities of either GIR-QUESCAT (University of Salamanca – Spain) or LEPABE (University of Porto – Portugal) is quite limited considering the amounts normally required to perform experiments in the SER and SEMR (subchapter 5.2). For that reason, the commercial CO_2 sorbent from Sasol, K-MG30, was used during the SER and SEMR experiments carried out in subchapter 5.2.

Since there was not enough time to perform a catalyst screening that would probably result in the selection of a more adequate material, a commercial catalyst supplied by Johnson Matthey was used in chapter 5, which ultimately led to significant formation of coke and undesired liquid products. An in-house prepared catalyst, which could potentially be more adequate than the one used, could have been tested and used if not subject to the same restrictions above-mentioned for the hydrotalcite.

The size of the Pd-based membrane and membrane module used in subchapter 5.2 in the SEMR limited the amount of catalyst and sorbent that could be used during the experiments, thus limiting mostly the breakthrough times of CO_2. Moreover, since a comparison between the SEMR and both SER and TR was to be established, the limited size of the membrane also limited the size of the reactors to be used during both SER and TR experiments. The relatively high thickness of the membrane (100 μm) was another limiting feature that did not allow the attainment of higher H_2 recoveries in the permeate side during SEMR experiments.

6.3 Perspectives

Following the limitations presented, several possibilities of work to be developed in the near future might be perspectivated. For the more realistic simulation of the GSR process, more complex kinetics that predict not only the conversion of glycerol into gas products, but also into liquid products and coke are necessary. Furthermore, the equilibrium of the several reactions involved should also be taken into consideration. That way it would also become possible to simulate the GSR process in multifunctional reactor concepts such as SER, MR and SEMR, which involve the shift of the thermodynamic equilibrium. For that, equations related to the sorption phenomena (in the sorbent) and permeation (through the membrane) should be considered as well, yielding a system of partial differential equations where the time coordinate has to be accounted as well. Also, more complex models could be developed and validated for conditions closer to real operation. For example, considering external and internal mass and heat transfer resistances and radial profiles.

The incorporation of highly improved hydrotalcites, such as the one developed and tested in chapter 4, in SER and SEMR for GSR would also be desirable. The fact that such materials show such high sorption capacities, for example, would allow the attainment of much higher breakthrough times and, consequently, the need for less frequent sorbent regeneration. With that in mind, it would be desirable that the synthesis process of the hydrotalcites was scaled up so that more significant amounts of material could be produced in each batch.

A deep catalyst screening aiming to find an appropriate GSR catalyst that is less selective towards undesired liquid products and coke and more selective towards H_2 should be carried out. At the same time, it would be important to find an equilibrium between price and performance. While Ni-based catalysts are cheaper, noble metal-based catalyst are typically more active and stable [5]. Among the noble metals, Ru is the least expensive [6], for which it could

constitute a strong candidate. On the other hand, huge research has been done on Ni-based catalysts [6], which has been leading to the progressive optimization of their performance in GSR. For that reason, Ni-based catalysts would definitely be another strong possibility. Finally, the synthesis and use of hybrid materials who are able to catalyze GSR and simultaneously capture the produced CO_2 should be considered as well.

The use of longer and thinner membranes (ca. a few units of μm), which would allow the use of higher amounts of both catalyst and/or sorbent (longer CO_2 breakthroughs) and the attainment of higher recoveries of H_2 in the permeate side, should be considered to be incorporated in the SEMR. That way, not only a better performance of such hybrid reactor would be obtained, but also the associated costs would possibly be reduced.

Finally, a deep economic analysis of the GSR process should be carried out in order to more precisely assess the feasibility of using biodiesel-derived glycerol for syngas and/or H_2 production through GSR or even, eventually, combining both biodiesel production process and GSR in the same plant. Moreover, the use of intensified reactor concepts such as SER, MR and SEMR at industrial scale should be economically assessed as well.

6.4 References

[1] Pompeo, F., G. Santori, and N.N. Nichio, *Hydrogen and/or syngas from steam reforming of glycerol. Study of platinum catalysts.* International Journal of Hydrogen Energy, 2010, 35(17), 8912-8920.

[2] Tran, N.H. and G.S.K. Kannangara, *Conversion of glycerol to hydrogen rich gas.* Chemical Society Reviews, 2013, 42(24), 9454-9479.

[3] Lin, Y.-C., *Catalytic valorization of glycerol to hydrogen and syngas.* International Journal of Hydrogen Energy, 2013, 38(6), 2678-2700.

[4] Cheng, C.K., S.Y. Foo, and A.A. Adesina, *Glycerol Steam Reforming over Bimetallic Co−Ni/Al2O3.* Industrial & Engineering Chemistry Research, 2010, 49(21), 10804-10817.

[5] Silva, J.M., M.A. Soria, and L.M. Madeira, *Challenges and strategies for optimization of glycerol steam reforming process.* Renewable and Sustainable Energy Reviews, 2015, 42, 1187-1213.

[6] Sundari, R. and P.D. Vaidya, *Reaction Kinetics of Glycerol Steam Reforming Using a Ru/Al2O3 Catalyst.* Energy & Fuels, 2012, 26(7), 4195-4204.

Appendix A. Supporting information for subchapter 3.1

Methodology

The total Gibbs energy is defined as follows:

$$nG = \sum_{i=1}^{N} (n_i \bar{G}_i) \quad \textbf{(A.1)}$$

where nG is the total Gibbs free energy and $\bar{G}_i$ and n_i are the partial molar Gibbs free energy and the molar quantity of species i in the gas mixture, respectively. $\bar{G}_i$ and the fugacity of species i in the gas mixture, $\hat{f}_i$, can be defined as:

$$\bar{G}_i = \bar{G}_i^0 + RT\, ln\left(\hat{f}_i / f_i^0\right) \quad \textbf{(A.2)}$$

$$\hat{f}_i = y_i P \hat{\varphi}_i \quad \textbf{(A.3)}$$

where $\bar{G}_i^0$ is the partial molar Gibbs free energy of species i at its standard state, R and T are the ideal gases constant and operating temperature, respectively, f_i^0 is the fugacity of species i at its standard state, y_i is the molar fraction of species i in the gas mixture, P is the total pressure in the reactor and $\hat{\varphi}_i$ is the fugacity coefficient of compound i in the gas mixture. After considering the restraints of the mass balances ($\sum_i (n_i a_{ik}) = A_k$), the minimum Gibbs free energy of the system is expressed as [1-3]:

$$\sum_{i=1}^{n} n_i \left(\Delta G_{fi}^0 + RT\, ln(P) + RT\, ln\left(y_i\right) + RT\, ln(\hat{\varphi}_i) + \sum_k (\lambda_k a_{ik}) \right) = 0 \quad \textbf{(A.4)}$$

where n_i is the molar flow rate of species i, a_{ik} and A_k the number of atoms of the k[th] element present in each molecule of species i and the total mass of the kth element in the feed, respectively, ΔG_{fi}^0 is the standard Gibbs free energy of formation of species i and λ_k is a Lagrange multiplier.

When solids are included as well, the vapor-solid phase equilibrium must also be taken into consideration. If solid carbon is considered, Eq. (A.4) becomes:

$$\sum_{i=1}^{n} n_i \left(\Delta G_{fi}^0 + RT\, ln(P) + RT\, ln(y_i) + RT\, ln(\hat{\varphi}_i) + \sum_k (\lambda_k a_{ik}) \right) + \left(n_C \Delta G_{fC(s)}^0 \right) = 0 \quad \textbf{(A.5)}$$

where n_C and $\Delta G_{fC(s)}^0$ are the molar flow rate and the standard Gibbs free energy of formation of solid carbon, respectively.

The property method used during the simulations was the Soave-Redlich-Kwong method, which is appropriate for nonpolar or mildly polar mixtures (e.g. hydrogen, carbon dioxide, methane, etc.) and for high temperature processes [4].

In order to simulate a SEMR, the sequential modular approach illustrated in Fig. A.1 was employed.

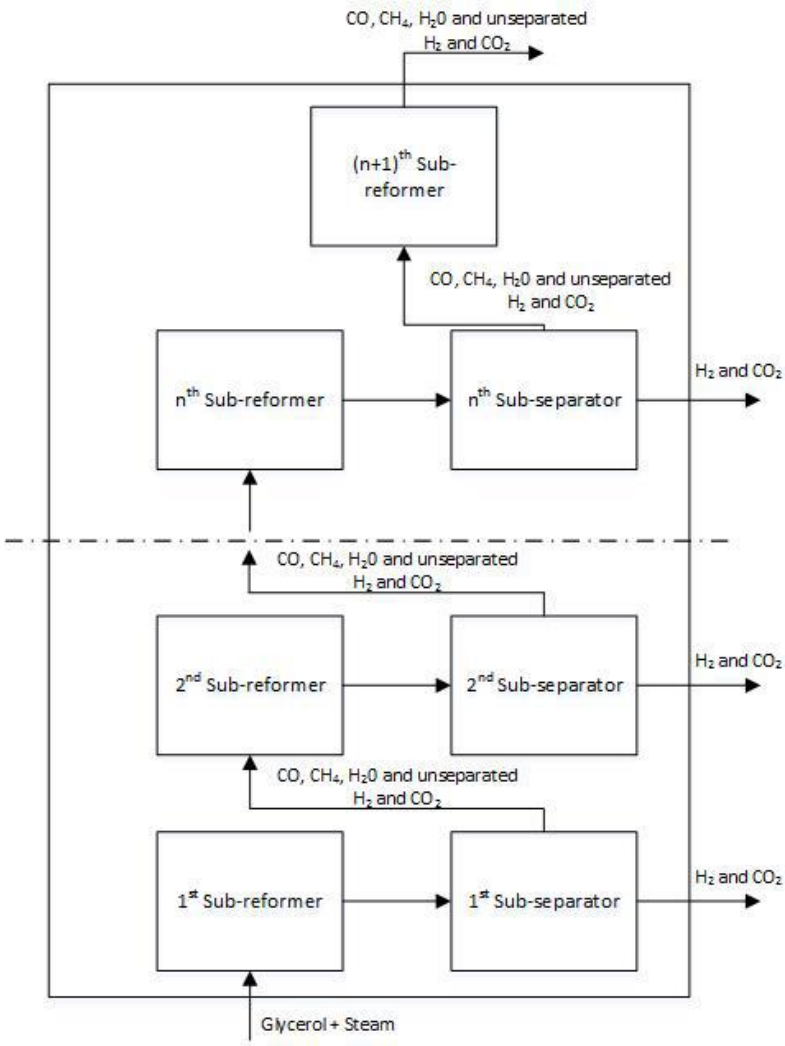

Fig. A.1 - Sequential modular simulation diagram of the SEMR with ASPEN PLUS.

References

[1] Jin, Y., Z. Rui, Y. Tian, Y. Lin, and Y. Li, *Sequential simulation of dense oxygen permeation membrane reactor for hydrogen production from oxidative steam reforming of ethanol with ASPEN PLUS.* International Journal of Hydrogen Energy, 2010, 35(13), 6691-6698.

[2] Faungnawakij, K., R. Kikuchi, and K. Eguchi, *Thermodynamic evaluation of methanol steam reforming for hydrogen production.* Journal of Power Sources, 2006, 161(1), 87-94.

[3] Nikoo, M.K. and N.A.S. Amin, *Thermodynamic analysis of carbon dioxide reforming of methane in view of solid carbon formation.* Fuel Processing Technology, 2011, 92(3), 678-691.

[4] Wang, W., *Thermodynamic analysis of glycerol partial oxidation for hydrogen production.* Fuel Processing Technology, 2010, 91(11), 1401-1408.

Appendix B. Supporting information for subchapter 3.2

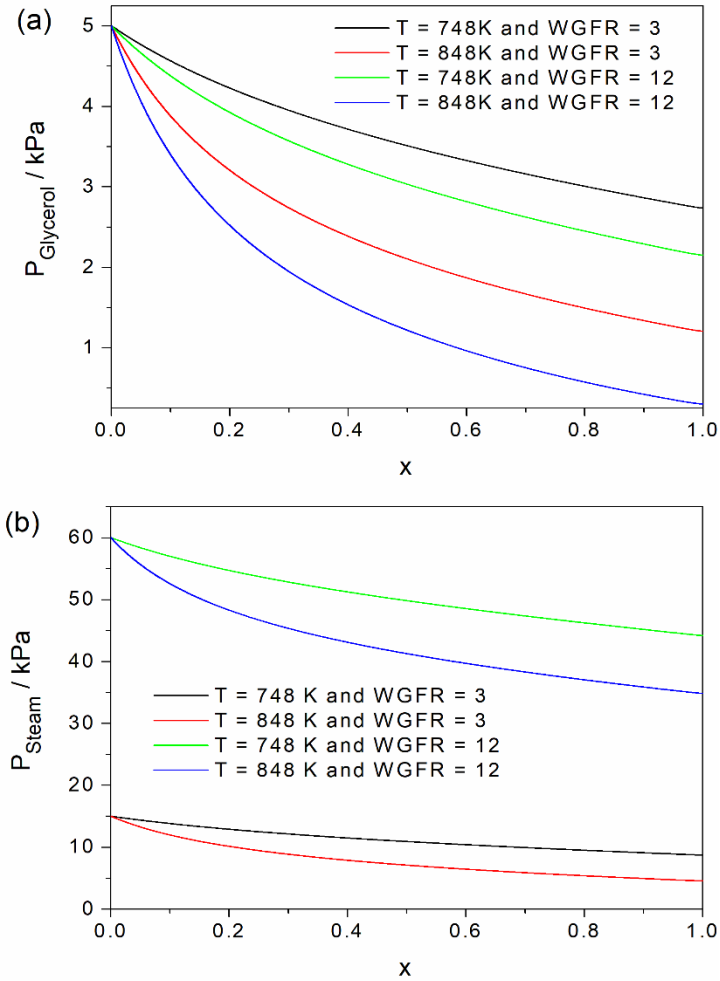

Fig. B.1 - Simulated profiles of (a) glycerol partial pressure and (b) steam partial pressure under different temperatures, WGFRs and at 1 atm.

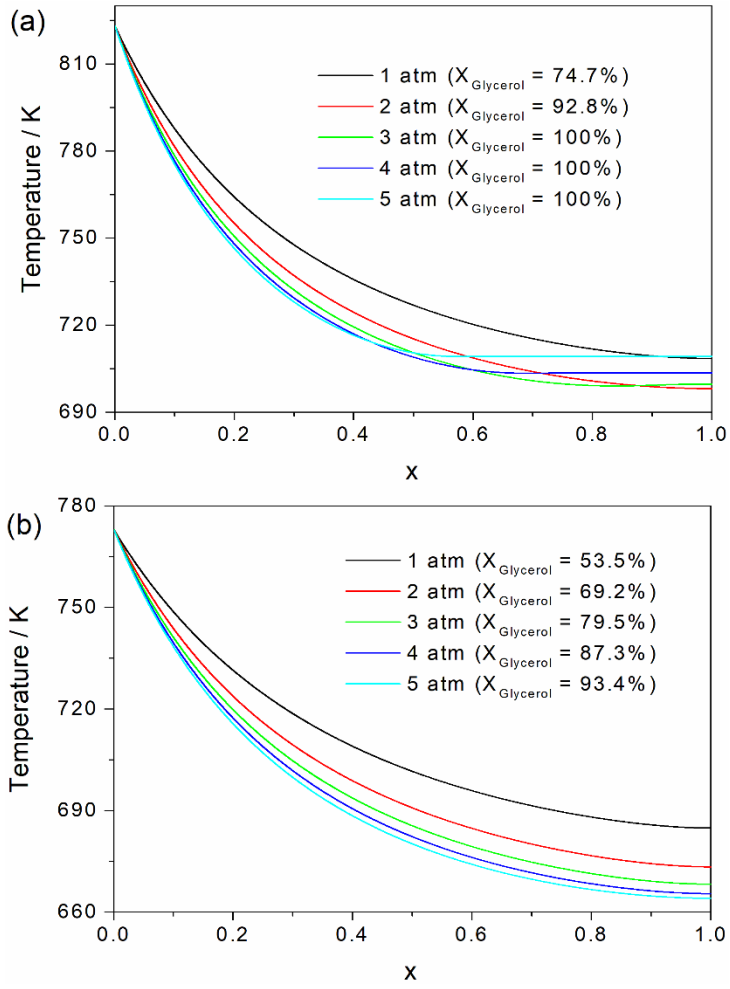

Fig. B.2 - Temperature profiles obtained under different pressures at (a) 823 K and (b) 773 K at WGFR of 9.

Appendix C. Supporting information for subchapter 4.1

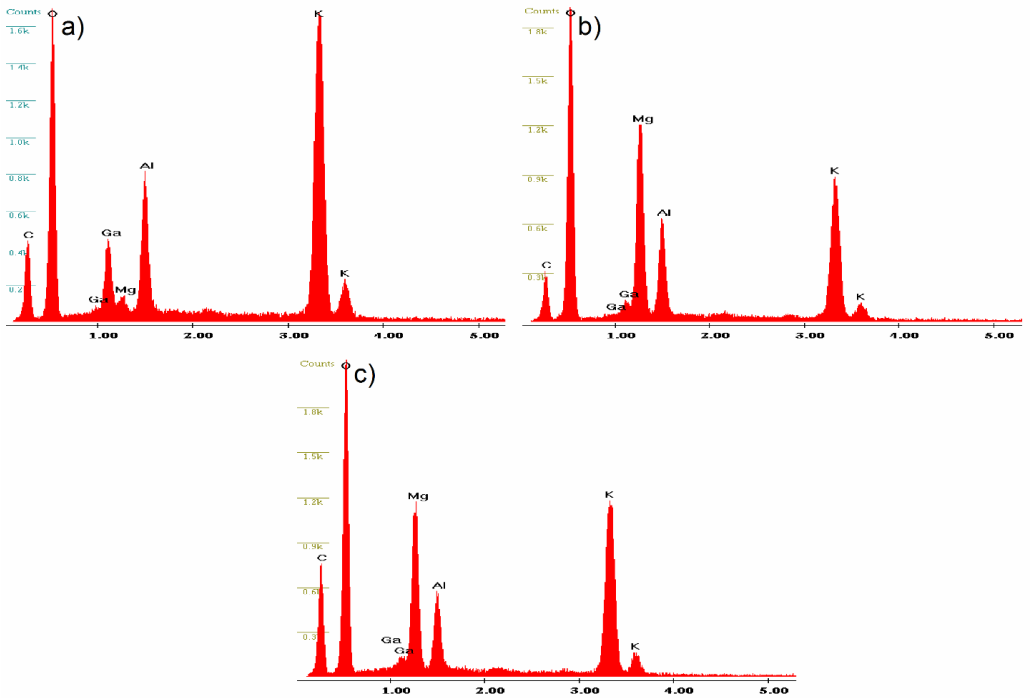

Fig. C.1 - EDS analyses for cK-HTCGa MW after CO_2 sorption tests at 573 K showing the C, O, K, Mg, Al and Ga distribution in a a) large flat surface zone (Z1), b) irregular shape zone (Z2) and c) needle-like zone (Z3).

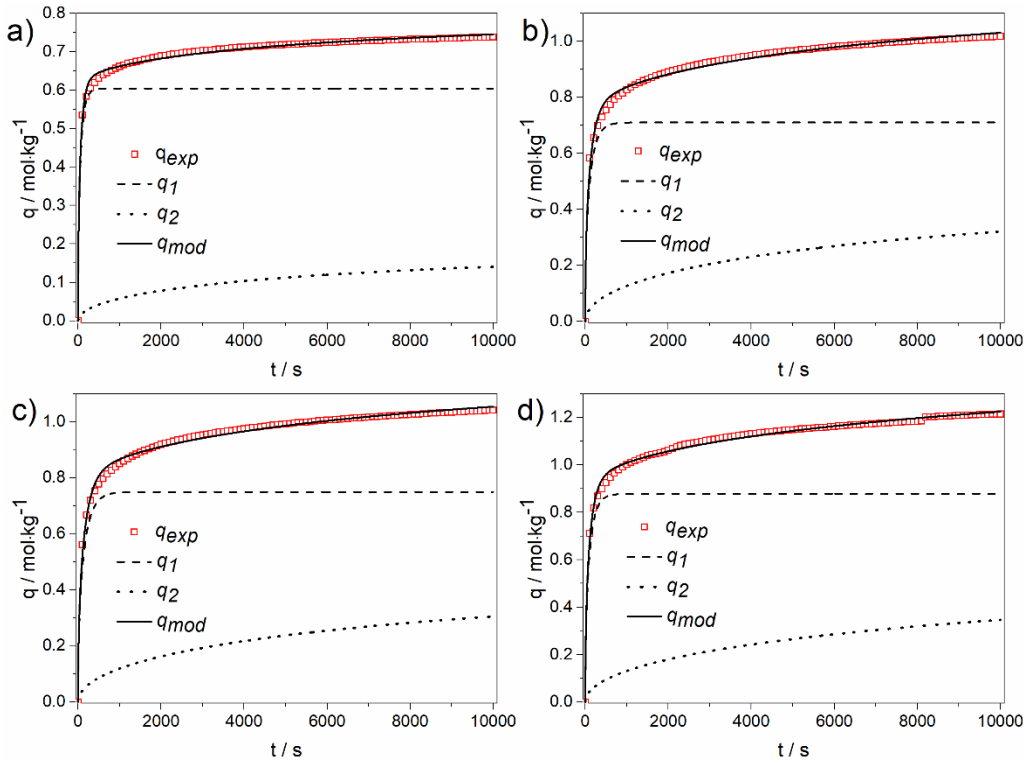

Fig. C.2 - Uptake curves (expressed in mol·kg^{-1}) for CO_2 sorption at 0.20 bar and 573 K for a) cHTC, b) cK-HTC, c) cK-HTC MW and d) cK-HTCGa MW.

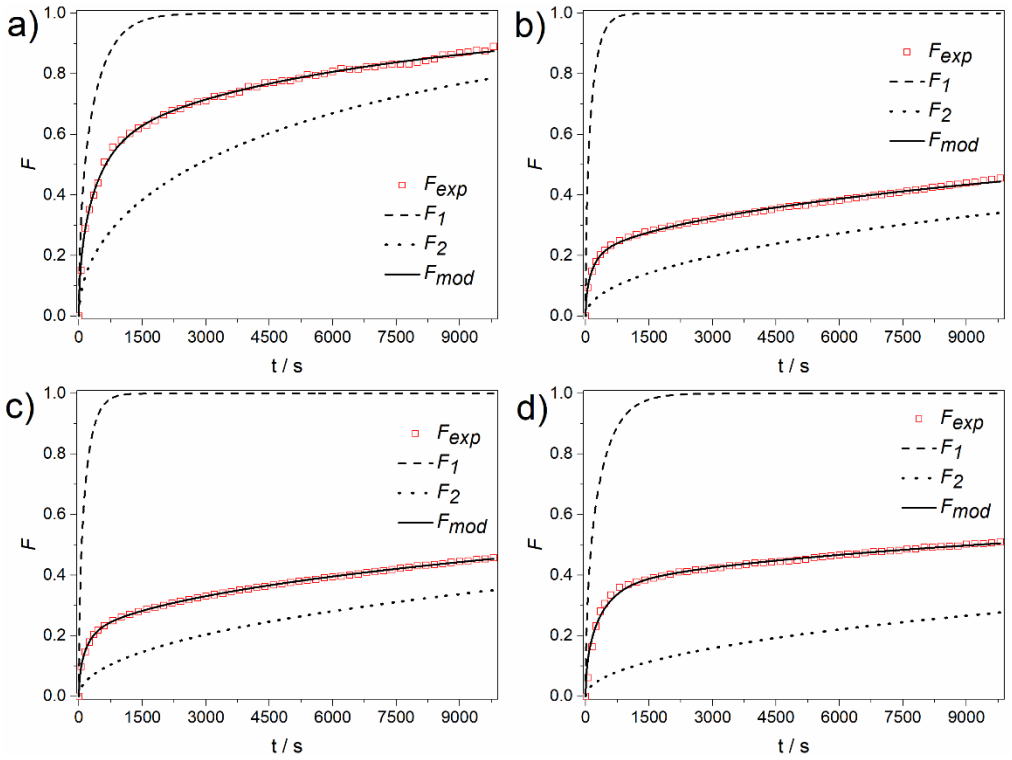

Fig. C.3 - Uptake curves for CO_2 sorption when pressure is increased from 0.20 bar up to 0.51 bar and at 573 K for a) cHTC, b) cK-HTC, c) cK-HTC MW and d) cK-HTCGa MW.

Table C.1 - Parameters of Eq. (4.1.3) obtained through fitting of the experimental CO_2 uptakes for the four samples when pressure is increased from 0.20 bar up to 0.51 bar and at 573 K.

Sorbent	$\frac{D_1}{r^2} \times 10^4$ **/ s^{-1}**	$\frac{D_2}{r^2} \times 10^6$ **/ s^{-1}**	$\frac{(q_1 - q_0)}{(q_\infty - q_0)} \times 100$
cHTC	2.16	10.93	41
cK-HTC	5.28	1.28	16
cK-HTC MW	4.84	1.36	16
cK-HTCGa MW	2.31	0.80	32

Here q_0 represents the equilibrium CO_2 sorption capacity at 573 K and 0.20 bar obtained for each material.

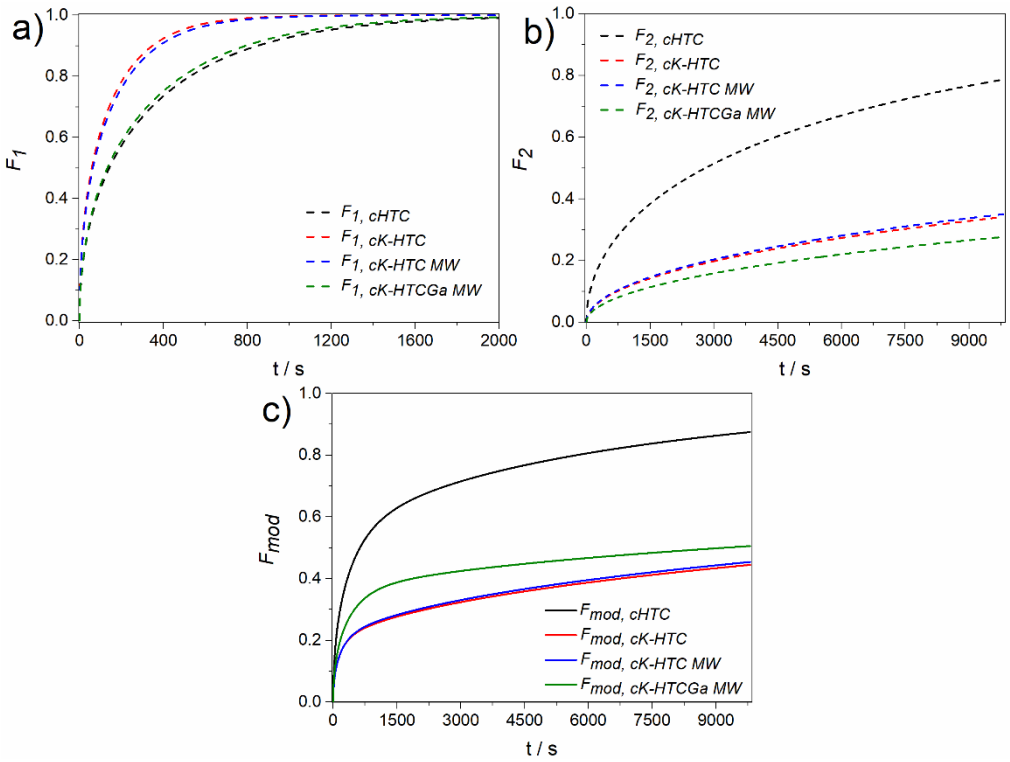

Fig. C.4 - Comparison of the uptake curves for the case in which the pressure is increased from 0.20 bar up to 0.51 bar obtained through non-linear fitting of Eq. (4.1.3) to the experimental data for the different samples: a) F_1, b) F_2 and c) F_{mod}.

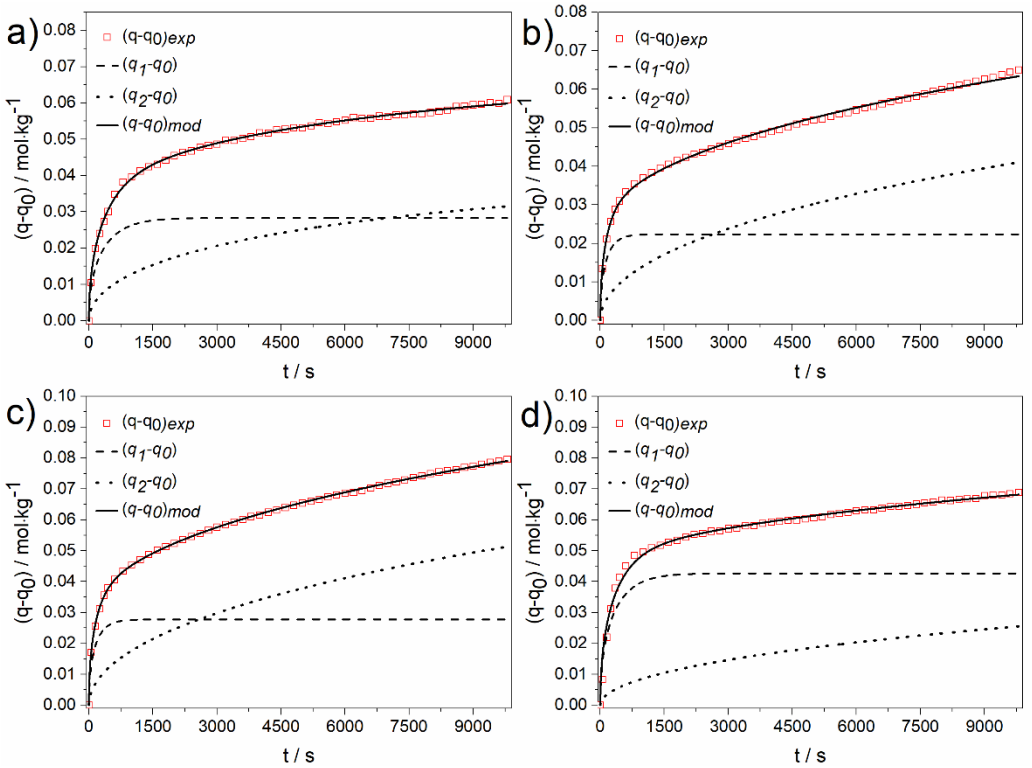

Fig. C.5 - Uptake curves (expressed in mol·kg^{-1}) for CO_2 sorption when pressure is increased from 0.20 bar up to 0.51 bar and 573 K for a) cHTC, b) cK-HTC, c) cK-HTC MW and d) cK-HTCGa MW.

Appendix D. Supporting information for subchapter 4.2

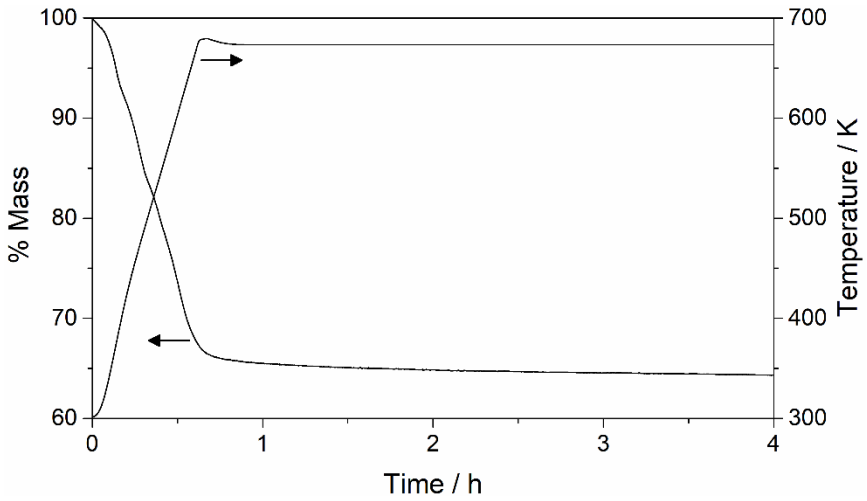

Fig. D.1 - TG of sample fK-HTCGa MW at 673 K during 4 h.

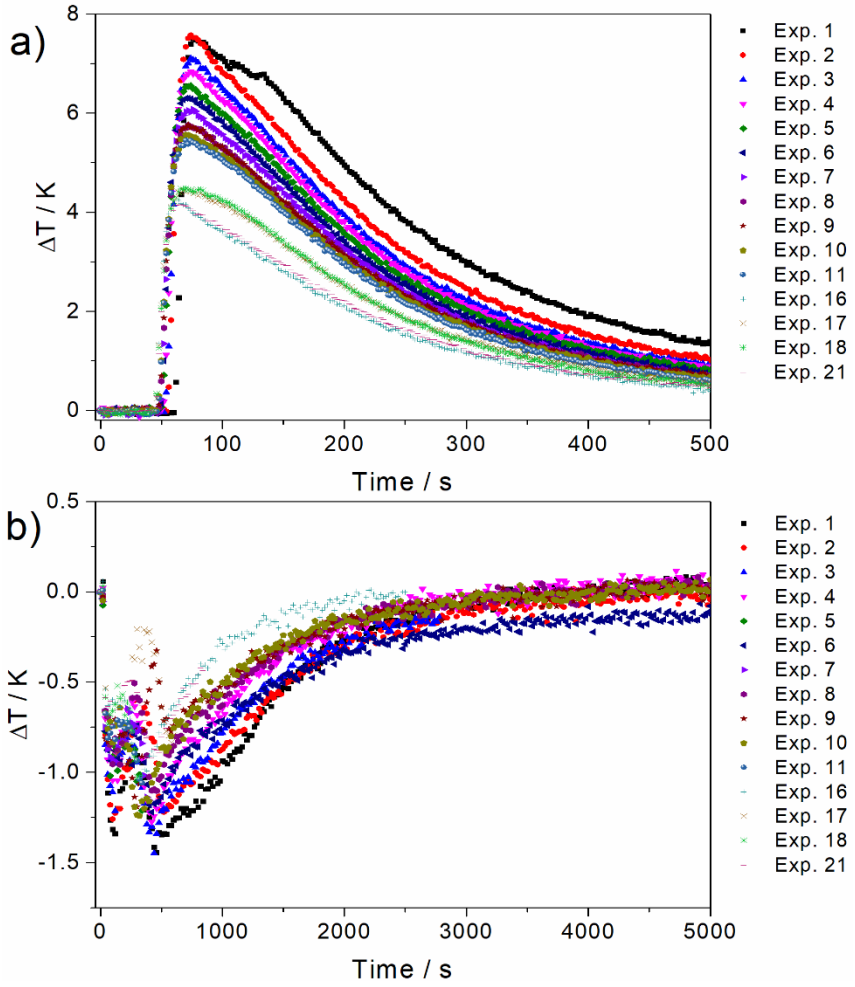

Fig. D.2 - Temperature profiles obtained by the thermocouple placed at 80 mm during the stabilization (experiments 1-11) and verification (experiments 16-18 and 21) cycles performed at 673 K, 15 vol% CO_2 balanced with N_2, under dry conditions and total pressure of 6 bar for a) sorption and b) desorption.

The initial oscillations observed in Fig. D.2 (b) are due to the depressurization of the system to atmospheric pressure at the beginning of regeneration.

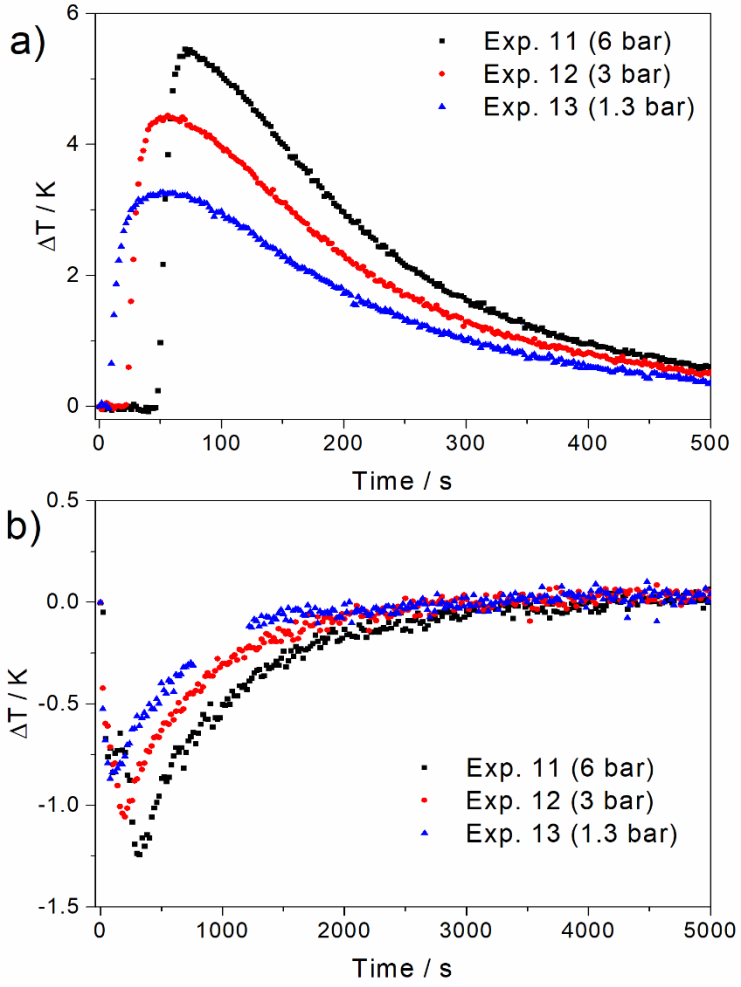

Fig. D.3 - Temperature profiles obtained by the thermocouple placed at 80 mm during the cycles performed at different total pressures (experiments 11-13), 673 K, 15 vol% CO_2 balanced with N_2 and under dry conditions for a) sorption and b) desorption.

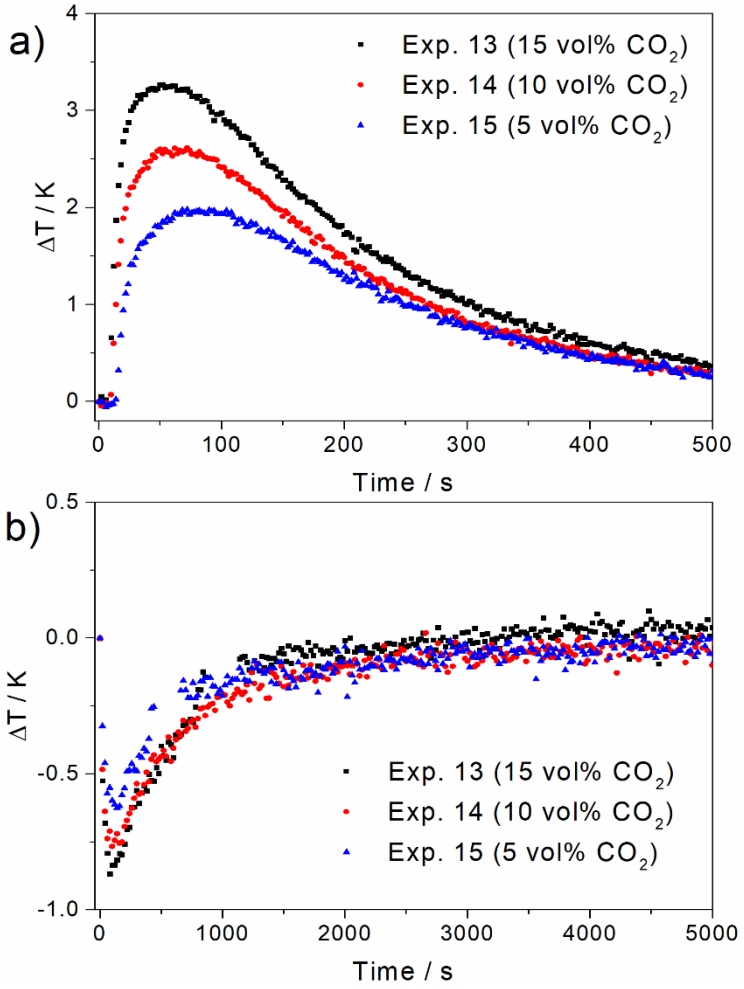

Fig. D.4 - Temperature profiles obtained by the thermocouple placed at 80 mm during the cycles performed at different CO_2 contents (experiments 13-15) balanced with N_2, 673 K, 1.3 bar and under dry conditions for a) sorption and b) desorption.

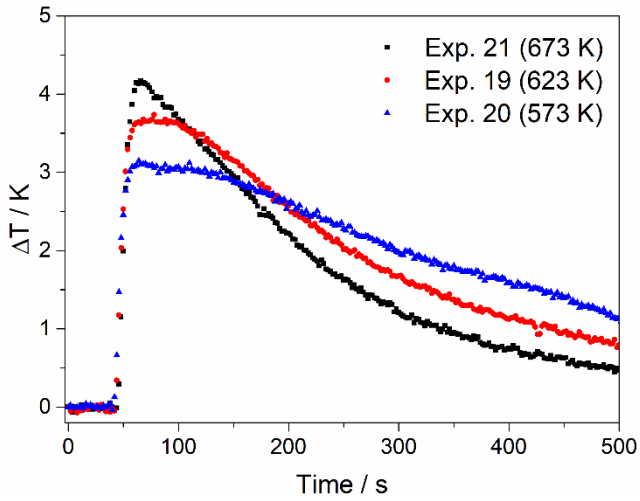

Fig. D.5 - Temperature profiles obtained by the thermocouple placed at 80 mm during the cycles performed at different temperatures, 15 vol% CO_2 balanced with N_2, under dry conditions and 6 bar (experiments 19-21).

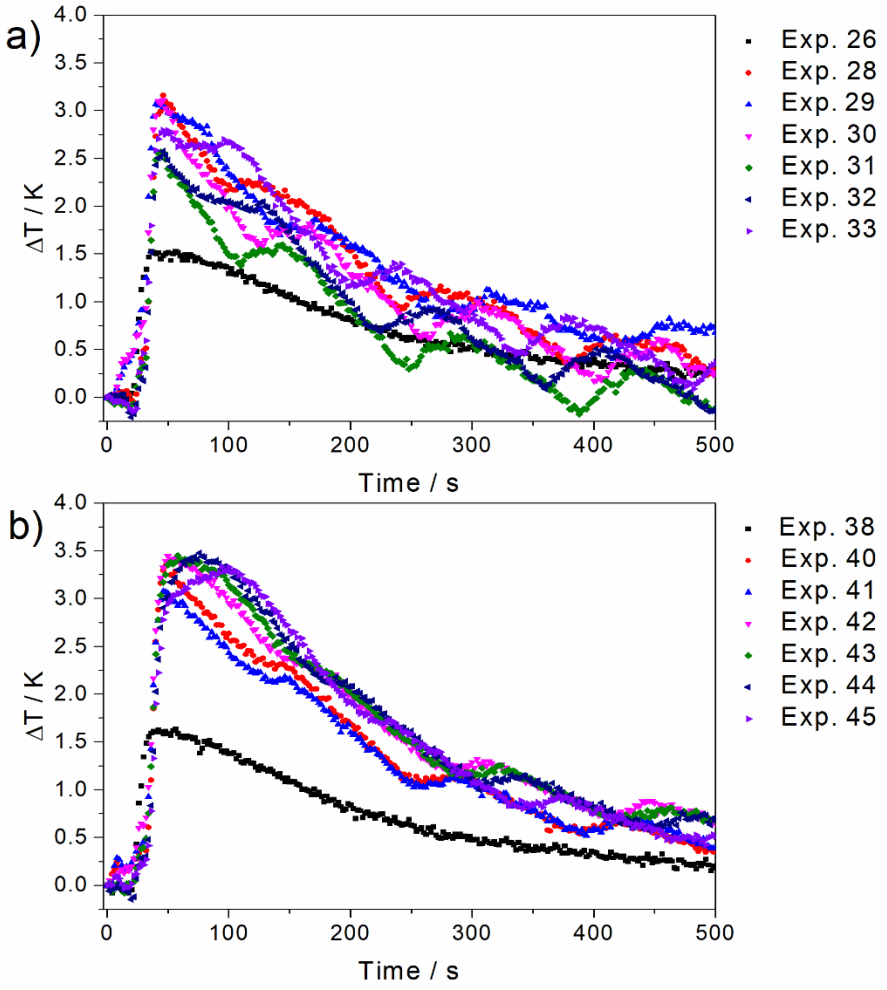

Fig. D.6 - Temperature profiles obtained by the thermocouple placed at 80 mm during sorption for the cycles performed at 673 K, 15 vol% CO_2, total pressure of 6 bar and a) 5 vol% H_2O (experiments 28-33) and b) 10 vol% H_2O (experiments 40-45) balanced with N_2 and comparison with the respective dry cycles performed under the same conditions (experiment 26 and 38, respectively).

Appendix E. Supporting information for subchapter 5.2

Other results of the sorption-enhanced reactor tests

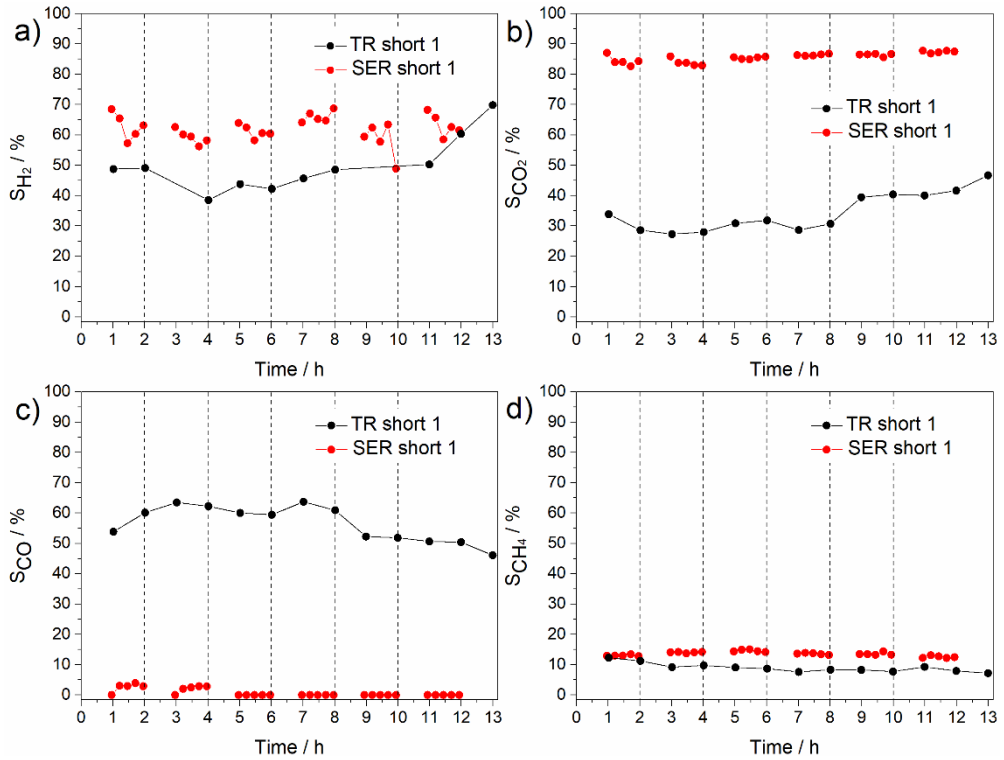

Fig. E.1 - Comparison of the evolution of the selectivities towards (a) H_2, (b) CO_2, (c) CO and (d) CH_4 over time between TR short 1 and SER short 1 experiments (conditions provided in Table 5.2.1). The vertical dashed lines represent the moments at which sorbent regeneration with N_2 was performed.

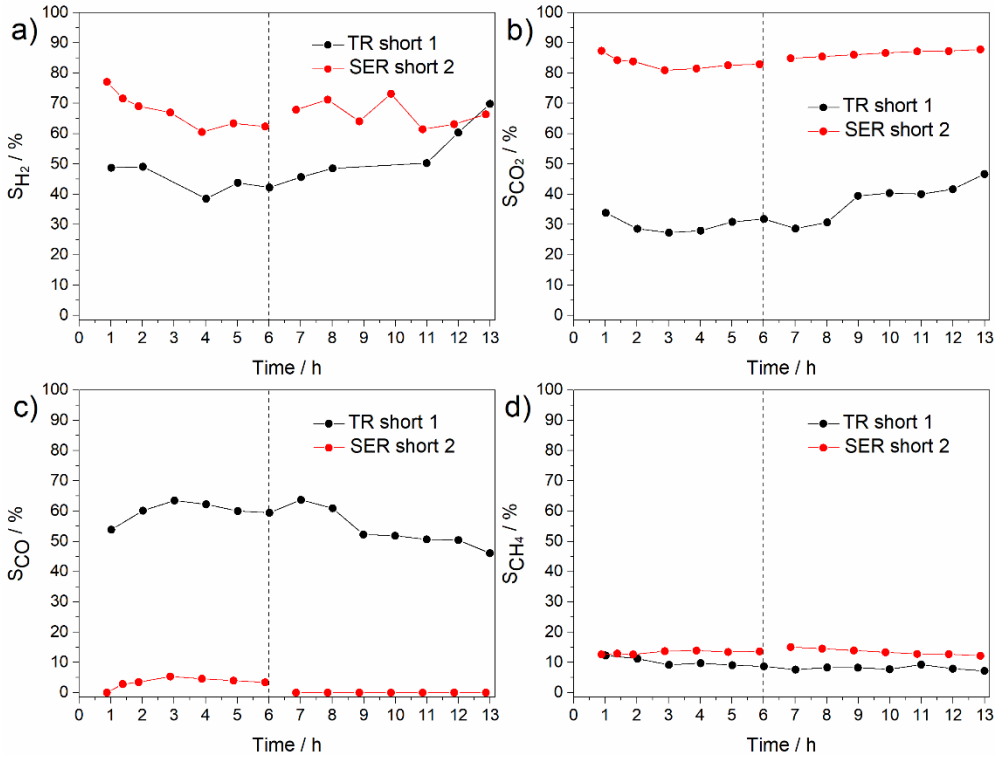

Fig. E.2 - Comparison of the evolution of the selectivities towards (a) H_2, (b) CO_2, (c) CO and (d) CH_4 over time between TR short 1 and SER short 2 experiments (conditions provided in Table 5.2.1). The vertical dashed line represents the moment at which sorbent regeneration with N_2 was performed.

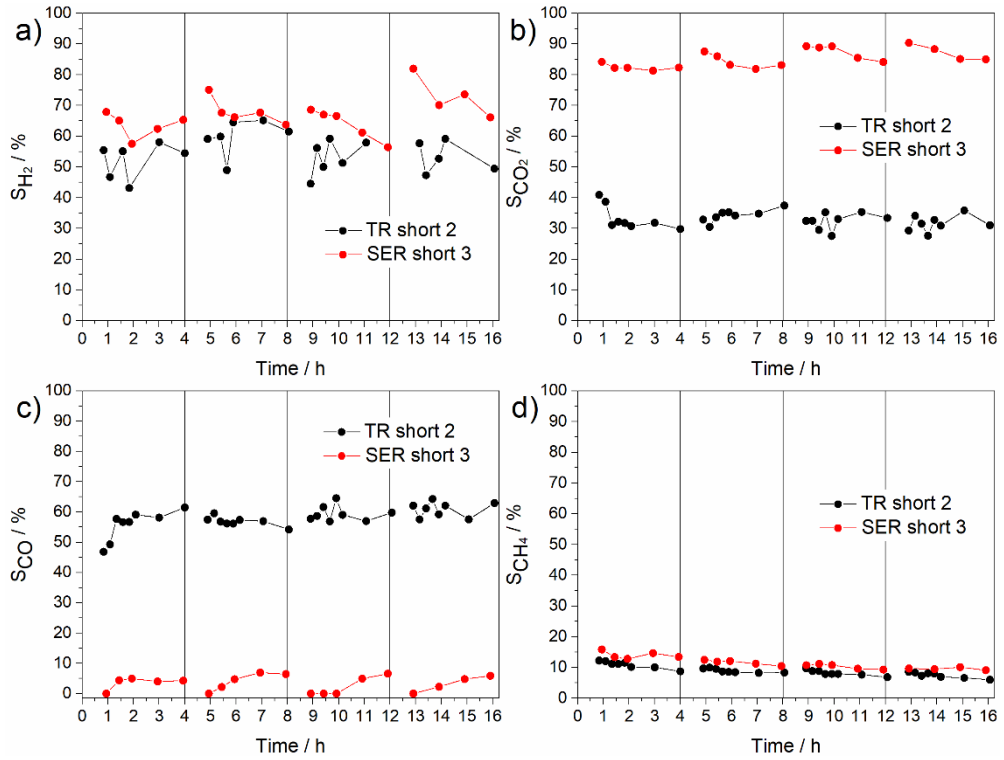

Fig. E.3 - Comparison of the evolution of the selectivities towards (a) H_2, (b) CO_2, (c) CO and (d) CH_4 over time between TR short 2 and SER short 3 experiments (conditions provided in Table 5.2.1). The vertical solid lines represent the moments at which oxidative regeneration was performed.

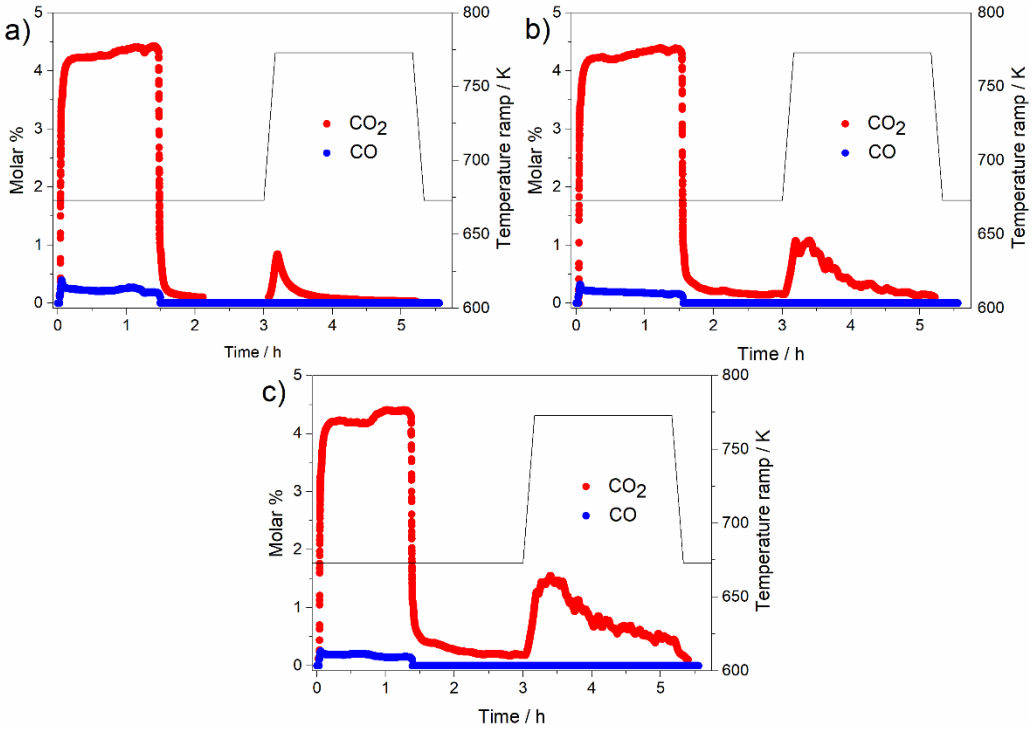

Fig. E.4 - Concentration profiles of CO_2 and CO obtained during oxidative regeneration performed during SER short 3 experiment at (a) 4 h, (b) 8 h and (c) 12 h. Continuous black lines indicate oven temperature set point.

Permeation tests

Before performing the GSR reaction in the SEMR, the 100 μm-thick Pd-Ag membrane was activated in situ at 673 K by feeding 200 $mL_N \cdot min^{-1}$ of pure H_2 at 5 bar. The H_2 in the permeate side was continuously swept in counter-current mode with 200 $mL_N \cdot min^{-1}$ of N_2 at atmospheric pressure. The membrane activation procedure was carried out for 1 week after which the permeating H_2 flux stabilized. Afterwards, pure H_2 permeation tests were performed under a wide range of driving forces, having been observed that the experimental data was in agreement with Sievert's law (Eq. (E.1)) (as shown in Fig. E.5):

$$J_{H_2}^{Siev} = P_{H_2}/\delta \left(\sqrt{p_{H_2,retentate}} - \sqrt{p_{H_2,permeate}}\right) \quad \textbf{(E.1)}$$

where $J_{H_2}^{Siev}$ is the H_2 permeating flux, P_{H_2} is the permeability of the membrane, δ is the membrane thickness, their quotient $\left(P_{H_2}/\delta\right)$ represents the membrane permeance, $p_{H_2,retentate}$ and $p_{H_2,permeate}$ are the partial pressures of hydrogen in the retentate and in the permeate side, respectively.

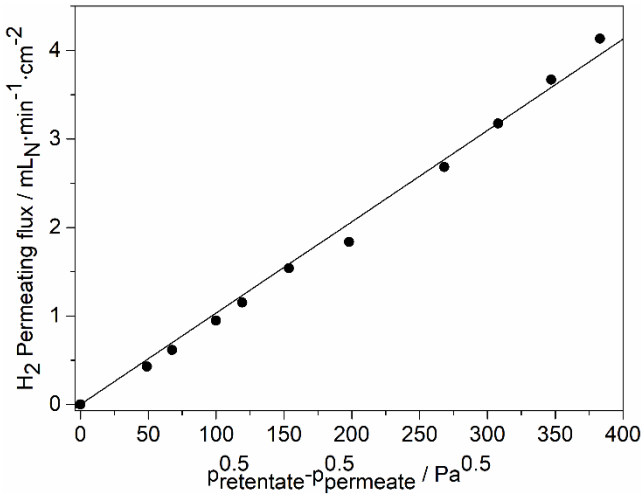

Fig. E.5 - H_2 permeating flux as a function of the difference between the square roots of H_2 partial pressures in the retentate and permeate sides of the Pd-Ag membrane.

This means, as expected, that the diffusion of hydrogen through the metal lattice of this thick membrane is the limiting step, as observed in other works for similar membranes [1, 2].

The permeability of the membrane was determined through the fitting in Fig. E.5 and a value of $7.68 \times 10^{-9}\ \mathrm{mol \cdot m^{-1} \cdot s^{-1} \cdot Pa^{-0.5}}$ was obtained, which is similar to the values usually obtained for similar membranes [1, 3].

Other results of the sorption-enhanced membrane reactor tests

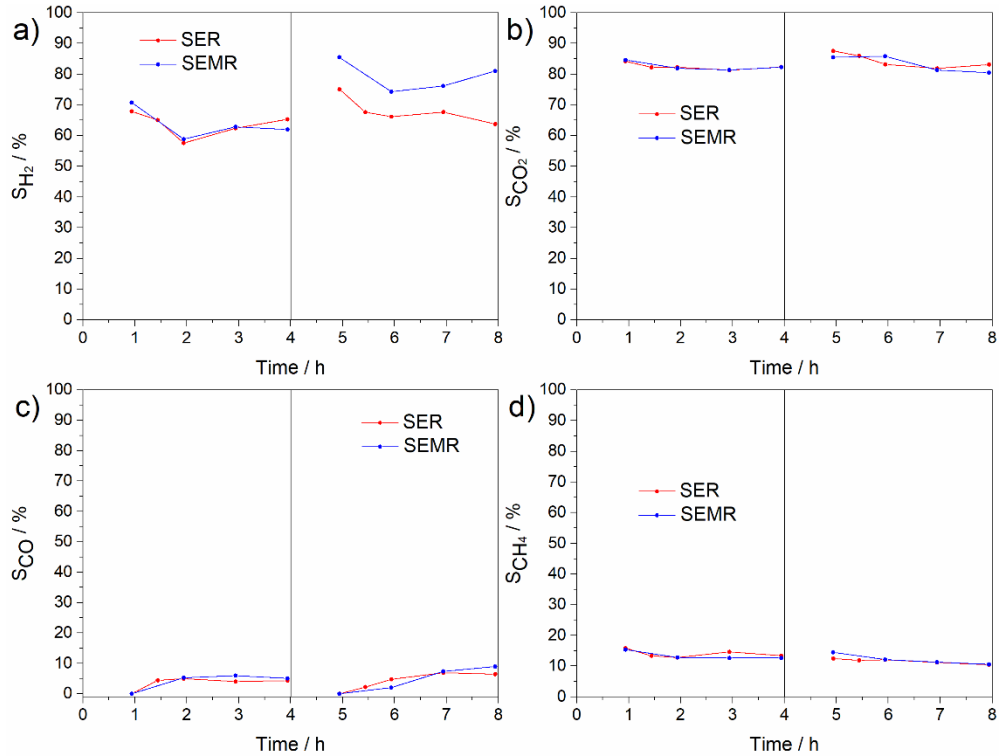

Fig. E.6 - Comparison of the evolution of the selectivities towards (a) H_2, (b) CO_2, (c) CO and (d) CH_4 over time between SER and SEMR. The vertical solid line represents the moment at which oxidative regeneration was performed.

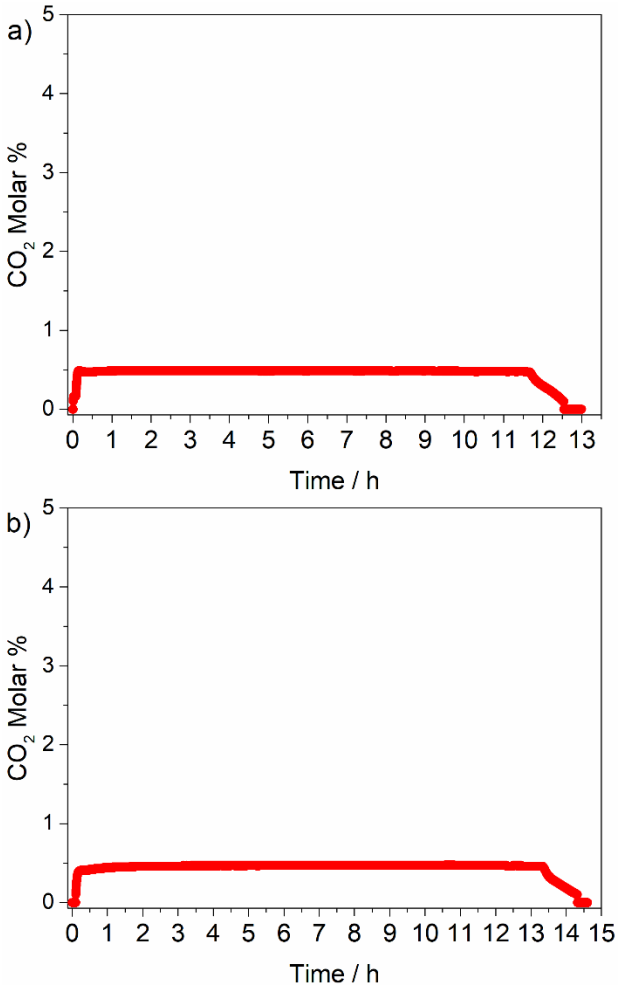

Fig. E.7 - Concentration profiles of CO_2 obtained during oxidative regeneration performed in the SEMR at (a) 4 h and (b) 8 h (conditions provided in Table 5.2.1).

References

[1] Pérez, P., C.A. Cornaglia, A. Mendes, L.M. Madeira, and S. Tosti, *Surface effects and CO/CO2 influence in the H2 permeation through a Pd–Ag membrane: A comprehensive model.* International Journal of Hydrogen Energy, 2015, 40(20), 6566-6572.

[2] Miguel, C.V., A. Mendes, S. Tosti, and L.M. Madeira, *Effect of CO and CO2 on H2 permeation through finger-like Pd–Ag membranes.* International Journal of Hydrogen Energy, 2012, 37(17), 12680-12687.

[3] Santucci, A., F. Borgognoni, M. Vadrucci, and S. Tosti, *Testing of dense Pd–Ag tubes: Effect of pressure and membrane thickness on the hydrogen permeability.* Journal of Membrane Science, 2013, 444, 378-383.